Flux creep in pulsed laser deposited superconducting $YBa_2Cu_3O_7$ thin films

by

E. J. MARITZ

Dissertation presented for the degree of Doctor of Philosophy in Physics at the University of Stellenbosch

Promoter:

Prof. I.P. Krylov, Department of Physics, University of the Western Cape

Co-promoters:

Prof. R. Pretorius, Department of Physics, University of Stellenbosch

Prof. P.R. de Kock, Department of Physics, University of Stellenbosch

5 February 2002

DECLARATION

I, the undersigned, hereby declare that the work contained in this dissertation is my own original work and that I have not previously in its entirety or in part submitted it at any university for a degree.

Signature:..... Date: 5 February 2002

E. J. MARITZ

ABSTRACT

High temperature superconductivity is an important topic in contemporary solid state physics, and an area of very active research. Due to it's potential for application in low temperature electronic devices, the material has attracted the attention of researchers in the electronic engineering and material science fields alike. Moreover, from a fundamental point of view, several questions remain unanswered, related to the origin of superconductivity of this class of materials and the nature of quantised magnetic flux present in magnetised samples.

In this work, flux creep phenomena in a thin superconducting $YBa_2Cu_3O_7$ film deposited by pulsed laser deposition, is investigated near the critical temperature $0 \leq T_c - T \leq 10$ K. Creep activation energy U_0 and critical current density j_c were determined as a function of temperature close to T_c, providing important data to a problem of high-T_c superconductivity which is still a matter of debate. In particular it is still an open question whether restoring the temperature in a creep freezing experiment in fact restores the film to it's original state before the freezing. The most important novel results concern the regime of critical fluctuations in the vicinity $T_c - T < 1$ K.

We studied the isothermal relaxation of trapped magnetic flux, and determined that the long time decay follows a power law, where the exponent is inversely proportional to the creep activation energy. The temperature dependence of the critical current density $j_c(T)$ of the $YBa_2Cu_3O_7$ film close to T_c was obtained during warming runs. It was determined that $j_c(T)$ follows a square root dependence on T to high accuracy in the range $0.2 \leq T_c - T \leq 1.5$ K.

During flux creep experiments an interesting phenomenon called *creep freezing* related to the strong temperature dependence of the relaxation rate was observed. A pronounced slowing of relaxation with only a small drop in temperature from a starting temperature close to T_c was detected. Experiments were conducted by initiating an isothermal flux decay run. At a certain point the temperature was slightly lowered, and the flux decay stopped within experimental accuracy. When the temperature was restored to the initial value, the flux decay resumed at the previous rate before cooling. An argument based on vortex drift velocity was employed to explain the phenomenon qualitatively.

During the course of this investigation, a pulsed laser deposition (PLD) system was designed and built from scratch. PLD involves the interaction of a focussed laser pulse with a multi-elemental solid target material. Material ablated from the target forms a fast moving plume consisting of atomic and molecular particles, directed away from the target, and towards a usually heated substrate on which the particles condense layer by layer to form a thin film. The substrate temperature and background gas are carefully controlled to be conductive to the growth of a desired phase of the multi-elemental compound.

The PLD system proved to be quite versatile in the range of materials that could be deposited. It was used to deposit thin films of different materials, most notable were good quality superconducting $YBa_2Cu_3O_7$, thermochromic VO_2, and magnetoresistive $La_xCa_{1-x}MnO_3$. Metallic Au and Ag layers were also successfully deposited on $YBa_2Cu_3O_7$ thin films, to serve as protective coatings. The critical temperatures of the best superconducting films were 90 K as determined by resistivity measurement. The optimal deposition conditions to deposit high quality superconducting $YBa_2Cu_3O_7$ thin films was found to be: deposition temperature 780°C, laser energy density 2-3 J/cm^2, oxygen partial pressure 0.2 mbar, and target-substrate distance 35 mm. This yields film with $T_c \sim 90$ K. It was found that deposition temperature plays the predominant role in determining the quality of $YBa_2Cu_3O_7$ thin films deposited by PLD.

OPSOMMING

Hoë temperatuur supergeleiding is tans ’n aktuele onderwerp van vastetoestandfisika en dit is ’n gebied van baie aktiewe navorsing. Weens die potensiaal vir toepassings van hoë temperatuur supergeleiers in elektronika, het dié klas materiale die aandag van fisici and elektronici getrek. Verskeie fundamentele vraagstukke bly steeds onbeantwoord, veral met betrekking tot die oorsprong van supergeleiding in hierdie materiale en die gedrag van gekwantiseerde magnetiese vloed (*“vortekse”*) in gemagnetiseerde monsters.

In hierdie werk word diffusie van vortekse in dun supergeleidende $YBa_2Cu_3O_7$ films ondersoek naby die kritieke temperatuur ($0 \leq T_c - T \leq 10$ K). Die temperatuur afhanklikheid van die diffusie aktiveringsenergie U_0 en die kritieke stroomdigtheid j_c word bepaal naby T_c. Dit verskaf belangrike inligting tot probleme in hoë temperatuur supergeleiding wat tans nog onbeantwoord bly. In die besonder is dit steeds ’n ope vraag of die herstel van die aanvanklike temperatuur in ’n vloedstollings eksperiment waarlik die film tot die oorspronklike toestand herstel. Die belangrikste nuwe resultate hou verband met die gebied van kritieke fluktuasies van die orde parameter in die omgewing $0 < T_c - T < 1$ K.

Ons het die isotermiese ontspanning van vortekse verstrik in die kristalstruktuur bestudeer, en bepaal dat die lang tydsverval ’n magsverwantskap handhaaf, waar die eksponent omgekeerd eweredig is aan U_0. Die temperatuur afhanklikheid van die kritieke stroomdigtheid $j_c(T)$ van die $YBa_2Cu_3O_7$ film naby T_c is bepaal tydens verhittingslopies. Daar is bevind dat naby T_c, j_c ’n vierkantswortel verband met T volg, tot hoë noukeurigheid in die gebied $0.2 \leq T_c - T \leq 1.5$ K.

Gedurende vorteksdiffusie eksperimente is ’n interessante verskynsel naamlik *vloedstolling* (*“flux freezing”*) waargeneem. Dit hou verband met die sterk temperatuur afhanklikheid van die vervaltempo van die magnetiese moment van ’n gemagnetiseerde film. ’n Skerp daling van die vervaltempo, weens slegs ’n klein temperatuurdaling vanaf die begin temperatuur naby T_c, is waargeneem. Gedurende eksperimente is daar aanvanklik ’n isotermiese vloedontspanning teweeg gebring. Op ’n sekere tydstip is die temperatuur effens verlaag, waarby die vloedontspanning tot stilstand gekom het binne grense van waarneming. Wanneer die temperatuur weer herstel is na die oorspronklike, het die vloedontspanning voortgegaan teen die tempo voor die temperatuurverlaging. ’n Verklaring wat gebaseer is op vorteks dryfsnelheid was aan die hand gedoen om hierdie gedrag te verklaar.

’n Groot komponent van die projek was om die dun $YBa_2Cu_3O_7$ films self te vervaardig. Tydens hierdie ondersoek, is ’n gepulseerde laser deposisie (*“PLD”*) sisteem eiehandig ontwerp en gebou. PLD behels die interaksie van ’n gefokuseerde laser puls met ’n teiken bestaande uit ’n multi-element vastestofverbinding. Materiaal wat verdamp (“*ablate*”) word, vorm ’n snelbewegende pluim bestaande uit atomiese en molekulêre deeltjies. Dit beweeg vanaf die teiken na ’n verhitte substraat, waarop die deeltjies kondenseer om laag vir laag ’n dun film te vorm. Die substraat temperatuur en agtergrond gas word sorgvuldig beheer om die groei van die verlangde fase van die multi-element verbinding teweeg te bring.

Die PLD sisteem is baie veeldoelig ten opsigte van die verskeidenheid materiale wat suksesvol neergeslaan kan word. Dit was aangewend om verskillende materiale neer te slaan, onder andere supergeleidende $YBa_2Cu_3O_7$, termochromiese VO_2, en magnetoresistiewe $La_xCa_{1-x}MnO_3$. Geleidende Au en Ag lagies is ook suksesvol neergeslaan op $YBa_2Cu_3O_7$ dun films, om te dien as beskermingslagies. Die kritieke temperatuur van die beste supergeleidende films was 90 K soos bepaal deur weerstandsmetings. Die optimale neerslaan toestand vir hoë kwaliteit $YBa_2Cu_3O_7$ dun films was: substraat temperatuur 780°C, laser energiedigtheid 2 - 3 J/cm^2, suurstofdruk 0.2 mbar, en teiken-substraat afstand 35 mm. Daar is bevind dat die substraat temperatuur die deurslaggewende rol speel tydens die neerslaan proses om die kwaliteit van die supergeleidende films te bepaal.

DEDICATION

To Anna-marie, for believing with me,
and Etienne, for joining us on the way.

ACKNOWLEDGEMENTS

The author would like to express his appreciation to:

- Prof. Igor Krylov of the department of Physics, University of the Western Cape, promoter, for his guidance, active participation, continuous support and constructive discussions throughout this investigation,

- Prof. René Pretorius of the department of Physics, University of Stellenbosch, co-promoter, for initiating this project and helping to draw it to a satisfactory close,

- Prof. Runan de Kock of the department of Physics, University of Stellenbosch, co-promoter, for helpful discussions and his careful reading of the manuscript,

- Dr. Stephan Senz from the Max Planck Institute of Microstructure Physics in Halle(Saale), Germany, for his help with x-ray diffractometry,

- Drs. Christopher Curran and Emmanuel Nyenachi, for fruitful collaboration and discussions during their time as post-doctoral fellows at the NAC,

- Dr. Torsten Freltoft, of Sophion, Denmark, for guidance with PLD early on, during his sabbatical at the National Accelerator Centre (NAC),

- Dr. Chris Theron, NAC, for his help with Rutherford backscattering analysis, and assistance with computing,

- Prof. Chris Demanet, of the department of Physics, University of the Transkei, for helpful comments on AFM work,

- Mr. Lawrence Ashworth, NAC, for expert help with mechanical apparatus,

- Messrs. Hennie Smit and Ron Quantrill, NAC, for design of mechanical devices and the PLD system,

- Ms. Sue Marais of the Central Analytical Facility, University of Stellenbosch, for operating the atomic force microscopy system,

- Drs. Malik Maaza and Khalid Bouziane, of the department of Physics, University of the Witwatersrand, for fruitful time of collaboration on the deposition of vanadium oxide,

- Prof. Piet Walters and Mr. Ulrich Deutchlander of the department of Physics, University of Stellenbosch, for expert help with the excimer laser,

- Mr. Herbert Pienaar, of the department of Geology, University of Stellenbosch, for expert help on x-ray diffractometry measurements,

- My parents for their ongoing support,

- My wife, Anna-marie, for her enduring encouragement and love.

Contents

List of Figures

List of Tables

Chapter 1

Introduction

1.1 Magnetic flux creep phenomena

The discovery of high-temperature superconductivity in copper-oxide-based materials caused great expectations of a new class of superconducting electronic devices at liquid nitrogen temperature and higher. This euphoria amongst the scientific and technological communities diminished as researchers found that the persistent supercurrents in these materials decay with time. It also became evident that superconducting materials with T_c beyond the 130 K range would not be forthcoming rapidly.

The difficulty with the current decay is not related to resistivity, but rather to a dissipation occasioned by thermally activated motion of magnetic flux inside the superconductor[1, 2]. This magnetic relaxation has now become a fascinating and widely studied phenomenon on it's own right; while technological exploitation of high-temperature superconductivity has progressed nonetheless.

The relaxation is typically observed in measurements of the magnetic dipole moment of high-temperature superconductors. The dipole moment (or magnetisation) is observed to decrease with time, in an approximately logarithmic manner. Large magnetic relaxation rates have been observed in all the known families of high-temperature superconducting materials.

Magnetic relaxation was first studied in low-temperature superconductors, but the effect was typically so small that it took especially sensitive experimental techniques to detect it. Anderson and Kim[3, 4] devised a model to describe the effect. Using the concept of thermal activation of magnetic vortices out of pinning centers, which proceeds at a rate proportional to a Boltzmann factor $\sim \exp(-U/kT)$, where U represents the activation energy, they predicted a logarithmic decay with time. This *magnetic flux creep* leads to a redistribution of vortices in a magnetised sample, causing a change in the magnetic moment with time. The magnetic moment then decays when vortices escape at the periphery of the sample.

Comparably very strong relaxation was discovered in bulk single crystals of $YBa_2Cu_3O_7$ by Worthington *et al*[5] and by Yeshurun and Malozemoff[6]. In Yeshurun *et al*'s experiments the rate of magnetic relaxation was large, with a 20% decrease over two decades in time at 50 K, and with higher rates at higher temperatures. It soon became clear that the basic Anderson-Kim[3, 4] theory failed to explain some important details of magnetic flux creep in high-temperature superconductors. Careful analysis over many orders of magnitude of time revealed significant deviations from logarithmic time behaviour. Most of this work has been done in the region of the phase space of magnetic field—temperature ($B-T$), which lies outside the regime of critical fluctuations where the fluctuations of the amplitude of the superconducting order parameter $|\psi|$ are of the same order as $|\psi|$ itself. Outside this region all the fluctuation degrees of freedom involve only the phase of the order parameter, which can be described by fluctuations in the position of the vortices[7]. Thus earlier flux creep was studied far below the critical temperature.

In this work, we report measurements of the remanent flux creep in thin superconducting films deposited by pulsed laser deposition, over a range of temperatures up to $T_c - T = 0.05$ K, where it was experimentally possible to get into the usually inaccessible long-time limit of the persistent current decay. The functional form of the time dependence of magnetisation of a thin film is reported, and also the functional forms of both U and critical current density j_c in the range $T_c - T = 10 - 0.05$ K.

1.2 Pulsed laser deposition

The study of laser ablation - the emission of material by the interaction of a laser with a surface, dates back to 1962 (F. Breech and L. Cross[8]), not long after N. Basov demonstrated the first laser[9]. A focused ruby laser was used to vapourise and excite atoms from solid surfaces and thus characterise the elements ejected by photon emission spectroscopy. Their work initiated the field of laser microprobe emission spectroscopy with applications in geology, the biological sciences and the production industry. An important later development of laser ablation is in the area of laser surgery, of particular significance are eye surgery and the ablation of arterial blockages. J.F. Ready[10] employed high-speed photography to study the temporal and spatial profile of the ablated plume of ejected material. He showed that the plume from a carbon block emerged after the peak of the laser pulse and had it's maximum brightness about 120 ns after the start of the laser plume. The plume lasted several microseconds. The velocity of the plume's leading edge was estimated to be 2×10^6 cm/s.

The first demonstration of laser deposition of thin films was performed by H.F. Smith and A.F. Turner[11] in 1965. They ablated a variety of materials with a ruby laser and demonstrated that thin films could be grown this way. This application area developed very slowly as sputtering and chemical vapour deposition (CVD) techniques yielded better quality films. Only in the nineties did the quality of pulsed laser

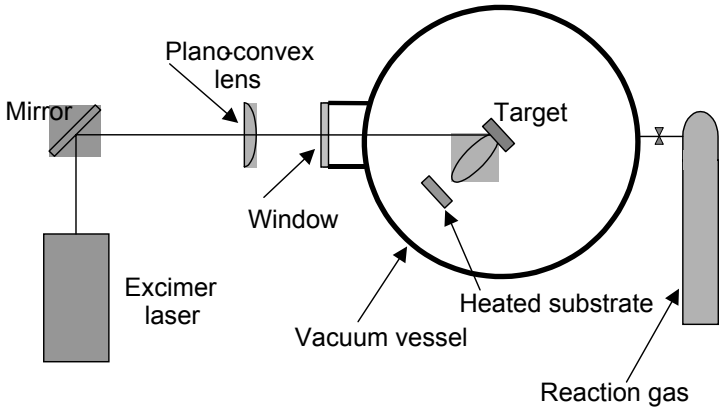

Figure 1-1: *Planar view of the optical path and deposition principle of the PLD system. Notice that the incoming laser path makes a 45° angle with the normal of the target surface.*

deposited films improve to such an extent as to rival CVD and MBE techniques. The development of pulsed laser deposition (PLD) as a serious deposition technique was dependent on the improvement of available lasers. The development of Q-switched YAG lasers and excimer lasers provided the necessary energetic laser beams.

The observation that laser ablation transfers a multicomponent solid stoichiometrically and allows oxygenation and other chemistry to occur in transit from target to substrate is truly remarkable. Virtually all materials - metals, semiconductors, and insulators - can be deposited. This almost unique property of PLD explains why the advent of high-T_c superconductors prompted many laboratories to use PLD techniques to prepare and study these materials. The first successful deposition of high temperature superconducting (HTS) materials ($YBa_2Cu_3O_7$) was achieved in 1987 by D. Dijkkamp *et al*[12] and X.D. Wu *et al*[13]. In fact, one can observe that it was the discovery of HTS materials that gave the impetus to PLD to develop to the mature technique that it is today[14]. It has been demonstrated that the composition of rather complex multi-elementary materials can be reproduced in the film under appropriate conditions of laser-energy density and deposition angle with respect to the target surface normal[15].

Fig. 1-1 show a simple schematic of a pulsed laser deposition system, where an excimer laser pulse is incident on a stoichiometric target of the material of interest.

The evaporated material is predominantly ejected in the forward direction and under suitable back-

ground pressures of oxygen (0.1 mbar) and substrate temperatures of around 750°C, high quality superconducting films are grown *in situ*. **Table 1.1** summarises some of the work done recently, quoted from Saenger[16]. This indicate the broad versatility of the technique.

Table 1.1: *Brief summary of HTSC materials deposited by PLD.*

Material	**Laser**	**Reference**
$Ba_{1-x}KBiO_3$	ArF	B.M. Moon *et al.*, 1991[17]
$La_{1.85}Sr_{0.15}CuO_x$	KrF	M.Y. Chern *et al.*, 1992[18]
BiSrCaCuO	Nd-YAG	A. Cheenne *et al.*, 1990[19]
$HoBa_2Cu_3O_{7-x}$	KrF	D.B. Geohegan *et al.*, 1988[20]
$Nd_{2-x}Ce_xCuO_4$	KrF	A. Gupta *et al.* 1989[21]
$YBa_2Cu_3O_7$	XeCl, KrF[12], Nd-YAG, ArF	J. Narayan *et al.*, 1987[22]
$SaBa_2Cu_3O_7$	XeCl	R.A. Neifeld *et al.*, 1988[23]
TlMaCaCuO	Nd-YAG, KrF	B. Johs *et al.*, 1990[24]

Several unique features of PLD can be identified:

1. PLD requires relatively little sophisticated equipment. The most expensive and sophisticated part is the excimer laser, which is a general purpose laser, and is normally used in other capacities alongside PLD work, thus making it's operation more cost effective.

2. In striking contrast to sputtering which can be very preferential concerning the atomic species sputtered, the laser pulse is relatively indiscriminate in it's ablation of the target. Thus PLD leads to stoichiometric ablation due to congruent evaporation. Rather complex multi-element materials can be deposited relatively easy, provided a single-phase, homogeneous target can be fabricated. The complexity of the deposition process is reduced to the simpler process of preparing a high-quality target.

3. Deposition parameters such as chamber pressure, target-substrate distance, target orientation with respect to the laser beam, laser energy density, *etc.* can be independently controlled, enabling a greater degree of freedom in the deposition system design and deposition conditions.

4. The efficiency of target use is superior as compared to any other technique since a predominant amount of the evaporated material is forward directed and can be collected effectively on a substrate.

5. The fabrication of multi-layers is fairly straightforward with rapid substitution of targets into the path of the laser beam. Automated systems are capable of producing sophisticated thin film structures.

1.3 Structural properties of $YBa_2Cu_3O_7$

1.3.1 Tetragonal and orthorhombic phases

$YBa_2Cu_3O_7$ is a material rich in interesting phenomena, both from a purely scientific point of view, as well as technological. A high critical current density can be achieved at 77 K, making the material attractive for electronic devices operating at liquid nitrogen temperature[25]. Commercially available HTS SQUID's[1] using $YBa_2Cu_3O_{7-\delta}$ (YBCO) film are examples of technological applications of processed YBCO thin film. Bulk HTS materials can only be produced as ceramics, which makes it's use in the power applications difficult, and this field is still not at the level of real life utility. The manufacture of flexible tapes and cable for power applications have met more success with the $Bi_2Sr_2CaCu_2O_8$ (BSCCO) materials than with YBCO, while YBCO is the most successful HTS material for thin film based applications.

Superconductivity in the copper oxide systems occurs near a structural instability (orthorhombic $\leftrightarrow$ tetragonal) as well as a metal-insulator transition which can be controlled by so-called oxygen doping (**Fig. 1-2(a)**). At low temperatures, the metallic phase becomes superconducting, while the insulating phase shows long range antiferromagnetic order. Superconductivity with $T_c \simeq 92$ K was discovered[28] in the system Y-Ba-Cu-O in a sample with a mixture of phases, and later the superconducting compound was identified as $YBa_2Cu_3O_y$, with $y \simeq 7.0$. The structure of most of the high temperature superconductors are layered perovskite with large anisotropy, and $YBa_2Cu_3O_7$ is no exception[29]. In the system $YBa_2Cu_3O_{7-\delta}$ there exist two thermodynamically stable structures; the orthorhombic, superconducting $YBa_2Cu_3O_7$ ($\delta = 0$) and the tetragonal insulating $YBa_2Cu_3O_6$ ($\delta = 1$). Unit cells are shown in **Fig. 1-2(b-c)**, and their similarity is apparent. The position of the cations are essentially the same in both, while some reordering takes place amongst the oxygen atoms. In this chapter, extensive use is made of the work of C.P. Poole *et al*[30].

1.3.2 Crystallographic parameters

X-ray diffraction and neutron diffraction studies were done to discover the structure of the superconducting compound. The structural parameters of $YBa_2Cu_3O_7$ at room temperature are listed[2] in **Table 1.2** below, quoted from J.D. Jorgenson *et al*[27]. Comparing **Table 1.2** with the unit cell displayed in **Fig. 1-2(b)** reveals that the yttrium atom occupies the central position of three blocks stacked on top of each other, with a barium atom in the centre of each of the other two blocks. Each block is a cube

[1] (**S**uperconducting **QU**antum **I**nterference **D**evice)

[2] The reader should note that some authors refer to the O-atoms at $(0,\frac{1}{2},0)$ as O(4) and at (0,0,0.1581) as O(1)[31]. This work uses the other nomenclature.

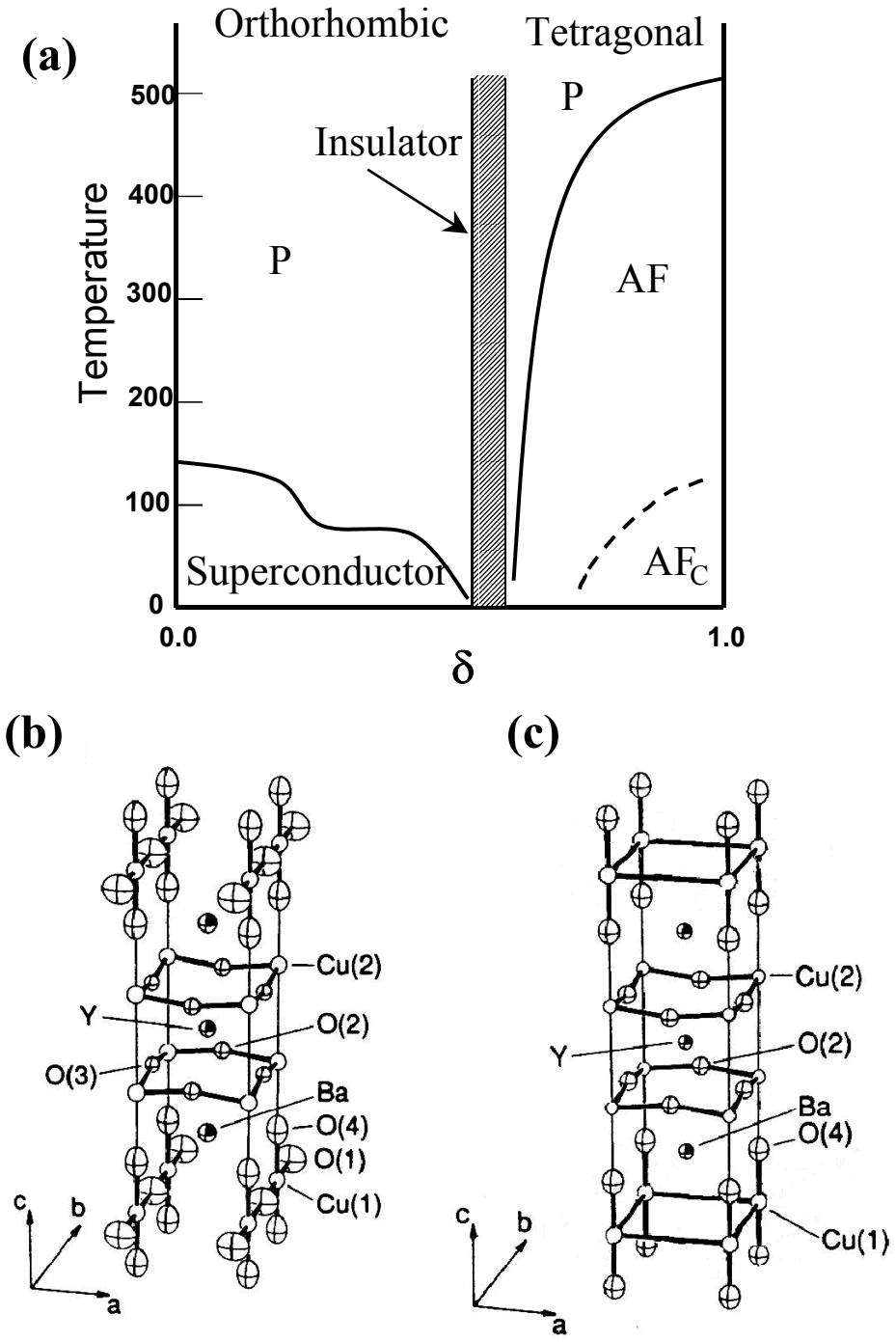

Figure 1-2: *(a) Schematic phase diagram for $YBa_2Cu_3O_{7-\delta}$ as a function of oxygen concentration δ on the "chain" sites. The paramagnetic (P) and antiferromagnetic (AF) phases are shown, as well as an antiferromagnetic phase found at lower temperatures (AF_c) where the spins on the Cu chains order[26]. (b) Orthorhombic ($YBa_2Cu_3O_7$) and (c) tetragonal ($YBa_2Cu_3O_6$) phases of the YBCO system[27]. YBCO films with the c-axis pointing perpendicular to the substrate plane are called c-axis orientated film.*

Table 1.2: *Crystallographic data of* $YBa_2Cu_3O_7$

Space group *Pmmm*, $\rho_c = 6.38$ g/cm^3
Lattice parameters $a = 0.38198(1)$ nm, $b = 0.38849(1)$ nm, $c = 1.16762(3)$ nm

Atom	**x**	**y**	**z**	**Occupancy**
Y	$\frac{1}{2}$	$\frac{1}{2}$	$\frac{1}{2}$	1.0
Ba	$\frac{1}{2}$	$\frac{1}{2}$	0.1839(2)	1.0
Cu(1)	0	0	0	1.0
Cu(2)	0	0	0.3547(1)	1.0
O(1)	0	$\frac{1}{2}$	0	1.0
O(2)	$\frac{1}{2}$	0	0.3779(2)	1.0
O(3)	0	$\frac{1}{2}$	0.3776(2)	1.0
O(4)	0	0	0.1581(2)	1.0

of the original perovskite unit cell. Copper atoms occupies the corners of the three blocks, and oxygen atoms occupies some of the positions between the copper atoms. The three mirror planes signified by the space group *Pmmm* is also easy to observe from **Fig. 1-2**. No crystallographic phase transitions was ever observed in going from room temperature down to 10 K. The cations in $YBa_2Cu_3O_6$ occupy the same relative positions although the exact coordinates differ marginally. When physical properties of YBCO is discussed, the subscript c is usually used to indicate the property as measurement in the direction parallel to the c-axis (vertical in **Fig. 1-2**). Because of the similarity of the crystal along the $a-$ and $b-$directions, there are very seldom any distinction made between the $a-$ or $b-$directions. Twinning, which interchange a and b, also makes the distinction between the two crystallographic directions superfluous. Thus the subscript ab is used to indicate that the property is measured in the $ab-$plane.

1.3.3 Oxygen ordering in $YBa_2Cu_3O_7$

It was recognised very early in the study of high temperature superconductivity that copperoxide plays a dominant role in the structure of virtually all HTS materials. $YBa_2Cu_3O_{7-\delta}$ is no exception and it is important to understand the oxygen ordering in it. As shown in **Fig. 1-2(b)**, the Cu(1) atom at $(0, 0, 0)$ and the O(1) atom at $(0, \frac{1}{2}, 0)$ form chains along the $b-$axis of the unit cell. The atoms Cu(2) are strongly bonded to the four oxygen atoms O(2) and O(3), forming the basis of a pyramid, and are weakly bonded to the oxygen atom O(4) at the apex. Because of this feature, there exists structural two-dimensional layers of copper and oxygen atoms perpendicular to the $c-$axis. Both the copper oxide plane and the chains contribute to the superconducting properties. The oxygen atoms in these layers are slightly shifted from their ideal perovskite positions, producing the puckering of the layers indicated in **Fig. 1-2**.

When $\delta = 0.0$, all the oxygen positions are filled, and when $1.0 \geq \delta > 0.0$, it has been shown

that the oxygen vacancies are always confined to the O(1) sites in the copper oxide chains[31]. Also, the total oxygen stoichiometry decreases smoothly with increasing temperature of the sample, and the vacancies associated with this decrease are confined to the O(1) sites[27]. As heating continues, oxygen escapes from the lattice, while concurrently, the positions $(\frac{1}{2}, 0, 0)$ are gradually filled up to a maximum occupancy of about 0.2 until the structure from orthorhombic *Pmmm* becomes tetragonal *P4/mmm* at about 700°C, see **Fig. 1-2(c)** and **Fig. 1-3.** In the tetragonal phase the positions $(\frac{1}{2}, 0, 0)$ and $(0, \frac{1}{2}, 0)$ are symmetrically equivalent, and these positions are completely empty at $\delta = 1.0$. This transition, induced by oxygen stoichiometry, is a function of the temperature and the oxygen partial pressure in the sample container. At one atmosphere of O_2 pressure, the orthorhombic phase exists over the range $0.0 \leqslant \delta \leqslant 0.5$, the tetragonal phase forms at $\delta \approx 0.5$ and exists over the range $0.5 \leqslant \delta \leqslant 1.0$. As δ increases over 0.5, the oxygen diffuses from the O(1) sites and escapes from the lattice until the O(1) are empty at $\delta = 1.0$. The orthorhombic phase is superconducting, with T_c decreasing as δ increases from 0.0 to 0.5, **Fig. 1-2(a)**. The tetragonal phase is semiconducting.

YBaCuO is prepared by heating in the $750 - 900$°C range in the presence of various concentrations of oxygen. The compound is tetragonal at the highest temperatures, increases it's oxygen content through oxygen uptake and diffusion[32] as the temperature is lowered, and undergoes a second-order phase transition of the order-disorder type at about 700°C to the low-temperature orthorhombic phase, as indicated in **Fig. 1-3**. Quenching by rapid cooling from a high temperature can produce the tetragonal phase at room temperature, and slow annealing favours the orthorhombic phase. A sample stored under sealed conditions exhibited no degradation in structure or change of T_c four years later[33]. However, exposure to air is known to degrade the material in a matter of weeks due to interaction with moisture.

1.4 Substrates

1.4.1 Criteria for substrate selection

The choice of substrate is a very important factor in the growth of high quality YBCO thin films. YBCO as other HTS materials, possess a challenging set of properties which makes the growth of high quality single crystalline thin films difficult. The material is composed of four elements that must be deposited within close tolerance of the correct ratio to ensure best superconducting properties such as high critical temperature and high critical current density. Film growth takes place at elevated temperatures in an oxygen ambient. This environment places specific restrains on the choice of substrate, since the material must be inert in this ambient, and also not reactive with the metallic components of the superconductor.

The crystallinity of thin films is extremely important. Due to the anisotropic nature of YBCO, the crystallographic alignment of the film must be correct. From an application point of view, the alignment

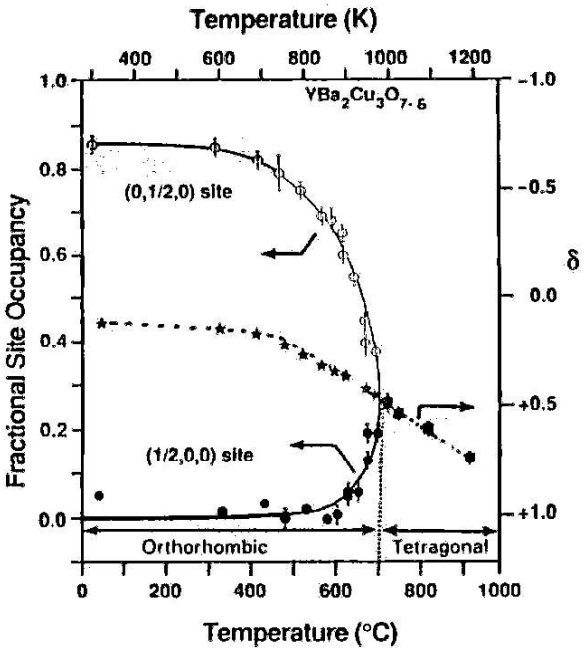

Figure 1-3: *Fractional occupancies of the ($\frac{1}{2}$,0,0) (bottom) and (0,$\frac{1}{2}$,0) (top) sites (scale on left), and the oxygen content parameter δ (center, scale on right) for quench temperatures of YBaCuO in the range 0-1000°C. The δ parameter curve is the average of the two site-occupancy curves. Since the allowed occupancy for the ($\frac{1}{2}$,0,0) site in the tetragonal phase is two atoms per unit cell, the fractional occupancies for this site must be doubled to yield the number of oxygen atoms per unit cell.[27]*

with c-axis perpendicular to the substrate plane is the best, to ensure highest critical current through the film. In addition it is desirable that the mosaic spread be kept as small as possible. This means the a/b-directions of the film's grains should be aligned.

Ideally, the substrate should provide mechanical support but not interact with the film except for sufficient adhesion, and provide a template for atomic ordering. In practice, the substrate exerts considerable influence on film characteristics.

The most important issues regarding substrate selection is discussed point by point[34];

1. *Chemical compatibility:* Ideally there should be not chemical reactions between the film and the substrate. The relative high temperatures required for growing films make the compatibility requirement more critical than it would be if the high quality film could be grown at lower temperature. Thus, the substrate must be unreactive in the oxygen-rich ambient required for growth and processing. Oxide substrates are more likely to tolerate the growth requirements of HTS materials than non-oxide materials.

2. *Thermal-expansion match:* Many film-substrate combinations will be more or less mismatched with regard to thermal expansion. This may result in loss of adhesion or film cracking during thermal cycling. The brittleness of YBCO increases the possibility of cracking. The problems introduced the thermal-expansion mismatch are most severe if the system must tolerate extreme temperatures, whether it be during film growth, processing, or in the life of the finished product.

3. *Surface quality:* It is at the surface where the film-substrate interaction takes place, so naturally, all deviations from the perfect state could potentially influence the film growth negatively. The surface must be atomically flat, dense and free of twins and other structural inhomogeneities. Numerous surface defects can be encountered, ranging from the atomic scale : point defects, dislocations and twin boundaries, to the macroscopic scale polishing scratches, surface warp and cracks.

4. *Substrate homogeneity:* Not only surface quality, but also the quality of the bulk is likely to affect film growth. Phase purity is important, otherwise the surface quality is likely to suffer. Grain boundaries should not reach to the surface, and the substrate should have the theoretical density and thus no voiding. Any such bulk imperfections are likely to influence the surface, which will induce defects in the film.

5. *Substrate thermodynamic stability:* A phase transition of the substrate within the processing and utilisation temperature range can have dramatic effects on the surface quality of the substrate and cause tremendous stress buildup in the film, possibly leading to cracks.

6. *Lattice match:* The first criterium generally considered in selecting a substrate for epitaxial growth is it's lattice match with the film. Studies indicated that for epitaxial films to grow, a lattice mismatch of less than 15% is required[35]. The ability to obtain singularly orientated film is improved by minimising the lattice mismatch as much as possible, although several substrates with large lattice mismatch have been used successfully to deposit HTS film on, for example YBCO on MgO, discussed later.

7. *Coincidence sites:* In general, lattice match is not the only important factor to ensure good epitaxy; there must be a number of coincidence sites between the two lattices. These are atomic positions (preferably occupied by atoms with similar sizes and valences) that coincide on either side of the surface[34]. Frequently, this is the case where the film and substrate have similar crystal structures. R. Guo *et al*[36] have shown that the primary consideration for substrate selection is similarity in interatomic structure, including the ionic distributions and distances. The *in situ* growth of YBCO on MgO(001) is a good example of epitaxial film growth despite the relatively large mismatch of 8.8%, due to large number of coincidence sites.

Table 1.3: *Summarised data on $SrTiO_3$ and MgO.*

Quantity	**$SrTiO_3$**	**MgO**
lattice parameter	0.39050 nm	0.42115 nm
lattice mismatch μ	-1.3%	-8.8%
structure	cubic	cubic
density	5.12 g/cm^3	3.58 g/cm^3
melting point	2080°C	2800°C
thermal expansion coeffient	9×10^{-6} K^{-1}	8×10^{-6} K^{-1}
dielectric constant ε	277	9.65

Substrates were purchased as 10 × 10 mm squares of 0.5 mm thick, with the surface flat to a specification of 1 μm across a two inch diameter. The surface roughness was specified as within 1.5 nm[37]. Using a contactless interferometric measurement the supplier of the substrates determined the roughness parameter $R_a \simeq 0.5$ nm, R_a being the average deviation from the mean line within the assessment length. Due to the relatively close lattice match with these substrates, the epitaxial relationship [001] || [001] is satisfied for MgO and $SrTiO_3$. **Table 1.3** summarised certain important parameters of the substrates under discussion[38]**.**

The lattice mismatch, μ, is calculated as

$$\mu = \frac{a_{film} - a_{substrate}}{\frac{1}{2}(a_{film} + a_{substrate})} \times 100\%. \tag{1.1}$$

1.4.2 $SrTiO_3$

$SrTiO_3$ belongs to the class of perovskite materials, crystals of the formula ABO_3, known for the FCC-derivative structure formed by the oxygen and the larger ion, in this case Sr. **Figure 1-4(a)** shows the Sr^{2+} ions forming a simple cubic sublattice, and the oxygen atoms taking the face centered positions to form the FCC lattice. The body-centered octahedral position is filled with the Ti^{4+} ion to accomplish charge neutrality[39]. In $SrTiO_3$ the oxygen octahedron coordinating Ti is larger than necessary, being expanded by the large Sr nearest neighbours. This causes the Ti to be slightly unstable in the sense described by Pauling's first rule, and the Ti can be easily displaced from the body-centered position, causing a change in crystal symmetry. As room temperature the structure of $SrTiO_3$ is tetragonal, with the Ti displaced less than 0.01 nm. This causes a permanent dipole, rendering the material ferroelectric. A cooperative alignment of adjacent dipoles then occurs, leading to a net polarisation that extends over many unit cells. The temperature at which the transition occurs is know as the Curie temperature, T_C. For $SrTiO_3$, $T_C = -55$°C. During the cubic-to-tetragonal transformation, the unstable Ti ion is displaced in one of the six [100] directions by an external electric field. This transformation give rise to

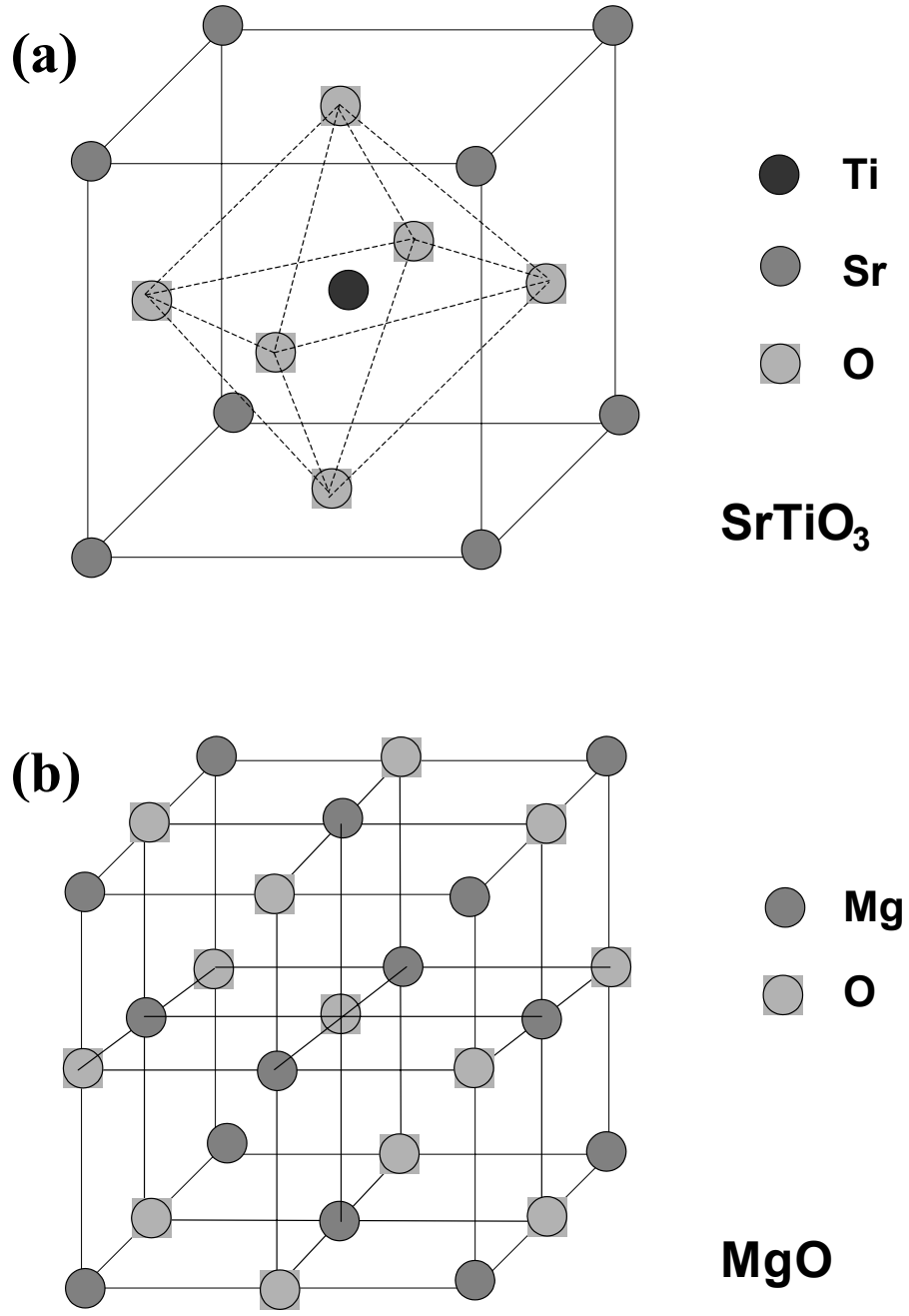

Figure 1-4: *(a) The crystal structure of $SrTiO_3$. (b) The crystal structure of MgO.*

a change in crystal dimensions. The coupling between the crystal dimensions and the applied field is the origin of the piezoelectric effect, useful in electromechanical applications where electrical energy is converted into mechanical energy, or *vice versa*.

$SrTiO_3$ has a large number of coincidence sites with $YBa_2Cu_3O_7$. The lattice mismatch relative to $YBa_2Cu_3O_7$ is 1.3%, the lattice parameter being slightly larger than the $YBa_2Cu_3O_7$ *a*- or *b*-axis parameter. $SrTiO_3$ is able to support high quality YBCO films $T_c \sim 90$ K and $j_c(90\text{ K}) \sim 5\times10^6$ A/cm^2, but it's high dielectric parameter bar $SrTiO_3$ from being used for any high frequency electronic applications[34].

1.4.3 MgO

MgO has a NaCl crystal structure and it has a 8.8% lattice mismatch with $YBa_2Cu_3O_7$. The Mg- and O-ions form simple cubic sublattices, shifted such that the O-ions occupy central positions in the Mg-sublattice, as shown in **Figure 1-4(b)**. MgO has a low dielectric constant of $\varepsilon = 9.65$, and because it is readily available and fairly inexpensive, it has received a good deal of interest[34]. In spite of the large lattice mismatch, high quality YBCO thin film has been deposited. Critical temperatures of 90 K can be achieved, depending on the correct deposition conditions and substrate quality. The transition width is usually larger than those of films deposited on $SrTiO_3$, typically $2-3$ K. Several studies have reported improved superconducting properties after the substrates have been treated. Thermal annealing of MgO substrates in oxygen produces films with good structural and superconducting properties[40, 41]. MgO is hygroscopic, and thus cannot be used in processes that require the presence of water.

1.5 Type-II superconductivity in $YBa_2Cu_3O_7$

1.5.1 Superconducting phases

$YBa_2Cu_3O_7$ is a type-II superconductor, indicating that superconductivity is not destroyed by magnetic field entering into the material, but the sample remains superconducting until the applied field reaches the second or upper critical field, B_{c2}. Magnetic field penetrates the bulk of the superconductor in the form of quantised flux tubes or magnetic vortices when the field is higher than the first or lower critical field B_{c1}[42, 43]. **Fig. 1-5** illustrate the magnetic phase diagram for type-II superconductors. The lower region bordered by the curve $B_{c1}(T)$ is the *Meissner phase* where the sample is in the flux free state. Type-I superconductors has only a Meissner state, and the superconductivity is destroyed if the applied field is greater then $B_{c1}(T)$. The region between the curves $B_{c1}(T)$ and $B_{c2}(T)$ is the so-called *mixed phase* where magnetic field has penetrated the sample in the form of vortices, each of total flux $\Phi_0 = hc/2e = 2.0679\times10^{-7}$ G·cm^2.

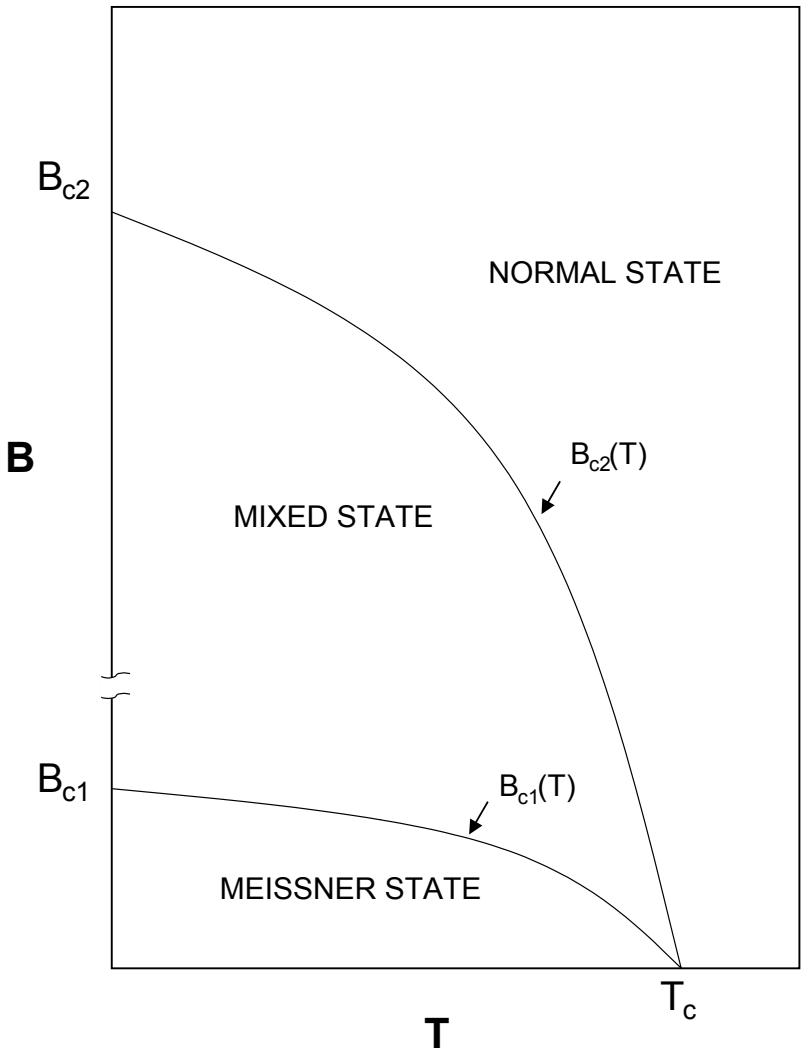

Figure 1-5: *Magnetic phase diagram showing the mixed and Meissner states of a type-II superconductor separated by the $B_{c1}(T)$ line. Note that $B_{c2}(0)$ in HTS can be up to four orders of magnitude larger than $B_{c1}(0)$.*

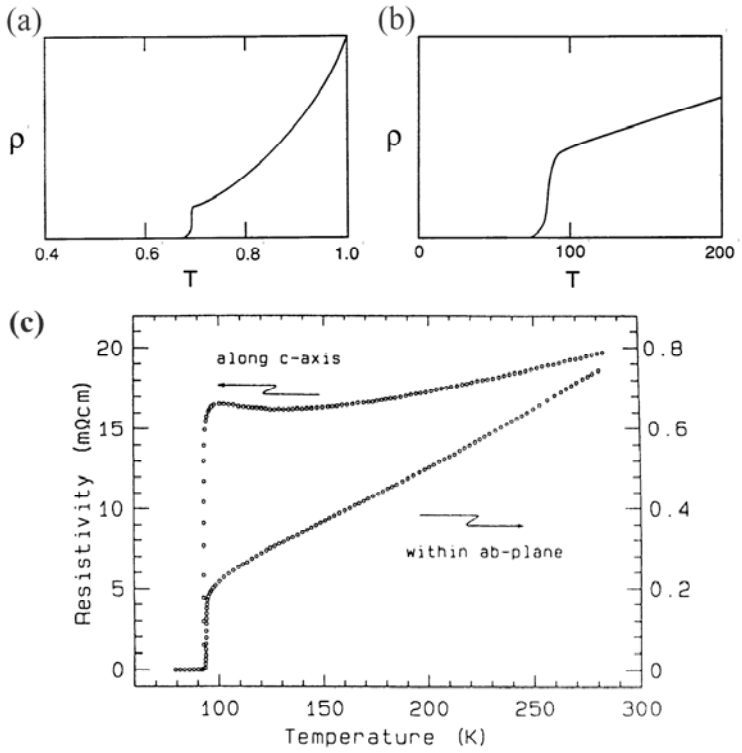

Figure 1-6: *Abrupt drop of the resistivity to zero at the superconducting transition temperature T_c (a) for a low-temperature superconductor in the Bloch T^5 region and (b) for a high temperature superconductor in the linear region. The temperature is given in Kelvin scale, while the resistivity scales are arbitrary. (c) Zero field resistivity determined with current flowing along the c−axis and within the a/b−plane of a YBCO single crystal[44].*

1.5.2 Normal state resistivity and superconducting transition

In striking contrast to metallic and alloy superconductors, with critical temperatures all in the range $2 - 23$ K, all high-T_c superconductors have $T_c \geqslant 38$ K, and the most important ones, $T_c > 77$ K. The classical metallic superconductors' resistivity obeys Bloch's law

$$\rho(T) = \rho_0 + \alpha T^5 \tag{1.2}$$

at low temperatures, ρ_0 being the residual resistivity due to impurity scattering, as illustrated in **Fig. 1-6(a)**.

Good metallic conductors such as silver and copper has room temperature resistivity of the order of 1.5 $\mu\Omega$ cm, at liquid nitrogen temperature it decreases by a factor of $2 - 8$.

High-temperature superconductors have transition temperatures that are in the linear region, shown

in **Fig. 1-6(b)**. Furthermore, unlike low temperature superconductors, HTSC's resistivity is highly anisotropic, associated with the highly conducting Cu-O planes found in the compound's crystal lattice[5]. HTSC have room temperature resistivity of about 2 orders of magnitude larger than copper. The resistivity drops 2 to 3 times in a linear fashion to the liquid nitrogen temperature range, and the resistivity drops to zero at 92 K in an extent of 1.5 K for the highest quality single crystal samples. Below T_c, $YBa_2Cu_3O_7$ exhibits zero resistivity and perfect diamagnetism if the applied field is below B_{c1}. The sharpness of the drop to zero is an indication of the materials' phase purity. **Fig. 1-6(c)** show the zero-field resistivity of single crystalline $YBa_2Cu_3O_7$ with current directions within the a/b-plane and along the c-axis[44]. The temperature dependence of the normal-state resistivity is markedly different for the two crystallographic orientations. The resistivity of the sample along the a/b-plane is metallic, but the resistivity along the c-direction is metallic in the higher temperature region (above 150 K) and semiconducting at lower temperatures. The ratio of the resistivity's, ρ_c/ρ_{ab}, is about 25 at 300 K and about 70 near T_c.

T_c is usually measured at the point where $\rho(T)$ has decreased 50%. This corresponds to the temperature position where $\frac{d\rho}{dT}$ peaks. For the transition width, ΔT, two approaches could be used: (a) the temperature difference between the 10% position and the 90% position of the resistivity transition curve, or (b) the full width at half maximum (FWHM) of $\frac{d\rho}{dT}$ over the transition. The two approaches usually yield very similar values for both T_c and ΔT. Resistivity data of YBCO is given in **Table 1.4**.

Table 1.4: *Resistivity data of* $YBa_2Cu_3O_7$

T	$\boldsymbol{\rho_{ab}}$	$\boldsymbol{\rho_c}$	$\boldsymbol{\rho_c/\rho_{ab}}$	$\boldsymbol{\delta\rho_{ab}/\delta T}$	$\boldsymbol{\delta\rho_c/\delta T}$[45]
K	$m\Omega$ cm	$m\Omega$ cm		$\mu\Omega$ cm/K	$\mu\Omega$ cm/K
250	0.72	18.5	26	3	50
100	0.23	16.5	71	4	-40

When heated, the resistivity of $YBa_2Cu_3O_7$ begins to deviate from linearity at about $600-700$ K, near the oxygen-loss related orthorhombic-tetragonal phase transition, where it changes from metallic to semiconducting above the transition. The resistivity increases rapidly with temperature above 700 K[46]. The resistivity of $YBa_2Cu_3O_7$ is 2 orders of magnitude greater along the c-axis than parallel to the a/b-plane, thus $\rho_c/\rho_{ab} \sim 100$.

1.5.3 Vortices

The present understanding of magnetic penetration of type-II superconductors started with a paper by A.A. Abrikosov[47] who developed a phenomenological theory of the magnetisation of superconducting alloys in which he showed that the flux entered the specimen in quantised superconducting vortices

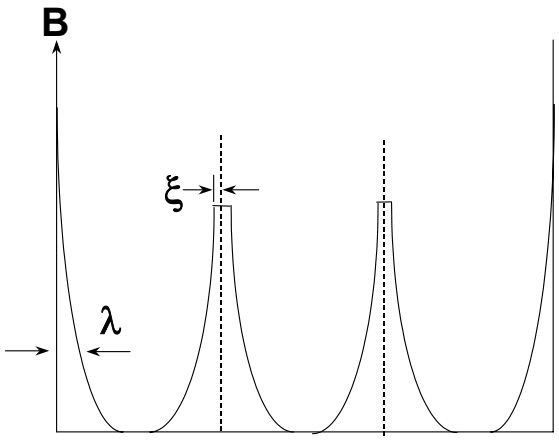

Figure 1-7: *Cross sectional sketch of the mixed state. The vortex cores of radius ξ are in the normal state, while current circulate the core. The current density drops exponentially, with a characteristic scale of λ, known as the penetration depth.*

(also known as fluxons or flux lines). Vortices confine the penetrated flux to units of very small area. The field is highest at the core of radius $\sim \xi$ (known as the coherence length), and it is surrounded by a region of larger radius λ within which magnetic field and screening current circulating the core are present together, see **Fig. 1-7**. The current density of this shielding currents decays exponentially from the core. The penetration depth λ is a measure of the penetration of a parallel external magnetic field into a superconductor's surface, analogous to the radio frequency skin depth for normal metals. Near T_c, Ginzburg-Landau theory predicts the following approximate forms for the penetration depth and the coherence depths:

$$\lambda(T) = \lambda(0)\left(1-\frac{T}{T_c}\right)^{-\frac{1}{2}} \tag{1.3a}$$

$$\xi(T) = \xi(0)\left(1-\frac{T}{T_c}\right)^{-\frac{1}{2}} \tag{1.3b}$$

An interpretation is that ξ indicates the distance over which the amplitude of the superconducting wave functions can vary appreciably, for example from 0 in the vortex centre to 1 outside the vortex. The

Table 1.5: *Certain superconductivity parameters of* $YBa_2Cu_3O_7$.

	c-direction	ab-plane
Penetration depth λ (nm)	450	150
Coherence length ξ (nm)	0.5	1.5
First critical field B_{c1} (G)	200	800
Second critical field B_{c2} (G)	2×10^7	6.7×10^6
Critical current density j_c (A/cm^2)	4.2×10^5	2.9×10^6

local density of vortices are directly proportional to the internal local magnetic field density. Vortices usually assume a two dimensional triangular lattice[48]. For type-II superconductors we have $\lambda > \xi$, while for type-I superconductors, the condition $\lambda < \xi$ is valid. The two characteristic lengths are also anisotropic in $YBa_2Cu_3O_7$ — their data are tabulated in **Table 1.5**, along with B_{c1}, B_{c2}, and j_c.

Note that we have the situation: $B_{c1}^c < B_{c1}^{ab} \ll B_{c2}^{ab} < B_{c2}^c$, where the superscript indicate the direction of the applied field relative to the crystal axis of $YBa_2Cu_3O_7$. **Fig. 1-8**[49] shows the temperature dependence for the principal length scales in superconductivity, and the first critical field. **Fig. 1-8(a)** is a sketch of the temperature dependencies of the penetration depth (λ) and coherence length (ξ). The absolute values of these quantities can be quite different; in fact, for the high$-T_c$ materials $\lambda \gg \xi$. However, according to the Ginzburg-Landau theory, near T_c they have the same temperature dependence, see eq. 1.3[50]. In **Fig. 1-8(b)**, the open circles are measured changes in magnetic penetration depth λ as a function of reduced temperature. The first critical field B_{c1} determined for B parallel and perpendicular to the $c-$axis of a single crystal $YBa_2Cu_3O_7$ is shown in **Fig. 1-8(c)**. The 0 K values are 800 G and 200 G respectively[49].

The drop to zero resistivity is a good indicator of superconductivity from an applications point of view, and easy to measure. A susceptibility measurement is a thermodynamic indicator of the superconducting state because magnetisation is a thermodynamic variable. Filamentary paths in a thin film or ceramic sample can produce sharp drops in resistivity at temperatures higher than the temperatures at which there are pronounced drops in susceptibility, which requires extensive regions of superconductivity.

1.6 Magnetic flux creep

1.6.1 Pinning and Lorentz force

The property of type-II superconductors that is technologically most important is their ability to carry a large bulk current density **j** with essentially no dissipation. When a bulk type-II superconductor is submitted to a magnetic field larger than the lower critical field B_{c1}, the flux penetrates the superconductor

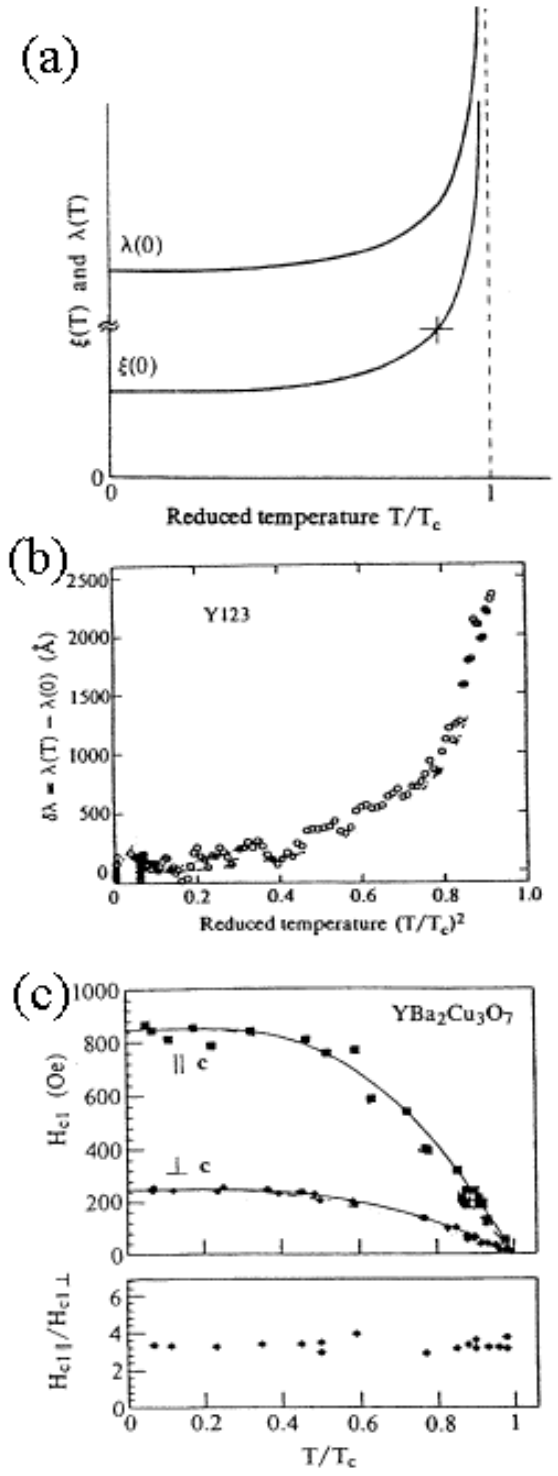

Figure 1-8: *(a) Schematic diagram of the temperature dependencies of the peneration depth (λ) and coherence length (ξ). (b) The data are measured changes in magnetic penetration depth λ as a function of the square of reduced temperature. (c) H_{c1} of H parallel and perpendicular to the c-axis of single crystal $YBa_2Cu_3O_7$*[49].

in the form of Abrikosov vortices. These vortices become trapped at pinning centres (grain boundaries, point defects, oxygen vacancies (in HTS materials), inclusions, cavities, and other defects to the perfect crystal lattice). Pinning occurs when a vortex core at the site of a defect has a lower energy because the defect depresses superconductivity. Thermal energy, even at cryogenic temperatures, is sufficient to free pinned vortices at a constant average rate. The vortices are subjected to a Lorentz force density $\frac{1}{c}\mathbf{j} \times \mathbf{B}$, and an opposing pinning force $\mathbf{F}_p$ keeping the vortices stationary at pinning sites. Once released from a pinning site the Lorentz force acts to move the vortices perpendicular to the direction of the transport current, generating noise voltages and heat until it become trapped again at another pinning centre. In certain models of pinning, only some vortices are actually pinned, while the rest are kept stationary due to their mutual repulse forces. The macroscopically averaged current density is related via quasistatic (displacement current term omitted) Maxwell's equation $\boldsymbol{\nabla} \times \mathbf{B} = (4\pi/c)\mathbf{j}$ to the vortex density gradient, which is the result of pinning. A sample carrying a macroscopic screening current is in a state which, from a thermodynamic point of view, is only metastable. The magnetisation of such a sample is bound to decay via thermally activated motion of the vortices, known as flux creep[3, 4]. Flux-creep, under steady state conditions, becomes progressively slower with time as the flux-density gradients are gradually reduced by vortex displacement.

1.6.2 Flux creep electrodynamics

Following the review of Y. Yeshurun *et al*[1], we adopt a simple geometry to discuss the relation between magnetic field, current density and vortex motion in a superconductor. In **Fig. 1-9**, the field B, j and v are parallel to the z, y, and $x-$axes respectively. The macroscopically averaged current density j is related to the vortex-density gradient, established by pinning, through the quasistatic Maxwell's equation (Ampère's law)

$$\frac{\partial B_z}{\partial x} = -\frac{4\pi}{c} j_y \tag{1.4}$$

in which the displacement current term is omitted. The basic equation determining the decay of the current density j is given by Maxwell's equation

$$\frac{\partial B}{\partial t} = -c\frac{\partial E}{\partial x}, \tag{1.5}$$

where we are using a simplified geometrical arrangement with the field $B \| z$, and the current $j \| y$, and with the electric field generated by the vortex motion

$$\mathbf{E} = \frac{1}{c}\mathbf{B} \times \mathbf{v} \tag{1.6}$$

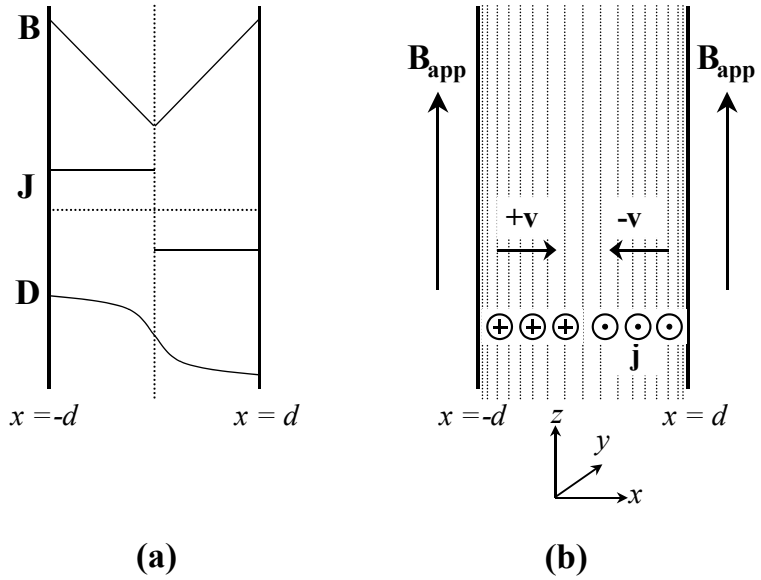

Figure 1-9: *(a) Schematic plot (using the Bean model) of* $\mathbf{B}$, $\mathbf{j}$ *and the flux-line current density* $D = vB$ *as functions of coordinate* x *in an infinite superconducting slab placed in a parallel field* $\mathbf{B}_{app}$. *(b) Schematic diagram showing the current density and the flux-line velocity* v *in the slab. The field* B, j *and* v *are parallel to the* z, y, *and* $x-$*axes respectively.*

also parallel to the y-axis. The velocity of the vortices is parallel to the Lorentz force, $\mathbf{v} = v\hat{\mathbf{x}}$. Using eq. 1.6 in Faraday's law, we obtain the equation of continuity for the vortex lines,

$$\frac{\partial B}{\partial t} = -\frac{\partial}{\partial x}(vB), \tag{1.7}$$

vB being identified as the *flux–line current density*. Relating the magnetic field and the current via $\boldsymbol{\nabla} \times \mathbf{B} = (4\pi/c)\mathbf{j}$, we obtain the corresponding dynamic equation for the current density,

$$\frac{\partial j}{\partial t} = \frac{c}{4\pi}\frac{\partial^2}{\partial x^2}(vB). \tag{1.8}$$

The differential equations 1.7 and 1.8 describe a non-linear diffusion process. The important factor in the above equations is the velocity v of the vortices, which is due to thermal activation over the pinning barrier $U(j)$

$$v = \omega x_0 e^{-U(j)/kT}, \tag{1.9}$$

ω being the effective attempt frequency and x_0 the hop distance. The Boltzmann factor $e^{-U(j)/kT}$ is simply the occupation number of the states with energy $U(j)$ in the ensemble of flux lines[51, p 145]. This equation is reminiscent of the dynamics of atomic diffusion[52], with $e^{-U(j)/kT}$ being the fraction of vortices with an energy of $U(j)$ or more; i.e.. the fraction that is able to jump. For an atomic diffusion process, this frequency is of the order of the atomic vibration $\sim 10^{13}$ s^{-1} whereas for the case of the flux line the value $\omega \sim 10^6 - 10^{11}$ s^{-1}[44]. Blatter *et al.*[7] solved eq. 1.8 assuming complete field penetration and neglecting field dependence of the barrier $U(j)$, leading to a dynamic equation for the current density of the form

$$\frac{\partial j}{\partial t} \approx \frac{j_c}{\tau_0} e^{-U(j)/kT}. \tag{1.10}$$

This equation can also be determined rather directly[2]. An electric field is associated with a time-varying superconducting current and all thermal activated forward vortex motion can be described by the simple rate equation

$$\frac{\partial j}{\partial t} \propto E = B\omega x_0 e^{-U(j)/kT}. \tag{1.11}$$

The above equation was solved by Geshkenbein and Larkin[53] yielding

$$U(j) = kT \ln(t/t_0) \tag{1.12}$$

with $t_0 = \tau_0 kT/j_c|\partial U/\partial j|$, the time constant t_0 in the range 10^{-3} s to 1 s. For eq. 1.12 we can find the time evolution of the screening current density $j(t)$ by simple inversion, ie.

$$j(t) = U^{-1}(kT \ln(t/t_0)) \tag{1.13}$$

provided the functional dependence of $U(j)$ on j is known. Eq. 1.12 is general and is independent of the specific functional form of $U(j)$. $U(j)$ should be invertible, since we have $U(j_c) = 0$ and $U(j)$ increases with decreasing current density j.

1.6.3 The Anderson-Kim model : linear $U(j)$ model

The important quality that we need to know is the activation energy $U(j)$, in particular, it's functional dependence on the current density j. P.W. Anderson and Y.B. Kim developed a simple model which assumes thermal activation of uncorrelated vortices of vortex bundles over a net potential barrier which depends linearly on applied current density j, thus

$$U = U_0 - \frac{1}{c} jBx_0 V \tag{1.14}$$

where V is the volume of the "jumping" flux bundle and x_0 is the hopping distance. $\frac{1}{c}jBx_0V$ is the effective reduction in the barrier due to the work done by the Lorentz force in moving the flux bundle over the distance x_0. The relation can be rewritten as

$$U = U_0 \left(1 - \frac{j}{j_{c0}}\right) \tag{1.15}$$

where $j_{c0} = cU_0/Bx_0V$ is the critical current density at which the barrier vanishes. As the critical current density could be defined as the current density at with the Lorentz force is exactly balanced by the pinning force, it follows that $j_c = j_{c0}$. Combining eq. 1.12 and eq. 1.15 one obtains the famous logarithmic time decay of the diamagnetic current j_c,

$$j(t) = j_{c0}\left[1 - \frac{kT}{U_0}\ln\left(\frac{t}{t_0}\right)\right], \tag{1.16}$$

or, to be able to use the equation from $t = 0$, it is usually rewritten as

$$j(t) = j_{c0}\left[1 - \frac{kT}{U_0}\ln\left(1 + \frac{t}{t_0}\right)\right], \tag{1.17}$$

such that $j(t = 0) = j_{c0}$. The factor in square brackets represents a correction to the current density, called the *"flux-creep reduction factor"*. To eliminate the unknown j_{c0} in equation 1.15, it is convenient to evaluate a normalized relaxation rate S defined as the logarithmic derivative of the magnetisation or current density (in the Bean critical state the magnetization M is proportional to the current density j)[1, p 937]

$$S = \frac{1}{M}\frac{dM}{d\ln t} = \frac{d\ln M}{d\ln t} = \frac{d\ln j}{d\ln t}. \tag{1.18}$$

1.6.4 Deviations from Anderson-Kim : Non-linear $U(j)$ models

High temperature superconductors exhibit giant flux creep effects[6]. The small coherence length associated with HTSC's leads to low pinning energies, and thus a large degree of thermal activation. Deviations from the logarithmic decay rate (eq. 1.15) have been reported by various investigators[6, 54, 55]. In order to explain deviations from Anderson-Kim behaviour, C.W. Hagen and R. Griessen suggested that a distribution of activation energies should be taken into account[56]. Another theory, the collective pinning theory has also been suggested. It describes a form for $U(j)$ which diverges as $j \to 0$. Feigel'man *et al*[57] suggested an interpolation formula between the high-current Anderson-Kim limit and the

low-current regime which is frequently used, such that

$$U(j) = \frac{U_c}{\mu}\left[\left(\frac{j_c}{j}\right)^{\mu} - 1\right]$$

where μ could be regarded as a fitting parameter.

The energy scale for the pinning barrier U is determined by the collective pinning energy U_c. Furthermore, the dependence of U, on the transport current density is due to the Lorentz force, so that the barrier vanishes at the critical current density j_c,

$$U(j \to j_c) \approx U_c\left(1 - \frac{j}{j_c}\right)^{\alpha} \tag{1.19}$$

Up until now no theory has existed for the exponent α, and it's calculation poses a very interesting problem related to the theory of phase transitions and self-organized criticality. Using eq. 1.19 with an exponent $\alpha = 1$ in accordance with Anderson's proposal, we obtain the famous logarithmic time decay of the diamagnetic current j_c, eq. 1.17.

The temporal decay of the transport current is thus determined by the ratio kT/U_c, which can be found experimentally by measuring the relaxation of the diamagnetic moment of a sample in the critical state (introduced in the next section). The activation energy U_c is therefore an experimentally accessible quantity, and will be the subject of some of our investigation in Chapter 5. Typical experimental results for the activation energy obtained in magnetic relaxation experiments at low temperatures, are in the range $U_c \sim 100 - 1000$ K.

A logarithmic dependence of the activation barrier on critical current density j describe single-vortex creep within weak collective creep theory and has been measured experimentally by E. Zeldov *et al*[58]. The suggested form is

$$U(j) = U_0 \ln\left(\frac{j_c}{j}\right). \tag{1.20}$$

This formula is an exact result for the case when the vortex motion is controlled by the intrinsic pinning in a layered system when the field is parallel to the layers, and provide a good approximation for the creep activation barrier in the single-vortex creep regime[59]. If we apply eq. 1.12 to eq. 1.20, it results in

$$\frac{j(t)}{j_c} = \left(\frac{t}{t_0}\right)^{-kT/U_0}, \tag{1.21}$$

as a time-dependent current relationship during flux relation. M.P. Maley *et al*[55] have studied magnetic relaxation in $YBa_2Cu_3O_7$ for the temperature range $10 - 30$ K, and found good agreement with the form eq. 1.20 for the pinning potential.

1.7 Critical state models

To solve practical problems in the realm of magnetic penetration of type-II superconductors, a family of models, known as critical state models, have been suggested in the literature. Initially developed by C.P. Bean[60, 61], these models attempt to shed light on the field and current distributions in type-II superconductors when they are subjected to magnetic fields and currents. In Section 1.6.1, we introduced the Lorentz force density $\frac{1}{c}\mathbf{j} \times \mathbf{B}$ acting on vortex lines. The forces acting on the line system can be decomposed in the following way: (1) due to the repulsive interaction between vortices, regions of high line density (high B) tend to expand towards the regions of low density. This can be described in terms of a pressure p in the two-dimensional lattice system, where the force density is $-\boldsymbol{\nabla} p$. This force is balanced by a pinning force due to defects. The pinning force can not be arbitrary large, thus

$$\left|\frac{1}{c}\mathbf{j} \times \mathbf{B}\right| = |\boldsymbol{\nabla} p| \leqslant \alpha \tag{1.22}$$

where α is the threshold value. When $\left|\frac{1}{c}\mathbf{j} \times \mathbf{B}\right|$ exceeds α, the vortices move and dissipation occurs until the condition eq. 1.22 is satisfied again. In practice the line density B will adjust itself so that the threshold condition $|\boldsymbol{\nabla} p| = \alpha$ is realised at all points. This state is called the *critical state*, first described by C.P. Bean[60, 61]. We can get some physical feeling for this critical state by thinking of a sand hill. If the slope of the sand hill exceeds some critical value, the sand starts to flow downwards in an avalanche. The analogy is rather good, since it has been shown (by careful experiment with pick-up coils) that, when the system becomes over-critical, the lines do not move be single units, but rather in the form of avalanches of typically 50 vortices or more[42].

The critical state models serve as models for the magnetisation of type-II superconductors. These models postulate that for low applied fields or currents, the outer part of the superconductor is in a so-called *critical state*, with certain values of the current density and non-zero magnetic field, and that the interior is shielded from these fields and currents (i.e. the interior is in the Meissner state with $B = 0$).

The basic premise of the critical state model is that there exists a limiting macroscopic superconducting current density $j_c(B)$ that a type-II superconductor can carry; and further, that any electromotive force, however small, will induce this full current to flow locally. In this picture we have Meissner screening currents where the total field is zero, and critical current flowing perpendicular to the field axis where the field has penetrated the sample, the sense depending on the sense of the electromotive force that accompanied the last local change of field, according to Lenz's law[61].

The critical state models do not take the realistic magnetic phase diagram into account. The lower critical field does not feature in the critical state models; the material is assumed to transform directly

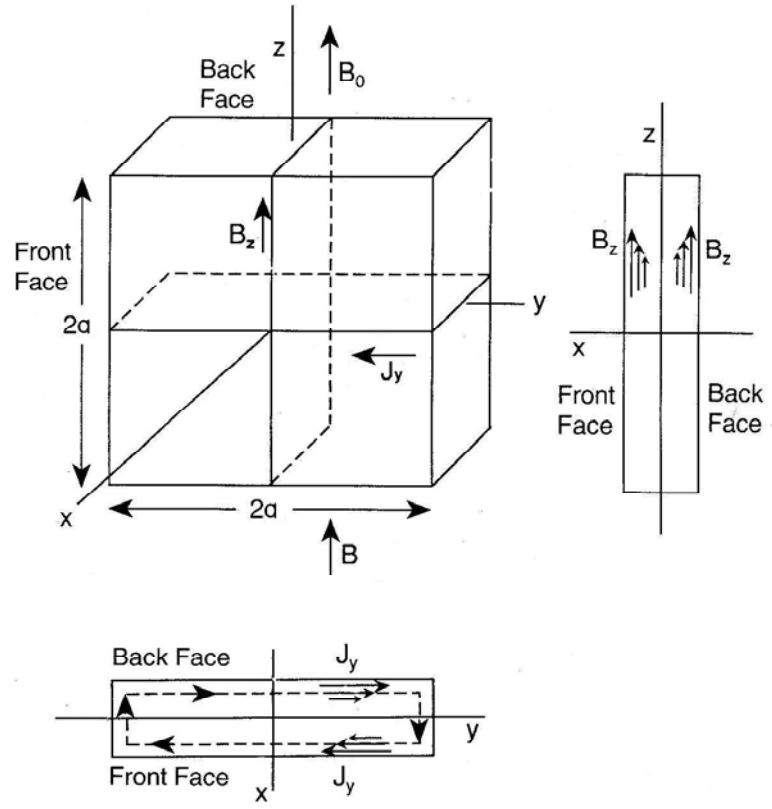

Figure 1-10: *Superconducting slab of thickness* $2a$ *oriented in the* y, z*-plane with externally applied magnetic field* B_0 *directed along* z*. The induced shielding current density* j_y *flowing in the* $y-$*direction inside the front and back faces is shown. [30]*

(locally) from the flux free Meissner state to the mixed state in the presence of applied field. Since the lower critical field is usually quite low, this simplifying assumption is considered acceptable.

Various critical state models have been suggested, ref. [30]pp 368-9. These models differ on the model relationship between the critical current density $j_c(B)$ and the local magnetic field B. The Bean model assumes a field independent critical current density,

$$j(B) \ = j_c, \tag{1.23}$$

while the Kim or *fixed pinning* model[62] makes the pinning force constant, and so arrives at

$$j(B) = \frac{j_c}{1 + |B(x)| / B_K}. \tag{1.24}$$

Consider a bulk superconducting slab, as a shown in **Fig. 1-10**. The critical state models assume

the magnetic field would penetrate the sample from outside, such that at the periphery of the sample the field is equal to the applied field $\mathbf{B}_{app} = B_0\widehat{\mathbf{z}}$, and the interior field $B(x)$ would then decrease towards the center of the sample. If the applied field is small enough, there would be a field free region $-a \leq x \leq a$ in the slab. Critical currents flow where the field is present in accordance to the Maxwell equation (in the steady state we have $\partial\mathbf{E}/\partial t = 0$):

$$\boldsymbol{\nabla} \times \mathbf{B} = \frac{4\pi}{c}\mathbf{j}. \tag{1.25}$$

or simplified to

$$\frac{dB_z(x)}{dx} = -\frac{4\pi}{c}j_y(x) \tag{1.26}$$

for **Fig. 1-10**. Meissner screening at the scale of the penetration depth λ is neglected, thus the critical current is zero beyond the point where the field vanishes. When the applied magnetic field increases in magnitude, the internal magnetic field and current penetrate further and for sufficiently strong fields they are present throughout the sample.

1.7.1 The Bean model

The original model proposed by C.P. Bean[60, 61] is commonly employed to explain magnetisation phenomena due to it's mathematical tractability. Without diverting to much into the mathematical detail, a brief description of the Bean model is provided here. The discussion is focussed on the rather easy graphical representation of the Bean model, which simplicity is the main reason for it's widespread use. Consider a zero-field cooled (ZFC) superconducting slab with coordinate system as shown in **Fig. 1-10**, where an applied field $B_{app} = B_0$ is applied in the z-direction. One can then write down the current distribution using $j(B) = j_c$ (see **Fig. 1-11**)

$$j_y(x) = \left\{ \begin{array}{ll} j_c & -a \leq x \leq -a' \\ 0 & -a' \leq x \leq a' \\ -j_c & a' \leq x \leq a \end{array} \right\} \tag{1.27}$$

$$a' = \left\{ \begin{array}{ll} a\left(1 - \frac{B}{B^*}\right) & |B_0| \leq B^* \\ 0 & |B_0| > B^* \end{array} \right\} \tag{1.28}$$

$$B^* = \frac{4\pi}{c}j_c a \tag{1.29}$$

where the region $-a' \leq x \leq a'$ designates the flux free region. When the applied external field B_0 exceeds the characteristic field B^* the flux has fully penetrated the slab. The slab is then completely in the critical state. Following eq. 1.26, B_z should be a linear function of x:

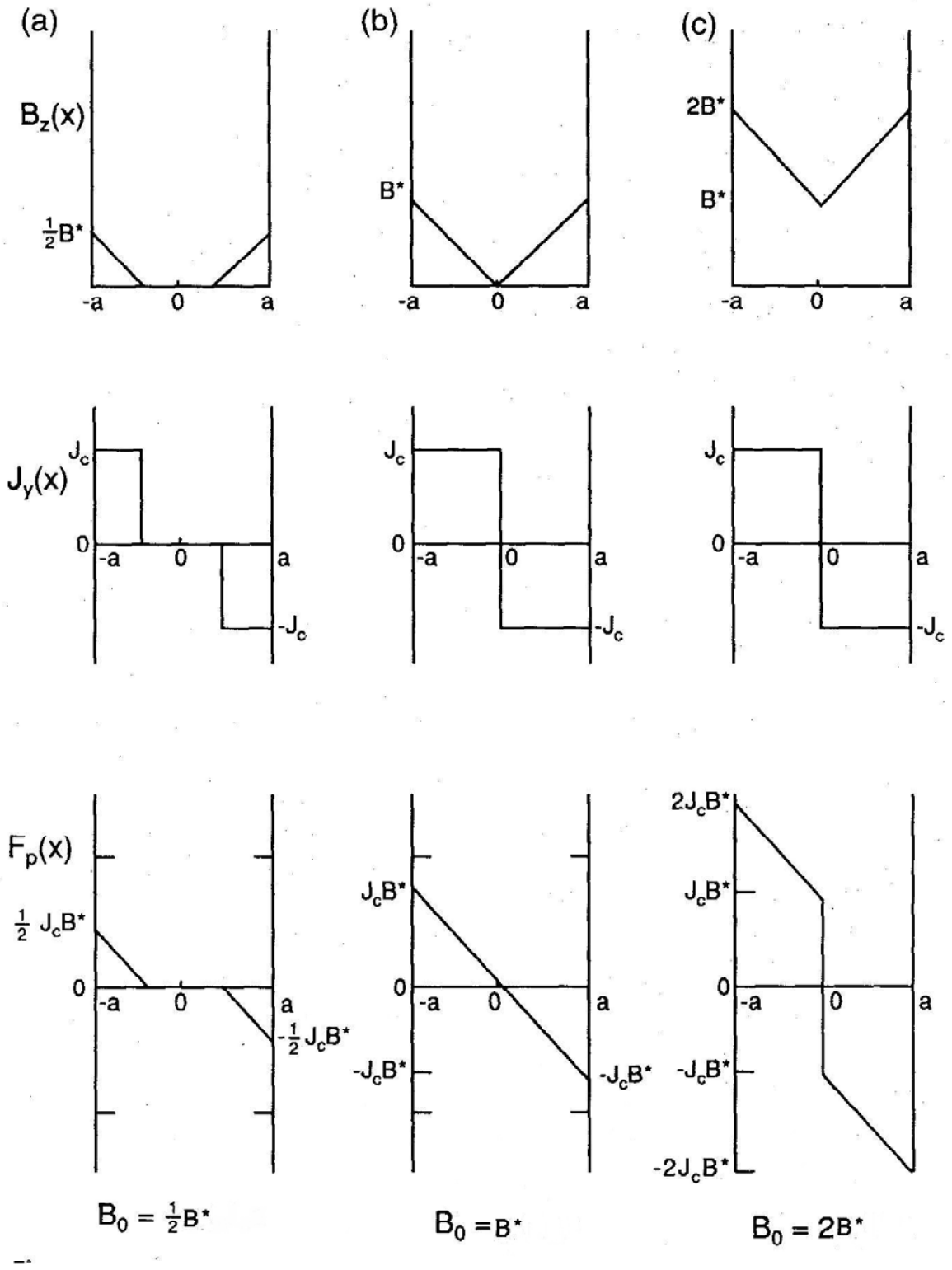

Figure 1-11: *Dependence of the internal magnetic field $B_z(x)$, and pinning force $F_p(x)$ on the strength of the applied magnetic field B_0 for normalised applied fields given by (a) $B_{app}/B^* = \frac{1}{2}$, (b) $B_{app}/B^* = 1$, and (c) $B_{app}/B^* = 2$, $B^* = 4\pi j_c a/c$. The figures are drawn for the Bean model. There is a field-free region in the centre for case (a), while case (b) represents the situation where the Meissner state has been completely destroyed. [30]*

$$B_z(x) = \left\{ \begin{array}{ll} B_0 \left(\frac{a'+x}{a'-a}\right) & -a \leq x \leq -a' \\ 0 & -a' \leq x \leq a' \\ B_0 \left(\frac{x-a'}{a-a'}\right) & a' \leq x \leq a \end{array} \right\}. \tag{1.30}$$

These expressions match the boundary condition $B_z(0) = B_0$ on the two surfaces $x = \pm a$. When B_0 is further increased, the internal field also increases, as shown in **Fig. 1-11**. Finally, we have $a' = 0$, and eqs. 1.27 and 1.30 is not valid anymore. For $B_0 > B^*$, we have

$$\begin{aligned} J_y(x) &= \left\{ \begin{array}{ll} j_c & -a \leq x \leq 0 \\ -j_c & 0 \leq x \leq a \end{array} \right\} \\ B_z(x) &= \left\{ \begin{array}{ll} B_0 - B^* \left(\frac{a+x}{a}\right) & -a \leq x \leq 0 \\ B_0 + B^* \left(\frac{a-x}{a}\right) & 0 \leq x \leq a \end{array} \right\}. \end{aligned} \tag{1.31}$$

The magnitude of j_c is fixed by the characteristics of the particular superconducting sample, and depends on such factors as the superconducting material, granularity, twinning, concentration of defects, grain boundaries, etc.

1.7.2 Hysteresis

When a sample is zero-field cooled and then cycled through a magnetisation cycle, by applying a harmonic field for example, the sample experiences magnetic hysteresis. Hysteresis is the phenomenon when the dependence of the magnetisation on applied field, $M(H)$, does not follow the same functional form for increasing as for decreasing H. This is well known for ferromagnetic materials such as cobalt, and it is due to a magnetic domain structure, whereby domains of uniform magnetisation shrink, expand or even rotate magnetic orientation, see e.g. C. Kittel[63] chapter 16. Analogs of this phenomenon exists in other types of materials: for example antiferromagnetics, ferroelectrics, and ferroelastics. The important property of these materials is that the motion of domain boundaries are generally not reversible, leading to hysteretic behaviour. We can extend this analogy under the Bean model if we imagine that a connected volume where the current flows in a particular direction constitutes a domain. In **Fig. 1-11(a)** the slab is divided in a domain where there a current flowing anti-clockwise and a domain without any current in the center. In **(b)** and **(c)** the domain boundary has moved to the center (the boundary became a singularity) and the entire slab constitutes a single domain.

To further understand the origin of this hysteresis, we explore graphically (see **Fig. 1-12**) the behaviour of a superconducting slab through magnetic cycling. After the field reached it's maximum value $B_{\max} = 2.5B^*$, the field is decreased to a value $B_{\min} = -B_{\max}$. The current density flowing in the

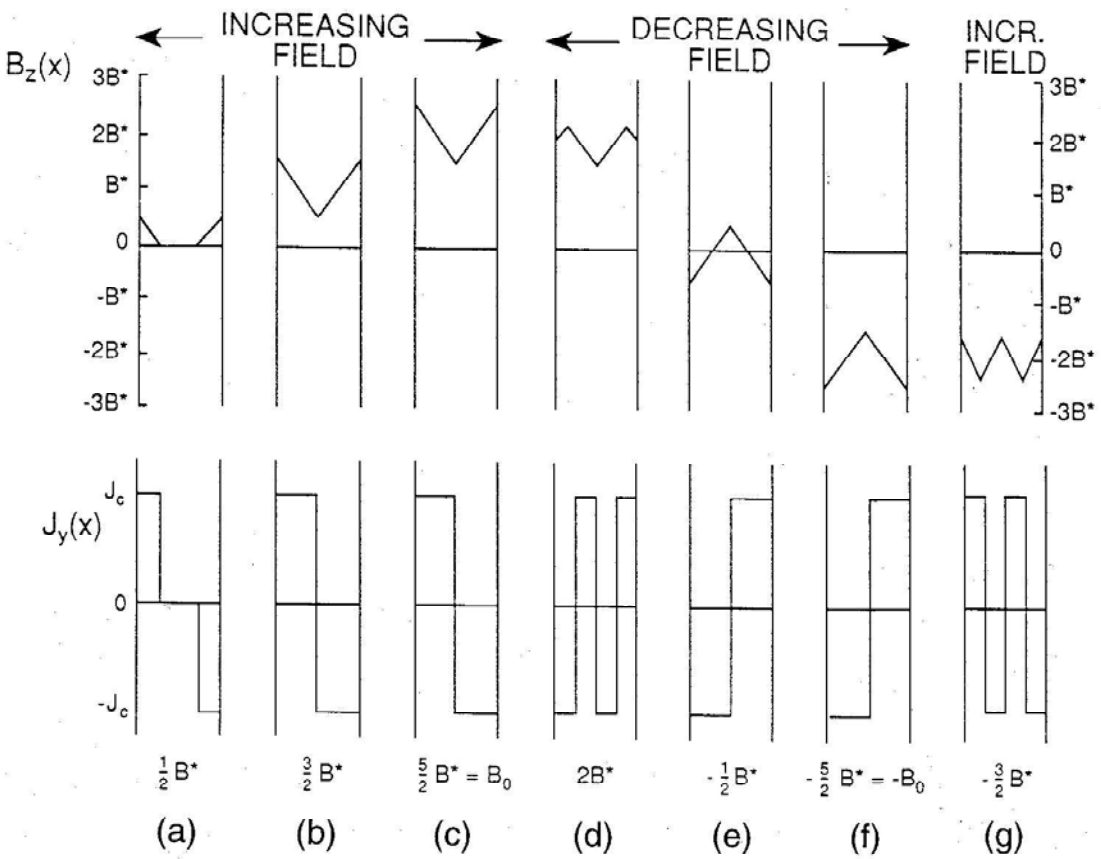

Figure 1-12: *Applied field cycle with B_{app} started at 0, increased from $0.5B^*$ to $2.5B^*$, decreased through zero to the negative value of $-2.5B^*$, and then starts to increase again. Plots are shown for the internal field $B_z(x)$ and the current density $J_y(x)$ for successive values of B_0[30].*

slab are fixed to the value $\pm j_c$. This represent the basic clue as to how to draw the graphs. Secondly, the magnetic field spatial gradient is fixed to $\pm B^*/a$, and $B(\pm a) = B_{app}$ always (boundary condition). These three rules leads us to a unique set of graphs as representative of the current and field distribution during magnetic field cycling.

Shown in **Fig. 1-12** are the current and field profiles during field cycling, reference is made to this figure throughout this paragraph. The sample starts with no internal field or current, and with no applied field. When the applied field is increased, field starts to penetrate the sample from the sides, and current starts to circulate around the periphery as shown in **(a)**. At $B_{app} = B^*$, the magnetic field has reached the centre, and the entire sample is in the critical state. The current has penetrated the full sample, with $j = \pm j_c$ everywhere, and the current flowing in opposite directions in the two halves of

the sample. In **(b)** and **(c)** we see the situation where the applied field has increased beyond B^*. The internal field continue to increase, while the current distribution remains the same as at $B_{app} = B^*$.

The applied field is decreased in **(d)**. The internal magnetic field starts to decrease from the periphery, while still keeping the required gradient of $\pm B^*/a$. The current at the periphery started to circulate in the opposite direction, in step with the direction of change of magnetic flux that induced it. The applied field is further reduced **(e)** and the current distribution completely reverses it's direction. The applied field finally reaches it's minimum value **(f)** where upon the field starts to increase again.

Domains are easy to identify in **Fig. 1-12**: **(a)** to **(c)** are similar to **Fig. 1-11** with a 'no current' domain and an 'anti-clockwise' domain becoming larger with increasing B_{app}; in **(d)** a second 'clockwise' domain appeared on the periphery due to a decreasing B_{app}; in **(e)** the boundary of the 'clockwise' domain with the 'anti-clockwise' domain moved inside to completely annihilate the 'anti-clockwise' domain; in **(f)** there are still only the 'clockwise' domain, and finally in **(g)** with an increase in B_{app} an 'anti-clockwise' domain appeared again. Clearly the domain boundaries move in an irreversible manner; i.e. always inward, but never outward. This is the origin of hysteresis in the Bean model. The analogy with ferromagnetism is evident, and this domain concept, however simplistic in the Bean model, serves to explain hysteresis in type-II superconductors qualitatively.

The term *hysteresis loops* is ordinarily reserved for loops involving magnetisation M. **Fig. 1-13** show plots of reduced magnetisation $4\pi M/B^*$ versus applied field B_{app} for various values of maximum field B_0. The magnetisation saturates at $4\pi M = \frac{1}{2}B^*$, which corresponds to the situation depicted in **Fig. 1-11(c)** and **Fig. 1-12(b)** where $B_{app} \geq B^*$. **Fig. 1-13(a)** shows a hysteresis curve in which saturation has not yet taken place; the maximum applied field was less than B^* ($B_0 < B^*$). **Fig. 1-13(b)** shows a hysteresis curve where B_0 just exceeds B^* ($B_0 = \frac{5}{4}B^*$), and saturation was achieved (point **e**). With **Fig. 1-13(c)**, the sample went into saturation at point **e**. The applied field was then substantially increased up to $B_0 = 3B^*$, so that the field and current profiles correspond to **Fig. 1-12(c)**.

Fig. 1-14 shows the dependence of average field $\langle B \rangle$ on the applied field $B_{app} = B_0$. Using the definition of relationship $4\pi M = B - H$, we have in our notation

$$4\pi M = \langle B \rangle - B_{app}, \tag{1.32}$$

thus one can see that **Fig. 1-14** is simply **Fig. 1-13(c)** with B_{app} added.

To determine the saturation magnetisation, one calculates the limiting value of $\langle B \rangle$ when B_{app} is increased. Using eq. 1.31, we have

$$\langle B \rangle \quad = \quad \frac{\int_{-a}^{a} B(x)dx}{2a} = B_{app} + \frac{1}{2}B^* \tag{1.33}$$

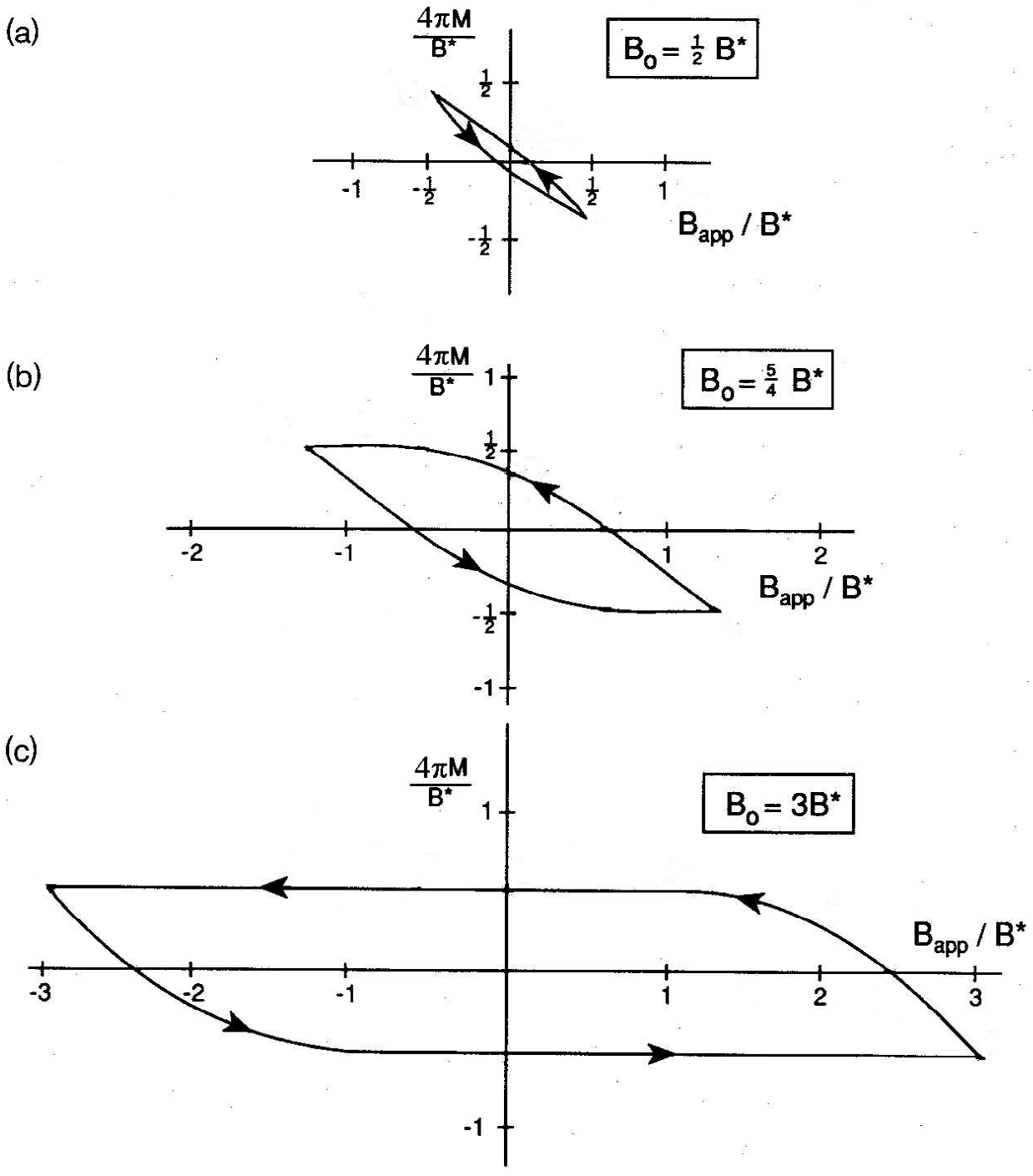

Figure 1-13: *Hysteresis loops of magnetisation $4\pi M$ versus applied magnetic field B_{app} cycled over the range $-B_0 \leq B_{app} \leq B_0$ for three cases: (a) $B_0 = \frac{1}{2}B^*$, (b) $B_0 = \frac{5}{4}B^*$ and (c) $B_0 = 3B^*$[30].*

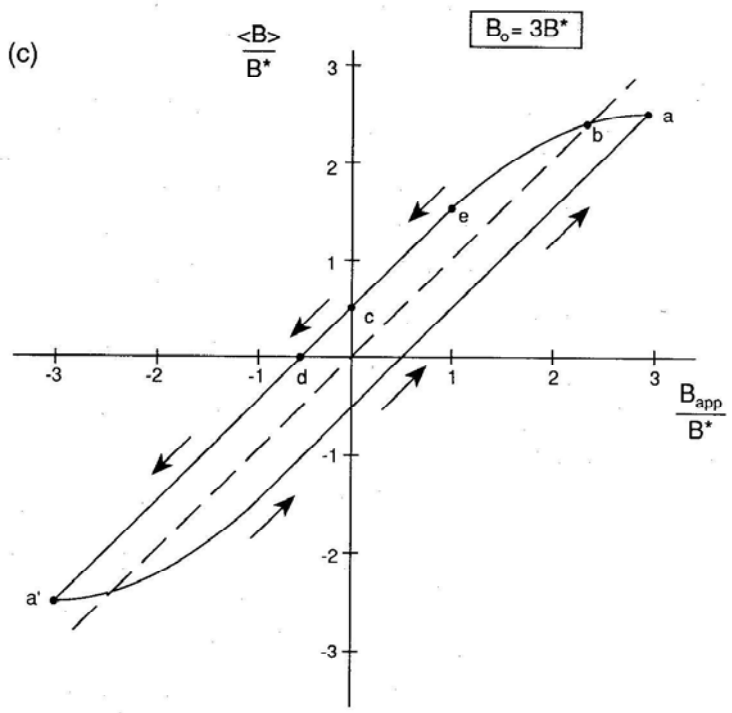

Figure 1-14: *Dependence of the average field* $\langle B \rangle$ *on the applied field* B_{app} *when the latter is cycled over the range* $-B_0 \leq B_{app} \leq B_0$ *for the case* $B_0 = 3B^*$. *[30]*

$$4\pi M = \frac{1}{2}B^* \tag{1.34}$$

in the limit $B_0 > B^*$.

1.7.3 Critical state in disk-shaped superconductors

The extension of critical state models towards the realm of superconducting thin films began shortly after the successful production of thin film high temperature superconductors. It was quickly realised that many practical applications of HTSC will be as thin films, and it became therefore necessary to understand the behaviour of a thin film when magnetised. Here, as in the case for bulk superconductors, it is assumed that the material behaves quasi-statically - i.e. that the influence of the term $\partial \mathbf{E}/\partial t$ of the Maxwell equation is insignificant.

There has been various attempts to adapt the critical state framework to disk-shaped type-II superconductors with external magnetic fields applied perpendicular to the disk. J.D. Frankel[64], and M. Däumling and D.C. Larbalestier[65] employed numerical methods to obtain field and current patterns

in disk-shaped superconductor thin films assuming constant critical currents and also Anderson-Kim[4] type critical currents. For superconducting films, very weak magnetic field can penetrate into the film if it is applied perpendicular to the film plane, because of large demagnetisation effects. P.N. Mikheenko and Y.E. Kuzovlev[66] found analytic solutions for the disk-shaped thin film problem, and J. Zhu *et al*[67] expanded on their work to provide a framework to the critical state in periodic external magnetic fields. The main results of Mikheenko and Kuzovlev with Zhu *et al* 's adaptations are presented.

Consider a disk-shaped superconducting film of radius R and thickness d with external magnetic field B applied along the z-direction ($\mathbf{B} = B\hat{\mathbf{z}}$), perpendicular to the plane, after the sample is zero-field cooled. For the axially symmetrical current configuration only the circumferential current component is non-zero; circulating current in the film are treated as having uniform density in the $z-$direction of the film. The Bean assumption of field independent critical current density is made ($j_c(B) = j_{c0}$).

The magnetic moment M is (in cgs units)

$$M = \frac{1}{2c}\int_0^R \int_0^{2\pi} I(r) r^2 dr d\theta, \tag{1.35}$$

where $I(r) = jd$ is the surface current density. The radial and z-directional fields are[68] p 177, respectively,

$$B_r(r,z) = \frac{2}{c}\int_0^R G_r(r,\rho,z) I(\rho) d\rho \tag{1.36}$$

and

$$B_z(r,z) = \frac{2}{c}\int_0^R G_z(r,\rho,z) I(\rho) d\rho, \tag{1.37}$$

The functions G_r and G_z are defined as

$$G_r(r,\rho,z) = \frac{1}{\sqrt{(\rho+r)^2+z^2}}\left[-K(k) + \frac{\rho^2+r^2+z^2}{(\rho-r)^2+z^2}E(k)\right] \tag{1.38}$$

and

$$G_z(r,\rho,z) = \frac{1}{\sqrt{(\rho+r)^2+z^2}}\left[K(k) + \frac{\rho^2-r^2-z^2}{(\rho-r)^2+z^2}E(k)\right] \tag{1.39}$$

where

$$k^2 = \frac{4\rho r}{(\rho+r)^2+z^2} \tag{1.40}$$

and K and E are respectively complete elliptic integrals of the first and the second kind, defined

as[69]

$$K(k) = \int_0^{\pi/2} \frac{d\theta}{\sqrt{1-k^2\sin^2\theta}} \tag{1.41a}$$

$$E(k) = \int_0^{\pi/2} \sqrt{1-k^2\sin^2\theta}\, d\theta. \tag{1.41b}$$

The Meissner state

In the Meissner state, where the flux penetration into the sample in limited to a depth of the order of the penetration depth λ, one can assume, as a simplification

$$B_z(r, z=0) = 0, \qquad r < R. \tag{1.42}$$

Mikheenko and Kuzovlev[66] using calculations by Landau[70], found

$$B_r(r, z \to 0) = -\frac{2}{\pi} B \,\mathrm{sign}(z) \frac{r}{\sqrt{R^2 - r^2}}, \tag{1.43}$$

where B is the uniform external applied field ($\mathbf{B} = B\hat{\mathbf{z}}$) and the surface current density,

$$I(r) = -\frac{c}{4\pi} BF\left(\frac{r}{R}\right), \tag{1.44}$$

where F is defined as[66]

$$F(x) = \left\{ \begin{array}{ll} \frac{4}{\pi}\frac{x}{\sqrt{1-x^2}} & x < 1 \\ 0 & x > 1 \end{array} \right\}. \tag{1.45}$$

The magnetic field in the film plane generated by the shielding current is

$$B_z(r, z=0) = BQ(r/R) \tag{1.46}$$

where Q is defined as[66]

$$Q(x) = \left\{ \begin{array}{ll} -1 & x < 1 \\ \frac{2}{\pi}\left(-\arcsin\frac{1}{x} + \frac{1}{\sqrt{x^2-1}}\right) & x > 1 \end{array} \right\}. \tag{1.47}$$

The critical state

The intermediate state occurs as soon as magnetic vortices start to penetrate the film from the outside. We assume that vortices penetrate the sample symmetrically from the side to a radius $a(B)$ in the external field. The critical surface current, $I_c = j_c d$, flows in a ring, $a < r < R$, while the inner disk,

$0 < r < a$, remains free of vortices. Mikheenko and Kuzovlev[66] found analytic solutions for this case:

$$I(r) = -\frac{2}{\pi} I_c \arctan\left[\frac{r}{R}\sqrt{\frac{R^2 - a^2}{a^2 - r^2}}\right]\theta(a - r) - I_c\theta(r - a), \tag{1.48}$$

where

$$a = \frac{R}{\cosh\left(\frac{B}{B_c}\right)} \tag{1.49}$$

$$B_c = \frac{2\pi}{c} I_c = \frac{2\pi}{c} j_c d \tag{1.50}$$

and θ is the Heaviside step function

$$\theta(x) = \left\{ \begin{array}{lll} 1 & \text{if} & x \geq 0 \\ 0 & \text{if} & x < 0 \end{array} \right\}. \tag{1.51}$$

Fig. 1-15 shows the reduced surface current density distribution $I(r)/I_c$ for various applied fields B_0/B_c, applied to a superconducting disk of unit radius. The case of $B_0/B_c = 0.1$ agrees with the Meissner state solution of eq. 1.44 while the other profiles show increasing flux penetration into the film as calculated by eq. 1.48. D. Gupta *et al*[71] expanded on this model to cast the problem into matrix form. Using that formalism he was able to find current profiles and hence magnetic field profiles for arbitrary constituent current-field relationships $j = j(B)$.

Harmonic applied field

The contribution of Zhu *et al*[67] was to extend the 2D-model of Mikheenko and Kuzovlev to incorporate the case of applied perpendicular harmonic fields, i.e. $B = B_0 \cos \omega t$. Consider the case when the external field is monotonically decreased to a field B ($|B| \leq B_0$), after having been increased monotonically from zero to the maximum field B_0 (the amplitude). Analytical solutions to current and field patterns can be found for this case. If we notice that

$$B = B_0 + B^*, \qquad B^* = B - B_0, \tag{1.52}$$

the problem can be treated as a superposition of the following two cases:

1. In the ZFC sample, the external field is increased monotonically from zero to B_0. The sample has a critical surface current of I_c.

2. In the ZFC sample, the external field is decreased monotonically from zero to $B^* = B - B_0$.

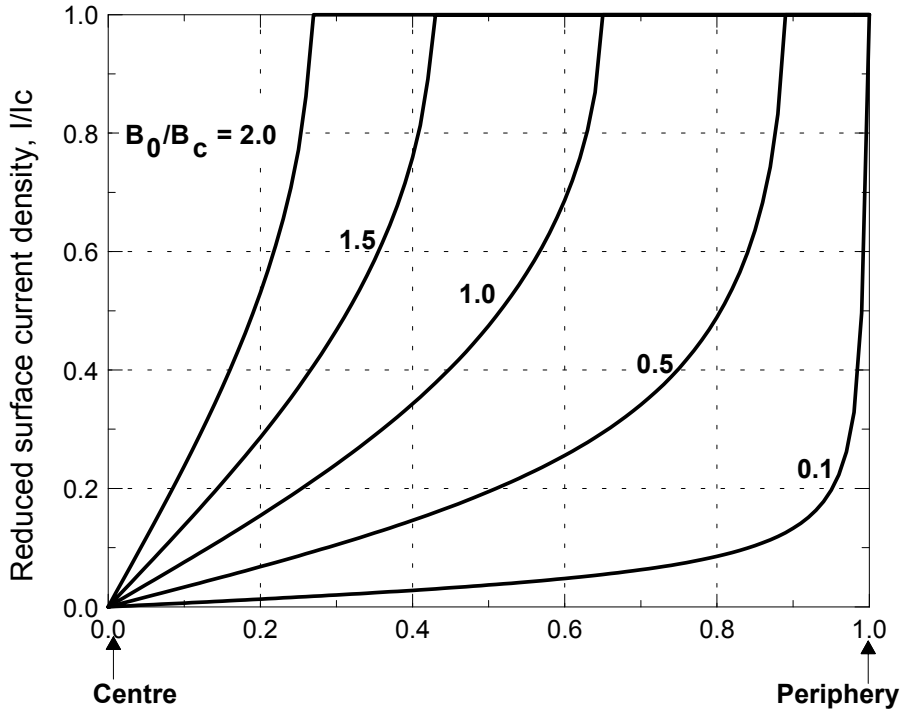

Figure 1-15: *j_c-limited surface current calculated by the 2D-critical state model proposed by J. Zhu et al.[67] for various levels of external magnetic field B_0/B_c with values as indicated in the graph.*

However, the critical surface current flowing in the sample is $2I_c$.

The shielding currents of the second case can be easily found by substituting $-I_c$ with $2I_c$, and B with B^* into solutions for the first case:

$$I(r) = 2I_c \frac{2}{\pi} \arctan\left[\frac{r}{R}\sqrt{\frac{R^2-b^2}{b^2-r^2}}\right]\theta(b-r) + 2I_c\theta(r-b), \tag{1.53}$$

and

$$b = \frac{R}{\cosh\left(\frac{B-B_0}{-2B_c}\right)}, \tag{1.54}$$

where b is the radius to which the vortices have penetrated into the disk sample in the second case. The critical surface current $2I_c$ in the second case can be understood this way: a shielding surface current $-I_c$ is introduced in the ring $a < r < R$ in the first case, and a shielding surface current $+2I_c$ in induced in the ring $b < r < R$ in the second case; the net shielding surface current of the sample is $+I_c$ in the ring $b < r < R$ after summing the currents from both cases, satisfying the critical state model

and the critical surface current criterion $|I(r)| \leq I_c$. Superposing solutions of the magnetic moment and current patterns for case 1 and case 2 give the exact analytical solutions of the magnetic moment and the shielding current,

$$M = -\frac{2}{3\pi} B_0 R^3 S\left(\frac{B_0}{B_c}\right) - \frac{2}{3\pi}(B - B_0) R^3 S\left(\frac{B - B_0}{-2B_c}\right), \tag{1.55a}$$

$$S(x) = \frac{1}{2x}\left[\arccos\frac{1}{\cosh x} + \frac{\sinh|x|}{\cosh^2 x}\right], \tag{1.55b}$$

and

$$\begin{aligned} I(r) = & -I_c \frac{2}{\pi} \arctan\left[\frac{r}{R}\sqrt{\frac{R^2 - a^2}{a^2 - r^2}}\right]\theta(a - r) - I_c\theta(r - a) \\ & +2I_c \frac{2}{\pi} \arctan\left[\frac{r}{R}\sqrt{\frac{R^2 - b^2}{b^2 - r^2}}\right]\theta(b - r) + 2I_c\theta(r - b). \end{aligned} \tag{1.56}$$

If the external field is increased after the minimum field $-B_0$ is reached, current and field patterns can be calculated in a similar way as presented above. Using eq. 1.56 we calculated the surface current distribution I/I_c in a unit radius ZFC disk-shaped superconducting thin film with the applied magnetic field cycled from zero to $B/B_c = 3$ and down to $B/B_c = -3$, shown in **Fig. 1-16**. We define $B_c = 2\pi I_c/c = 2\pi d j_c/c$. Snapshots are taken at certain key field strenghts, and correlated with positions on the hysteresis loop in **Fig. 1-17**. **Fig. 1-17** shows the magnetic moment $M(B)$ which we calculated using eq. 1.55 the same superconducting disk in a time-varying periodic weak external magnetic field; external fields are applied after the sample becomes superconducting. Here $M_0 = (2/3\pi)B_c R^3$. Position **g**, where B is zero while the magnetisation is not, is known as the *remanent* magnetisation case.

1.8 Scope of Investigation

One of the main aims of this investigation was to design and construct a pulsed laser deposition system *from scratch*. This PLD system was used in an effort to produce good quality superconducting $YBa_2Cu_3O_7$ thin films. We report measurements of the remanent flux creep in thin superconducting films deposited by pulsed laser deposition, over a range of temperatures up to $T_c - T = 0.05$ K, where it was experimentally possible to get into the usually inaccessible long-time limit of the persistent current decay. The functional form of the time dependence of magnetisation of a thin film is investigated, and also the functional forms of both $U(T)$ and critical current density $j_c(T)$ in the range $T_c > T > T_c - 10$ K.

The aim of **Chapter 2** is to discuss all the experimental methods employed to investigate YBCO

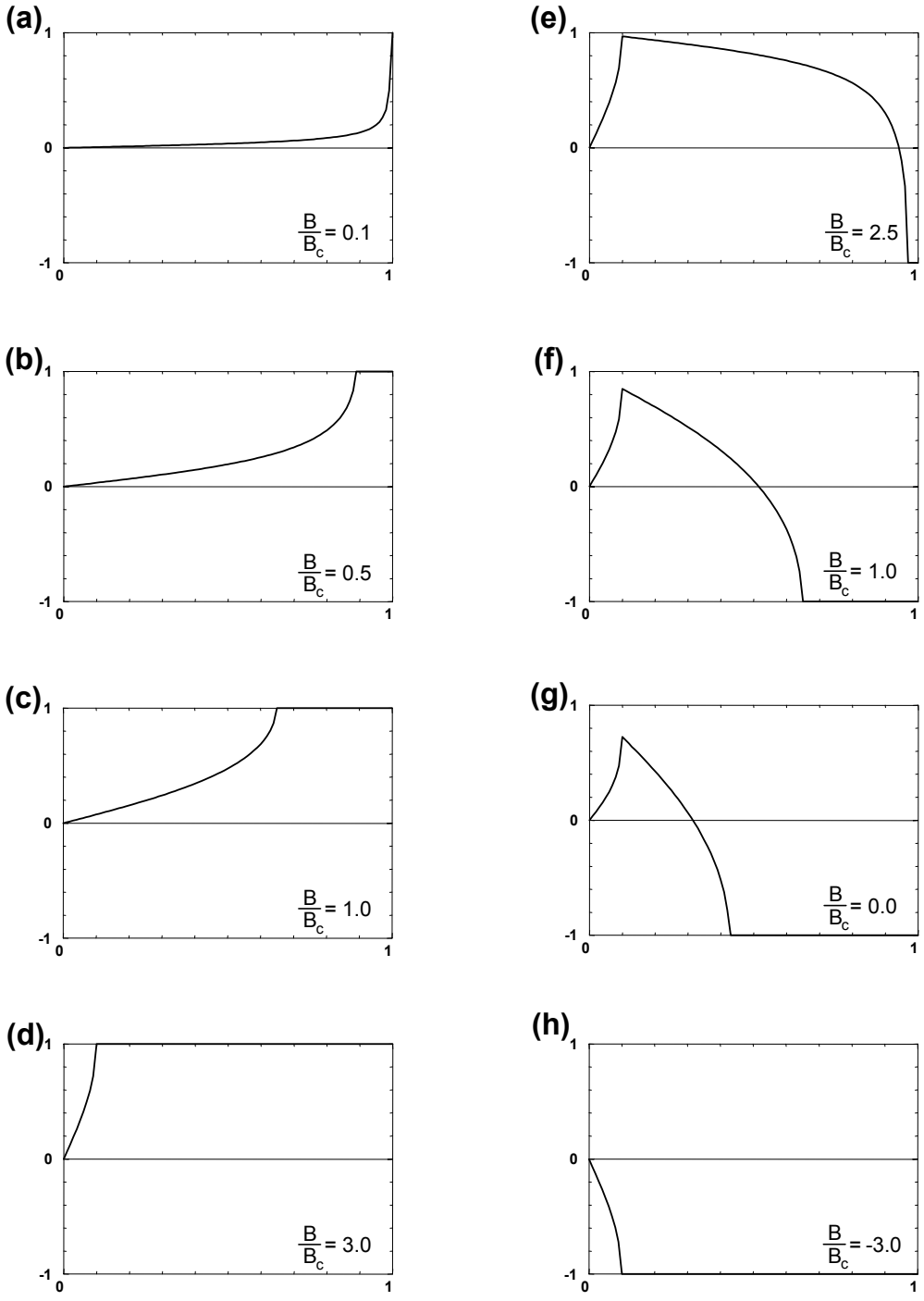

Figure 1-16: *Surface current density I/I_c profile of a superconducting thin film of unit radius in the critical state. The profiles correspond to various applied field strenghts B/B_c= (a) 0.1, (b) 0.5, (c) 1.0, (d) 3.0, (e) 2.5, (f) 1.0, (g) 0.0, (h) –3.0.*

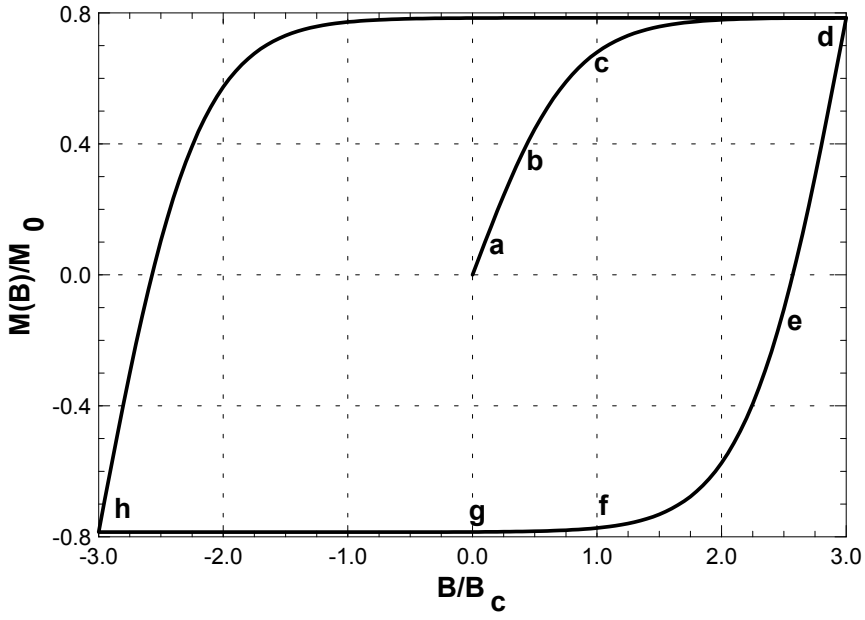

Figure 1-17: *Magnetic moment -$M(B)/M_0$ calculated using eq. 1.55 for a 2D superconducting disk-shaped superconductor in a periodic external magnetic field; external fields are applied after the sample becomes superconducting. The labeled points correspond to graphs in* ***Fig. 1-16****. Here $M_0 = (2/3\pi)B_cR^3$, and the magnetic moment saturates at M_{sat}=$\frac{\pi}{4}M_0$.*

thin films deposited by PLD for this study. This includes Rutherford backscattering spectroscopy (RBS), x-ray diffraction (XRD), atomic force microscopy (AFM), resistivity measurements and susceptibility measurements. The physics and instrumentation considerations are briefly discussed in each case.

In **Chapter 3**, pulsed laser deposition (PLD) is introduced, and the design and implementation of the PLD system is given in detail. One of the main aims of this investigation was to design and construct a pulsed laser deposition system from scratch. This chapter fulfills an additional role as a technical document and user guide for the NAC's PLD system. The layout of this chapter is as follows: First, current understanding of the PLD process will be reviewed, and then the design of the PLD system will be discussed. Practical considerations will be addressed throughout the discussion. A typical deposition run will be reviewed. The chapter concludes with a discussion of certain problematic aspects of the system, and suggestions to remedy it and extend the work.

The main purpose of **Chapter 4** is to investigate the structural properties of $YBa_2Cu_3O_7$ thin films produced by PLD under various deposition conditions. The structural properties studied are

stoichiometry, investigated by Rutherford backscattering spectroscopy (RBS); crystallinity, investigated by x-ray diffraction (XRD); and surface morphology investigated by atomic force microscopy (AFM). The spatial distribution of thickness and stoichiometry of depositants is investigated using RBS. The critical temperature of each film is determined by resistivity and susceptibility methods. A series of about 40 YBCO films was deposited on MgO(100) under various conditions. Naturally, not every deposition was optimal, thus there is a degree of scatter in the data presented. However, several trends can be identified for varying deposition parameters, which will be discussed in this chapter.

Several experiments were performed to gain understanding of the flux creep behaviour of YBCO thin films close to T_c, reported in **Chapter 5**. The experimental study of flux creep in high temperature superconductors presents a number of practical problems to solve. In this chapter, we recount how temperature stability was achieved, and magnetic field generated by a magnetised sample was accurately measured. Finally the studies of the remanent flux creep in a YBCO thin film were reported. Notable aspects are the reduction of noise at the SQUID sensor, and the reproducible magnetisation of the sample.

The conceptual framework to understand the experimental results of this chapter is provided by the critical state model and the theory of flux creep. The magnetisation of a thin film superconductor is best visualised with a hysteresis diagram, showing induced magnetic field versus applied field, proportional to drive current. A number of loops were recorded under varying conditions, to probe the sensitivity of the magnetisation process to magnetisation rate and the maximum current during magnetisation. These loops also revealed the sensitivity of the local critical current density to applied field.

The decay of the remanent flux was investigated since it revealed properties of the flux creep mechanism. This was studied near T_c, where limited experimental results were achieved in the past. The phenomenon of flux freezing is studied. The temperature dependence of j_c was extracted from data of SQUID signal versus temperature as a magnetised sample is slowly warmed up to $T > T_c$.

Regarding the use of physical units, we resorted to common practice among the publications of the *American Physical Society (APS)* and the *Institute of Physics (IOP)*. Whenever experiments are considered, we used practical, laboratory units : millibar (mbar), centimeter (cm), millimeter (mm), micrometer (μm), minute (min), hour (h), degrees Celsius (°C). We have however consistently replaced Ångstrom with nanometer (nm). For theoretical calculations, we used the *CGS* system. When we discussed sampled heating during sample preparation, we used °C, while when we discussed cooling the samples we used the Kelvin scale (K).

Chapter 2

Experimental Methods

2.1 Rutherford backscattering spectrometry

2.1.1 Introduction

In Rutherford Backscattering Spectrometry (RBS)[72] measurements, a mono-energetic ion beam is directed onto the sample under study, and the elastically backscattered particles are detected by a solid state detector. RBS is ideally suited for analysis of the primary quantities of interest in high-temperature superconducting thin films, which are film thickness, identity of elemental constituents, their concentrations and depth distributions. RBS has the further advantage of being highly quantitative, allowing analysis to be made fast and non-destructively while remaining insensitive to chemical bonding effects within the sample. Thus RBS is a fast and direct method for obtaining elemental depth profiles in solids. There are three basic parameters which are of importance in the RBS, each related to an analytical capability of the method:

1. The kinematic factor K (mass analysis);
2. The differential scattering cross section (quantitative analysis);
3. The energy loss of a particle (depth analysis).

The energy of the backscattered particle is entirely determined by its own mass m, the mass M of the target atom and the scattering angle θ, measured in the laboratory system of co-ordinates. The typical geometry for backscattering is shown in **Fig. 2-1**. The kinematic factor is defined as the ratio

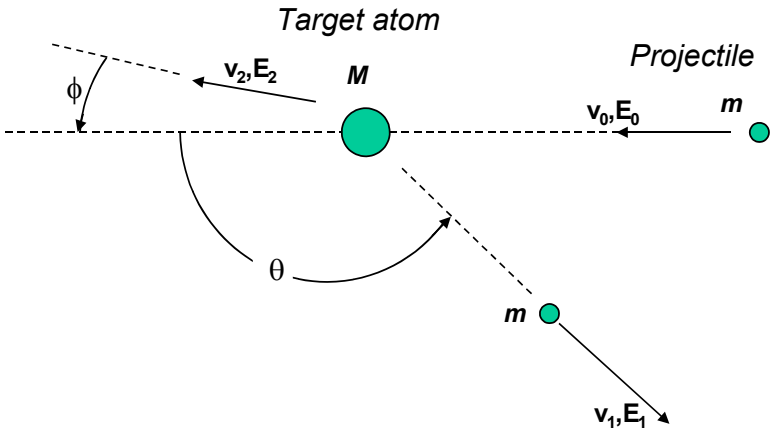

Figure 2-1: *Schematic representation of an elastic collision between a projectile of mass m, velocity v_0 and kinetic energy E_0 and a target mass M, which is initially at rest. After the collision, the projectile and the target mass have velocities and energies $\mathbf{v}_1$, E_1, and $\mathbf{v}_2$ and E_2, respectively. The angles θ and ϕ are positive as shown. All quantities refer to a laboratoty frame of reference.[72]*

of the projectile energies after (E_1) and before (E_0) collision,

$$K = \frac{E_1}{E_0} = \left[\frac{m\cos\theta + \sqrt{M^2 - m^2\sin^2\theta}}{m+M} \right]^2 . \tag{2.1}$$

This equation indicates the dependence of the energy of the backscattered particle on the target mass. By measuring the energy E_1 of the backscattered particles the mass M of the atoms from which they are scattered can be determined. The differential scattering cross section $\frac{d\sigma}{d\Omega}$ is described by following expression in the laboratory system:

$$\frac{d\sigma}{d\Omega} = \left(\frac{zZe^2}{2E_0\sin^2\theta} \right)^2 \frac{\left[\cos\theta + \sqrt{1 - \left(\frac{m}{M}\sin\theta\right)^2} \right]^2}{\sqrt{1 - \left(\frac{m}{M}\sin\theta\right)^2}}, \tag{2.2}$$

where z and Z are the atomic numbers of the projectile and target atom respectively and Ω is the finite solid angle subtended by the detector. The differential scattering cross section is directly related to the scattering probability and connects the backscattering yield to quantitative analysis[72].

When a projectile penetrates a target, it loses it's energy to the electrons of the target atoms by ionisation and excitation as well as by nuclear collisions. When the projectile undergoes an elastic collision it can change its trajectory into an outward direction with respect to the target surface. During its outward path it again loses energy to the target atoms until it emerges from the target. By measuring this energy loss, the depth to which the particle has penetrated can be determined. The energy loss per unit length is expressed as a stopping power, $\frac{dE}{dx}$. The stopping cross section is given as $\varepsilon = \frac{1}{N}\frac{dE}{dx}$, where N is the atomic density of the target. Both stopping power and stopping cross section depend upon the composition of the target and is a relatively slowly varying function of projectile energy. In general, for small energy losses, $\frac{dE}{dx}$ does not change much and there exists a linear relation between energy loss (ΔE) and depth (t) that can be expressed as $\Delta E = [S]t$, where $[S]$ is called the backscattering energy loss factor. In the so-called surface approximation, where the target film is very thin, it can be assumed that $\frac{dE}{dx}$ of the projectile does not change and can be evaluated at the energy E_0 for it's incoming path and $E_1 = KE_0$ for its outgoing path. Thus, the energy lost by a projectile (mass m) which was backscattered by an atom (mass M) at depth t, can be approximated as:

$$\Delta E = [S]t = \frac{K}{\cos\theta_1}\frac{dE}{dx}|_{E_0} + \frac{1}{\cos\theta_2}\frac{dE}{dx}|_{KE_0} \tag{2.3}$$

in which θ_1 and θ_2 are the angles between the surface normal and the outgoing particle direction respectively.

In a compound target, the energy loss is calculated or measured from the stopping power of the projectile in the compound, while the scattering occurs between the projectile and a given atom of the compound molecule. A_mB_n is given in the same way as equation 2.3 as

$$\Delta E_A = [S]_A^{A_mB_n}t = \frac{K_A}{\cos\theta_1}\frac{dE}{dx}|_{E_0} + \frac{1}{\cos\theta_2}\frac{dE}{dx}|_{K_AE_0} \tag{2.4}$$

where K_A is the backscattering kinematic factor of element A. The application of additivity of stopping cross sections for compound targets is based on Bragg's rule which states that $\varepsilon^{A_mB_n} = m\varepsilon^A + n\varepsilon^B$, where ε^A and ε^B are the stopping cross sections of the individual atoms A and B. The total energy loss in the compound A_mB_n can thus be given as:

$$\Delta E = [S]^{A_mB_n}t = \frac{m}{m+n}[S]_A^{A_mB_n}t + \frac{n}{m+n}[S]_B^{A_mB_n}t \tag{2.5}$$

The energy spectra of backscattered particles give quantitative information on the atomic density depth profiles of the atom in the sample. The height of the spectrum H gives the number of backscattered

particles with energy in a certain energy interval δE between E and $E + \delta E$, and is given by

$$H = n_0 \Omega \left(\frac{d\sigma}{d\Omega} \right) N \frac{\delta E}{[S] \cos \theta_1} \tag{2.6}$$

where n_0 is the number of incident particles, Ω the solid angle of the detecting system and N the atomic density, while $\frac{d\sigma}{d\Omega}$ and $[S]$ are given by equations 2.2 and 2.3 respectively[72].

The height of spectrum peak H_A for element A in compound $A_m B_n$ can be given in the same way as equation 2.6:

$$H_A = n_0 \Omega \left(\frac{d\sigma}{d\Omega} \right)_A N_A \frac{\delta E}{[S]_A^{A_m B_n} \cos \theta_1} \tag{2.7}$$

where N_A refers to the density of atoms A in compound $A_m B_n$. A similar equation holds for H_B the height of the spectrum peak for element B. It is obvious that N_A and N_B are proportional to m and n, thus

$$\frac{H_A}{H_B} = \frac{\sigma_A}{\sigma_B} \frac{m}{n} \frac{[S]_B^{A_m B_n}}{[S]_A^{A_m B_n}} \tag{2.8}$$

where σ_A is the average differential scattering cross section given by

$$\sigma_A = \frac{1}{\Omega} \int \left(\frac{d\sigma}{d\Omega} \right)_A d\Omega \tag{2.9}$$

.

Extensive use has been made of the *RUMP* RBS simulation package[73]. Although RBS has many favourable features for determining depth profiles quantitatively, the technique does however, suffer from two serious limitations:

1. It is difficult to determine the identity of heavy atomic species, since the mass resolution decreases with increasing mass.

2. Low levels of light mass impurities in heavier mass substrates are difficult to measure because of the unfavourable ratio of scattering cross sections.

These limitations were not applicable for the current study, since Y, Ba, and Cu are well separated in terms of mass, yielding distinct peaks for the different metals in YBCO. The oxygen in YBCO overlaps with the substrate spectrum in the case of MgO and $SrTiO_3$, and most other substrates used in other studies.

2.1.2 Experimental considerations

RBS analysis was performed on deposited YBCO films at the National Accelerator Centre using the 6 MeV Van de Graaff accelerator. During RBS, mono-energetic $\alpha-$particles (range $2-3$ MeV) were directed towards the film at an angle of 10° to the film's surface normal to ensure that the $\alpha-$particles do not channel along aligned planes of an epitaxial sample, but rather the $\alpha-$particles are presented a sample with atoms randomly positioned when viewed along the incoming projectile path. The silicon surface barrier detector was situated at an angle of $\theta = 165^\circ$ from the incident beam, to be able to detect the backscattered $\alpha-$particles. The solid state detector was biased with +50 V. Samples were mounted on a motorised target holder which can hold 10 samples. The beam was collimated to a diameter of 2 mm and the beam current was typically ~ 50 nA ($\sim 1.5 \times 10^{11}$ singularly ionised $\alpha-$particles per second), and a total integrated charge of ~ 10 μC ($\sim 3 \times 10^{13}$ $\alpha-$particles) was used. The beam transport and sample holder were housed in vacuum chambers evacuated to a vacuum of better than 10^{-6} mbar during the RBS run.

The detector was connected to a system of analysing electronics consisting of a preamplifier, amplifier, analogue to digital converter and multichannel analyser. This electronic system was connected to a computer workstation which controlled the experimental run and captured the backscattering spectrum. The spectra were later downloaded to a desktop computer and analysed using the *RUMP* package[73]. **Fig. 2-2(a)** shows the RBS spectrum of a $YBa_2Cu_3O_{7-x}$ thin film deposited on a $SrTiO_3$ substrate, while **Fig. 2-2(b)** shows the RBS spectrum of a $YBa_2Cu_3O_{7-x}$ thin film deposited on a MgO substrate, both spectra were obtained using 3.0 MeV $\alpha-$particles. Indicated just above the channel axis are the surface positions of the various elements present in the samples, found by eq. 2.1. YBCO/MgO presents RBS spectra with well separated peaks when the films is thin enough, allowing accurate determination of compositions. For thicker films, where a substantial overlap of peaks occur, a certain amount of inaccuracy is introduced in the film characterisation, but satisfactory results are still obtained. With YBCO/$SrTiO_3$ films, the situation was slightly more complex, because the Sr^{38} and Ti^{22} peaks overlapped with the Y^{39} and Cu^{29} peaks, complicating the determination of thickness and stoichiometry. Knowledge of the set-up geometry and the energy of the incoming $\alpha-$particles enables one to calculate a theoretical spectrum of a $YBa_2Cu_3O_7$ thin film deposited on some substrate using *RUMP*. One needs to enter the correct atomic density of $YBa_2Cu_3O_7$ (0.750276×10^{23} atoms/cm^3) into the parameter model for the thin film structure. By adjusting the film thickness and it's composition the best fit is achieved through an iterative process done "by hand". RBS studies fulfilled a crucial role in this study: to verify the composition of YBCO films, since deviations from the perfect cation ratios of Y:Ba:Cu=1:2:3 lead to a degrading of superconducting properties.

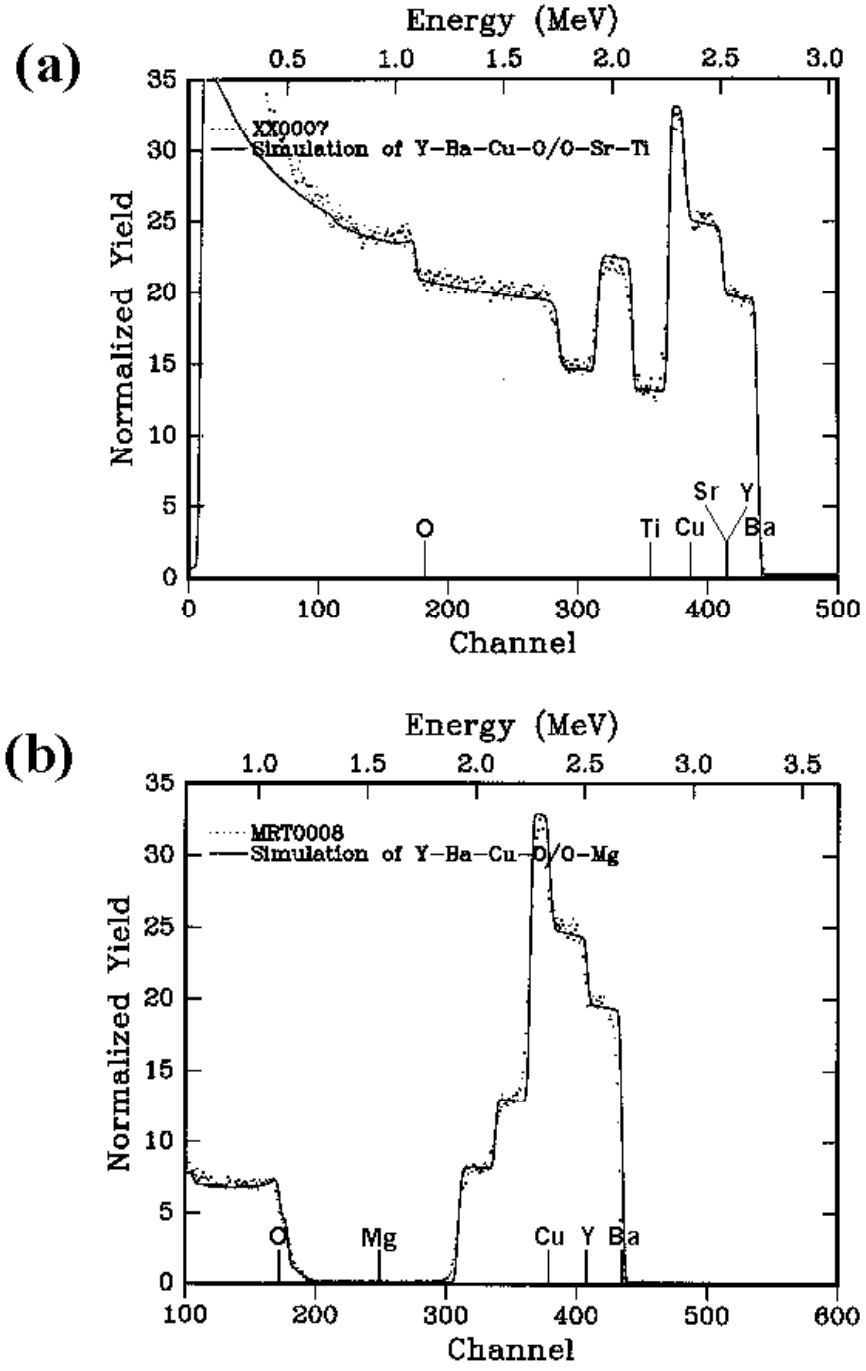

Figure 2-2: *RBS spectrum of $YBa_2Cu_3O_7$ deposited on (a) $SrTiO_3$ and (b) MgO. There are no interaction between the YBCO films and the substrates, since the back edges of the Y, Ba and Cu peaks are straight down.*

2.1.3 Error analysis

We analyse the uncertainty in determination of elemental ratio's from a RBS spectrum. The number of $\alpha-$particles emitted from a radio-active source in a fixed amount of time can be modelled by the Poisson distribution, as determined experimentally by E. Rutherford and H. Geiger[74]. We can safely assume that for mono-energetic $\alpha-$particles arriving at a target from an accelerator, the number distribution per length of time would also have a Poisson distribution. Similarly, the amount of $\alpha-$particles scattered by different elements would have Poisson distributions.

Let us assume we have different elements $1, 2, 3, ...n$ in the thin film sample in a RBS experiment, where the number of $\alpha-$particles scattered by each element and observed by a detector is stochastic variables $L_1, L_2, L_3...L_n$. Then $L_i \sim \text{Poisson}(\lambda_i)$ and the expected value is $\text{E}(L_i) = \lambda_i$ and variance $\text{var}(L_i) = \lambda_i$. The number of $\alpha-$particles from element i observed in a channel p (corresponding to a energy range $E_p...E_p + \delta E$) is L_{ip} and $L_{ip} \sim \text{Poisson}(\lambda_{ip})$ and we have $\sum_p \lambda_{ip} = \lambda_i$.

We observe in **Fig. 2-2(b)** that the barium shoulder (located in channels $A = \{409...421\}$) has contributions only from scattering against Ba nuclei. The shoulder height is an indication of the amount of Ba present in the film, as indicated by eq. 2.7. The average in the channel range A yields an estimate of the peak height,

$$\widehat{\lambda}_{\text{Ba}} = \overline{\lambda}_{\text{Ba},\ A} = 2868.3, \tag{2.10}$$

where the hat signifies that the number is an estimator for the parameter λ_{Ba}.

For yttrium, we are confronted with a combined shoulder with Ba, which is deconvoluted in the following manner:

In any given channel p, where we have contributions from two different elements 1 and 2, we have $L_{1p} + L_{2p} \sim \text{Poisson}(\lambda_{1p} + \lambda_{2p})$. Thus $\text{E}(L_{1p} + L_{2p}) = \lambda_{1p} + \lambda_{2p}$ and $\text{var}(L_{1p} + L_{2p}) = \lambda_{1p} + \lambda_{2p}$.

In the channels 382...401 we have contributions from Y and Ba only. Again, we determine the average in the channel range $B = \{382...401\}$ as an estimate for $\text{E}(L_{\text{Ba},\ B} + L_{\text{Y},\ B}) = 3631.2$. Thus

$$\widehat{\lambda}_{\text{Y}} \simeq \text{E}(L_{\text{Ba},\ B} + L_{\text{Y},\ B}) - \widehat{\lambda}_{\text{Ba}} = 762.9 \tag{2.11}$$

The parameter for the Poisson distribution for copper is extracted from the very last shoulder, which lies in the range $C = \{315...326\}$. We have

$$\widehat{\lambda}_{\text{Cu}} = \overline{\lambda}_{\text{Cu},\ C} = 1167.6 \tag{2.12}$$

Having extracted the parameters $\widehat{\lambda}_{\text{Y}}$, $\widehat{\lambda}_{\text{Ba}}$ and $\widehat{\lambda}_{\text{Cu}}$, we can determine the elemental ratio's. Eq. 2.8

relates an elemental ratio to the peak height ratio H_A/H_B. The factor

$$\frac{\sigma_A}{\sigma_B} \cdot \frac{[S]_B^{A_m B_n}}{[S]_A^{A_m B_n}} \doteq R^*_{AB} \tag{2.13}$$

is treated as an unknown to be determined heuristically, since calculation would be prohibitively complicated. We investigate the case Ba/Y:

The theoretical ratio for Ba/Y is $N_{\mathrm{Ba}}/N_{\mathrm{Y}} = \frac{2}{1} = 2$, and the peak ratio is $\widehat{\lambda}_{\mathrm{Ba}}/\widehat{\lambda}_{\mathrm{Y}}$, thus

$$\frac{H_{\mathrm{Ba}}}{H_{\mathrm{Y}}} = \frac{\widehat{\lambda}_{\mathrm{Ba}}}{\widehat{\lambda}_{\mathrm{Y}}} = \frac{N_{\mathrm{Ba}}}{N_{\mathrm{Y}}} \cdot R^*_{\mathrm{Ba,\ Y}} \tag{2.14}$$

and $R^*_{\mathrm{Ba,\ Y}} = 1.8799$. We now determine the variance $\mathrm{var}(N_{\mathrm{Ba}}/N_{\mathrm{Y}})$. Thus

$$\mathrm{var}\left(\frac{N_{\mathrm{Ba}}}{N_{\mathrm{Y}}}\right) = \frac{\mathrm{var}\left(H_{\mathrm{Ba}}/H_{\mathrm{Y}}\right)}{R^*_{\mathrm{Ba,\ Y}}} = \frac{\mathrm{var}\left(\widehat{\lambda}_{\mathrm{Ba}}/\widehat{\lambda}_{\mathrm{Y}}\right)}{\left(R^*_{\mathrm{Ba,\ Y}}\right)^2}. \tag{2.15}$$

The expected value of the ratio of stochastic variables $Z \sim \mathrm{Poisson}(\theta)$ and $X \sim \mathrm{Poisson}(\lambda)$ is $\mathrm{E}(Z/X) = \theta/\lambda$, and the variance is

$$\mathrm{var}\left(\frac{Z}{X}\right) \cong \frac{\theta}{(\lambda-1)^2}\left(\frac{\theta}{\lambda-1}+1\right) \cong \frac{\theta}{\lambda^3}\left(\theta+\lambda\right), \tag{2.16}$$

as determined by simulation, valid for $\theta,\, \lambda \geqslant 400$, with error $\lesssim 1\%$[75]. We find

$$\sigma_{\mathrm{Ba,\ Y}} = \mathrm{stddev}\left(\frac{N_{\mathrm{Ba}}}{N_{\mathrm{Y}}}\right) = \frac{\left(\widehat{\lambda}_{\mathrm{Ba}}/\widehat{\lambda}_{\mathrm{Y}}^3\right)\left(\widehat{\lambda}_{\mathrm{Ba}}+\widehat{\lambda}_{\mathrm{Y}}\right)}{R^*_{\mathrm{Ba,\ Y}}} \tag{2.17}$$

$$= 0.0125. \tag{2.18}$$

If we treat one standard deviation above and below the mean as the error range, we have determined the relative Ba/Y ratio to an accuracy of 1.3%.

For the ratio Cu/Y we find $R^*_{\mathrm{Cu,\ Y}} = 0.5102$, and $\sigma_{\mathrm{Cu,\ Y}} = 0.00995$, thus we have determined the Cu/Y ratio to an accuracy of 0.7%. Thus the formula is $\mathrm{YBa}_{2\pm0.01}\mathrm{Cu}_{3\pm0.01}\mathrm{O}_{7-\delta}$.

2.2 X-ray diffraction measurements

X-ray diffraction (XRD) spectroscopy can reveal the microscopic and morphological structure of thin films. Most important for the purposes of this study, it can determine the orientation of crystal grains in a thin film, thereby showing whether the film has grown epitaxially or not. The film could also be

shown to be polycrystalline, single crystal or amorphous. The identification of any crystalline phases present and the determination of lattice parameters also constitute an important use of XRD[76].

The Bragg-Brentano geometry, also known as the $\theta - 2\theta-$ geometry, usually employed for powder samples, is also commonly used to determine which, if any, of a film's diffraction planes lie parallel to the substrate surface. $YBa_2Cu_3O_{7-\delta}$'s critical current density is much larger in the $a/b-$plane than in the $c-$axis direction. Thus, when growing $YBa_2Cu_3O_{7-\delta}$ thin films it is desirable to have the $c-$axis orientated perpendicular to the substrate surface to achieve a large in-plane critical current density. Thus one would expect to see only $(00l)$ lines for $c-$axis orientated films in the Bragg-Brentano measurement. **Fig. 2-3** introduces the various definitions of the angles used in this work. **Fig. 2-3(a)** shows the geometry for Bragg-Brentano measurement. The purpose of this set-up is to measure the intensity of the x-rays scattered through an angle of 2θ while the angle θ is scanned. A *Philips* diffractometer at the University of Stellenbosch was used to perform routine Bragg-Brentano measurements. The incident beam from the diffractometer's tube was monochromated with a focussing pyrolytic graphite crystal to select only the peaks due to the $Cu-K\alpha$ line ($\lambda = 0.154184$ nm) and to suppress the background and random reflections. The x-rays were produced with a voltage of 50 kV and a current of 40 mA applied to the tube. The diffractometer was controlled by a desktop computer, running *Difftech* software, which controlled the goniometer and stored the data from the detector on computer disk.

All the samples used in this study were checked for crystallinity and orientation of the c-axis. The films were mounted such that the surfaces were all in the correct plane, thus the irregular back surface (due to residual silver paint) did not cause trouble. This was accomplished by aligning the sample surface with the top surface of the mounting piece on a clean table surface and fixing the sample in that position with modelling clay.

All superconducting films reveal $c-$axis orientation and $YBa_2Cu_3O_7$ phase characteristics, with very little other contributions for impurity phases. Bragg-Brentano x-ray diffraction measurements were performed routinely on YBCO/MgO and YBCO/$SrTiO_3$ samples.

To obtain a better understanding of crystallinity of the films, two samples were selected (YBCO on each of MgO and $SrTiO_3$) and sent to the Max Planck Institute (MPI) of Microstructure Physics in Halle(Saale), Germany for detailed analysis. **Fig. 2-3(b)** shows the three-dimensional diagram of XRD set-up at the MPI. The sample holder x-ray diffractometer had three degrees of freedom in comparison to the one degree of freedom in the Bragg-Brentano set-up. One can imagine the stationary point (the origin in **Fig. 2-3(b)**) to be located on the sample surface and a perpendicular axis (marked by vector **n**) affixed to that point. The sample can rotate around the axis **n**, and the axis can also be tilted in two possible orthogonal directions: in the direction of the $y-$axis (the angle designated by θ), and in the direction of the $x-$axis (the angle designated by ψ). The horizontal plane is indicated by the $x-y$-plane.

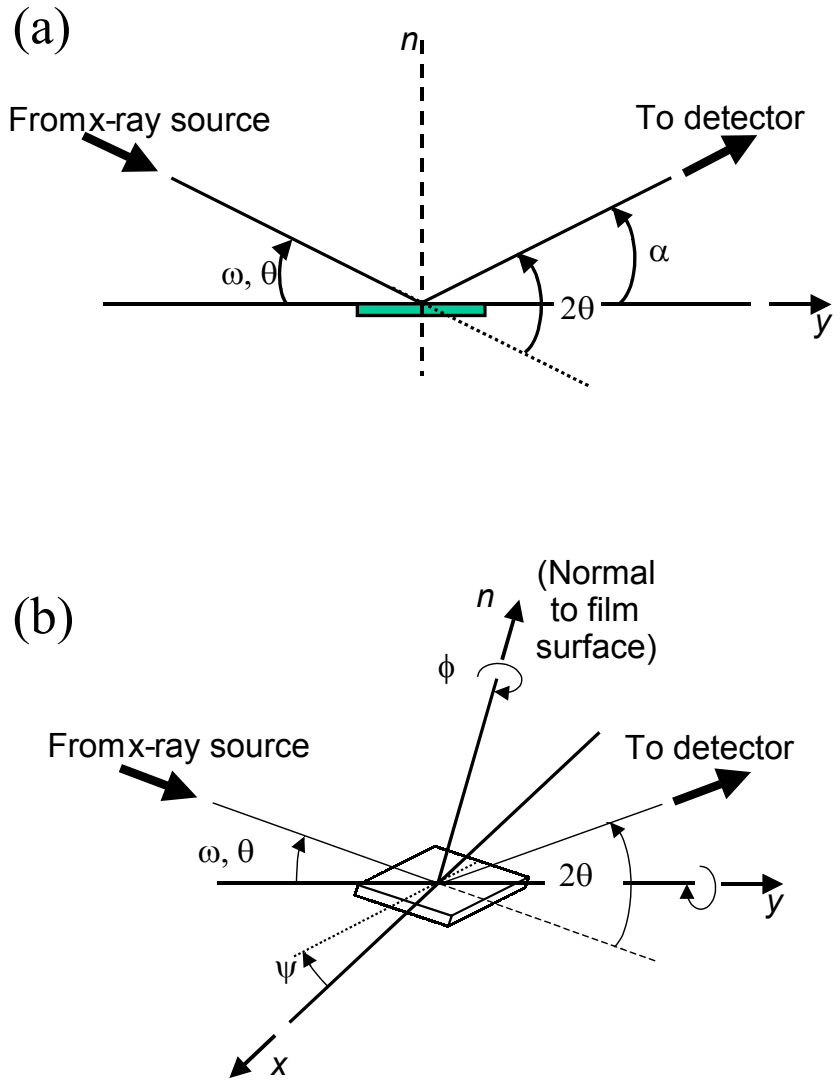

Figure 2-3: *Diagram showing the principal angles for XRD. (a) The geometry for Bragg-Brentano ($\theta-2\theta$) measurement. The purpose of this set-up is to detect or measure the intensity of the x-rays scattered through an angle of 2θ while the angle is θ scanned. (b) Three-dimensional diagram of general XRD set-up. The horisontal plane is indicated by the $x-y$-plane. The sample can be tilted out of the horizontal plane, indicated by the angle ψ (around the y-axis). The vector* $\mathbf{n}$ *denotes the normal to the sample surface, The sample can be rotated around the (movable) normal axis,* $\mathbf{n}$*, indicated by the angle ϕ. The origin, located on the film surface, was a stationary point in this geometry.*

The results of that study is presented in Chapter 4.

It should be noted that all 2θ angle values in this work are given for reflections with the Cu-Kα_1-line; for the purposes of calculations taken at $\lambda = 0.154184$ nm. The Cu-Kα_2-line ($\lambda = 0.1544390$ nm) forms a doublet with the Kα_1-line, thus they are inseparable on the spectra, while the Cu-Kβ_1-line ($\lambda = 0.1392218$ nm) show up as separate very faint lines[76]. The $d-$spacings for orthorhombic crystals can be obtained with

$$\frac{1}{d^2} = \frac{h^2}{a^2} + \frac{k^2}{b^2} + \frac{l^2}{c^2}. \tag{2.19}$$

.

2.3 Atomic force microscopy

2.3.1 Introduction

Atomic force microscopy (AFM) is a powerful tool for the examination of surfaces. In general, AFM enables one to detect surface morphology, nanoscale structures, and under ideal conditions, molecular- and atomic-scale lattices[77]. In the *contact-mode* AFM, the spatial variation of the tip-sample repulsive force or that of the tip height is converted into an image as the tip is scanned relative to the sample surface in a raster-line fashion, generating a three-dimensional topographical image[78]. Surface morphology can be accurately determined, and since the repulsive force is universal, AFM is applicable to conducting and insulating materials. In AFM it is commonly the repulsive force between the tip (located at the end of a cantilever) and sample that is measured, on the basis of the cantilever deflection.

In contact-mode AFM measurements, all the electrons of the surface atoms are involved in the repulsive interactions with the tip, so that the AFM image is described by the total electron density plot $\rho(r)$ of the surface. The forces range in strength from $10^{-9} - 10^{-7}$ N.

2.3.2 System set-up

The AFM system consists of the optical block (**Fig. 2-4**) and the base. The stepper motor, the alignment screws, and the sample scanner are installed in the base, and the sample is mounted on the top of the scanner. The optical block contains a viewing window at the top, a diode laser, mirrors, and a four-quadrant positional photodetector. The cantilever holder is fixed on top of the alignment screws, with the tip positioned over the sample. The optical camera attached to the viewing-window allows one to observe the cantilever for alignment of the laser beam and for positioning the tip over the sample area of interest. A laser beam is directed towards the cantilever. The atomic force microscope is mounted on a air cushioned granite table which stabilises the microscope to a high level of accuracy. The granite

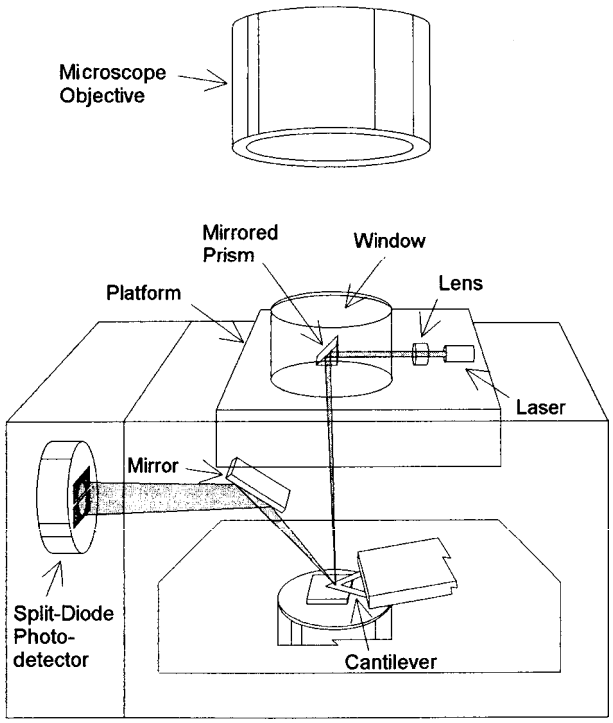

Figure 2-4: *Optical block system of the Atomic Force Microscope. The function of each component is described in the text.*

table was supported by rubber pads with a low ($\sim$ 1 Hz) natural frequency. The AFM is also shielded against acoustic noise by covering the system with a metal cylinder. The *Topometrix TMX2000 Explorer* atomic force microscope at the Institute of Polymer Science at the University of Stellenbosch was used operating in the contact mode. A Si_3N_4 V-shaped cantilever with an integrated Si_3N_4 (tip radius 30 nm) tip was used. Hooke's law, $F = -kx$, relates the cantilever's displacement to the force applied to the probe. Forces less than 10^{-10} N are detectable in ideal conditions, but 10^{-8} N was typically achieved in this study. The force constant of the stiff cantilever used was $k = 0.27$ N/m. It was found that stiff cantilevers produce better results on hard surfaces than less stiff ones. The surface analysis was conducted using the image processing software *SPMLab version 3.06*[79]. The probe is microfabricated from Si_3N_4 or silicon and the tip is sharpened to a tip radius of $10 - 50$ nm. For the investigation of flat surfaces, pyramid shaped probes with low aspect ratios are usually employed.

For the analysis of thin film superconductors, which present a hard, relatively flat, electrostatically neutral surface, a silicon nitride, pyramidal probe was used. We assume, with $YBa_2Cu_3O_7$ films, that the hardness of the sample is everywhere the same, thus there is no need to correct the image for indentation

effects. Contact mode AFM was used, where the probe tip scans the surface, coming into direct contact with the sample. As the probe scans, various topographic features deflect the cantilever. Tip-sample adhesion, which leads to hysteresis in the force-distance curve, is a direct consequence of the surface forces. In ambient-condition experiments, this hysteresis is enhanced by the capillary forces associated with the contamination layer. Since we operated the AFM at a constant force, this did not influence our measurements.

When the tip comes close to the sample, the cantilever is deflected from it's equilibrium position in response to the force experienced by the tip. It bends towards the sample when the force is attractive. This due to van der Waals (VDW) forces, eg. a Lennard-Jones-type potential. When the sample is moved further towards the tip, the attractive force gradient exceeds the spring constant of the cantilever, and the tip jumps to the surface. The typical forces between the tip and the sample surface in the contact-mode is $10^{-9} - 10^{-8}$ N. When operating the AFM in open air, the capillary action of the ever present thin film of moisture on the sample surface must also be taken in to account.

Scanner

In the AFM system, the driving motion is performed by piezoceramic actuators, which change their dimensions under applied voltage. A hollow piezoelectric tube was used, which can move the sample in all three mutually perpendicular directions. The application of different voltages to each pair of electrodes on the tube's outer surface induces a tube bending, which provide lateral motion to the sample attached to the tube. Application of different voltages to the outer and inner electrodes shrinks or extends the tube, which moves the sample vertically. Nonlinearity of the response of the tube is corrected by the computer software.

Tip-sample approach

The tip was brought close to the sample by stepper motor control, while the final adjustment of the tip-sample separation, to the value at which the probe interaction reaches the set-point level determined by the user, is performed by the piezoelectric scanner. The tip-sample alignment is controller by a feedback mechanism. The difference Δ between the actual and set-point values of the probing interaction is used for feedback control. The electronic feedback system generates the response to the scanner, to adjust the vertical position to eliminate the difference Δ.

Two scanning methods usually applied. In the *constant-height* method, in which the feedback mechanism is turned off, one detects the changes in the probing interaction at a constant tip-sample separation. In the *constant-interaction* method, in which the feedback mechanism is activated, one detects the variations of the local $z-$height of the tip with respect to the sample surface at a fixed interaction strength.

This is the method employed in this study. In our system, each scan line consists of 512 points, and scanning proceeds with line scanning frequencies in the $1 - 60$ Hz range. A plane-fit adjustment was performed when the sample surface was not exactly perpendicular to the scanner $z-$axis.

Contact mode

In the contact mode, the repulsive force is measured by recording the cantilever deflection, by way of the movement of the reflected laser beam at the photodetector. We used the constant interaction method, in which the cantilever is kept under a constant force through a feedback loop. The constant force implied a constant displacement for the cantilever. The vertical displacement of the cantilever is proportional to the differential signal from the vertical segments of the photodetector $\Delta V = V_{up} - V_{down}$. The reduced differential signal $\Delta V/(V_{up} + V_{down})$ is used in the feedback signal to keep the cantilever force at the required set-point. The operating force is in the range $10^{-9} - 10^{-7}$ N. The topographic data are then obtained from the control variables, for example the voltages applied to the piezocrystals. Resolution in the $z-$direction is limited by the level of vibrations between the probe and the surface. The amount of displacement can then be accurately calculated from the difference in light intensity on the sectors.

Surface descriptors

Various important surface descriptors can be calculated using *SPMLab*:

- Average roughness :
$$R_a = \frac{1}{N} \sum_{i=1}^{N} \left| Z_i - \overline{Z} \right| \tag{2.20}$$
- where N is the total number of points in the image matrix and $\overline{Z}$ is the average height : $\overline{Z} = \frac{1}{N} \sum_{i=1}^{N} Z_i$, Z_i being the height of the i^{th} point above a reference point. The area RMS height is defined as
$$R_{RMS} = \sqrt{\frac{1}{N} \sum_{i=1}^{N} \left(Z_i - \overline{Z} \right)^2} \tag{2.21}$$
- For line analysis, the following parameters are usually employed:

    1. maximum peak to valley height in the profile:

$$R_t = Z_{\max} - Z_{\min}$$

2. maximum height of the profile above the mean line :

$$R_p = Z_{\max} - \overline{Z} \tag{2.22}$$

- More representative of the entire line profile are the mean values of R_p and R_t, defined by :

$$R_{pm} = \frac{1}{Y}\sum_{i=1}^{Y}(R_p)_i \tag{2.23}$$

$$R_{tm} = \frac{1}{Y}\sum_{i=1}^{Y}(R_t)_i. \tag{2.24}$$

In the Topometrix algorithms for line profile measurements of this type, Y is 20, which take into account the 20 highest points in the profile.

2.4 Resistivity measurements

Resistivity measurements of superconductors are the easiest and most direct to establish the presence of the superconducting phase and the vicinity and width of the transition. Naturally, for a resistive transition to take place only one current path in the sample needs to undergo this transition. This makes the resistivity measurement a way of establishing an upper bound for T_c and ΔT, and is not always representative of the quality of the bulk of the sample. Susceptibility measurements were a good complementary test since it depends on the quality of the sample as a whole. This topic is discussed in detail in the next section.

Our resistivity set-up was a four-point probe type configuration with a temperature sensor in contact with the sample. Shown in **Fig. 2-5** is a schematic diagram of the resistivity set-up. Contact pads where made on the sample surface by dripping tiny drops of conductive silver paint on the sample at the four corners and allowing it to dry. The sample was mounted on a synthetic board of 1 mm thick, with contact electrodes which could be pressed or clamped to make contact with the sample's contact pads. The measurement set-up was housed in a copper cylinder of diameter 35 mm and length 80 mm. A *LakeShore* Si-diode was placed below the sample, and it was glued to the back of the board with thermal conducting *Apiezon Type-N* grease. The Si-diode was connected to a *LakeShore DRC-91CA* temperature controller, which was used to monitor the sample temperature. The sample, together with the silicon diode and a resistive heater was housed in a cylindrical copper cell. A laboratory power supply was used to regulate the heater power.

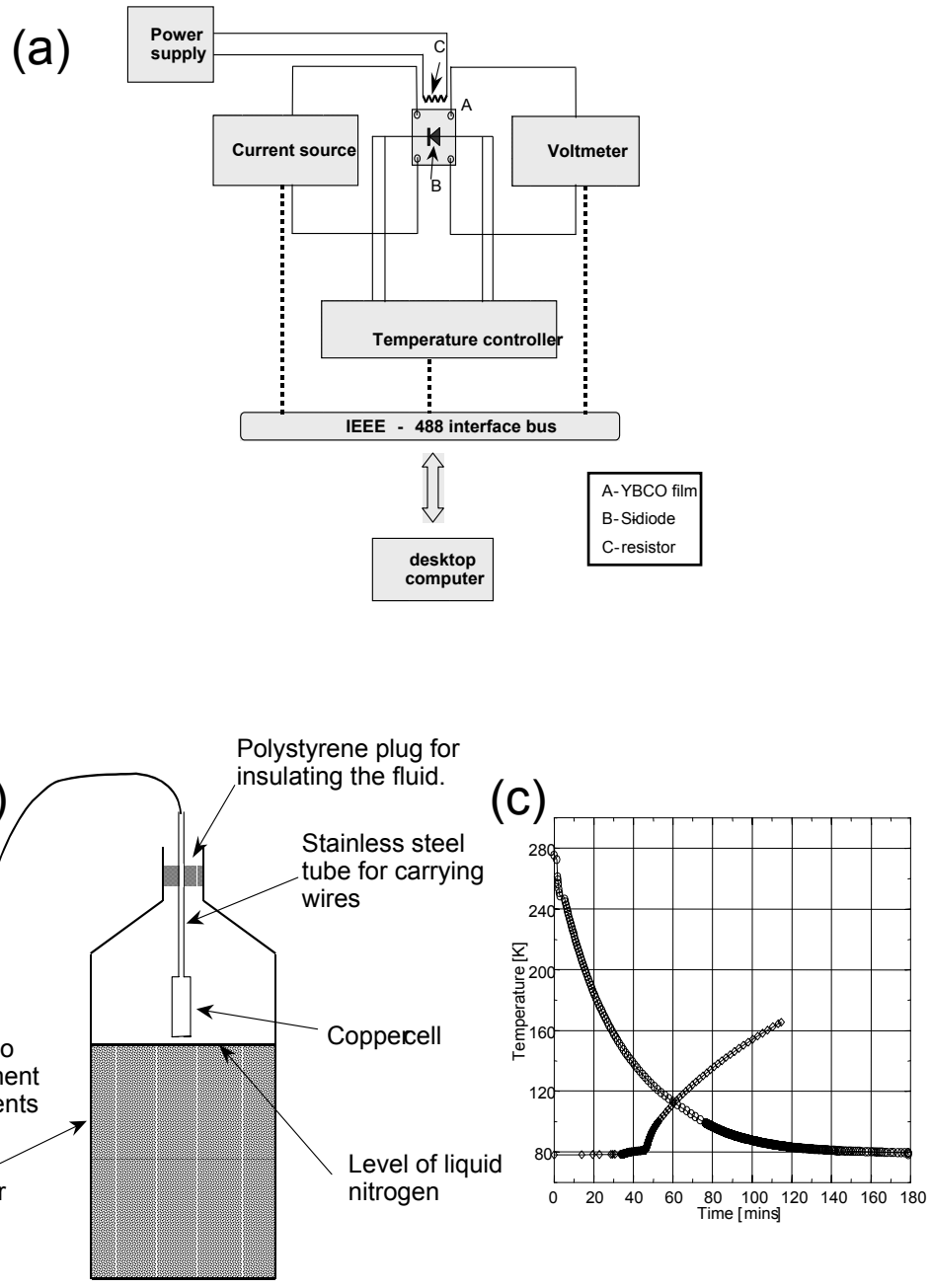

Figure 2-5: *(a) Schematic diagram of the resistivity set-up. The current source provided a constant current of* $\sim$ *1 mA while the voltage and temperature is computer recorded via the IEEE-488. (b) Schematic diagram of the cooling set-up. This film, together with the temperature sensor and resistor was housed inside a copper cylinder. (c) Temperature vs. time graph for cooling and heating characteristics of the resistivity meaturement system.*

A thin wall stainless steel tube was connected to the copper cylinder to house all the electric wires running to the cylinder. The wires ran in a braided copper sleeve which was earthed to the dewar, to shield electromagnetic noise. The pipe also shielded electromagnetic noise. The copper cell had the effect to homogenise the temperature of the nitrogen vapour inside the cell. The cell was cooled by lowering it into a dewar filled with liquid nitrogen. The cell was always kept above the level of the liquid nitrogen, to be cooled slowly to ~ 78 K by the vapour in the dewar.

The fixed current of about $0.1 - 10.0$ mA ± 1 μA was provided by a *Keithley 224* current source, and the voltage was monitored using a *Keithley 128* sensitive voltmeter to an accuracy of ± 10 nV. The current source, voltmeter and temperature controller were connected to a *IEEE-488* communications bus, which was plugged in to a slot in a desktop computer. This arrangement allowed the automated recording of data from the measurement devices; data was stored on a hard disk for later analysis.

Initially, before the resistivity measurement was run, a quick quality check was conducted: Using an ordinary multimeter the resistance of the film was checked. Invariably a low resistance (< 10 Ω) sample was found to be superconducting, while a high resistance sample (> 1 kΩ) was found to be non-superconducting. **Fig. 2-6** shows resistivity versus temperature graphs for a YBCO thin film deposited on MgO. The sample was deposited at 780°C, and the ambient oxygen partial pressure was 0.2 mbar. The difference in temperature between the point where the resistivity has dropped 50% and where the regression line on the transition part cuts the temperature axis is regarded as the halfwidth of the transition (see **Fig. 2-6(b)**). Two times the halfwidth yields the transition width $\Delta T = 2$ K. The critical temperature is $T_c = 86.5$ K.

2.5 Susceptibility measurements

2.5.1 Introduction

It is highly desirable to use non-contact methods to probe the superconductivity of thin film HTS materials, since contact methods usually renders the film useless for further processing to manufacture devices or to investigate the surface. A susceptibility measurement is thought to yield a better view of the superconductivity of a film than the resistivity measurements. Susceptibility is defined as the (complex) ratio $\chi = \chi' + \mathrm{i}\,\chi''$ between the induced magnetisation and the applied magnetic field; $\mathbf{M} = \chi\mathbf{B}$. For a superconducting transition to be observed, using a resistivity measurement, only one conducting path needs to undergo a superconducting transition to render the resistance zero. However, for a transition in the susceptibility, where current flows in circular paths inside the material, the bulk of the film must undergo a transition for the susceptibility to show a sharp change. The susceptibility method thus yields information about the homogeneity of the sample. One would expect sharp transitions to correspond

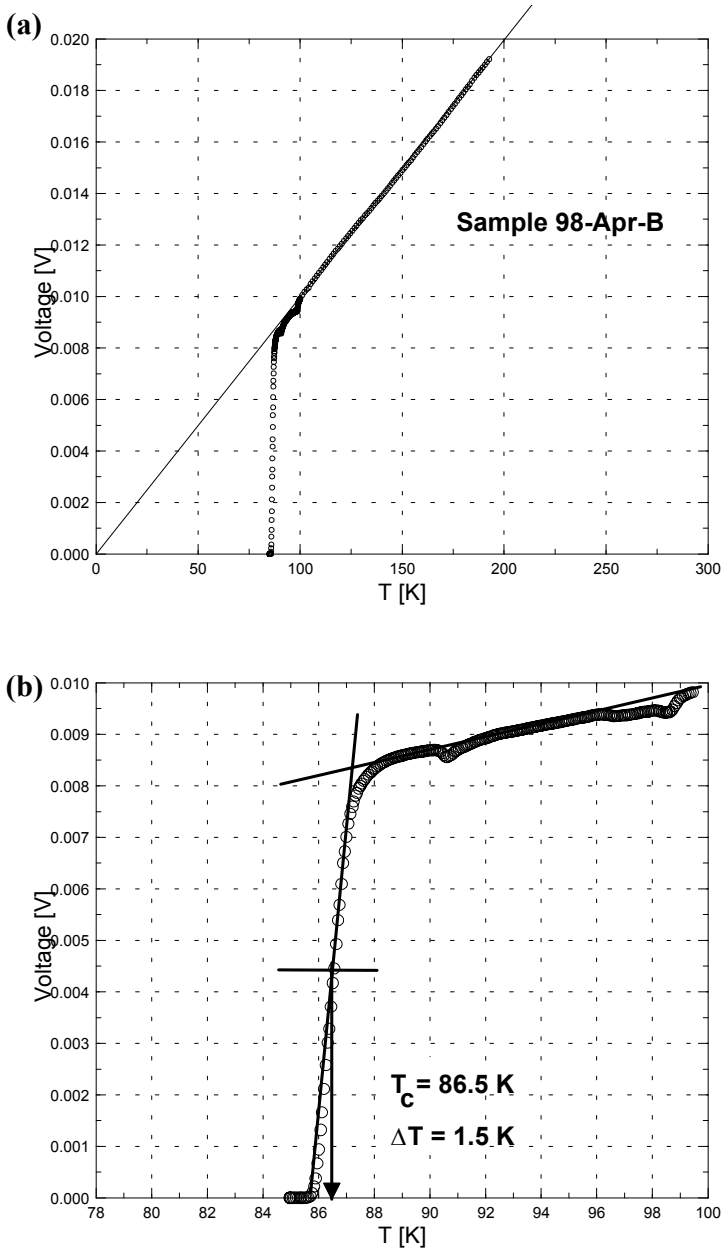

Figure 2-6: *Resistivity versus temperature graphs for YBCO film deposited on MgO. The difference in temperature between the point where the resistivity has dropped 50% and where the regression line on the transition part cuts the temperature axis is regarded as the halfwidth of the transition (see (b)). This method yields* $\Delta T = 2$ *K. The critical temperature is* T_c= 86.5 *K.*

to single-phase homogeneous samples, while broad or multiple transitions would suggest inhomogeneous or even multi-phase material. Mutual inductance and resonant frequency circuits are commonly used to record magnetic transitions, see [80] and references therein.. Inductance type experiments are in fact a very sensitive probe for various properties of superconductors. Early on S. Hatta *et al*[81] explored the use of inductive measurements to probe the Meissner effect in HTS thin films. They placed a coil-wound inductance very close to a HTS film, facing it directly. The onset of superconductivity was precisely determined, and the broad transition observed was an indication of the quality of the film of the material. A decrease of inductance was observed due to the transition to a superconducting (Meissner) state.

2.5.2 Experimental set-up

The susceptibility characterisation was performed using a two coil configuration, **Fig. 2-7**[82, 83, 84, 85].

A primary or drive coil was placed co-axially above the superconducting film, along it's normal axis, situated in the center of the square film (usually 10×10 mm in size). The sample was placed with the superconducting film facing the coils. The secondary or pick-up coil was placed co-axially inside the primary coil in the transformerlike configuration. However, one half of the pick-up coil's wires was wound clockwise, while the other half was wound anti-clockwise in a gradiometer configuration. When the pick-up coil was carefully aligned inside the primary coil such that their centres coincide, the induced currents in the pick-up coil would cancel each other completely in the absence of a film when a harmonic voltage was applied over the primary coil. When a superconductor is placed in close proximity of the coil configuration, as described above, currents are induced on the film's surface, which in turn would generate an oscillating magnetic field. This field is picked up by the pick-up coil, but due to asymmetry on the configuration, the lower half of the pick-up coil picks up more field than the upper half. The pick-up coil would also sense the field from the drive coil, but the resultant induced current from the drive coil would be zero. Only the contribution from the film is finally measured at the ends of the pick-up coil as a voltage $V(t)$, yielding a clear signal of the superconducting transition.

Fig. 2-7(a) shows the geometric set-up of the susceptibility apparatus. The drive coil (outer) has 30 turns, with the spacing between each turn $\delta h_D = 0.15$ mm, radius $r_D = 1.85$ mm. The pick-up coil was wound around a 1.0 mm diameter wooden core, it has 15 turns in each section, the inter-turn spacing is $\delta h_P = 0.19$ mm, the radius is $r_P = 1.0$ mm, and the gap is $g_R = 2.9$ mm. The drive coil is $h_D = 10$ mm removed from the film, and the pick-up coil is $h_P = 8.0$ mm removed from the film. The wire diameter was 0.1 mm. The sample is placed on a perspex sample holder with the film facing the coils, and a silicon diode temperature sensor is glued on to the back of the sample using thermally conductive grease. The coils are housed in a non-magnetic tufnol structure, which allows for precise movement of the pick-up coil versus the drive coil, and also the distance between the film and the drive coil. Thus h_P and h_D can

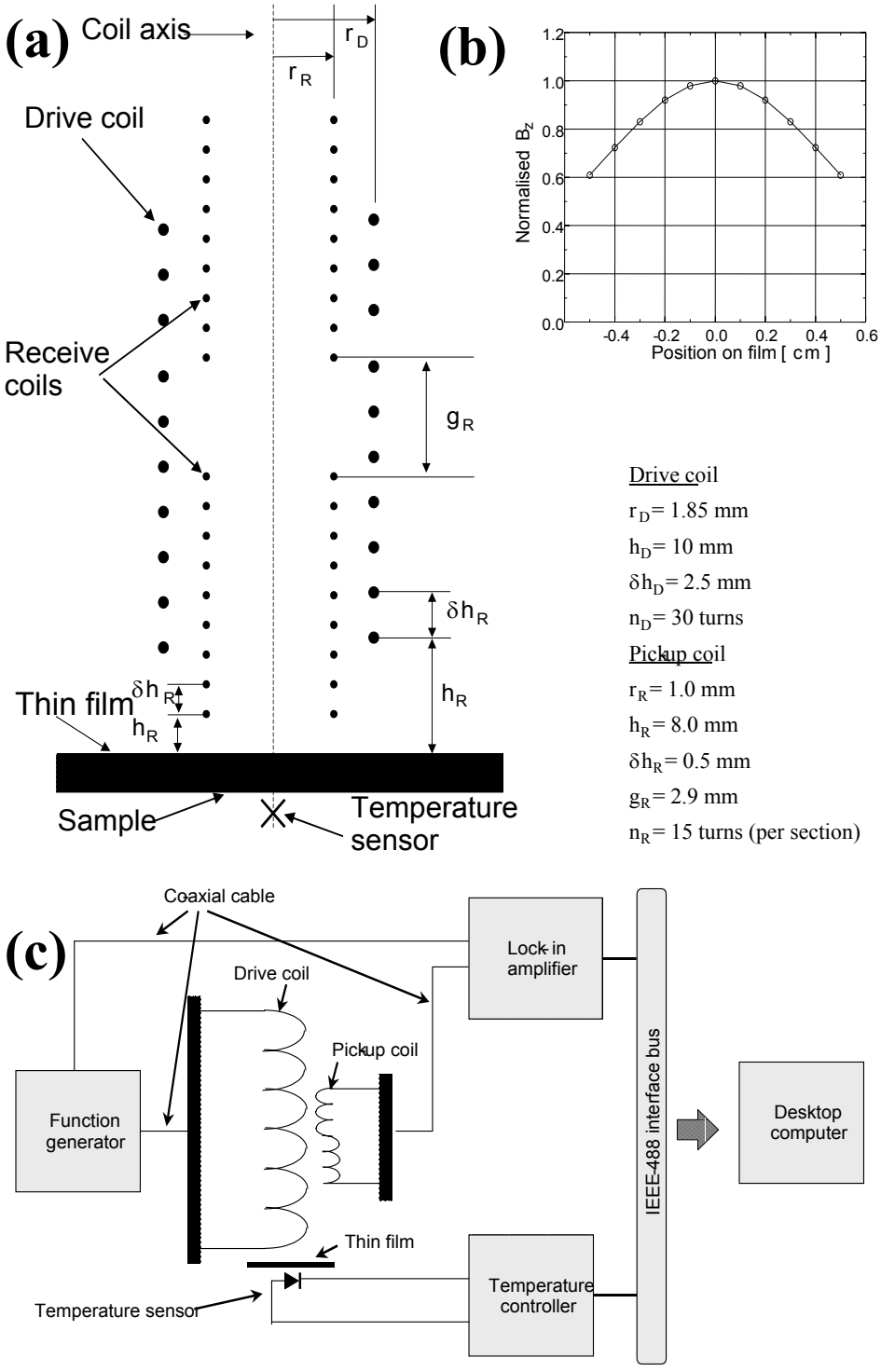

Figure 2-7: *(a) Geometry of the drive/pick-up coil system. (b) Relative B_z distribution at the film surface. (c) Schematic diagram of the measurement set-up. The pick-up coil is placed out side the drive coil for clarity. Inside the experimental cell, the coils' leads were connected to co-axial cables.*

be independently adjusted. We introduce a cylindrical coordinate system on the coil set-up, the $z-$axis is the coil axis, positive direction away from the film toward the coils. The origin is where the coil axis cuts the film surface.

Fig. 2-7(b) shows the normalised magnetic field component B_z on the film surface. The B_z field component of a current ring located in the $z = 0$ plane with radius ρ is (see e.g. J.D. Jackson[68], pp 177-8)

$$b_z(r, z, \rho) = \frac{2}{c} \frac{I}{\sqrt{(\rho + r)^2 + z^2}} \left[K(k) + \frac{\rho^2 - r^2 - z^2}{(\rho - r)^2 + z^2} E(k) \right] \tag{2.25}$$

with

$$k^2 = \frac{4\rho r}{(\rho + r)^2 + z^2}. \tag{2.26}$$

Thus, the $z-$component of the magnetic field is

$$B_z(r) = \sum_{i=1}^{n_D} b_z(r, h_D + i \times \delta h_D, \rho). \tag{2.27}$$

We developed a dynamic linked library (*dll*) in the *C* programming language to be linked into the Excel spreadsheet for rapid calculation of the elliptic functions $E(k)$ and $K(k)$. This enabled us to model the drive coil in Excel and to calculate the field at various points along the film surface, as shown in **Fig. 2-7(b)**. Clearly, the magnetic field at the periphery of the film $r = 0.5$ cm is $\sim 60\%$ of the field in the centre. Thus, it is an approximation to model the magnetic field as spatially uniform perpendicular field $\mathbf{B} = B_0 \cos \omega t \, \hat{\mathbf{z}}$ through-out the rest of the analysis.

The structural arrangement for the experimental set-up was very similar to that of the resistivity system, see **Fig. 2-5(b).** The tufnol structure was housed inside a closed copper cylindrical cell of diameter 60 mm and height 105 mm. The cell was lowered into a liquid nitrogen dewar until the bottom of the cylinder touched the liquid nitrogen. This allowed the sample to cool slowly down from room temperature to 77 K in the presence of the exchange gas (nitrogen). The final cooling from $120 - 77$ K proceeded quite slowly at a rate of about 1 K per minute. A stainless steel tube was used to carry all connecting co-axial cables and twisted pair wires to the experimental cell.

The film was cooled to low temperatures, and the temperature was continuously monitored. Data from the lock-in amplifier and the temperature controller were recorded by a desktop computer via a *IEEE-488* interface. Software was written in the *Pascal* programming language to control the settings of the waveform generator and the lock-in, and to record the in-phase X and quadrature amplitudes Y versus T.

All wires running to the silicon diode were twisted in matching pairs and placed inside a grounded braided shield. The signals to and from the coils were carried in co-axial cables housed in the stainless

steel tube. **Fig. 2-7(c)** is a diagrammatic representation of the measurement devices connected to the two-coil set-up. Magnetic field is excited by the drive coil, which is driven by a *Hewlett-Packard 33120A* function generator operating at 100 kHz with a sine wave waveform, 10 V peak to peak. The pick-up coil's signal is compared to the drive signal by a *EG&G* lock-in amplifier capable of performing measurements up to 100 kHz. The drive coil and the lock-in amplifier was both connected to the function generator in a parallel configuration, and this enabled the lock-in to determine the amplitude of the in-phase X and quadrature (90° signal) Y components of the output voltage signal relative to the input signal.

Fig. 2-8 shows the result of a balancing test to determine the position of the pick-up coil where the contribution of the drive coil is cancelled exactly. The distance axis is arbitrary. The voltage measurement records a dramatic fall in voltage towards the position at 3 mm. From it's maximum (at 6 mm), the drop in voltage was 600 fold.

2.5.3 Model

The susceptibility measurement can be understood *qualitatively* in terms of the critical state model for disk-shaped superconductors in harmonic $B-$fields from J. Zhu *et al*[67] as introduced in Chapter 1, Section 1.7.3. The current in the drive coil i_0 (e.m.f. $\mathcal{E}_0 = -L\frac{di_0}{dt}$) give rise to a magnetic field $\mathbf{B}(t)$ at the film surface through Faraday's law. The field component B_z is important, since it determines the current distribution in the film, giving rise to a hysteretic relationship between the magnetic moment m and the applied field.

For the purpose of our analysis, we imagine a Cartesian co-ordinate system with origin at the intersection of the coil axis and the film surface, and the coil axis being the $z-$axis, the positive sense in the direction of the coils as viewed from the film. We assume a uniform $z-$directed field $\mathbf{B}(t) = B_0 \cos\omega t\ \hat{\mathbf{z}}$, in phase with i_0.

Similarly, the pick-up coil senses the magnetic field originated by m of the film, related by $B_{1z} = 2m/z^3$. Because the field decreases so rapidly, the field at the higher part of the pick-up coil is negligible. The magnetic moment induces an e.m.f. $\mathcal{E}_1$ in the pick-up coil through $\mathcal{E}_1 = -\frac{1}{c}\frac{\partial\Phi_1}{\partial t}$, Φ_1 being the flux from the film threading the pick-up coil.

The quantities that are measured are the drive voltage V_0 from the function generator and the pick-up voltage V_1 at the lock-in amplifier. If we assume that there are no phase shifts in the co-axial cables at experimental frequencies $f \lesssim 100$ kHz, we can assume $V_0 = \mathcal{E}_0$ and $V_1 = \mathcal{E}_1$. We see that voltages V_0 and V_1 lag 90° in phase behind their respective magnetic fields. The phase difference between V_0 and V_1 is determined by the phase difference between B_z and m, which in turn is determined by the shape of the hysteresis loop.

If we define dimensionless field β and magnetic moment μ as follows:

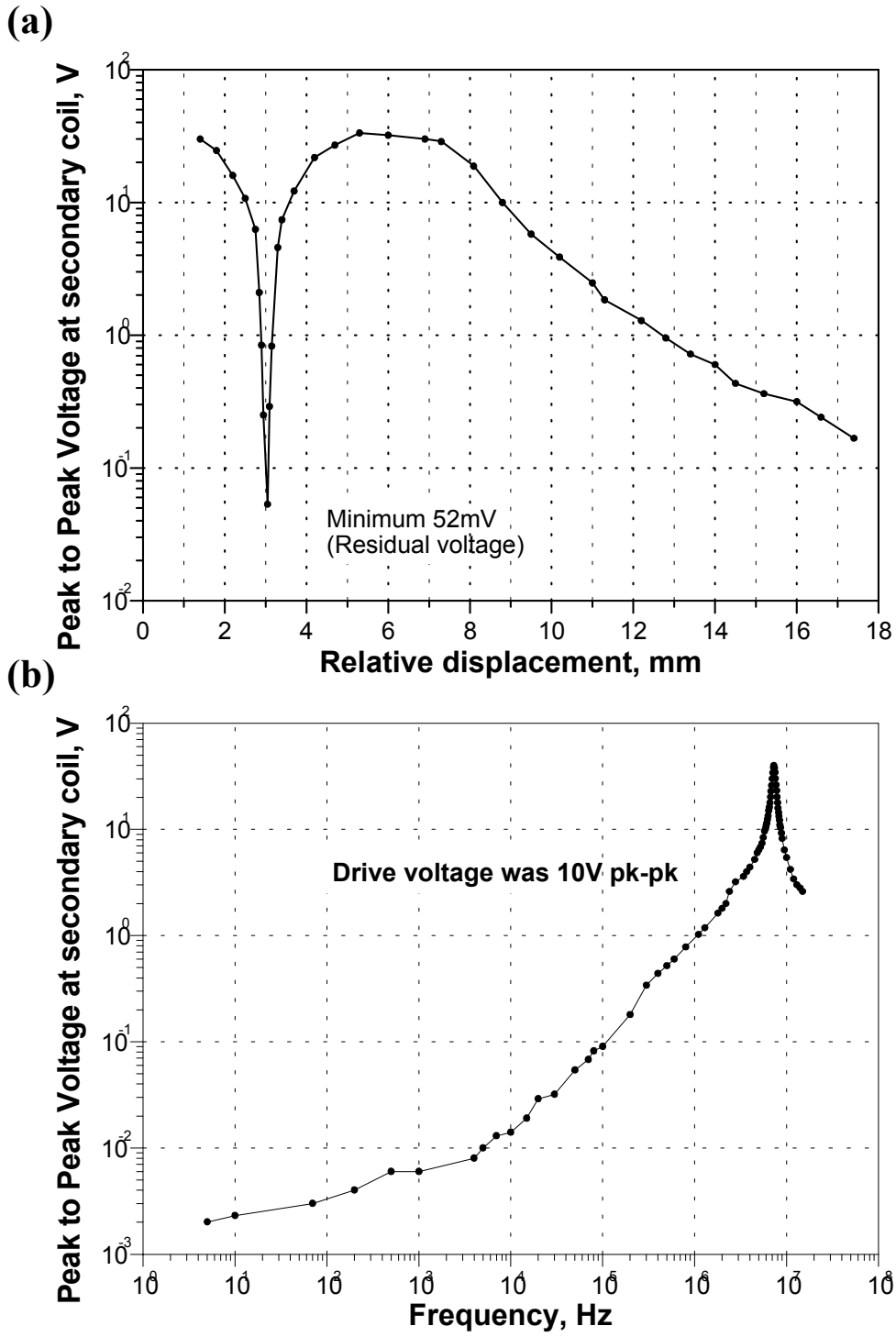

Figure 2-8: *The results of a balancing test to determine the position of the pick-up coil where the contribution of the drive coil is cancelled exactly. (a) Peak-to-peak voltage* $2(X^2 + Y^2)^{1/2}$ *vs. displacement of the pick-up coil. The distance axis is arbitrary. The voltage measurement records a dramatic fall in voltage towards the position at 3 mm. From it's maximum (at 6 mm), the drop in voltage was 600 fold. (b) Frequency resonance of the coil system in the minimum position indicated in (a).*

$$\beta_0 = \frac{B_0}{B_c} \tag{2.28a}$$

$$B_c = \frac{2\pi}{c} j_c d \tag{2.28b}$$

$$\beta(t) = \frac{B_0}{B_c} \cos\omega t = \beta_0 \cos\omega t \tag{2.28c}$$

$$m_0 = \frac{2}{3\pi} R^3 B_c \tag{2.28d}$$

$$\mu(\beta) = \frac{m}{m_0} \tag{2.28e}$$

We now cast magnetic moment of the superconducting thin film (from eq. 1.55) in dimensionless form:

$$\mu(\beta_0, t) = \mp\beta_0 S(\beta_0) \pm (\beta_0 \mp \beta) S(\beta_0/2 \mp \beta/2) \tag{2.29a}$$

$$S(x) = \frac{1}{2x}\left(\arccos\frac{1}{\cosh x} + \frac{\sinh|x|}{\cosh^2 x}\right) \tag{2.29b}$$

where the upper and lower branches of the hysteresis loop are indicated. **Fig. 2-9** shows the result of calculation of the reduced magnetic moment $\mu(\beta_0, t)$ for the phase angles $0 - 720°$ (two cycles) for different values of applied magnetic field amplitude $\beta_0 = 0.1,\ 1.0,\ 3.0,\ 5.0,\ 10.0$. The saturation level $\mu(\beta_0, t)$ of is

$$\mu_{sat} = \pi/4 \simeq 0.785.$$

Fig. 2-9(a) is the applied magnetic field $\beta(t)$ of arbitrary amplitude, and **Fig. 2-9(b)-(f)** shows the resulting hysteresis loop and output magnetic moment μ.

We now determine the first two Fourier components of the magnetic moment (ignoring the constant term which is zero). The general form of the Fourier expansion for μ is

$$\mu(\beta_0, t) = \sum_{n=0}^{\infty} (a_n \sin n\omega t + b_n \cos n\omega t) \tag{2.30}$$

where a_1 is the $90°-$phase (quadrature) component and b_1 is the in-phase component:

$$a_1(\beta_0) = \frac{2}{\tau}\int_0^\tau \mu(\beta_0, t)\sin\omega t dt \tag{2.31a}$$

$$b_1(\beta_0) = \frac{2}{\tau}\int_0^\tau \mu(\beta_0, t)\cos\omega t dt, \tag{2.31b}$$

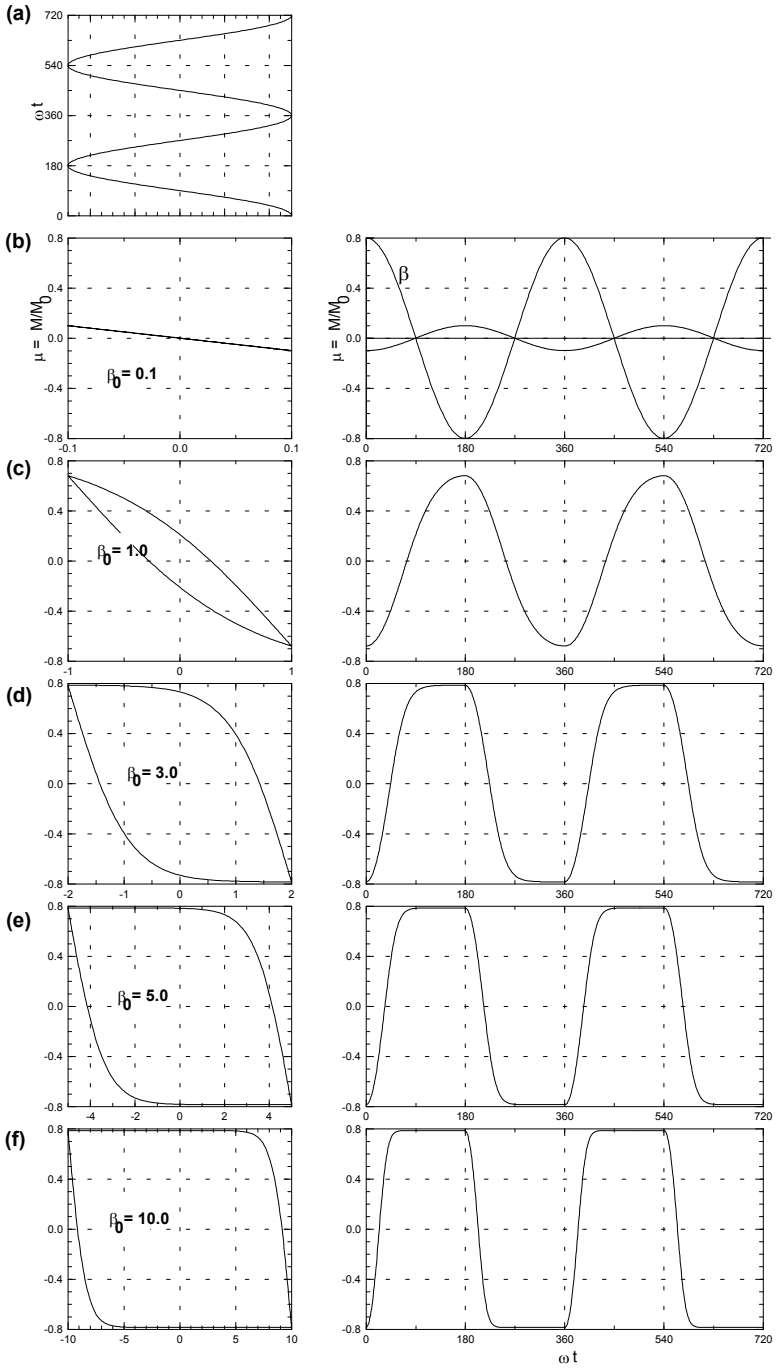

Figure 2-9: *The resulting magnetic moment* $\mu(t) = m/m_0$ *for various levels of uniform applied magnetic field* $\beta(t) = \beta_0 \cos \omega t$. *(a) Applied magnetic field of arbitrary amplitude. (b) Reduced magnetic field* $\beta_0 = 0.1$ *(c)* $\beta_0 = 1.0$ *(d)* $\beta_0 = 3.0$ *(e)* $\beta_0 = 5.0$ *(f)* $\beta_0 = 10.0$.

$\tau = 2\pi/\omega$ being the period.

We determine the component functions a_1 and b_1 for values in the range $0 \leq \beta_0 \leq 100$ by numeric integration; the results are shown in **Fig. 2-10.** The size of the in-phase component b_1 grows initially faster than a_1, because the hysteresis loop is elongated for low values of $\beta_0 \lesssim 1$. b_1 has a turning point at $\beta_0 \simeq 1.6$, and then slope upward to approach zero slowly from below. a_1 always has a positive slope, climbing very steeply to $a_1 = 0.8$ at $\beta_0 \simeq 5.5$, and then slowly approaching unity from below. When $\beta_0 = 3$, we have $a_1 = 0.65$ and $b_1 = -0.67$, thus $a_1 \simeq b_1$. In **Fig. 2-9(d)**, the upper turning point of the graph $\mu(\omega t)$, occurs approximately at $3\pi/4 + 2\pi n$, $n = 0, 1, 2...$ This can be expected since with almost equal components a_1 and b_1, one would expect $\mu(\omega t)$ to have upper turning points between that of $-\cos\omega t$ (π) and $\sin\omega t$ $(\pi/2)$.

Asymptotic values of a_1 and b_1 can easily be calculated from eq. 2.31 if we keep in mind that $\mu(\beta_0 \to \infty) = \pm\frac{\pi}{4}$, the sign depending on the branch of the hysteresis loop in question. Thus

$$a_1(\beta_0 \quad \to \quad \infty) = 1 \tag{2.32a}$$

$$b_1(\beta_0 \quad \to \quad \infty) = 0. \tag{2.32b}$$

We continue our analysis by determining the influence of a temperature dependent critical current $j_c(T)$ on the situation. The magnetic moment is expressed in terms of the two components a_1 and b_1:

$$m(t) \quad = \quad m_0 \left(b_1 \cos\omega t + a_1 \sin\omega t\right) \tag{2.33a}$$

$$= \quad \frac{2}{3\pi} R^3 B_c \left[b_1 \left(\frac{B_0}{B_c}\right) \cos\omega t + a_1 \left(\frac{B_0}{B_c}\right) \sin\omega t \right] \tag{2.33b}$$

where the temperature dependence is through j_c in B_c. In chapter 5 we show that close to T_c the critical current has a temperature dependence of the form

$$j_c(T) = j_{c0} \left(1 - \frac{T}{T_c}\right)^p \tag{2.34}$$

thus

$$B_c(T) = B_{c0} \left(1 - \frac{T}{T_c}\right)^p . \tag{2.35}$$

In the range $|1 - \theta| \leq 0.016$ we have $p = 2.0$, where $\theta = T/T_c$. We assume a similar relation to extend throughout : $0 \leq \theta \leq 1$. We calculate the reduced components defined as

$$a'(\theta) \quad = \quad \frac{B_c(\theta)}{B_0} a_1 \left(\frac{B_0}{B_c(\theta)}\right) \tag{2.36a}$$

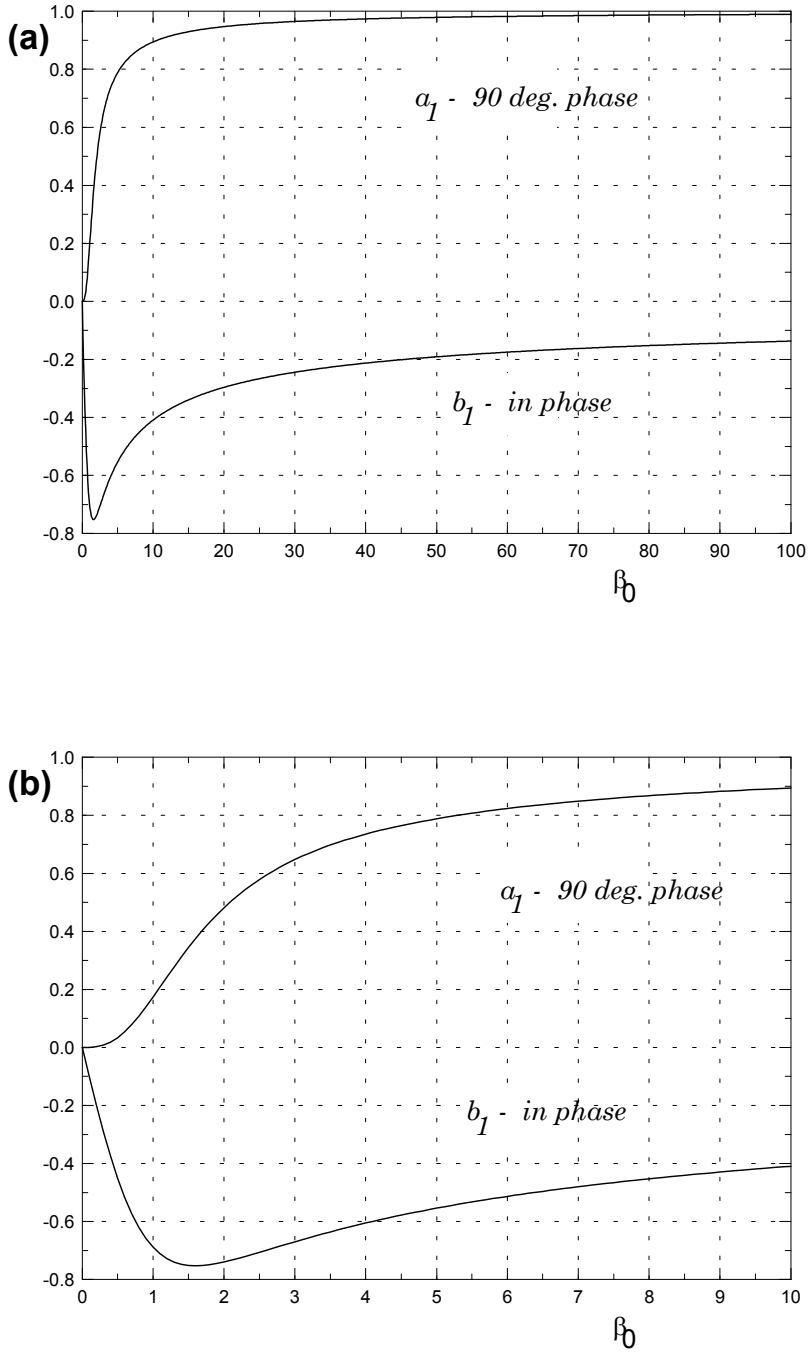

Figure 2-10: $90°-$*phase* a_1 *and in-phase* b_1 *Fourier components of the dimensionless magnetic moment* $\mu(\beta_0, t)$. *(a) The components in the range* $0 \leq \beta_0 \leq 100$. *(b) Close-up of the range* $0 \leq \beta_0 \leq 10$.

$$b'(\theta) \quad = \quad \frac{B_c(\theta)}{B_0} b_1 \left(\frac{B_0}{B_c(\theta)} \right). \tag{2.36b}$$

In the normal state $\theta > 1$, we have $j_c = 0$, thus $a'(\theta) = b'(\theta) = 0$. We assumed a unit radius and we dropped the prefactor $\frac{2}{3\pi}$ for the sake of algebraic simplicity in eq. 2.36. **Fig. 2-11** shows the result of the calculation of $a'(\theta)$ and $b'(\theta)$ for the temperature range $0 \leq \theta \leq 1$ for the exponents $p = 1.5$, 2.0, 2.5, 4.0, 6.0, 10.0 and values of $\beta^* = B_0/B_{c0} = 1$, 0.1, 0.01, 0.001.

We observe that the product of the critical current and the components a_1 and b_1 result in an in-phase component b' which in initially at zero at T_c and drops to -1 and a $90°-$phase component a' which starts and ends at 0 with an excursion to positive values ($a'_{\max} \simeq 0.241$). The position of the inflexion point in b' and the turning point in a' are approximately at the same value of θ.

Magnetic pick-up

A magnetic moment m produces a magnetic field, the $z-$component of which is

$$B_z = \frac{m}{r^3} \left(3\cos^2\theta - 1 \right), \tag{2.37}$$

where θ is the angle measured from the positive $z-$axis. Given the geometric parameters of the pick-up coil, we have at the edge of the coil ring closest to the film the following: $\theta_1 = \arctan(r_P/h_P) = 7.1°$ and $r_1 = (r_P^2 + h_P^2)^{1/2} = 0.81$ cm. Thus, at the edge of the first ring $B_z = 3.677 \cdot m$. In the centre of the first ring, $B_z = 3.906 \cdot m$, thus a 6% variation. Thus we can safely assume that B_z is constant within the surfaces bounded by the rings of the pick-up coil, as a good approximation. Thus, the total flux threading the pick-up coil is

$$\Phi_1 \quad = \quad 2M \cdot \pi r_P \cdot \sum_{i=0}^{n_P - 1} \left[(h_P + i\delta h_P)^{-3} - \left(h_P + g_P + (n-1+i)\delta h_P^{-3} \right) \right] \tag{2.38}$$

$$= \quad 2M \cdot \pi r_P \cdot (19.358 - 4.628) \tag{2.39}$$

$$= \quad \underbrace{0.926}_{\alpha} \cdot m \ [\mathrm{G} \cdot \mathrm{cm}^2] \tag{2.40}$$

We now analyse the voltage $V_1 = -\frac{1}{c}\frac{d}{dt}\Phi_1$ sensed by the lock-in amplifier. Using eqs. 2.33 and 2.36, we have

$$m(t) \quad = \quad \underbrace{\frac{2}{3\pi} R^3 B_0}_{m'} \left(b' \cos\omega t + a' \sin\omega t \right) \tag{2.41a}$$

$$= \quad m' \cdot \rho e^{i\omega t + \gamma} \tag{2.41b}$$

$$\rho \quad = \quad \sqrt{a'^2 + b'^2} \tag{2.41c}$$

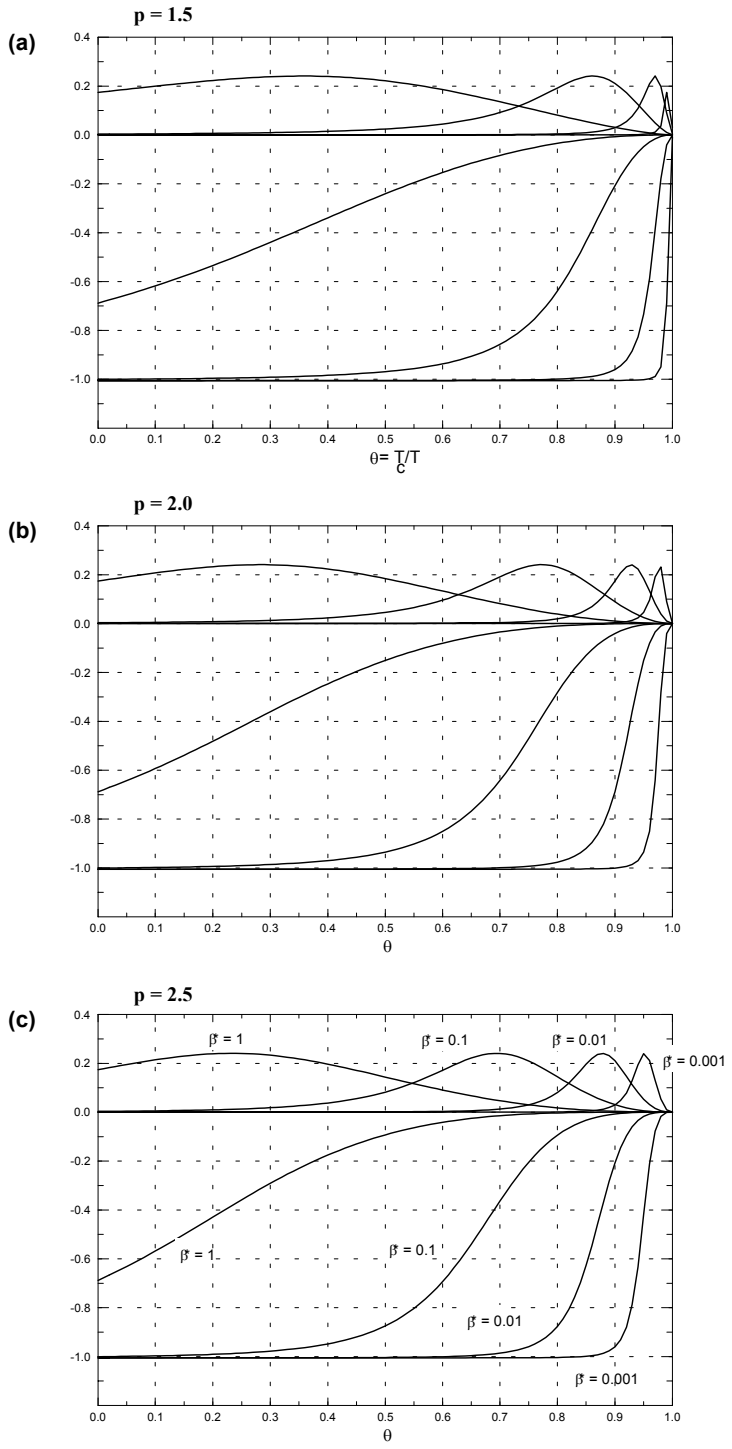

Figure 2-11: $90°-$*phase* $a'(\theta)$ *and in-phase* $b'(\theta)$ *for the temperature range* $0 \leq \theta \leq 1$ *and values of* $\beta^* = B_0/B_{c0} = 1,\ 0.1,\ 0.01,\ 0.001$ *for the exponents (a)* $p = 1.5$, *(b)* $p = 2.0$, *(c)*$p = 2.5$. *Note that* $a'(\theta) \geqslant 0$ *and* $b'(\theta) \leqslant 0$.

$$\gamma = \arctan \frac{a'}{b'} \tag{2.41d}$$

Thus

$$V_1 = -\frac{1}{c}\frac{d}{dt}\left(\alpha M' \cdot \rho \exp\left[i\left(\omega t + \gamma\right)\right]\right) \tag{2.42a}$$

$$= \frac{\omega}{c}\alpha M' \cdot \rho \exp\left[i\left(\omega t + \gamma - \frac{\pi}{2}\right)\right] \tag{2.42b}$$

and

$$X(t) = \frac{\omega}{c}\alpha M' \cdot \rho \cos\left(\omega t + \gamma - \frac{\pi}{2}\right) \tag{2.43a}$$

$$Y(t) = \frac{\omega}{c}\alpha M' \cdot \rho \sin\left(\omega t + \gamma - \frac{\pi}{2}\right). \tag{2.43b}$$

Since the voltage lags behind the current (and the associated magnetic field) by 90° in the case of both the drive and the pick-up coil, we are really sensing the phase difference γ between the applied magnetic field and the induces magnetic moment.

2.5.4 Discussion

We are now in a position to analyse the results of susceptibility measurements. Information that can be extracted are the likely dependence of j_c on T in the range T_c down to 77 K, hence the exponent p, and a lower limit for T_c, ie. the onset of superconductivity ($R = 0$ and j_c finite). **Fig. 2-12** shows the results of resistivity and susceptibility measurements performed on two $YBa_2Cu_3O_{7-\delta}$ thin films prepared on MgO substrates using PLD. Both films were epitaxial and $c-$axis orientated, as verified by XRD analysis. **Fig. 2-12(a & d)** show the resistivity (voltage) and susceptibility (in-phase X and quadrature Y components) data, and the same data is repeated in **(b)** and **(e)** respectively in the region close to the superconducting transition. Unfortunately, the resistivity and susceptibility measurements were not performed concurrently, thus the relative positions of the curves along the temperature axis is only reliable to an accuracy of ~ 0.5 K. The transition to zero resistivity (indicated by T_{c2}) and the onset of finite j_c (indicated by T_{c3}) is not necessary a concurrent occurrence in superconductors, as indicated by **Fig. 2-13**. The usual resistive transition temperature determined by the position where the resistance has dropped to half the pre-transition resistance value is indicated by T_{c1}. In practice we have $T_{c3} \leq T_{c2} < T_{c1}$.

Since the sign of the (X, Y) data is defined by the polarity of the function generator, the auto-tuning of the lock-in and it's autophase operation, it is completely acceptable when the data has a sign opposite

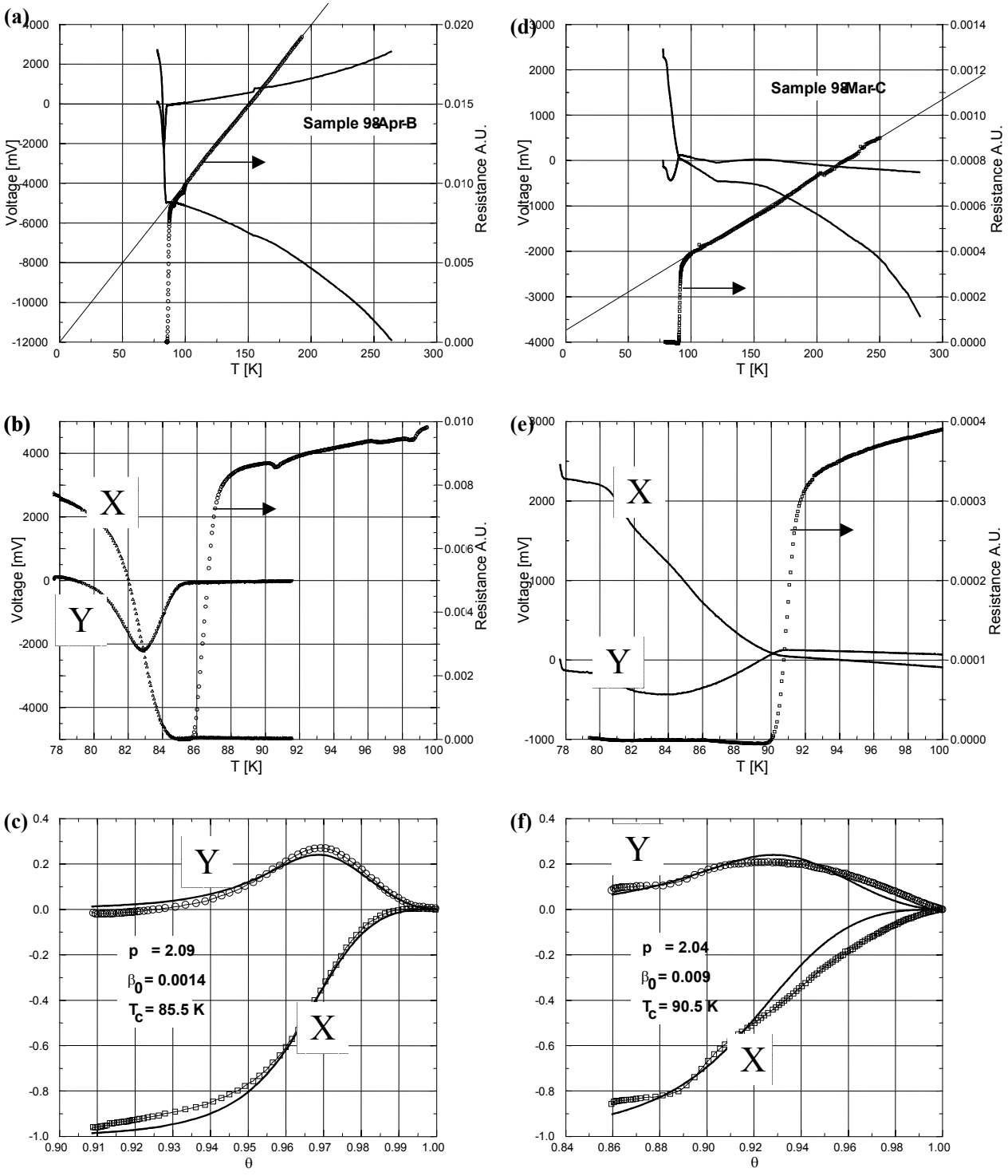

Figure 2-12: *Resistivity and susceptibility measurements performed on two $YBa_2Cu_3O_{7-\delta}$ thin films prepared on MgO substrates using PLD : (a) 98-Apr-B, and (d) 98-Mar-C. (b,e) Close-up of the data near the superconducting transition. (c,f) Fit of in-phase X and quadrature Y components to the data.*

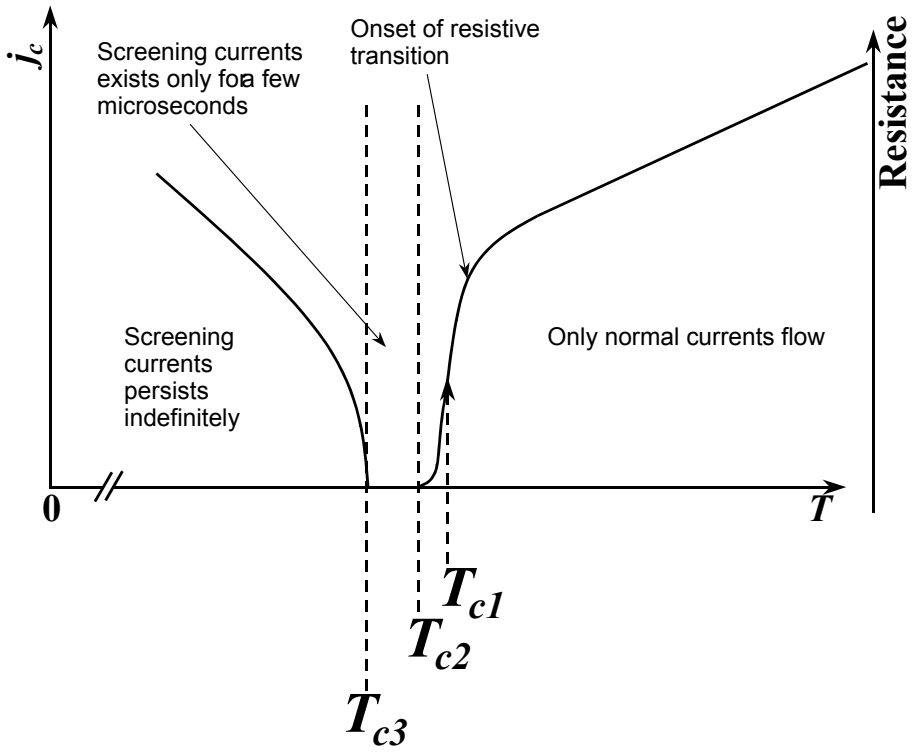

Figure 2-13: *Diagram of the relative positions of various critical temperature values.*

of the theory—it simple reversal of polarity somewhere in the circuitry can flip the sign. Thus, the data was multiplied by -1 to make comparison with the theory easier. The onset of finite j_c was identified. T_{c3} was determined for each case by visual inspection. In practice (and theory), $T_{c2} \simeq T_{c3}$. The exponent p, the amplitude β_0 and the scale factor λ was determined by least squares fitting. The results of the fitting procedure are tabulated below:

	98-Apr-B	**98-Mar-C**
T_c [K]	85.5	90.5
p	2.09	2.04
β_0	0.0014	0.009
λ	7982	2634
RMS	0.000774	0.00144

The fits for the data are good, and confirms that the model is reasonable. Especially, the signs and the relative sizes of the components in the range $0.9 < \theta < 1.0$ are correct, and the exponent p is close to 2, a value confirmed in chapter 5 when the critical state is investigated using a SQUID.

To be able to meaningfully compare results when examining different films where different methods were employed to determine the critical temperature, we used the $T_{c2} = T_c(R = 0)$ value extracted from resistive transitions and assume it corresponds to the onset of superconductivity (finite j_c) T_{c3} as determined by susceptibility measurement.

2.6 Data acquisition and computer control

Control and data acquisition software was developed in *Turbo Pascal (Borland)* using *IEEE-488* communication software units supplied by *Keithley* or *Hewlett-Packard*. Pascal units were written to control each instrument, change settings and take readings of all relevant parameters. Using these units, an experimental program could be rapidly developed and customised for the experiment in mind.

2.7 Summary

Rutherford backscattering spectroscopy (RBS) is a standard technique based on elastic scattering of light monoenergetic accelerated nuclei by nuclei of atoms in the sample under study, typically a thin film. The different mass of target nuclei give rise to an energy spectrum of backscattered particles, which are detected and counted. Analysis of the spectra by the *RUMP* computer package give accurate information regarding film composition, thickness, and possible interaction between film and substrate.

X-ray diffraction (XRD) spectroscopy is a standard technique to probe the crystallinity of samples, thin films in our case. Different geometries to measure Bragg reflection is discussed: the standard Bragg-Brentano ($\theta - 2\theta$) geometry, and the more general 3 degrees of freedom geometry for $\phi-$scans and pole figure plots.

Atomic force microscopy (AFM) is an ideal probe to investigate surface roughness found in certain YBCO thin film samples deposited by PLD. Both particulates arising from the deposition process and non-epitaxial film arising from non-ideal deposition conditions can be studied using AFM.

A cryo-insert containing an electric set-up for *standard four-point probe resistivity measurements* were designed. The method makes use of a constant current flowing between two contacts on the superconducting film and the voltage between the two other contacts is recorded, while the temperature is lowered to below T_c, or raised to room temperature. Liquid nitrogen is used a cooling agent. Critical temperature and the transition width can be extracted from the data.

A cryo-insert containing a two-coil transformer-like set-up for measuring film *susceptibility* was designed. The method operates with oscillating current in the frequency range $1 - 100$ kHz. Initially, the secondary astatically wound coil is positioned co-axially inside the primary coil such that the total

induced e.m.f. is zero due to cancellation in the two parts of the secondary coil. When the film has completed it's superconducting transition, currents induced in the film results in a disbalance in the secondary coil and a induced oscillating e.m.f. is detected using a lock-in amplifier.

A critical state model for thin superconducting films is applied to yield first order Fourier components $\sim \cos\omega t$ and $\sim \sin\omega t$. This used together with a simple model for critical current near T_c, $j_c \propto (1 - T/T_c)^p$, where $p \sim 2$. Good fits are obtained to experimental data, yielding T_c, and confirming the plausibility of the model. The model has the appealing property of being in algebraic closed form and in-phase and 90°-components are easy to calculate.

Chapter 3

Development of a Pulsed Laser Deposition System

3.1 System requirements

The starting point of this investigation was to design and build a pulsed laser deposition (PLD) system at the National Accelerator Centre. PLD involves the interaction of a focussed laser pulse with a multi-elemental solid target material, as shown in **Fig. 3-1(a)**[86, 87, 88]. Material ablated from the target form a fast moving plume consisting of atomic and molecular particles, directed away from the target, and towards a usually heated substrate on which the particles condense layer by layer to form a thin film. The substrate temperature and background gas are carefully controlled to be conducive to the growth of a desired phase of the multi-elemental compound. **Fig. 3-1(b)** show a photograph of the pulsed laser deposition system built as part of this study. The objective of the design was to produce a simple, adaptable system, capable of depositing high temperature superconductors (HTSC) and other materials in single layered or multi-layered thin films on a substrate of dimensions about 10 mm $\times$10 mm. A very high vacuum (i.e. base pressure at 2×10^{-6} mbar or better) system was desired, to deposit the films as pure as possible and to produce clean interfaces between different layers. To develop the design in detail, it was necessary to consider various deposition parameters required for a typical HTSC thin film; $YBa_2Cu_3O_7$ being the prototype superconductor. Recently, optimised parameters for YBCO have been published in the literature[89, 90]. These parameters are summarised in **Table 3.1**.

Using these parameters, YBCO films with critical temperature $T_c = 85 - 90$ K and critical current densities in excess of 10^6 A cm^{-2} at 77 K have been fabricated. The critical current density was estimated by magnetising the sample, as explained in Chapter 5. Deposition rates as high as $0.01 - 0.10$ nm per

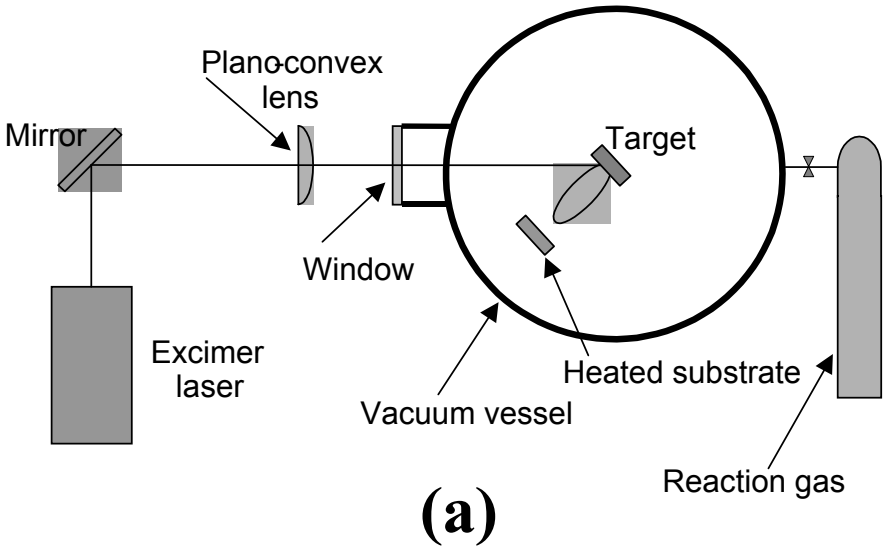

(a)

(b)

Figure 3-1: *(a) Planar view of the deposition principle and optical path of the PLD system. Notice that the incoming laser path makes a 45° angle with the normal of the target surface. (b) Full view of the pulsed laser deposition system with laser in the background (object on the right).*

Table 3.1: *Optimum range of conditions for the HTSC material YBCO.*

Laser energy density	2.5 - 3.5 J/cm^2
Laser wavelength	200 - 400 nm
Substrate temperature	680 - 780°C
Substrate-target distance	45 - 70 mm
Oxygen pressure	0.2 - 0.3 mbar

pulse depending on laser energy and target-substrate distance are possible. For example, to deposit a film of 300 nm at a deposition rate of 0.05 nm per pulse and a pulse frequency of 10 Hz, will take 10 min. The PLD system was designed to comply with the above specifications, and to have flexibility to vary any deposition parameter. Thus the specifications include:

- Laser wavelength 308 nm - XeCl excimer laser
- Variation in substrate-target distance of $20 - 70$ mm
- Substrate heater capable of heating up to 880°C
- Laser energy density could be varied by changing the laser energy or changing the laser spot size on the target. For this purpose the lens system was designed to facilitate 60 mm lateral movement of the lens.
- Oxygen introduction through a needle valve to accurately control the oxygen partial pressure inside the chamber during the deposition process.

Fig. 3-2 shows a planar view drawing of the PLD chamber. The chamber is 410 mm in diameter and 360 mm in height. Indicated in **Fig. 3-2** are the different parts of the system, which are discussed in further detail in the rest of the chapter.

3.2 Optics and laser

The optical components of the PLD system are indicated by **E** and **F** in **Fig. 3-2**. The laser beam is directed through a focussing lens and a flat window towards the target in position **B**. Notice that the laser beam is directed at the geometric centre of the chamber, and it strikes the target at a point in an off-axis position, about $2 - 7$ mm from the target's centre. This is to ensure that the target is evenly used, during target rotation.

All optics used in this system are of laser quality, implying that their surfaces are very flat (the surface features should be not higher than $\frac{1}{8}\lambda$ to $\frac{1}{20}\lambda$) and the materials are especially suited to the laser

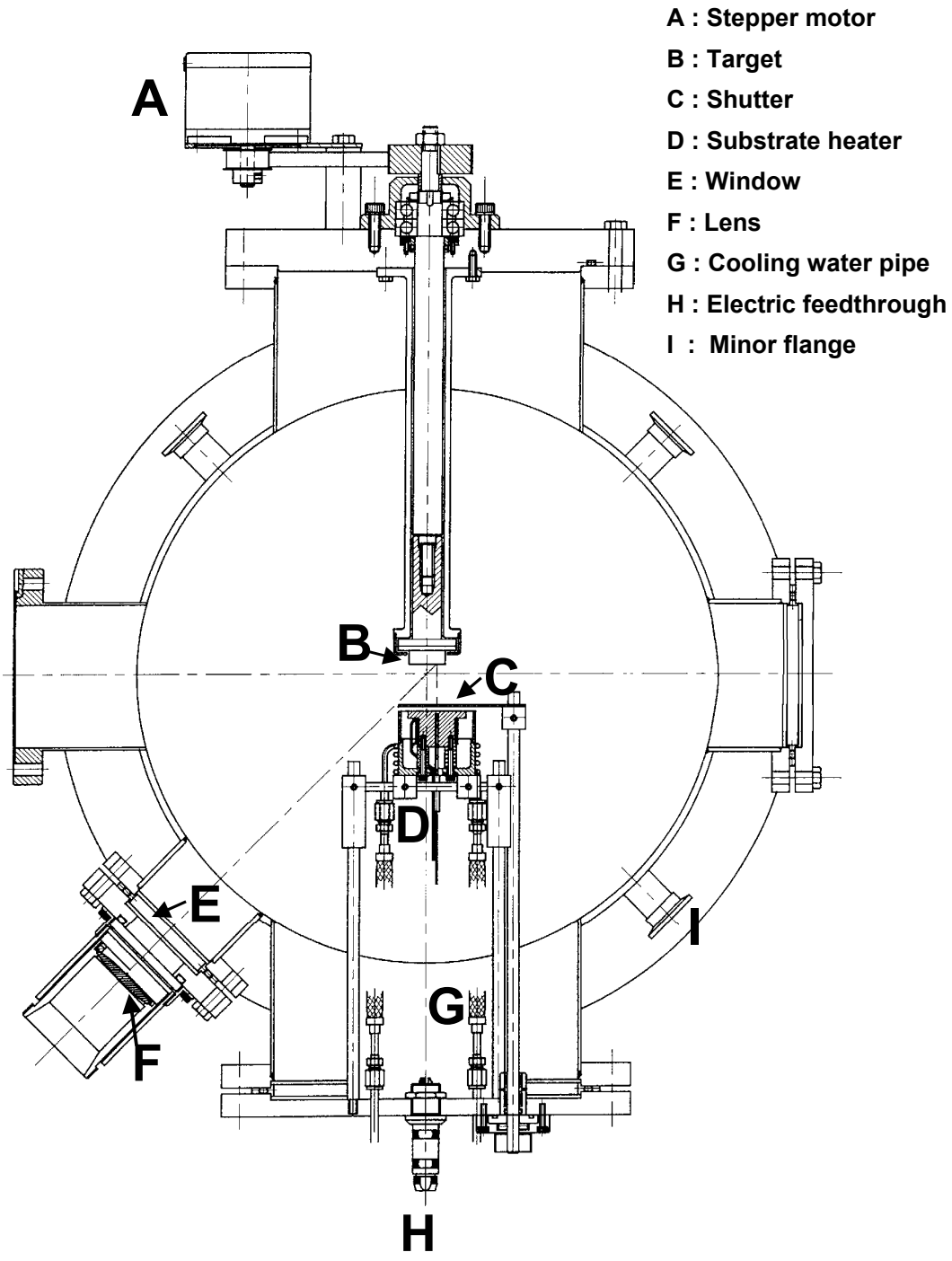

Figure 3-2: *Planar view of the PLD chamber.*

wavelength. The laser window and the lens are co-planarly situated at an angle of 45° to the normal of the target. The window is a 63.5 mm disk made from ultra violet grade fused silica and is seated on a viton O-ring to make a vacuum tight seal. The focusing plano-convex lens is also fabricated from ultra violet grade fused silica, diameter 50.8 mm and nominal focal length $f = 305$ mm (specified for wavelength $\lambda =$ 546 nm, green). The lens had the plane side facing the incoming beam. The window, lens and mirror were chosen to have their diameters larger than 1.5 times the laser beam waist (beam's full width at half maximum).

Due to chromatic aberration the focal length at $\lambda = 308$ nm is $f_{308} = 288$ mm. Chromatic aberration is the phenomenon that the index of refraction n_λ of an optical material is wavelength dependent. In the case of UV-grade fused silica we have: $n_{546} = 1.460$ and $n_{308} = 1.487$; subscripts are wavelength in nanometer. The focal length of the lens is specified for the green wavelength 546 nm, $f_{546} = 305$ nm. The thin lens equation relates the focal length to the index of refraction and the radius of curvature for the primary and secondary refracting surfaces of a lens:

$$\frac{1}{f} = (n-1)\left(\frac{1}{R_1} - \frac{1}{R_2}\right), \tag{3.1}$$

thus

$$f_{308} = \left(\frac{n_{546}-1}{n_{308}-1}\right) f_{546} = 288 \text{ nm}. \tag{3.2}$$

The lens was chosen to achieve the energy density range of $2-3$ J/cm^2 per pulse at the target suggested by **Table 3.1** for good laser ablation of the target. The position of the focussing lens can be adjusted, to select the size of the irradiated area in order to change the energy density. The lens could be clearly seen on the lower left hand side of **Fig. 3-2**. It is clamped into a threaded cylinder, with the threads cut such that one turn of the cylinder moves the lens exactly 1 mm inwards or outwards. The lens has a total movement range of about 60 mm; which is enough to easily bring the spot exactly in focus and to vary the spot size from about 0.01 cm^2 to 0.07 cm^2 and more.

The mirror indicated in **Fig. 3-1(a)** is a dielectric multilayer mirror optimised for a 45° incidence angle of the laser beam. It is situated on the laser table and it is mounted on a adjustable holder capable of very finely aiming the laser beam towards the lens opening at the PLD chamber. The mirror was placed before the lens in the optical setup to protect the mirror from high energy density pulses. **Table 3.2** indicates the losses for the excimer laser beam either being reflected or transmitted through the various optical component in the optical path. The total transmission coefficient through the optical path is

$$T = T_{mirror} \times T_{lens} \times T_{window} = 0.78, \tag{3.3}$$

Table 3.2: *Measured loss properties of element in the optical path.*

Optics	**Material**	**Loss**	**Notes**
Mirror	UV-grade fused silica	6%	optimised for 45°
Lens	UV-grade fused silica	10%	plano-convex
Window	UV-grade fused silica	10%	flat

the total loss is thus 22%.

The optics was cleaned regularly in alcohol to remove dust and fatty stains (like fingerprints) that might have collected on their surfaces. It is very important to keep the optics clean at all times since any dust or organic deposits can cause a build-up of heat on the optical element's surface which can lead to damage to the optics. Another source of lens contamination is residue of the deposition process that can deposit on the inner window surface. This can be removed by carefully washing the window with a fine cloth in an ultra fine abrasive suspension such as diamond dust or Vienna chalk suspended in distilled water or alcohol.

Lambda Physik excimer lasers (models EMG 101 MSC and EMG 203 MSC) at the Physics department of the University of Stellenbosch were used to deliver pulsed laser beams. The wavelength of the lasers is 308 nm (ultra violet) when operating with XeCl, the pulse duration is 30 ns. The pulsed frequency could be adjusted in the range $1 - 100$ Hz, with diminishing power with higher frequency, as shown in **Fig. 3-3(a)**.

Laser energy per pulse is measured with a pyroelectric detector. This detector produces a voltage pulse for each laser pulse incident on it's surface, and the voltage pulse's peak height is proportional to the laser pulse energy. The calibration factor for this energy meter was 1.8 J/V. By recording a series of pulses on a storage oscilloscope, the average pulse energy could be determined. Pulse energy per pulse did not deviate by more than 3% from the mean value for sufficient energetic laser pulses. About 20 pulses were taken on any given run on the oscilloscope, providing enough data to obtain the pulse energy. The oscilloscope is capable of providing a voltage reading accuracy of about 2 mV on a level of ~ 150 mV, thus an accuracy of 1%.

An electric discharge causes the excited excimer molecules to form, which in turn drives the lasing action, since the excited state is higher populated than the ground state. Excess heat is released in the gas, which is removed by cycling the gas through a series of heat exchangers to keep the laser medium in it's optimal condition. However with increasing pulse frequency, the heat exchange process lags behind and thus the laser medium is no longer optimal, causing the resultant pulse energy to drop. **Fig. 3-3(a)** shows the monotonic decrease of laser energy per pulse for increasing pulse frequency. Usually deposition was done at $5 - 10$ Hz, where the energy was quite high.

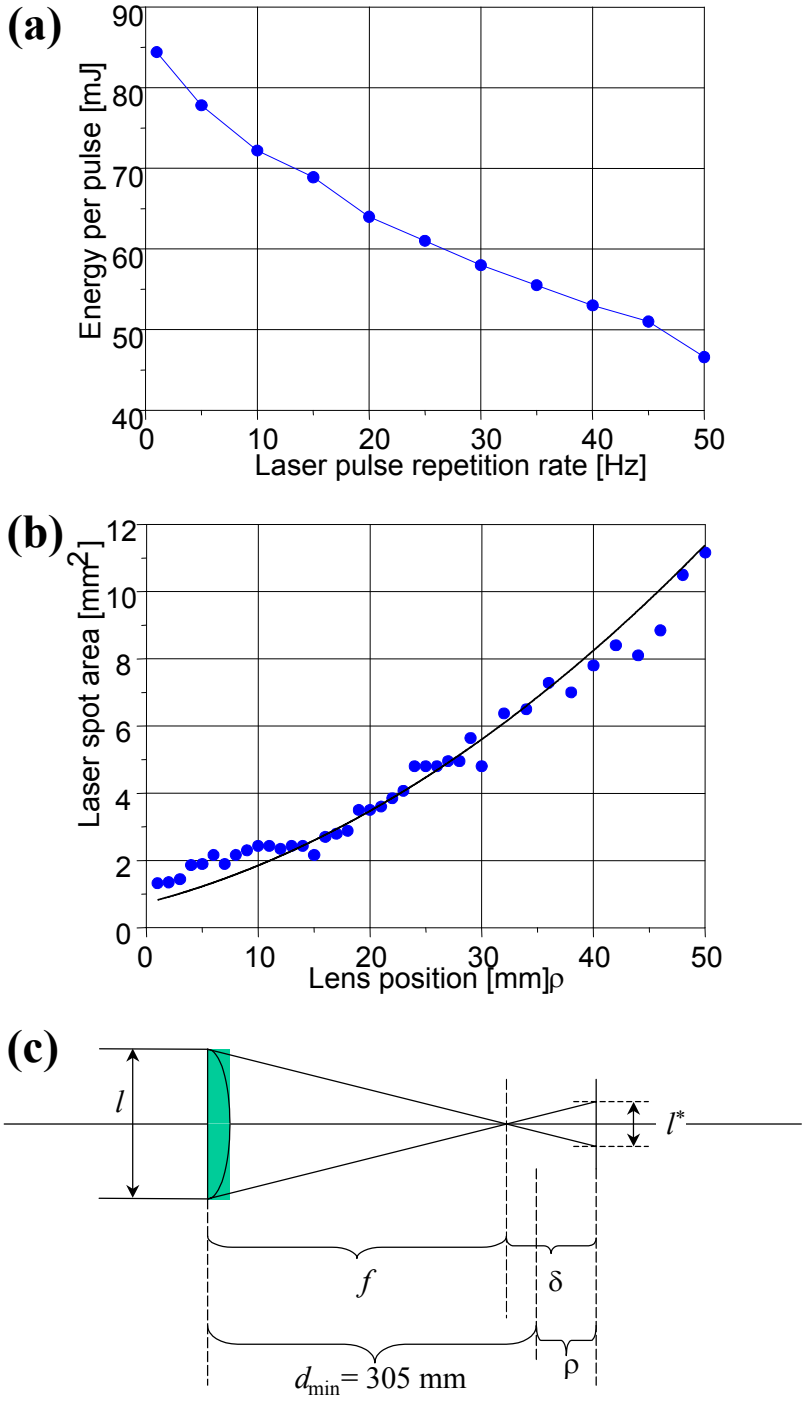

Figure 3-3: *(a) Dependence of the laser pulse energy on the laser pulse frequency. Laser voltage was 21.3 kV. (b) Spot area of incident laser pulse at the target for various positions of the focussing lens. The position of the lens in* ***Fig. 3-2*** *is taken to be the zero position, since it is the closest position that the lens can be to the target, designated by* $d_{\min} = 305$ *mm. The lens position in the graph is indicated by* $\rho = d - d_{\min}$*, the amount by which the lens is moved from it's zero position. The data points indicate spot area as determined by photographic paper, while the solid line are the result of calculation, using eq. 3.7. (c) Schematic diagram of the relevant distances in the lens set-up.*

The profile of the beam looks like a gaussian profile with the top flattened. The essential information about the two lasers used is summarised in **Table 3.3**.

Table 3.3: *Specification of the two lasers used in this project.*

Laser model	**EMG 101 MSC**	**EMG 203 MSC**
Energy per pulse	150-180 mJ	200-300 mJ
Aperture size	22 mm × 8 mm	22 mm × 8 mm
Frequency range	1-50 Hz	1-100 Hz

The rectangular aperture (width : 22 mm × height : 8 mm) of the laser causes a rectangular beam of the same dimensions. To obtain the desired energy density, the beam is focussed down to a spot on the surface of the target, the spot size is in the range of $0.01 - 0.08$ cm^2. To determine the spot size of the focussed beam on the target black photographic paper is illuminated at the target surface. The mark left by the pulse is indicative of the spot size. However, due to the non-uniform nature of the beam spatial profile this method can only serve as a rough estimate. **Fig. 3-3(b)** shows the dependence of the spot size on the position of the lens. An alternate method to obtain the spot size is by geometrical optics. The spot area of the laser is given by (refer to **Fig. 3-3(c)**).

$$a' = a\frac{\delta^2}{f^2} = a\frac{(d-f)^2}{f^2} \tag{3.4}$$

$$d = d_{\min} + \rho = f + \delta. \tag{3.5}$$

Here a' is the spot area, a is the aperture area, δ is the amount by which the distance from the lens to the target differs from the lens' focal length f (= 288 mm). ρ is the distance that the lens is removed from it's closest (zero) position, $d_{\min} = 305$ mm. The lens has a 60 mm range of movement to change spot size. Using eq. 3.4 to obtain a numerical formula for the spot area yielded:

$$a' = \frac{a}{f^2}\left(\rho^2 + 3.4\rho + 2.89\right) = 2.1219 \times 10^{-3} \times \left(\rho^2 + 3.4\rho + 2.89\right) \ ...[\text{cm}^2] \tag{3.6}$$

with an RMS error of 0.258, and δ expressed in units of cm. By least squares optimisation, the above could be improved by using

$$\frac{a}{f^2} = 2.535 \times 10^{-3}, \tag{3.7a}$$

$$a' = 2.535 \times 10^{-3} \times \left(\rho^2 + 3.4\rho + 2.89\right) \ ...[\text{cm}^2] \tag{3.7b}$$

yielding a RMS error of 0.150. The best least squares fit using a general quadratic is

$$\begin{aligned} a' &= p_0 + p_1\rho + p_2^2\rho \ ...[\mathrm{cm}^2] \\ p_0 &= 3.95 \times 10^{-3} \\ p_1 &= 0.00529 \\ p_2 &= 1.66 \times 10^{-3}, \end{aligned} \tag{3.8}$$

yielding a RMS error of 0.0957. Eq. 3.7 is used through this work since it has the pleasing property of agreeing with eq. 3.4 in all aspects except the value of a, which could be explained as the result of beam divergence, a common property of excimer lasers. The alternate value of a, (a^*), implied by Eq. 3.8 is $a^* = 2.10$ cm^2, an 19% increase on $a = 1.76$ cm^2.

3.3 Heated substrate holder

The growth of high quality thin films of high temperature superconductors can only take place under conditions where the substrate is heated above the crystallization temperature of the compound to be deposited. The heater (indicated by **D** in **Fig. 3-2**) must thus be able to heat up substrates to temperatures of up to 850°C in a reactive ambient such as oxygen. The design of the substrate heater is adapted from a design by V. Kumar and A.K. Gupta[91], see **Fig. 3-4**. They used a *Thermocoax* heating element which was coiled and welded under a steel plate. The *Thermocoax* heating element from *Philips* consists of a current-carrying core of nickel-chromium 80/20 and an *Inconel 600* (a zirconium copper alloy) sheath, with MgO fine powder as insulant between the core and the sheath. The sheath can withstand high temperatures up to 950°C in a reactive environment like an oxygen ambient. The element is 1 mm in diameter and the hot length is about 500 mm. The substrate was glued on the steel plate with silver paint. Kumar and Gupta found that the temperature changes by about 5°C for a distance of 10 mm from the center which is sufficiently uniform to deposit high-quality superconducting film on substrates of 10×10 mm in size.

In our design, a *Thermocoax* heating element is wound around in a flat spiral and brazed to a flat stainless steel cylinder, on top of which the substrate is placed. A nickel based brazing paste from *Degussa* was used. The cylinder is 10 mm thick and it's diameter is 45 mm. It was necessary to braze the heating element into the cylinder to ensure an intimate contact with it and thus insure the optimal transfer of heat. In prior designs where the element was simply clamped into the cylinder, the element failed due to overheating - the heating block could not absorb the heat quick enough.

The temperature is monitored using a type-*K chromel-alumel* thermocouple connected to an *Ascon*

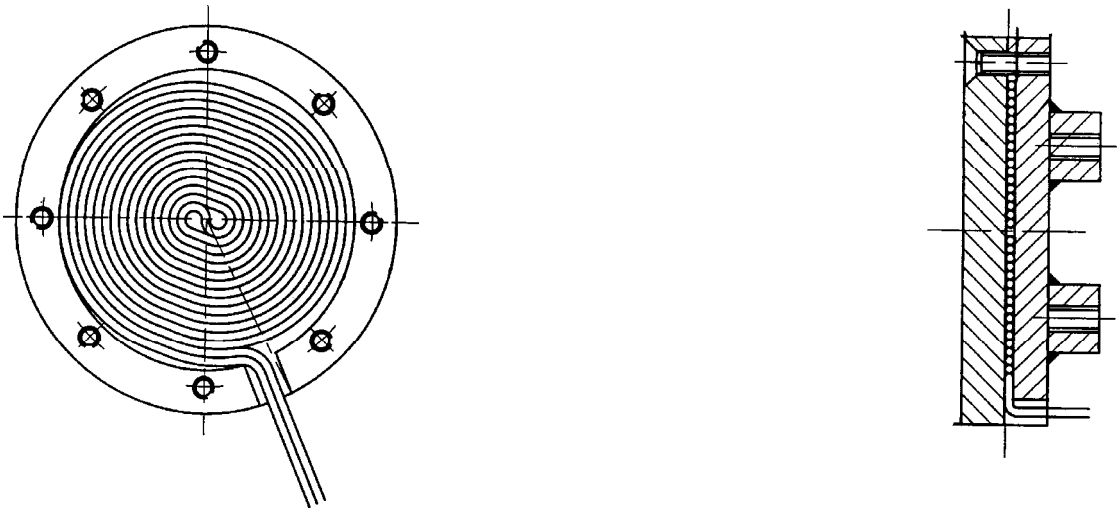

Figure 3-4: *Drawing of the substrate heater. On the left is a planar view, and on the right is a cross-sectional view.*

PID-type temperature controller. The thermocouple is inserted into the heating cylinder via a hole in the cylinder located 1 mm below the upper surface. The thermocouple has a 0.5 mm diameter sheath in which the thermocouple measuring tip is housed. The small diameter ensure a fast response of the thermocouple to changes in temperature. The substrate heater can reach a temperature of about 800°C in around 15 min when powered by a power of 350 W (see **Fig. 3-5(a)** and **(c)**). **Fig. 3-5(b)** shows the cooling characteristic of the sample holder in the presence of an oxygen ambient at 900 mbar. The electric power to heat the element is fed through an electric feedthrough indicated by **H** in **Fig. 3-2**. The temperature controller can be tuned to optimise the control in a specific temperature region. The substrate heater is shown in the bottom part of the photograph in **Fig. 3-6(a)**. The substrate can be heated up to a temperature of 850°C as sometimes needed for the crystal forming phase of the deposition procedure.

The substrate is pasted to the cylinder with thermal conducting silver paint (silver diluted in methyl iso-butyl ketone - MIBK), while the substrate assembly is surrounded by a water cooled cylindrical radiation shield to prevent excessive heating of the chamber walls (actually, the water cooling was never used, since the vacuum chamber walls did not heat up to more that 40°C). We found that the silver

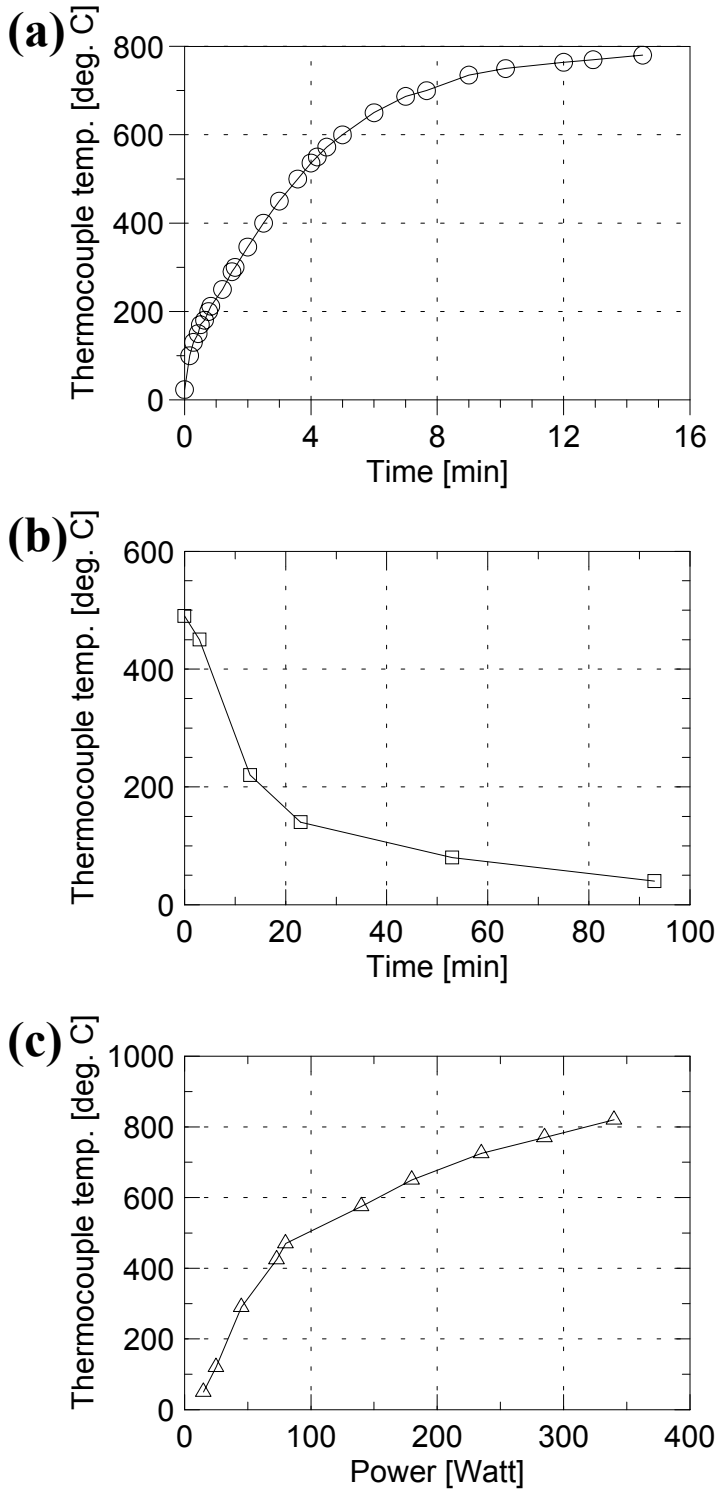

Figure 3-5: *(a) Heating up the substrate heater : This plot shows the time elapsed since the heating started; the heater power was 300 W. (b) The cooling characteristic of the sample holder in the presence of a oxygen ambient at 900 mbar. (c) The temperature that can be reached with a radiation shield for various levels of electrical power.*

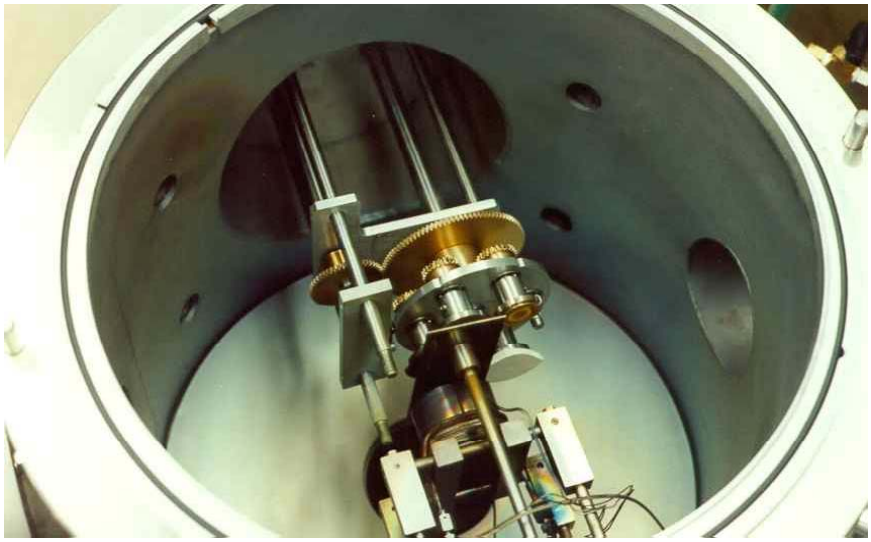

(a)

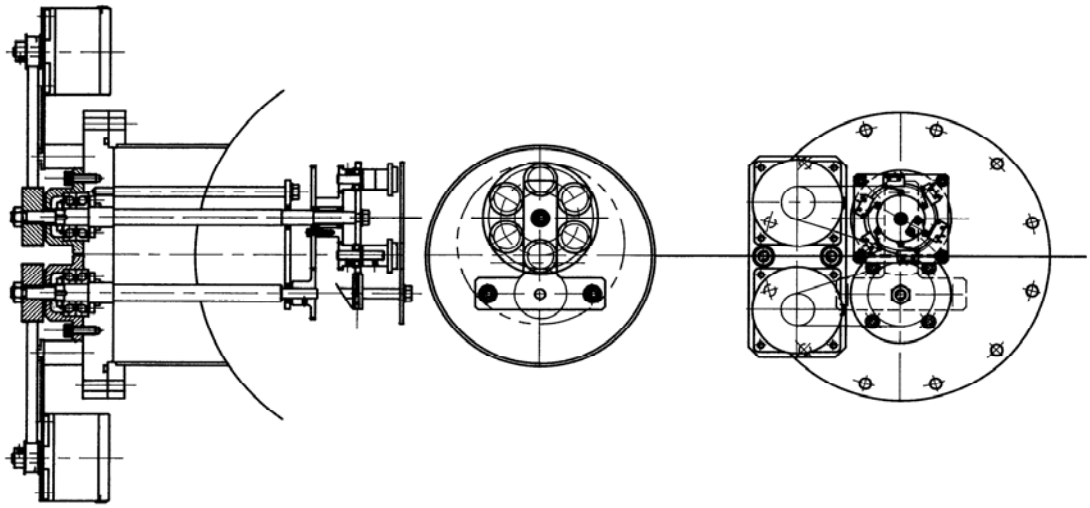

(b)

Figure 3-6: *(a) Inside view of the PLD system. In the center the multitarget system with it's six target holders is visible. The brass gears are used to rotate the targets and the target carousel. At the bottom is the substrate heater system, with a shutter to shield the substrate from the plume when desired. (b) Drawing of the multi-target system. On the left is a cross-section of the system showing the two driving stepper motors. In the middle is a schematic of the multi-target carousel and on the right is a view from the outside of the multi-target system, showing the stepper motors used to drive the target selection and target rotation systems.*

paint trademarked *Electrolube* works best - the consistency of the paint is ideal for painting and effecting good thermal contact. The flatness of the substrate holder is essential to ensure a good thermal contact between heater and substrate. The radiation shield serves a second, very important purpose; it reflects some of the radiation back to the substrate heater, preventing some heat loss. This procedure raises the substrate temperature by some 25% in Celsius terms at a power of 100 W. In practice, the heating element slowly lost it's heating capability in the course of 18 months, and more power was necessary to heat the substrate to the same levels. This resulted that the original power source designed to drive the heating element was no longer adequate. A variable transformer (*Variac*) capable of delivering any voltage from 1 V to 240 V was used to provide the power.

3.4 Multi-target system and targets

A multi-target system was designed to facilitate the deposition of multilayered structures such as superconductor/isolator superlattices. The multi-target carousel can hold up to six targets, and is driven by two stepper motors: the first to rotate the target during ablation, and the second to select the desired target (**Fig. 3-6(b)**). Shown in **Fig. 3-6(a)** are the brass gears and the target holders. For better control of layer thicknesses, a computer-controlled laser triggering and target exchange system was implemented. The target system is connected to the flange opposite the substrate holder. The target is pasted to a target holder with a good heat conducting silver epoxy or alternatively clamped with screws to a removable target holder. The target holder slowly rotates via a stepper motor to facilitate even ablation of target material. The target axis runs through the geometric centre of the deposition chamber. Since the laser beam is directed to the geometric centre, the target axis is slightly displaced from the symmetry axis of the chamber to make such a procedure possible. An outside operated shutter was built in to enable the substrate to be shielded from the plume when necessary. A single target system was initially manufactured as indicated in **Fig. 3-2**.

The target used to deposit $YBa_2Cu_3O_7$ films was a phase pure orthorhombic YBa_2Cu_3-oxide target of which the raw materials was 99.995% pure. The bulk density was 4.95 g/cm^3 and the diameter was 25.4 mm, the thickness 6.4 mm. The target was produced using a low pressure calcination method[92]. The YBCO powders are prepared from a intimately mixed precursor powder produced by a co-precipitation method[93]. The precursor powders are prepared from a 99.995% purity $Y(NO_3)_3$, $Ba(NO_3)_2$ and $Cu(NO_3)_2$ solutions. The average particle size in the final powder was 1 μm[94].

3.5 Vacuum system and oxygen introduction

The PLD vacuum chamber is pumped by a *Pfeiffer* TPH240 turbomolecular pump capable of pumping 240 l/s at pressures of 10^{-3} mbar and lower (**Fig. 3-7(a)**). The roughing pump is a *Alcatel* 2015 rotary pump. Due to the pumping of oxygen during deposition, a synthetic oil should be used in the rotary pump instead of flammable mineral oil, known to cause explosions when pumping pure oxygen. *Fomblin YL VAC 25-6*, *Krytox 1525* or equivalent should be used. A base pressure of 1×10^{-6} mbar can be achieved, and the pumping characteristic is shown in **Fig. 3-7(b).** The chamber is vented with nitrogen when opened to minimise the introduction of atmospheric moisture into the chamber.

Oxygen content plays a critical role in the properties of high temperature copper oxide superconductors - a 5% reduction in oxygen content causes a drop in critical temperature of about 5 K−10 K. By depositing in a oxygen ambient of about 0.3 mbar good oxygen inclusion could be ensured. An oxygen intercalation procedure after deposition should also be carried out by annealing the thin film at 490°C in an over pressure of oxygen. Ultra high purity oxygen[1] is introduced to the vacuum chamber via a needle valve (attached on a minor flange, as indicated by **I** in **Fig. 3-2**). To maintain a pressure of ~ 0.1 mbar in the chamber, while the turbopump is running, the pneumatic valve was closed while the bypass value was opened (see **Fig. 3-7(a)**). This allowed accurate control of the chamber's pressure, while oxygen gas was flowing through the chamber.

3.6 Sample preparation

Thin film superconductors are usually deposited on almost lattice matched substrates like MgO and $SrTiO_3$. Substrates are typically of dimensions 10 mm × 10 mm × 0.5 mm, with one side polished to typical average roughness $R_a = 0.16$ nm and root mean square roughness $R_q = 0.20$ nm as determined by an atomic force microscope. Although substrates have been cleaned chemically by the suppliers prior to sending, a chemical cleaning procedure was followed to remove excess oils and other undesirable material on the substrates. The procedure consists of etching the substrates in a sequence of organic solvents, each time placing the container in an ultrasonic bath for 2 minutes. The sequence is: methanol → acetone → trichloroethylene → acetone → methanol → de-ionised water.

An investigation[40] of the effect of substrate preparation has shown that the heating of MgO substrates in oxygen at $1100 - 1200$°C for $12 - 24$ h improves the quality of the resulting $YBa_2Cu_3O_7$ thin film. This baking procedure causes a high density of atomic steps to form on the substrate surface. Higher critical temperature, lower normal state resistance, and improved critical current density result

[1] UHP oxygen consists of 99.995% O_2, with $N_2 < 40$ ppm, $H_2O < 3$ ppm, $CO_2 < 1$ ppm, $CO < 0.5$ ppm, total hydrocarbon < 0.5 ppm.

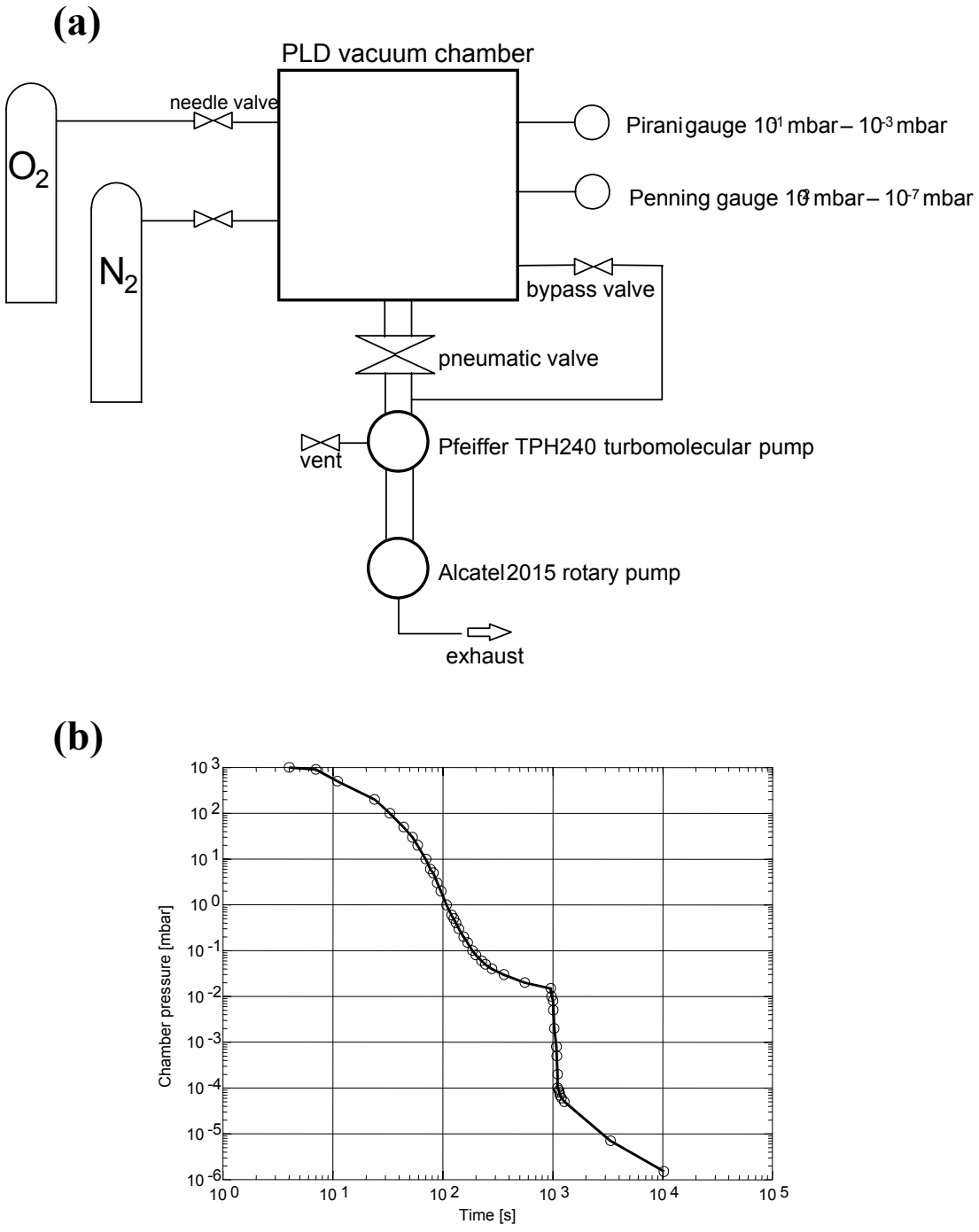

Figure 3-7: *(a) Schematic diagram of vacuum vessel with pumps and gauges. (b) Pumping characteristic of the pump system attached to the vacuum chamber.*

from this baking procedure.

Occasionally, during mounting, a substrate becomes contaminated with silver paste on the polished surface. Such a substrate should be cleaned in MIBK, and then further cleaned by the above procedure.

3.7 Deposition procedure

A typical deposition procedure has been illustrated in **Fig. 3-8**. The deposition procedure is also listed below, and the letters in the figure is mentioned at the appropriate places in the list below:

1. Mount substrate on substrate holder using silver paste. Substrates are usually MgO or $SrTiO_3$ of size 10 mm $\times$ 10 mm. Mount heat shield over substrate holder. Place shutter over substrate. Resurface target if necessary, to remove silver paint residue from the previous deposition run. It is imperative to ensure a complete wetting of the substrate back surface to guarantee good thermal contact with the substrate heater. The silver paint must dry completely before the substrate holder is replaced into the chamber. This will prevent bubbles from forming underneath the substrate surface while the heater is on.

2. Pump vacuum chamber for at least 4 hours to reach 2×10^{-6} mbar (**A**). Switch turbomolecular pump on only when 10^{-3} mbar has been reached. Cooling water or fan for turbopump should be present.

3. Switch on excimer laser system.

4. Heat substrate to desired temperature (usually 720°C or higher) (**B**).

5. Close pneumatic valve, open by-pass valve. This is to be able to accurately control the oxygen partial pressure in the chamber while still allowing the pumps to run.

6. Introduce oxygen to partial pressure of (usually) 0.3 mbar (**C**).

7. Switch on target rotator.

8. Measure and adjust laser energy.

9. Focus laser beam by adjusting lens if necessary. Adjust mirror if necessary.

10. Pre-ablate target for 1-2 minutes, while keeping shutter over substrate.

11. Open shutter to deposit to desired thickness (**D**).

12. Oxygen intercalation : Increase oxygen pressure to 900 mbar (**E**), decrease temperature to 490°C (**F**). Keep stable for 15 minutes (**G**).

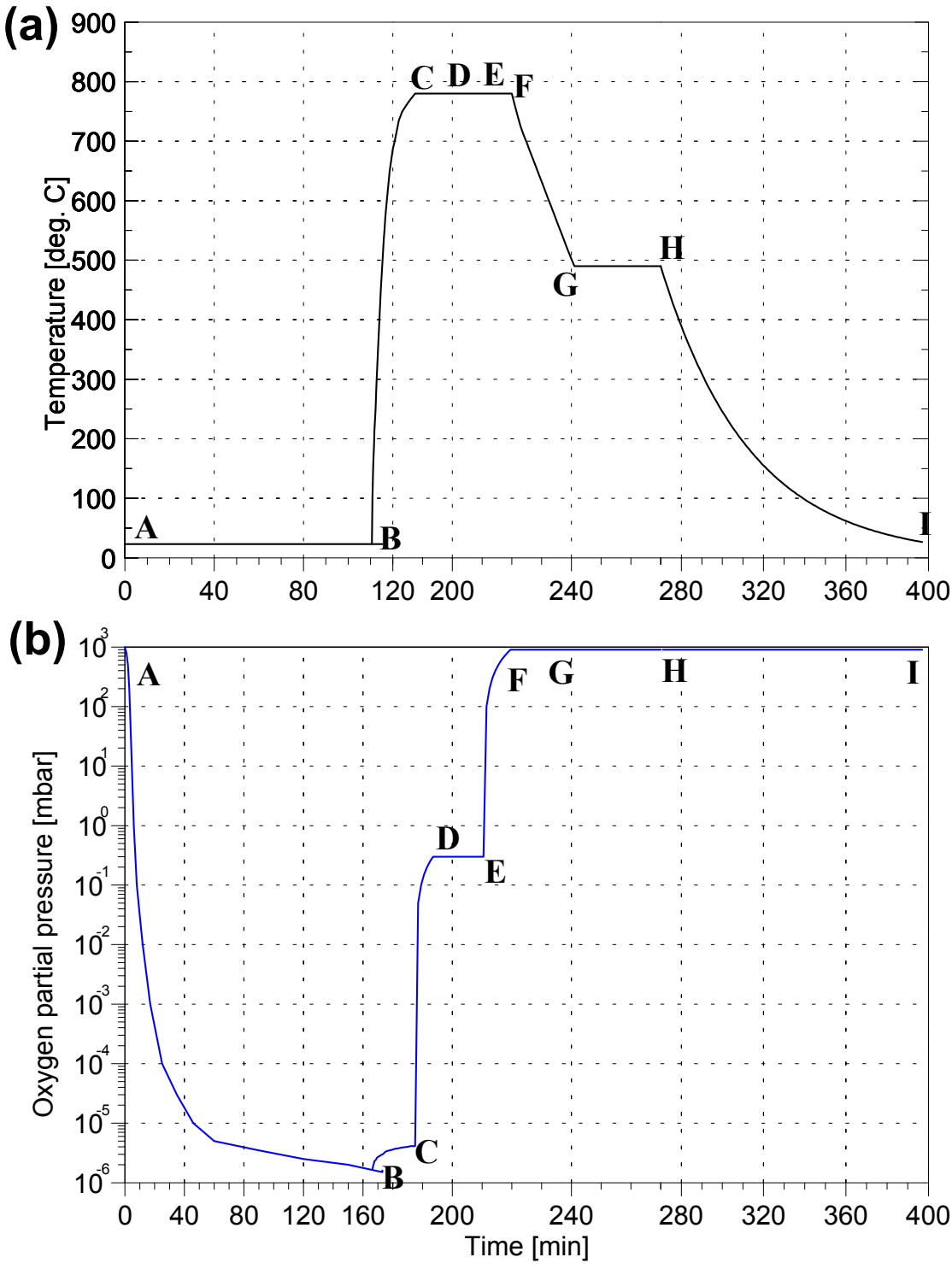

Figure 3-8: *Diagrammatic description of a typical PLD procedure, showing the (a) temperature and (b) oxygen partial pressure versus time for a varying time scale.*

13. Switch off the heater, allowing the substrate to cool to room temperature (**H**).

14. Open vessel to remove substrate, venting with nitrogen. Remove deposited sample (**I**).

3.8 Other materials deposited

Several other materials were deposited with the PLD system, and the results of these investigations are briefly mentioned. This includes the deposition of electrochromic materials (with Drs. Khalid Bouzaine and Malik Maaza), and magnetoresistive materials (with Dr. E.B. Nyeanchi).

3.8.1 Pulsed laser deposition of thermochromic VO_2 thin films

Introduction

This section contains work done in collaboration with Drs. M. Maaza and K. Bouziane from the University of the Witwatersrand; the results were recently published[95]. This section contains a summary of the publication.

A large number of transition metal oxides and sulphides are semi-conducting at low temperatures and metalic at high temperatures[96]. In vanadium oxide compounds (V_2O_3, V_3O_5, V_4O_7 and VO_2), this semiconducting/metal phase transition is first order[97]. VO_2 is of particular interest for solar technology applications[98] as switching infrared smart devices. This semi-conducting/metal phase transition which takes place near room temperature ($\sim$68°C) is correlated to a sharp optical transition[98]. This optical transition manifests itself as a large modulation of the optical transmission in the infrared spectral region versus temperature. This so-called *thermochromic* property offers the possibility to a self-control of solar radiation heating in architectural building industry and automotive sector.

To exploit the thermochromic property in technological applications, VO_2 is needed in most cases in the form of film-bases coatings. Different thin film deposition techniques have been tested successfully, such as sputtering, evaporation, sol-gel processing to obtain thermochromic VO_2 coatings with properties close to that of bulk crystals. These methods have yielded films of approximately correct stoichiometry, but other crystallographic phases were always present along with the desired VO_2. Pulsed laser deposition offers the possibility to overcome this chemical problem through it's ability for stoichiometric transfer due to congruent evaporation. This is possible without heating the substrate or controlling the ambient gas pressure or mixture during evaporation.

Experiments and results

A pressed powder pellet 15 mm in diameter and 2 mm with nominal composition VO_2 was used as a target. The target was mounted on the target holder of the NAC PLD system, and the chamber was evacuated to a base pressure of 2×10^{-6} mbar. The usual XeCl excimer laser was used to ablate the target. The energy density was varied in the range $0.5 - 2.7$ J/cm^2 using the lens of the PLD system. Silicon, quartz and sapphire substrates were used. The target-substrate distance was 25 mm. The laser pulses was fired at a rate of 10 s^{-1}, for 600 s per film.

Using RBS analysis (2 MeV He^+ ions) it was shown that the chemical composition of the films was within 10% of the original bulk; for the formula V_xO_2 it was found that $0.96 < x < 1.02$ with a laser energy density ≈ 1.3 J/cm^2. Laser ablation with excimer lasers is generally understood to cause heating confined to a thin surface layer, due to a large untraviolet absorption coefficient and poor thermal conductivity of the sintered VO_2 target. Atomic force microscopy reveals that the films on all substrates examined consist of compact almost spherical crystallites which are approximately 130 nm in diameter. This effective non-dependence from the nature of the substrate seems to indicate that the growth mechanism is imposed mainly by the laser-target interaction in the considered conditions.

The crystallographic structure of the films grown on the three different substrates was investigated by x-ray diffractometry using Cu$-K\alpha_1$ radiation. Only VO_2 lines were observed for all substrates, indicating the vanadiumoxide to be a single phase monoclinic VO_2 structure. The films were not epitaxial, but they were textured.

The three VO_2 coatings exhibited similar sharp electrical resistance transitions located between 64°C and 72°C. **Fig. 3-9(a)** shows the temperature dependence of the electrical sheet resistance of VO_2 on sapphire. The sudden drop of resistance on heating centered at 68°C is indicative of the VO_2 phase. Compared to films obtained by the usual vacuum deposition techniques[97], the electrical transition is sharper characterised by a small hysteresis of approximately 8°C in width.

Optical measurements were carried out on a Cary double beam spectrophotometer in the spectral range 300 nm $< \lambda <$ 3000 nm at normal incidence. VO_2 films on the different substrates exhibited similar optical properties. The optical transmission exhibits a strong temperature dependence in the infrared region ($\lambda > 1500$ nm) without a significant change in the visible region as in the case of usually deposited VO_2 films. However, the films produced by PLD shows a very abrupt change in optical transmission between 65°C and 70°C, which is not the case for films produced by other means[97]. **Fig. 3-9(b)** shows the optical transmission switching versus temperature from 30°C to 100°C for the same film at four different wavelengths: two in the visible and two the in infrared regions respectively. As shown is the switching in the visible region smaller than 5% while in the infrared it is larger than 35%. At 3000 nm, it is about 45%. The hysteresis loop is centered exactly at 68°C as in bulk VO_2

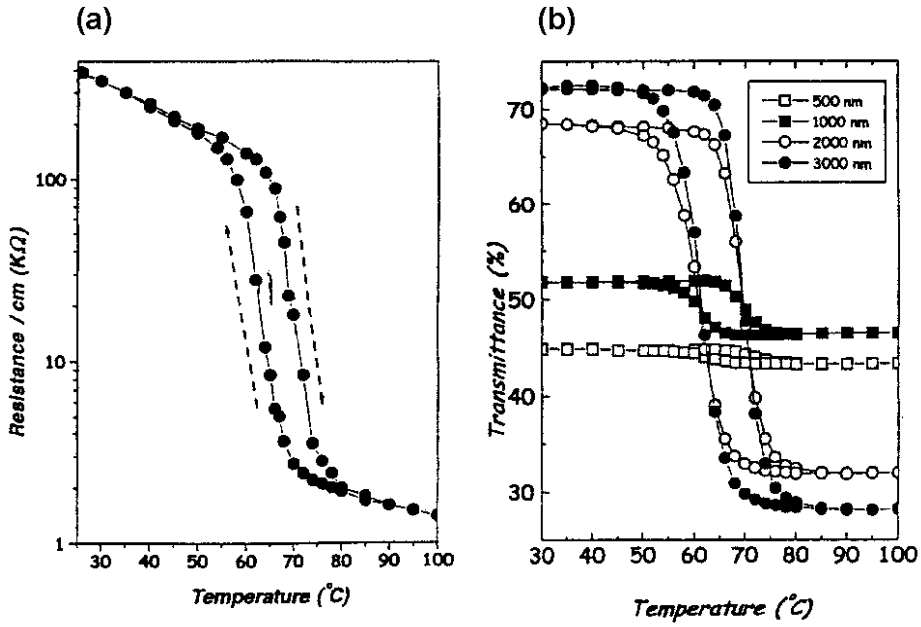

Figure 3-9: *(a) Temperature-electrical resistance hysteresis of VO_2 thin film deposited on sapphire. (b) Temperature-optical transmittance of VO_2 thin film on sapphire measured out at four wavelengths : 500 nm, 1000 nm, 2000 nm and 3000 nm.* [95]

crystals. The width of the hysteresis loop is 8°C, which is smaller compared to the values obtained on usually prepared films. As the difference in the optical transmission between the values at 80°C and 100°C is mot significant, one can conclude that the transition to the metallic phase is complete.

In conclusion, high quality stoichiometric VO_2 films were deposited using PLD. The film characteristics in terms of electrical and optical properties were very similar to that of the bulk, and superior to the films produced by other means.

3.8.2 Magnetoresistive materials

Studies of the perovskite compounds $RD\mathrm{MnO_3}$ (where R is a trivalent lanthanide element, such as La, Pr, or Nd and D is a divalent element such as Ca, Sr or Ba) have significantly increased in recent years because of the discovery of huge changes in their resistivity in the presence of an applied magnetic field. This is called colossal magnetoresistance (CMR) in order to distinguish it from giant magnetoresistance as observed in metallic multi-layers, for example in Fe-Cu superlattices. In the latter system, the highest magnetoresistance values have been just a 20-50% increase in resistance, while in the $\mathrm{LaCaMnO_3}$

resistance increases of a few thousand times have been reported. The potential for applying CMR materials in magnetic sensor devices has been one of the key factors behind the recent interest. E.B. Nyeanchi, I.P. Krylov *et al*[99][2] investigated thin films of CMR materials using the NAC PLD system. Pulsed laser deposition proved to be a successful technique for depositing CMR materials, due to PLD's ability to transfer the stoichiometry from target to film. Targets of $La_xCa_{1-x}MnO_3$ ceramic were prepared by solid state reaction of the constituent oxides which reacted in a furnace at a temperature of 1200°C in a flowing oxygen ambient. The films were prepared by laser ablating the target in an oxygen ambient pressure of 0.3 mbar and at a substrate temperature of 600°C. $LaAlO_3$ substrates were used. Samples were post annealed at 900°C in flowing oxygen to obtain good quality highly textured films. In **Fig. 3-10(a)** the data $M(T)$ for the film is shown together with $\rho(T)$ on a linear scale. The shape of the resistivity peak and all characteristic values of ρ are similar to the well known results for ferromagnetic films with the peak in the temperature range close to the experimental value $T_p = 205$ K. The only uncommon feature is that T_p is lower than $T_C \approx 240$ K as one can see in **Fig. 3-10(a)**. **Fig. 3-10(b)** shows a RBS spectrum of thin film $La_{0.70}Ca_{0.30}MnO_3$, the thickness was determined to be 250 nm. Measurements were taken using an incident $^4He^+$ beam of energy 3.045 MeV[99].

3.9 Conclusions

This PLD system proved to be quite versatile in being able to deposit different materials, most notable was good quality thermochromic VO_2 thin films, magnetoresistive $La_xCa_{1-x}MnO_3$ thin films, and superconducting $YBa_2Cu_3O_7$ thin films. Elemental Au and Ag layers were also successfully deposited on $YBa_2Cu_3O_7$ thin films, to serve as protective coatings. The critical temperature of the best superconducting films was 90 K as measured by resistivity measurement.

The heater system was particularly problematic, because of the ease with which the *Thermocoax* heating elements overheat if not properly thermally connected to the stainless steel block in which it is housed. Resistive heaters are quite commonly used in deposition chambers, see e.g. [100], but their tungsten heating elements degrade in oxygen rich ambients. The solution suggested by E.E. Inameti *et al* and N.J. Appleyard *et al*[101, 102] was to use inconel sheathed heating elements, e.g. *Thermocoax* by *Philips*.

Earlier attempts by us at simply clamping it between two steel disks resulted in the element failing within the first hour of usage. The solution was to braze the *Thermocoax* into the block. Different designs of substrate heaters were considered, and the system described previously was eventually selected due to it's simple design and the materials available. Other designs considered include using an optical

[2] The author, together with E.B. Nyeanchi deposited these films.

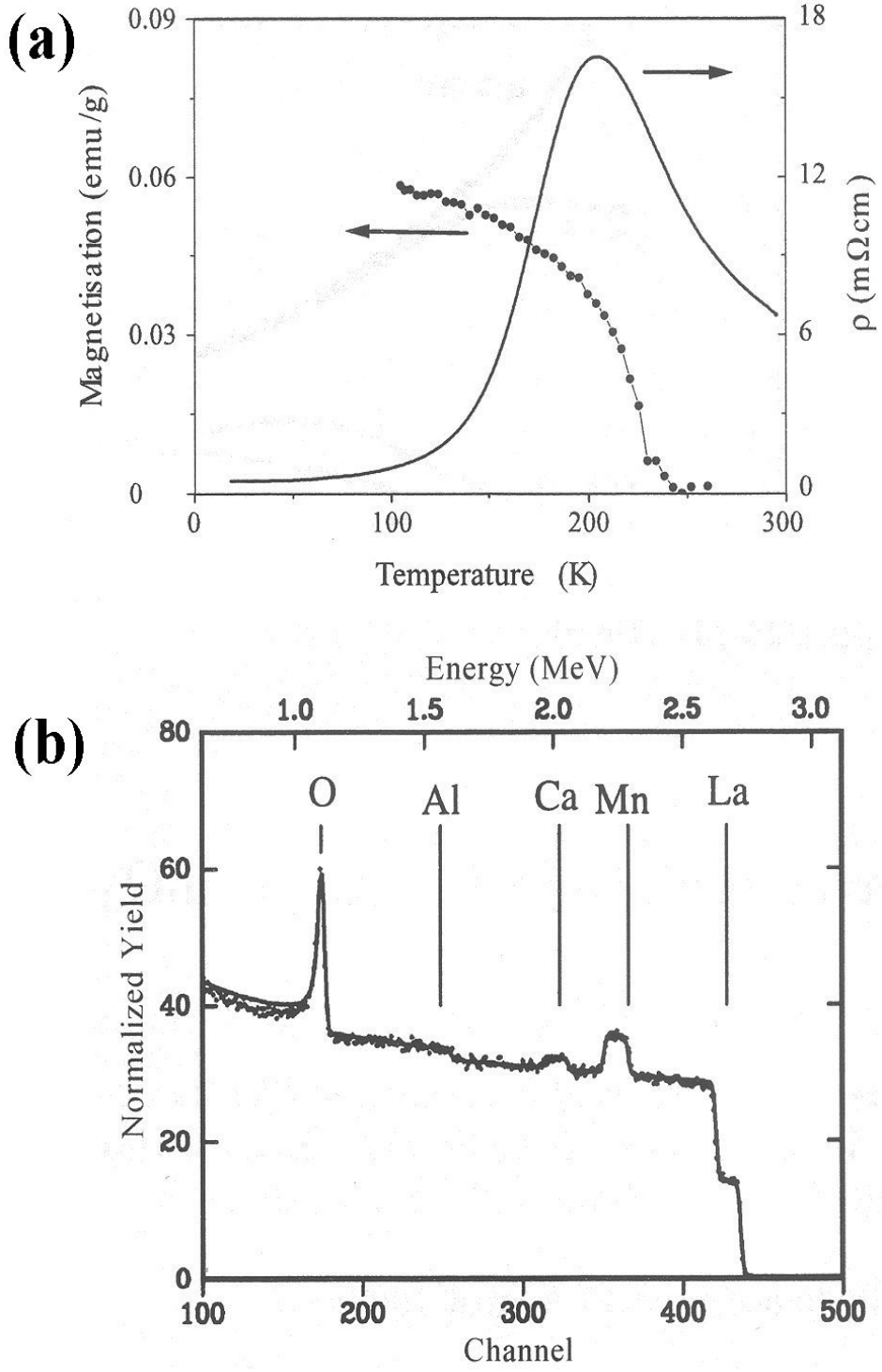

Figure 3-10: *(a) Magnetisation $M(T)$ data together with resistivity data for a $La_{0.70}Ca_{0.30}MnO_3$ thin film deposited on a $LaAlO_3$ substrate. (b) RBS spectrum of thin film $La_{0.70}Ca_{0.30}MnO_3$ on a $LaAlO_3$ substrate. Measurements were taken using an incident $^4He^+$ beam of energy 3.045 MeV. [99]*

waveguide (quartz rod) powered by a halogen lamp[103], and using quartz halogen projector bulbs inside a stainless steel heating block[104]. Using bulbs can be problematic in the event of explosion of the bulbs inside the chamber. Apart for interruption of the deposition process and possible damage to the film, are the very real possibility of damage to the turbomolecular pump when glass particles fall into it[101]. Ceramic heaters are also available commercially but cost considerations and adaptability demands made these options unattractive. The correct mounting of the substrates to the substrate heater is very important to achieve good thermal contact and thus the desired substrate temperature. One must ensure that the silver paint is evenly spread between the substrate and the substrate holder and properly dry before attempting to commence the deposition process. Non-shiny parts on a deposited film are indicative of non-epitaxial, amorphous film growth resulting from under heated parts of the substrate.

An *Ultimax* infrared pyrometer (model UX-20, designed for the range $600 - 2000°C$) was used to verify the temperature indicated by the thermocouple. Taking the emissivity of stainless steel into account ($\varepsilon \approx 0.4$), the temperature indicated by the pyrometer and that indicated by the thermocouple did not differ by more than 10°C in the range $650 - 800°C$.

Various improvements can be suggested for the present PLD system:

- The most important conversion to be considered is to convert the substrate holder to be able to hold multiple substrates. This would render the PLD system extremely useful, since it would enable the experimenter to spend more time depositing films rather than simply waiting for the system to pump down. In the design, careful attention should be paid to design a heating system where each substrate could be heated individually. Halogen lamp heating through a quartz tube could be considered at this point. This method has been successfully used by P. Vase *et al*[103] to heat large area substrates (2 inch diameter) up to 900°C with temperature uniformity better than $\pm 2°C$.

- The turn around time for deposition (the quickest time a deposition can be completed) is about $4\frac{1}{2}$ hours. Most of this time goes into pumping the system from 10^{-4} mbar to 10^{-6} mbar. A stronger turbomolecular pump would cut the turn around time down, possibly 50 minutes or more. Another improvement can be to replace certain viton O-rings with copper seals, as in ref. [105]. There are only a few flanges which need viton O-rings : at the substrate holder and the large lid on top; all others can be copper. In making this decision, certain cost considerations should be taken into account - it might be too costly to do the conversion.

- Large area deposition is a technique which has gained considerable momentum as a way to fabricate HTS wafers, see eg. [106]. This is an attempt to promote PLD to the arena of industrial processes.

Although this is a very promising field to pursue, I believe that the current system can not be easily converted to a large scale system due to the bulkiness of the substrate heating system which is already almost in the way of the laser beam. It would be much better to design a new custom made system for large area deposition.

- Off-axis deposition is a technique to reduce the deposition of particles onto the film (see Chapter 4). It would be possible to introduce this technique into the present PLD system since the substrate heater flange is large enough to allow for the mechanical feedthroughs necessary to allow rotation of the substrate.

- A load lock system can improve turn-around time by allowing exchange of samples without breaking vacuum. This can be considered as an alternative for a multiple substrate holder or it could be used in conjunction with it. A further improvement would be to separate the deposition and annealing stages, by having a separate chamber for annealing, attached to the main deposition chamber through a load lock type valve.

- A multi-target subsystem was developed for the PLD system. Such a subsystem has become a standard peripheral to PLD chambers, e.g. [107]. A further enhancement would be to automate the electronic control of the multi-target system, along with the laser triggering and other system parameters such as chamber pressure and substrate temperature. This would ensure much better control of the deposition conditions of thin films. Such systems have been developed quite successfully elsewhere[108].

- Silver paint was routinely used to ensure good thermal contact between the substrate and the substrate holder. This method has however several disadvantages:

    1. Difficulty in removing the substrate after deposition.
    2. The ease with which the samples are broken in the removal process.
    3. Difficulty in achieving a consistent good thermal bond.

R.P. Robertazzi *et al*[109] reported on a method were they clamped the substrate to the heating block, and inserted a thin ($\sim$1 μm) gold foil between the substrate and the block. They achieved very good reproducibility, since the clamping conditions can be very easily reproduced from deposition to deposition. It would certainly be to the benefit of our process to investigate this method.

Finally, material was presented on two different studies on which the author participated in. Thermochromic VO_2 thin films were deposited on silicon, quartz and sapphire substrates using the PLD

system. The thin films exhibited the desired optical transmittance transition at $\sim 65°$C. The results were published in ref. [95]

The author, together with E.B. Nyeanchi deposited magnetoresistive $La_xCa_{1-x}MnO_3$ thin films on $LaAlO_3$ substrates[99]. The samples exhibited the desired magnetoresistive transition at $-73°$C.

Chapter 4

Deposition Parameters and Physical Characterisation

4.1 Introduction

The main purpose of this chapter is to understand the PLD process as it pertains to the deposition of $YBa_2Cu_3O_7$ thin films in our system. In Chapter 1 we introduced the physical properties of $YBa_2Cu_3O_7$, in Chapter 2 we introduced the experimental methods used to investigate certain physical properties of our deposited films, and in Chapter 3 we described the PLD system in detail.

In the present chapter we aim to answer the following questions:

1. Can $YBa_2Cu_3O_7$ thin films be successfully deposited using our PLD system, with a quality comparable to those quoted in literature?
2. What are the optimal deposition parameters for our system, and what are their influence on the composition and critical temperature of the films?
3. What characteristics of the ablation plume can we infer from deposited films?
4. Are our films epitaxial? Is there any preferred orientation for the a-axis relative to the substrate?
5. Does the PLD process introduce fragments on the film surface, and to what extent? Does the energy density influence the number density of deposited fragments?

The principal deposition parameters are laser energy density on the target, the substrate temperature during deposition, the ambient oxygen pressure and the target-substrate distance. Also of vital

importance is the post-deposition anneal in oxygen, which allows for the intake of oxygen in the film to produce the correct oxygen composition. The entire phase space of deposition parameters is very large and it would have been prohibitively expensive and time consuming to deposit a film with every possible variation of deposition parameters.

Thus, in the interest of time and cost, one had to be led by published results to focus attention on the deposition ranges known to produce the desired result of high critical temperature. This can unfortunately be misleading since not every PLD system behaves exactly the same, due to different gas flow dynamics inside the chamber, and a host of other factors, including differences in temperature measurement, differences in laser energy determination and laser spot size estimation, and differences in oxygen pressure measurement. These factors dictate that published results can at best be guidelines, and that the best deposition parameters for each new system must be discovered by trial and error. It is shown that high quality films of $T_c \gtrsim 89$ K can be deposited with the PLD system. *Inter alia*, the optimum deposition parameters of the PLD system are determined.

The spatial distribution of thickness and stoichiometry of depositants are investigated by Rutherford backscattering spectroscopy (RBS)[72]. In this way the deposition plume is characterised, to determine the maximum area that can be satisfactory deposited without having to resort to plume scanning techniques. The critical temperature of each film is determined either by resistivity or susceptibility methods.

The composition of deposited films is probed by RBS, and the spectra are analysed using the *RUMP*[73] package. Confidence intervals for the elemental ratio's are determined as highlighted in Chapter 2. $YBa_2Cu_3O_7$ is usually deposited with the c-axis pointing perpendicular to the film plane, i.e. the a/b-plane coincide with the film's deposition plane. The substrate materials MgO and $SrTiO_3$ are both cubic (see Chapter 1), and the deposition plane is the (001) plane, polished flat. In this orientation, the critical current parallel to the film surface is optimised. Substrates are selected where the lattice mismatch with YBCO in the orientation of the c-axis perpendicular to substrate surface is small — we used MgO, and $SrTiO_3$ to a lesser extend due to cost, all purchased from *Kristalhandel Kelpin*. Using x-ray diffraction spectroscopy (XRD), the orientation of deposited film are verified to be c-axis orientated.

It is well known that the critical current density j_c of YBCO films are optimal when there are no a-axis oriented material present. Misalignment of grains are also known to degrade the value of j_c, e.g. see [110]. Thus, two films were selected and sent to the *Max-Planck-Institut für Mikrostrukturphysik at Halle(Saale)* for detailed x-ray analysis. The orientation of the a- and b-axis with respect to the substrate is established, as well as the mosaic spread (scattering of the a-axis around it's ideal direction relative to the substrate).

Surface microtopography is investigated by atomic force microscopy (AFM) on a group of films prepared under similar deposition conditions, except for varying laser energy density. The AFM analysis was conducted at the *Institute for Polymer Science at the University of Stellenbosch.* Several surface features are investigated, particularly the presence of large blobs originating from the ablation target, and the presence of graininess indicative of the film growth mode.

Finally, by comparing the results of this study to that of similar studies in the literature, this investigation is placed in the context of current research in this field.

4.2 Overview of laser ablation physics

It is now an established fact that one of the spin-offs of the discovery of high temperature superconductors is the rapid development of pulsed laser deposition. PLD is recognised as one of the best ways to produce high quality thin film HTS materials, and deposited films are commercially available.

4.2.1 Initial deposition of $YBa_2Cu_3O_7$

The first reported depositions by PLD of $YBa_2Cu_3O_7$ was in 1987 by D. Dijkkamp *et al*[12] and X.D. Wu *et al*[13]. Dijkkamp *et al* reported the deposition of $YBa_2Cu_3O_7$ on $SrTiO_3$ and Al_2O_3 as substrates. They used Y-Ba-Cu-O pellets with nominal composition $YBa_2Cu_3O_{7-\delta}$ as targets, and focused a KrF excimer laser ($\lambda = 248$ nm) onto the pellets. The estimated energy density per pulse (Φ) on the target was 2 J/cm^2, during a high vacuum deposition ($\lesssim 10^{-6}$ mbar). As-deposited samples where brown and shiny, but electrically insulating. After the deposition the films were annealed in 1 atmosphere oxygen at 900°C for 1 hour, followed by slow cooling to room temperature. This resulted in oxygen take-up, producing the desired low resistance and superconducting transitions. Epitaxial, superconducting $YBa_2Cu_3O_7$ films are black and shiny. Films deposited on $SrTiO_3$ yielded $T_c = 90$ K, $\Delta T = 10$ K, while films on Al_2O_3 yielded $T_c = 85$ K, $\Delta T = 20$ K. The difference between the $YBa_2Cu_3O_7$ on Al_2O_3 and on $SrTiO_3$ is caused by the large lattice mismatch between the $YBa_2Cu_3O_7$ on Al_2O_3 (-20.1%) as compared to $YBa_2Cu_3O_7$ on $SrTiO_3$ (-1.3%). Both x-ray diffraction analysis and RBS channelling showed that $YBa_2Cu_3O_7$ on $SrTiO_3$ where highly $c-$axis orientated, while $YBa_2Cu_3O_7$ on Al_2O_3 showed no preferred orientation.[12, 13]

4.2.2 Laser ablation and plume formation

There exists a vast literature on the laser ablation and plume formation process, and in laser-solid interaction in general. This was initially driven by the discovery of laser induced annealing and similar types of laser processing in the semiconductor industry. Apart from PLD, parallel applications of laser

ablation of solids developed, namely laser ablation spectroscopy, used by geologists to determine the composition of mineral samples, and also by industrial scientists. It has even found application in the manufacturing industry, where it is installed in assembly and processing lines to perform quality control of processed materials such as sheet steel. A third application is in the medical field, where powerful lasers are used to ablate tissue, as in the case of eye surgery, or to remove blockages in veins via fiber optics.

A complete discussion of ablation processes is beyond the scope of this thesis, but a qualitative description is necessary to be able to discuss experimental results. The current overview is based on the review papers by D.H. Lowndes[111] and D.G. Geohegan[112]. The laser ablation process can be thought of a occurring in three time regimes:

1. The evaporation of surface layers during the early part of the pulse.
2. Absorption of the rest of the pulse energy by the continuously evaporating material, resulting in a sustained plasma and isothermal plasma expansion.
3. Highly anisotropic adiabatic expansion of the plasma.

The three regimes are discussed in turn:

Evaporation of surface layer

The interaction of a laser pulse with the target is primarily determined by the laser energy density. Two thresholds can be identified: the first is the threshold for laser ablation (the energy density where measurable material removal starts) and the plume formation threshold. The evaporation threshold can be understood by the exponential increase in the vapour pressure with temperature predicted by the Clausius-Clapeyron equation. At a certain laser energy density, the rapid laser heating rates ($\sim 10^{11}$ Ks^{-1}) overcome the thermal diffusion and radiation losses and evaporation proceeds nonlinearly. The evaporants consist of atoms, ions, molecules, clusters and fragments.

Plasma heating

Heating of the plasma is thought to occur via inverse-Bremsstrahlung absorption of the laser light in electron-ion pairs[113, 114]. Emission spectroscopy of plasmas during the initial expansion indicate typical temperatures of ~ 10000 K, well above the boiling points of most materials ($\lesssim 10000$ K). Thus, during a ~ 30 ns laser pulse, a high pressure ($\sim 10 - 500$ atm.) bubble of hot plasma is formed $\lesssim 50$ μm from the target.

Using time-of-flight mass spectroscopy, C.H. Becker *et al*[115] found that by increasing the laser fluence from 2.5 J/cm^2 to 4.3 J/cm^2 resulted in a marked decrease in clusters of size $\gtrsim$ 100 nm; at 4.3 J/cm^2 the amount was less than 10% of the number at 2.5 J/cm^2. This indicates that the intense focused excimer beam is very efficient in photodissociating the clusters to produce smaller mass ions.

Expansion of the plume

Forward directionality The expansion of the bubble produces a supersonic beam. It is important to have the correct picture of the shape of the plasma bubble the moment that the laser pulse ended. The transverse dimensions are given by the laser spot size (typically $2-3$ mm), but in the direction perpendicular to the target, the initial plasma dimensions are only tens of micrometers. Thus, the high temperature plasma would start expanding and since there are no impediments to move away from the target, the plasma rapidly expands in the forward direction, giving rise to the well known forward directed plume. Atoms and ions attempting to move parallel to the target would undergo frequent scattering, due to the high density of the material in the parallel direction. Thus, the plume rapidly expands away from the target, causing the characteristic forward peaking.

Angular distribution of ablated species The angular distribution of the source $f(\theta)$ of atoms in the plume is usually of the form

$$f(\theta) \propto \cos^p \theta. \tag{4.1}$$

This results in a film thickness profile of

$$T(\theta) \propto \cos^{p+3} \theta, \tag{4.2}$$

the extra $\cos^3 \theta$ resulting since the flux emitted into a solid angle element $d\Omega$ would be deposited on a substrate area element $dA = D^2 \frac{d\Omega}{\cos^3 \theta}$, D being the target-substrate distance[116]. A well established, but initially counter-intuitive result is that the film thickness profile $T(\theta)$, becomes more sharply forward peaked as the spot size increases. R.E. Muencheusen *et al*[117] pointed out that a large diameter laser spot and a smaller laser spot scanned over the same area result in different angular distributions, the large spot area giving rise to more forward peaked plume. This was indeed empirically confirmed with our apparatus. Also, less peaking can be achieved by focussing the beam sharper or by decreasing the oxygen pressure slightly. When depositing lead and tungsten, A.D. Akhsakhalyan *et al*[118] found that $p \sim 7$ when the spot size was ≤ 200 μm (diameter) while $p \sim 23$ when the spot size was increased to ~ 2 mm (diameter). Thus, if the focussed laser spot is initially longer in the horizontal direction, the film will be elongated in the vertical direction.

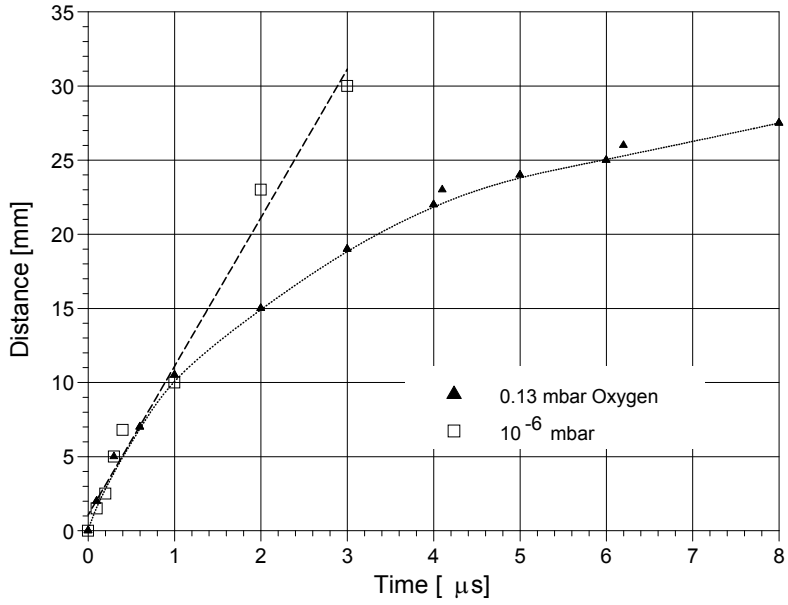

Figure 4-1: *Distance vs. time for the leading edge of the luminous plasma plume, measured along the normal to the YBCO target, in vacuum and in 0.13 mbar oxygen[119].*

Control of kinetic energy by gas-phase collisions In order to grow epitaxial thin films on crystalline substrates, the ablated species should have sufficient kinetic energy to break bonds in the surface layer to facilitate the formation of a crystalline structure at low substrate temperature. Where the substrate would allow heating to higher temperatures, without causing reaction with the ambient gas or the deposited species, the higher temperature would also facilitate the breaking of bonds necessary for the formation of an epitaxial layer. For example, at 680°C, good quality YBCO can be formed when the ablated species arrives with the correct kinetic energy, while at a substrate temperature of 780°C the kinetic energy of the depositants is less crucial.

At higher energies the ablated species can produce deeper lattice displacements, causing structural defects like excessive grain boundaries and misorientation in the film. The optimum kinetic energy appears to be $\leq$ 20 eV. Ambient gas, together with the substrate distance can be used to moderate the kinetic energy of the ablated species, via gas-phase collisions. At sufficiently high pressures, the gas-phase collisions completely thermalises the initial kinetic energy of the ablated material so that it is not delivered to the growing film surface.

Fig. 4-1 shows position (R) vs. time (t) for the leading edge of the plasma emission. D.B. Geohegan[119]

took fast CCD photographs of the expanding plume in vacuum and in 0.13 mbar of O_2. He found that the plume is initially ($t \leq 1$ μs) unaffected by the gas, but it slows down progressively. A *blast wave* model agrees well with the position at longer times, with $R = at^{0.4}$, ($a = 12.6$ mm$\cdot\mu$s$^{-0.4}$) with the range of the plume limited by attenuation.

4.2.3 Summary

Proper choice of pressure (P) and target-substrate distance (D) can accurately determine the kinetic energy of the arrived species, causing optimal growth conditions for the epitaxial film. Thus the overall picture is that a dynamic steady state exists during the laser pulse, in which a thin region of plasma just above the target surface continuously absorbs laser energy, while being fed evaporating material at its inner surface. The absorbed energy is converted into the thermal energy used for evaporation and the kinetic energy of the simultaneous outward plasma expansion. Activation energy for surface diffusion of deposited species is provided by kinetic energy, or by thermal energy via the heated substrate surface.

4.3 Influence of deposition parameters on film quality

4.3.1 Introduction

The electromagnetic properties of $YBa_2Cu_3O_{7-x}$ thin films strongly depends on the correct stoichiometry of the deposited layer. Incorrect stoichiometry leads to degrading or disappearance of the superconducting properties, e.g. [120]. Also, interaction of the deposited film with the substrate can compromise the superconductivity of the film.

4.3.2 Spatial distribution

Successful PLD is determined by the ability to reproduce the correct stoichiometry of the target at the substrate. Although it would seem that the property of congruent evaporation would virtually guarantee this, in reality, various secondary factors during deposition influence the outcome. One such factor is the pronounced forward peaking of the ablation plume as the atomic jet travels from the target to the substrate. The forward peaking causes the deposited layer to be thick in the middle, at the position closest to the ablated spot, thinning out towards the sides (assuming the substrate surface is parallel to the target surface).

Fig. 4-2 shows a photograph of the plume produced by a laser pulse. Clearly seen is the pronounced forward peaking due to the laser-target interaction and the shock wave nature of plume expansion in a

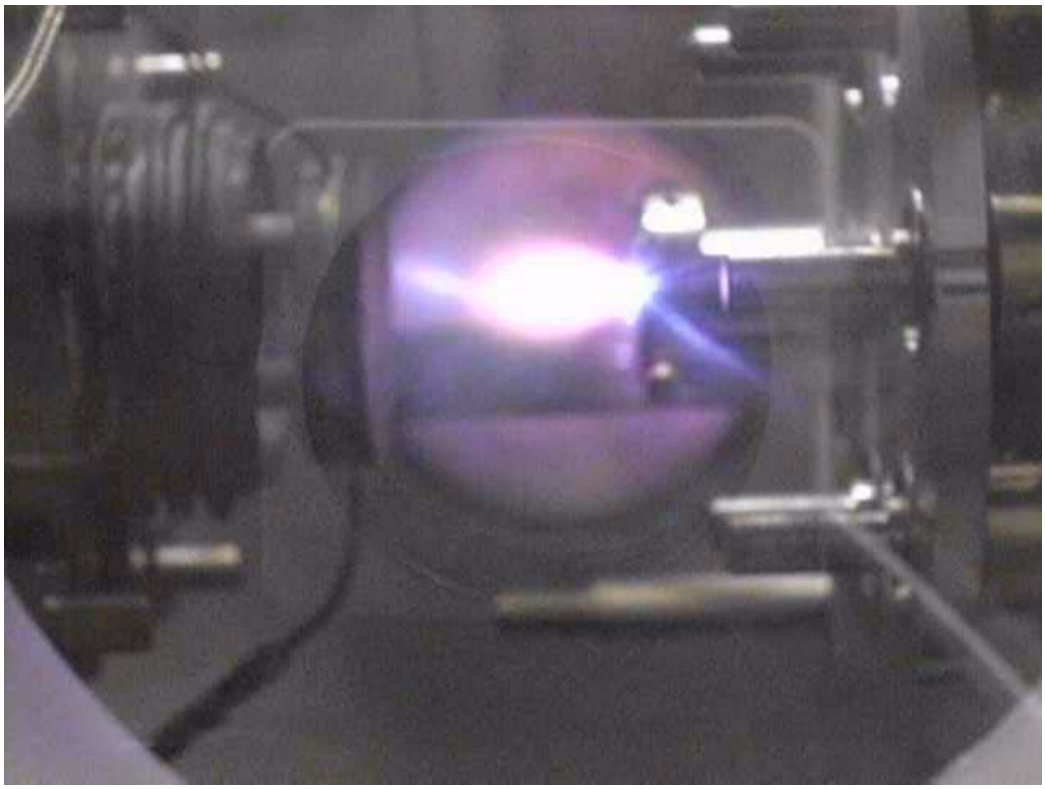

Figure 4-2: *Photograph of the plume produced by laser ablation of $YBa_2Cu_3O_7$ in a oxygen ambient of 0.3 mbar. The target holder is on the right and the substrate holder on the left.*

low pressure (0.3 mbar) ambient of oxygen. In this section the spatial distribution of the depositants is analysed.

Thickness and elemental distribution

The forward peaked plume produced by laser ablation causes the thickness of deposited films to be thinner towards the edges and thicker in the middle, as discussed in Section 4.2.2. An experiment was performed to establish the extent of the thickness and elemental distribution over a 20 × 20 mm area. In order to achieve proper separation of peaks with RBS, it was decided to deposit a very thin layer of $YBa_2Cu_3O_{7-x}$ on a large area SiO_2/Si substrate. This would result in a RBS spectrum with separated peaks for each cation in YBCO, and with the substrate peaks also far from the cation's peaks, due to the large difference in mass of Si and Cu, the lightest cation. The smoothness of the substrate would result in very sharp peaks. The amorphous SiO_2 buffer layer would prevent the YBCO from reacting with the Si substrate. A chemically inert buffer layer was necessary since YBCO is known to react with

Si[121]. A $400-500$ nm thick SiO_2 layer was formed by annealing a silicon wafer at 1000°C in a flowing oxygen ambient. The substrate was cut with a scribe, and de-greased in an ultrasonic bath using the following sequence of organic solvents: methanol, acetone, trichloroethylene, acetone, methanol and the deionised water.

YBCO was deposited on the 20×20 mm SiO_2/Si substrate at room temperature, with $P_{O_2} = 0.3$ mbar, the energy density at the target $\Phi = 3.4$ J/cm^2 and target-substrate distance $D = 35$ mm. The deposition oxygen pressure was chosen in the range of best film deposition. The deposition time was about 90 seconds, at a rate of 10 Hz, thus 900 pulses. The deposition rate at the centre was ~ 0.04 nm per pulse.

The thickness of the deposited film was determined by RBS. The sample was mounted on a goniometer-type sample holder in the RBS chamber. The sample was scanned in concentric circles with the radius being stepped from 0 to 10.5 mm in steps of 1.5 mm. The film was about 36 nm thick, so the RBS peaks were well separated. The RBS was performed in the usual geometry, using 3 MeV α-particles and an integrated charge of ~ 10 μC per spot. **Fig. 4-3(a)** shows the RBS spectrum of YBCO/SiO_2/Si at the centre of the deposition profile. **Fig. 4-3(b)** shows an enlargement of the RBS peaks of Y, Ba and Cu at the deposition centre and 10.5 mm from the centre (smaller peaks).

A very thin film generates a backscattering signal in the form of a Gaussian whose standard deviation is that of the system resolution. The area under each peak is proportional to the number of atoms per unit area and the scattering cross section of the element. The integrated yield Y of a element is given by

$$Y = n\Omega \frac{d\sigma}{d\Omega} Na \tag{4.3}$$

where n is the number of $\alpha-$particles is the RBS run, Ω is the scattering angle subtended by the detector, $d\sigma/d\Omega$ is the differential scattering cross section of $\alpha-$particles with the particular element, N is the number density per unit area of the element, and a is the area that the beam falls on. One can determine the experimental ratios Cu/Y and Ba/Y as follows:

$$\frac{N_{\mathrm{Ba}}}{N_{\mathrm{Y}}} = \frac{Y_{\mathrm{Ba}}(d\sigma/d\Omega)_{\mathrm{Y}}}{Y_{\mathrm{Y}}(d\sigma/d\Omega)_{\mathrm{Ba}}} \tag{4.4}$$

Using eq. 2.2, we calculated

$$\frac{(d\sigma/d\Omega)_{\mathrm{Ba}}}{(d\sigma/d\Omega)_{\mathrm{Y}}} = 2.0664 \tag{4.5a}$$

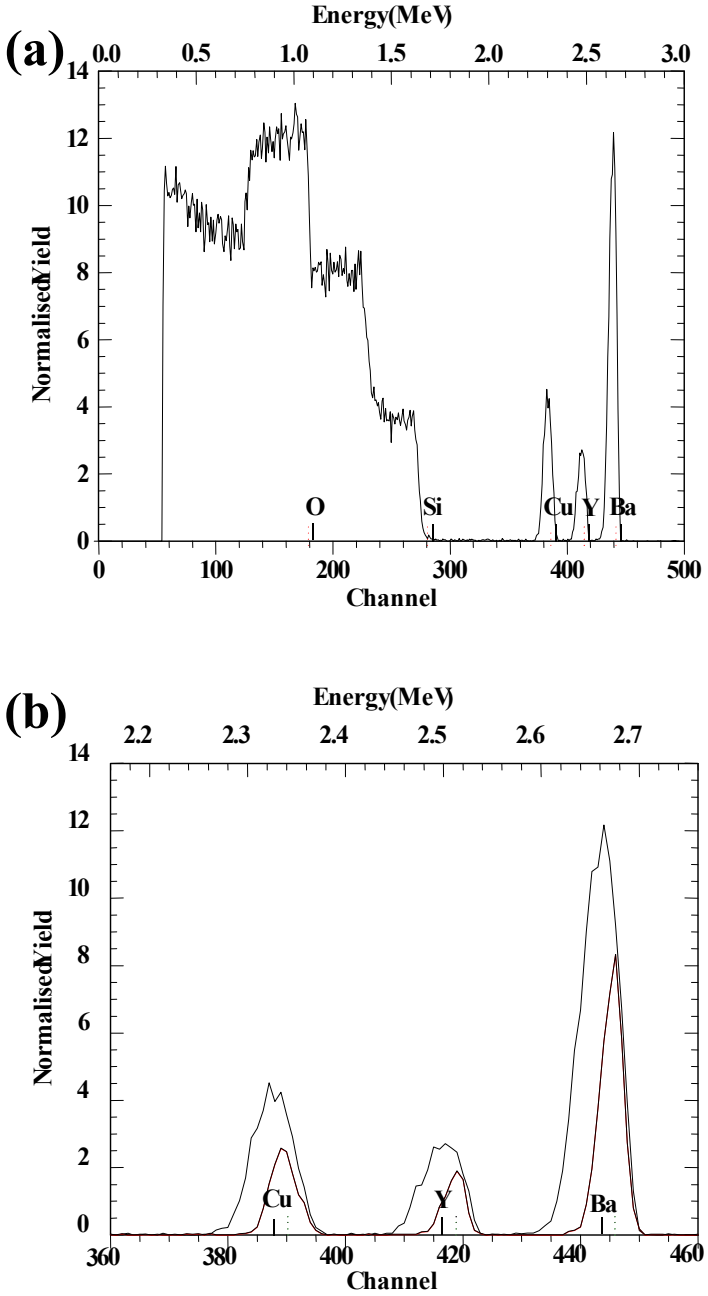

Figure 4-3: *(a) RBS spectrum of YBCO/SiO_2/Si at the centre of the deposition profile. (b) Enlargement of the RBS peaks of Y, Ba and Cu at the deposition centre and 10.5 mm from the centre (smaller peaks).*

$$\frac{(d\sigma/d\Omega)_{\mathrm{Cu}}}{(d\sigma/d\Omega)_{\mathrm{Y}}} \quad = \quad 0.5508. \tag{4.5b}$$

Using *RUMP*, the thickness is determined at the centre. By comparing the yield Y of each element at the centre to every other point, once can infer the thickness at each point as

$$d' = \frac{1}{3} \sum_{i \in \{\mathrm{Y,Cu,Ba}\}} \frac{Y_i'}{Y_i} d_0$$

Fig. 4-4 shows the thickness distribution (in nanometer) of the depositants on a large area silicon substrate. Clearly visible is the result of the forward peaking, namely a thick layer in the middle, becoming thinner to the exterior. The elongated shape of the deposition profile is due to the elongated shape of the laser beam - about 3 times longer than it's width. The plume tends to be more and more circular the narrower the beam is focused, thus because the vertical dimension is the narrowest, the plume tends to be more spread out in that dimension. This well documented phenomenon[116] is due to complex momentum transfer during the laser-solid interaction.

The exponents p from eq. 4.2 were determined for the horizontal and vertical directions. This was obtained by transforming the spatial coordinate to an angular coordinate by $\theta = \arctan(x/D)$, $D = 35$ mm and then performing least squares fits. The results are:

$$\begin{aligned} p_{horizontal}&: \quad 21.2 \\ p_{vertical}&: \quad 10.8. \end{aligned}$$

This corresponds with **Fig. 4-4** where the horizontal component is narrower that the vertical component. The values of the exponent p are within the range (6.0...22.0) quoted in the literature[116].

By utilising eqs. 5.7 and 4.5, the ratios $N_{\mathrm{Ba}}/N_{\mathrm{Y}}$ and $N_{\mathrm{Cu}}/N_{\mathrm{Y}}$ at all other points is calculated, and displayed in **Fig. 4-5.**

The arrival of $\alpha-$particles at the target surface is represented by a Poisson distribution. Using that model, the mean (expected value) of the ratio of the stochastic variables $Y \sim \mathrm{Poisson}(\theta)$ and $X \sim \mathrm{Poisson}(\lambda)$ is $E(Y/X) = \theta/\lambda$, and the variance is

$$\mathrm{var}\left(\frac{Y}{X}\right) = \frac{\theta}{(\lambda-1)^2}\left(\frac{\theta}{\lambda-1}+1\right), \tag{4.6}$$

θ and λ are the number of counts for each element in the ratio, i.e. the counts under each peak. **Fig. 4-5** shows the relative composition ratios along the (a) vertical and (b) horizontal axis of the deposition profile. The error bars indicates one standard deviation above and below each data point as determined by eq. 4.6. The wide error bars are resulting from low statistics. This indicates reasonably good stoichiometric ratios out to about 10 mm from the centre of the deposition profile. Clearly indicated

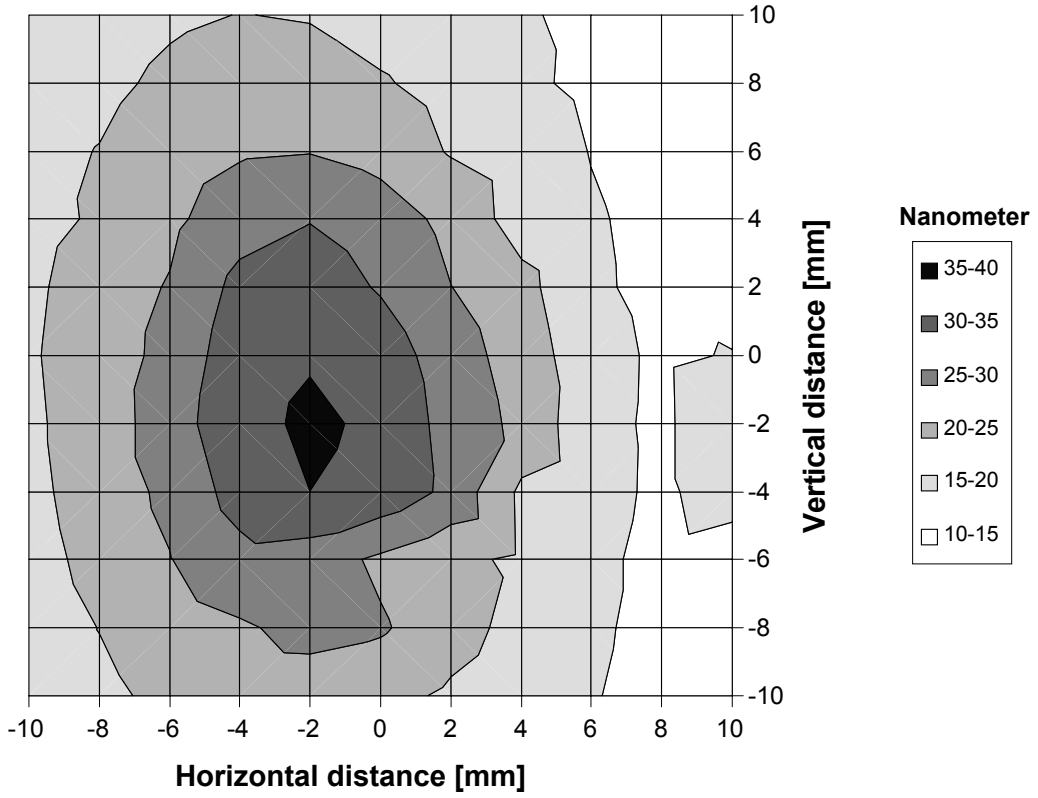

Figure 4-4: *The thickness distribution of YBCO deposited on a room temperature silicon substrate. Clearly visible is the result of forward peaking of the plume, namely a thick layer in the middle, becoming thinner to the exterior.* $P_{O_2} = 0.3$ *mbar,* $\Phi = 3.4$ J/cm^2 *and* $D = 35$ *mm.*

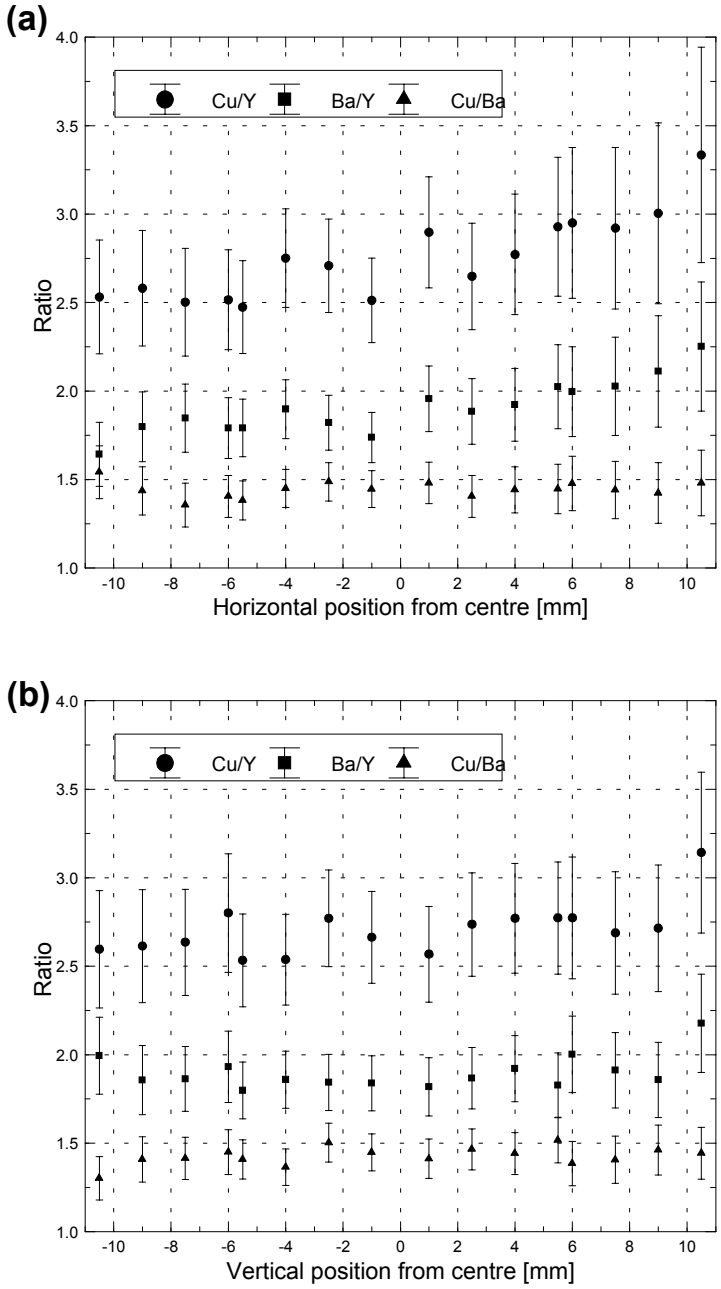

Figure 4-5: *The relative composition ratios along the (a) vertical and (b) horizontal axis on the deposition profile.*

on **Fig. 4-5** is the near perfect Cu/Ba ratio of 1.5 across the full extent (17° from the normal) of the sample. The Cu/Y and Ba/Y ratio indicates a Y-rich film, which could be explained in one of two ways. Either the laser energy density was not at the optimal value for correct stoichiometric deposition, or more likely, the target was eroded already, and was Y-rich, leading to slightly Y-rich samples. T. Venkatesan *et al*[15] also measured cation ratio's for YBCO deposited on silicon and found that the deposited layer became Y-rich towards wide angles ($\geq 20°$).

In conclusion, we have determined that the laser ablation process in our system delivers a highly forward peaked plasma plume, very similar to other systems as reported in the literature. The composition of the depositant is slightly Y-rich which could be due to an eroded target. Yttrium build-up in ablation targets is well known in the literature, eg. [122], and such targets needs to be resurfaced regularly. Most importantly, for our purposes, we can be sure that the system can deposit reasonable homogeneous samples over an area of 10×10 mm.

4.3.3 Important deposition parameters

As mentioned in section 4.2, PLD is a complex process, involving laser-solid and laser-gas interaction with various ramifications, the transport of an atomic beam through an ambient gas, and finally deposition and crystallisation of the atomic and molecular particles on the surface of a (usually) heated substrate. There are a number of deposition parameters which the experimentalist can vary to achieve the desired result. Deposition parameters such as laser energy density (Φ), laser wavelength(λ), substrate temperature (T_{dep}), substrate-target distance (D), oxygen partial pressure (P_{O_2}) can be changed independent of each other. When searching for the optimal deposition conditions for high quality $YBa_2Cu_3O_7$ thin film, the deposition parameters appear to be strongly correlated. Several investigators have studied the interdependence of these parameters in the deposition of $YBa_2Cu_3O_7$ thin films on MgO, $SrTiO_3$ and $LaAlO_3$ substrates. Consensus ranges for Φ, T_{dep}, D and P_{O_2}, has been published in the literature(e.g. [89, 90]), and are summarised below in **Table 4.1**:

Table 4.1: *Optimum range of conditions for the HTSC material YBCO.*

Laser energy density	2.5 - 3.5 J/cm^2
Laser wavelength	200 - 400 nm
Substrate temperature	680 - 780°C
Substrate-target distance	25 - 40 mm
Oxygen pressure	0.2 - 0.3 mbar

Analytical results by H.K. Sakeek *et al*[123] using energy dispersive x-ray spectroscopy showed that films placed beyond the tip of the PLD plume were Cu rich, while films had the correct stoichiometry

if placed within the plume or near the tip of the visible plasma plume. At the tip of the plume, the ejectants consists mainly of low velocity ($< 10^5$ cm/s) neutral oxide molecules and neutral atoms[124]. The length of the plume increases nonlinearly with energy density, thus a nonlinear $D - \Phi$ relationship exists for the optimal target-substrate distance; S.F. Xu *et al*[89] obtained the empirical relationship

$$(\Phi - \Phi_{th}) = D^2 \times 0.14 \text{ J cm}^{-4}, \tag{4.7}$$

where Φ_{th} is the laser ablation threshold of $YBa_2Cu_3O_7$, $\Phi_{th} \sim 1.0 - 2.0$ J cm^{-2}[125, 126]. Clearly the value of the constant on the right hand side of the eq. 4.8 must depend on P_{O_2}, and it corresponds merely to the best fit to data obtained by S.F. Xu *et al*[89]. Similarly H.S. Kim and H.S. Kwok[90] found an empirical relationship for P_{O_2} and D,

$$P_{O_2} D^2 = f(\Phi) \tag{4.8}$$

Thus one should decrease the target-substrate distance when the pressure is increased. This is reasonable since the plume becomes smaller when the pressure is increased. During routine depositions, it was observed that to maintain the plume length when increasing P_{O_2}, Φ must be likewise increased. Comparing Eqs. 4.7 and 4.8, the relationship

$$P_{O_2} D^2 = k(\Phi - \Phi_{th}) \tag{4.9}$$

is plausible, the constant k depending on parameters other than P_{O_2}, D and Φ. This phenomenological model is derived from the assumption that the best film is obtained at or near the plume tip. Increasing P_{O_2} would necessitate an increase in Φ to achieve optimal results by keeping the plume at the same length. Additional problems such as the transfer of fragments at high laser energy is not part of this model.

4.3.4 Film deposition

The aim of this study was not to explore functional relationships between the various deposition parameters in the fullest extend, since it would be prohibitively time consuming and costly, but to find the best deposition parameters for our PLD system. The studies mentioned above functioned as a guide to the optimisation process, but only a small subset of the parameter phase space could be explored. As a guide to the best oxygen partial pressure during deposition, the range $0.1 - 0.3$ mbar was used since the ablation plume appeared to be the brightest, signifying best reaction with ambient oxygen. The target-substrate distance was in the range $25 - 35$ mm, since the plume length was in that range,

Table 4.2: *Deposition conditions for sample 98-Apr-B.*

P_{O_2}	0.3 mbar
Φ	2.1 J/cm^2
T_{dep}	780°C
Thickness	355 ± 5 nm
Ba/Y	1.9 ± 0.2
Cu/Y	2.7 ± 0.2
$T_c(R = 0)$	85.5 K

depending on P_{O_2} and Φ. Most films used for this study were deposited for $5 - 20$ minutes with a laser pulse rate of 10 s^{-1}, yielding a film of thickness in the range $150 - 400$ nm. The deposition temperature was usually in the range $720 - 780$°C. Laser energy was $60 - 160$ mJ per pulse, and after attenuation by the optics and focussing, resulted in a energy density per pulse of $1 - 6$ J cm^{-2}, determined using the relation derived in Chapter 3. After deposition, films were annealed in 1000 mbar partial oxygen pressure at 490°C for 30 minutes, and allowed to cool in the same ambient.

Critical temperature was determined by resistivity or susceptibility measurement, as introduced in Chapter 2. To be able to meaningfully compare results when examining different films where different methods was employed to determine the critical temperature, we used the $T_c(R = 0)$ value extracted from resistive transitions and assumed it corresponds to the onset of superconductivity (finite j_c) as determined by susceptibility measurement, see **Fig. 2-13**.

Fig. 4-6(a & b) show the results of susceptibility and resistivity characterisation on a $YBa_2Cu_3O_7$/MgO (*sample 98-Apr-B*) film produced under standard conditions, given in **Table 4.2**.

The region close to the superconducting transition is shown in **Fig. 4-6(c)**. The resistive transition halfway at 86.5 K and the transition width (90/10) is 1.3 K. RBS measurements was performed using 3.0 MeV $\alpha-$particles.

Stoichiometry and thickness was determined by RBS, and crystallinity was checked by XRD with Cu$-K\alpha$-radiation, using the standard $\theta - 2\theta$ configuration. Shown in **Fig. 4-6(d)** is the measured RBS spectrum. The use of collimated beams of $\alpha-$particles of diameter 2 mm is fortunate, since fragments introduced by the deposition process can have no impact on the RBS spectra. The counts for this measurements was relative low, resulting in a relatively large amount of uncertainly in the peak heights. The peak heights are proportional to the surface density of atoms of the species in question, as indicated by eq. 2.7. The uncertainly in the actual composition derived from the *RUMP* fit can be determined by the range of the scatter of the peak heights, as described in Chapter 2. By again assuming a Poisson distribution for the RBS counts, one can estimate the uncertainty in composition determination by using eq. 4.6 applied on the peak heights. For the spectrum in **Fig. 4-6(d)** we have

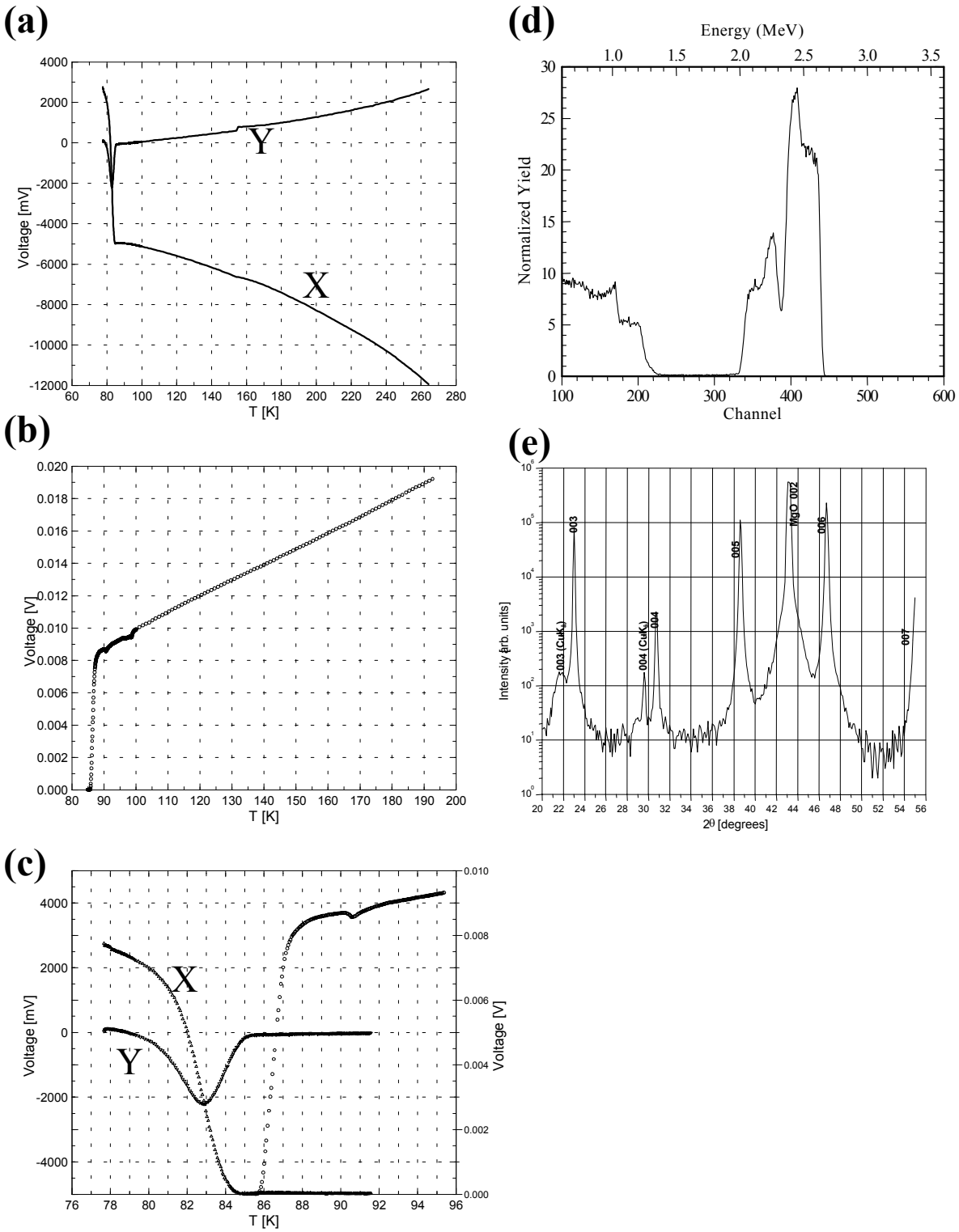

Figure 4-6: *Measurements performed on a $YBa_2Cu_3O_7$/MgO film produced under standard conditions: (a) Susceptibility measurement, (b) Resistivity measurement, (c) Susceptibility and resistivity data in the region of the superconducting transition, (d) RBS spectrum, (e) XRD spectrum.*

thus $YBa_{1.9\pm0.2}Cu_{2.7\pm0.2}O_{7-\delta}$, ratio's $1.0 : 1.9 \pm 0.2 : 2.7 \pm 0.2$, normalised to yttrium. The XRD spectrum on **Fig. 4-6(e)** indicates the presence of c-axis orientated material by the prominent $(00l)$ lines of $YBa_2Cu_3O_7$, and no significant evidence for other orientations can be found.

4.3.5 Influence of energy density on stoichiometry

The question whether the $YBa_2Cu_3O_7$ stoichiometry is dependent on laser energy density was examined. The rationale behind such a question is whether a similar problem exists as in the well known case for sputtering where there is selective sputtering of different elements in a composite sputtering target. Several films were deposited on MgO under identical conditions, except for a systematic change in energy density Φ from 1.6 J/cm^2 to 5.5 J/cm^2 at a deposition temperature of $T_{dep} = 780$°C and oxygen partial pressure $P_{O_2} = 0.2$ mbar. **Fig. 4-7(a)** shows that the correct Cu/Ba ratio of 1.5 could be consistently produced at $P_{O_2} = 0.2$ mbar for the whole range of Φ, but for Φ lower than 3.5 J/cm^2 the films were consistently slightly yttrium rich. At energy densities greater than 5 J/cm^2 the best results were achieved, yielding films with near perfect 1:2:3 stoichiometry.

4.3.6 Influence of deposition parameters on critical temperature

The influence of laser energy density Φ and oxygen partial pressure P_{O_2} on critical temperature was investigated. **Fig. 4-7(b)** shows the critical temperatures obtained at different values of Φ, compared with two other studies[89, 127]. The substrate temperature was $T_c = 780$°C, while $D = 35$ mm. P_{O_2} was varied, as indicated by marker shape. Films deposited with $P_{O_2} = 0.2 - 0.3$ mbar yielded higher T_c than films deposited with higher P_{O_2}. Films deposited with $\Phi = 2.0 - 4.5$ J/cm^2 yielded $T_c \geq 90$ K, while best film ($T_c \geq 87$ K) was achieved with $\Phi = 2.0 - 3.5$ J/cm^2 and $P_{O_2} = 0.2 - 0.3$ mbar. It is puzzling that the best film fall in the slightly Y-rich region according to **Fig. 4-7(a)** and no explanation can be offered. However, films with the worst stoichiometry, (Y-rich, $\Phi \leq 2$ J/cm^2) have a lower critical temperature $T_c \leq 87$ K. Films deposited at $P_{O_2} = 0.3$ mbar achieved highest T_c when $\Phi \sim 5$ J/cm^2, while the best films with $P_{O_2} = 0.2$ mbar was found using the lower $\Phi \sim 2 - 3$ J/cm^2. This seems to support eq. 4.9, where an increase in P_{O_2} calls for an increase in Φ to obtain the best film. The solid black curve indicate the "frontier" of best films obtained for various energy densities. High T_c (≥ 88 K) was achieved for a wide energy density range of $2.5 - 6.0$ J/cm^2. Too low energy density (≤ 2 J/cm^2) degrades the T_c, most likely due to non-stoichiometric film, as shown in **Fig. 4-7(a)**. Best stoichiometry was obtained above 5 J/cm^2, and those films had $T_c \geq 88$ K.

It must be taken into account that the measurement of energy density is rather difficult, making it hard to compare data from different studies. These references did not make mention of the precise way in which the energy density measurements were obtained, making comparison troublesome. The

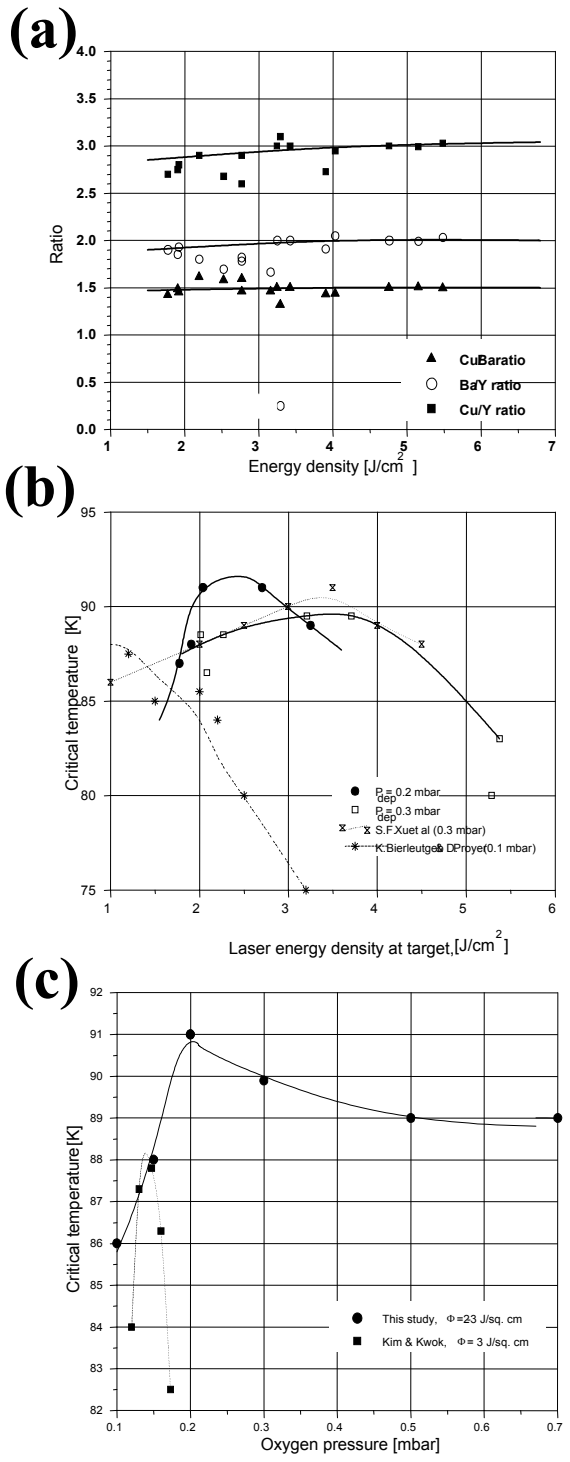

Figure 4-7: *(a) Cation ratios for films deposited with energy density* $\Phi \sim 1.5 - 6.5$ *J/cm*^{2}*. (b)* T_c *for laser energy ranging from* $1 - 5.5$ *J/cm*^{2}*. (c)* T_c *for oxygen partial pressure in the range* $0.1 - 0.7$ *mbar.*

consensus is that at $\Phi \geq 2.5$ J/cm^2 and $P_{O_2} \geq 0.2$ mbar critical temperatures close to or above 90 K can be achieved on MgO, $SrTiO_3$ and $LaAlO_3$ substrates.

Fig. 4-7(c) show the variation of T_c with P_{O_2} for films deposited with $D = 30 - 35$ mm, $T_{dep} = 740 - 780$°C and $\Phi = 2 - 3$ J/cm^2. Also shown is the result of a similar study by H.S. Kim and H.S. Kwok[90]. The present study shows that good film can be obtained using quite a wide range of P_{O_2}, while Kim and Kwok claim a narrow range of oxygen partial pressure. Although this study's data was selected from a group of films with a wider variation in deposition parameters, it can not explain the marked difference in the two sets of data.

Kim and Kwok[90] argue that best film is obtained when the atomic particles reach the substrate at a certain almost universal velocity. This velocity would be required for surface activation of the substrate. They pointed out that too fast ions and atoms can cause damage to the film. (Ba at 1.5×10^6 cm/s is 160 eV, which can cause sputtering damage.) Near the target, the plume species are fast ($> 10^6$ cm/s) and slow down as a function of target distance D. On the other hand, if the substrate is too far away, surface activation by moderately energetic ions and atoms will not possible. At the optimal distance, a decent flux of moderately energetic ions and atoms produce good quality films[128]. Kim and Kwok also invoke the *blast wave model* as used by Geohegan[119] to quantitatively motivate their scaling law for good film:

$$PD^2 = const. \tag{4.10}$$

This scaling law was derived from the assumption of an universal optimal atomic velocity for the plume shock wave to obtain best film. The reason why this study differs from Kim and Kwok[90] on the point of a very narrow range for P_{O_2} is the aspect of surface activation. Surface activation can be achieved in two ways, either by laser energy transferred to the plume species' kinetic energy, or by the temperature of the substrate.

Good film has been produced at low T_{dep}, but with the provision of high Φ. The alternative of high deposition temperature ($T_{dep} \geq 740$°C) seems to be at work here, making the effect of P_{O_2} much less pronounced; the system being much more forgiving for too low depositant kinetic energy if the surface activation energy supplied by virtue of surface temperature is sufficient.

4.3.7 Discussion

Several investigators have noted that when films are grown in an ambient gas at the lowest possible substrate temperature, an optimal target-substrate distance D exists for each deposition pressure P[111]. The example of YBCO on MgO deposited by Kim and Kwok[90] was mentioned earlier. They found that the best film deposited at $T_{dep} = 680$°C was obtained when P and D was related via a scaling

law, Eq. 4.8. Similarly W.P. Shen *et al* and Kwok[129] found optimal D for the deposition of epitaxial CdS films on InP(001) at 300°C in Ar ambient at various pressures $P = 0.01 - 0.26$ mbar. The film was characterised using x-ray rocking-curve measurements. Electrical resistivity was used to determined best film when depositing indium tin oxide at room temperature[130]. Resistivity was very sensitive to P, and low resistivity films were obtained only in a very narrow pressure range near 0.02 mbar. D.H. Lowndes[111] grew p-doped ZnTe films in ambient N_2 at 320°C and $D = 100$ mm, and observed a sharp peak in the hole mobility at a N_2 pressure of 0.07 mbar.

To understand these results qualitatively, one must invoke the concept of surface activation of atomic species. In the absence of a high substrate temperature, the incident species must have a certain kinetic energy to assist formation of the crystalline phase. The surface diffusion velocity is proportional to $\exp(-E_{acc}/kT)$, and when the surface temperature is too low, surface activation energy E_{acc} must be artificially lowered to break surface bonds. Too high energy atoms and ions (too low P or too small D) can cause damage by sputtering. Too low kinetic energy caused by too large D or too low P, will cause the atoms and ions to be fully thermalised by collisions and do not contribute sufficiently to surface bond-breaking or to activate diffusion.

J.P. Zheng and H.S. Kwok[130] showed that the electrical resistivity of indium tin oxide thin films is nearly independent of oxygen pressure when deposited at temperatures of $200 - 300$°C. Similarly high quality YBCO films can be grown at $T_{dep} = 750 - 800$°C for a broad range of oxygen pressures[111]. Thus, at high temperatures, the quality of PLD films becomes much less sensitive to the choice of pressure and target-substrate distance. Bonds can be broken and incident atoms can diffuse on the growing surface using only thermal energy. Consequently, at high deposition temperatures, a range of (P, D) values are expected to produce optimal film properties with properties degrading only when the PD product is too small[111].

4.4 Crystallinity and orientation of films

We have selected two films, one deposited on MgO and $SrTiO_3$ each as representative of our group of films. These films we sent for detailed analysis to the *Max-Planck-Institut für Mikrostrukturphysik in Halle(Saale)*. In particular, these films were investigated to determine the orientation of the a-axis with respect to the substrate. The deposition parameters, composition, thickness and critical temperature of the two films are given in **Table 4.3**.

Table 4.3: *Deposition parameters for samples 98-FEB-D and 98-JAN-A.*

Sample	98-FEB-D	98-JAN-A
Substrate	MgO	SrTiO3
T_c	88.0 K	89.5 K
ΔT_c	2 K	3 K
thickness	570 nm	220 nm
composition	1.0 : 2.0 : 3.0	1.0 : 2.0 : 3.0
T_{dep}	780°C	745°C
Φ	2.2 J/cm^2	6 J/cm^2
P_{O_2}	0.15 mbar	0.4 mbar
D	36 mm	26 mm

4.4.1 $YBa_2Cu_3O_7$ film on MgO

The film used for the detailed XRD study was representative of the YBCO/MgO samples, and it's critical temperature was $T_c = 88.0$ K as determined by susceptibility measurement. This film was 570 nm thick as determined by RBS and the deposition parameters are given in **Table 4.3***(98-FEB-D).*

Fig. 4-8 shows the $\theta - 2\theta$ scan of the film. All the $(00k)$ reflections are visible, as well as the (002) and (004) reflections of MgO, the odd reflections being extinct. No other peaks are visible, indicating than there are no randomly orientated impurity or superconducting phases. Also shown is a low incidence angle ($\omega = 5°$) scan to determine the amount of misorientation present in the film. The scattering angle 2θ, was varied from 5° to 80°, while the incidence angle ω was kept fixed at 5°. **Fig. 2-3(a)** indicates the angles involved. Four peaks are visible in the low angle region ($5° - 25°$), originating from grains tilted 5° to the sample surface. The identified peaks are given in **Table 4.4**:

Table 4.4: *Peaks indentified in low angle diffraction.*

$\boldsymbol{\omega}$	$\boldsymbol{2\theta}$	**plane**
5°	7.6°	(001)
5°	10.9°	unknown
5°	15.1°	(002)
5°	23.2°	(100)

If all the grains were c-axis orientated, these planes would not have been observed, thus there is a small amount of misaligned material present; comparing the intensities of the (001) reflection in the Bragg-Brentano measurement with the low angle scan suggests that about 2.5% of the material in the YBCO film can be misaligned. The c-lattice parameter can be determined from the position of the various peaks, by applying Bragg's law,

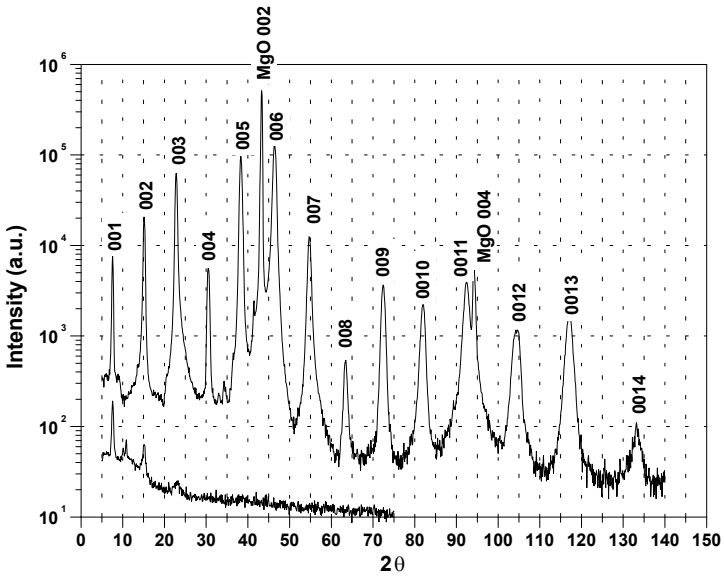

Figure 4-8: $\theta - 2\theta$*-scan of 570 nm YBCO on MgO. All the* $(00k)$ *reflections are visible* $(k = 1 - 14)$*, as well as the* (002) *and* (004) *reflections of MgO. Also shown, in the lower left-hand corner, is a low angle* $(\omega = 5^\circ)$ *scan to determine the amount of misorientation present in the film.*

$$2 \sin \theta d = n\lambda \tag{4.11}$$

for each reflection and calculating the average distance d. Thus $d = 1.172 \pm 0.003$ nm; there is a stretching of 0.3%, if we assume an equilibrium value of $c = 1.1676$ nm.

A rocking curve scan (**Fig. 4-9**) was performed to determine the spread in the c-axis orientation. This measurement determines the presence of grains that are not perfectly aligned with their c-axis normal to the film surface. For the (005) peak the XRD system was first brought into the $2\theta = 38.6^\circ$ position in the $\theta - 2\theta$-configuration. $(\omega = 19.3^\circ)$. Then the sample was rocked, changing ω from 17°to 21.5°, while keeping the source and detector stationary. This reveals a peak at $\omega = 19.5^\circ$, with $FWHM$ (full width at half maximum) of 0.83°. The $FWHM$ of rocking curves versus $FWHM$ of θ (not 2θ) in Bragg-Brentano measurements for the two peaks involved are shown in **Table 4.5**.

In both cases the $FWHM$ of the rocking curve is 0.5° larger than the $FWHM$ (θ) of the Bragg-Brentano measurements. This indicates that the extra 0.5° must be originating from slightly misaligned grains. This 0.5° spread is not surprising, given the rather large lattice mismatch of $YBa_2Cu_3O_7$ with MgO (8.8%).

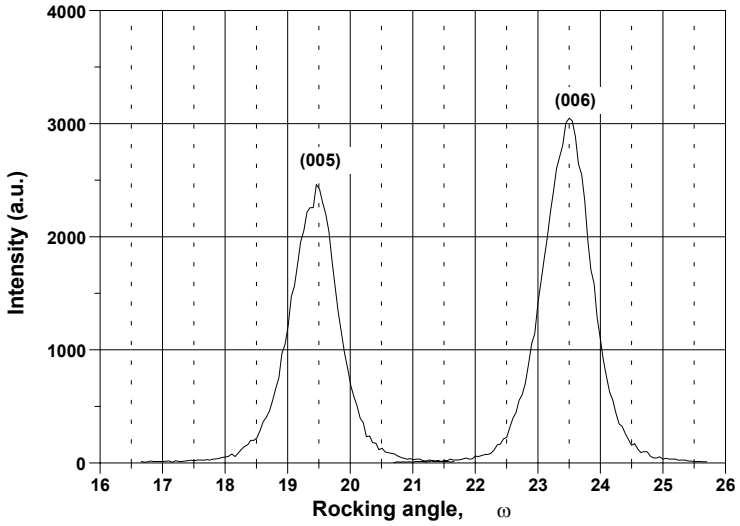

Figure 4-9: *Rocking curve scans of the YBCO* (005) *and* (006) *peaks for the* $YBa_2Cu_3O_7/MgO$ *sample. The FWHM for the peaks was 0.83° and 0.90° respectively.*

Table 4.5: *The* FWHM *of rocking curves versus* FWHM *of* θ *in Bragg-Brentano measurements.*

FWHM	**rocking curve ω**	**Bragg-Brentano θ**
(005)	0.8°	0.3°
(006)	0.9°	0.4°

4.4.2 $YBa_2Cu_3O_7$ film on $SrTiO_3$

Bragg-Brentano measurement of the $YBa_2Cu_3O_7$ film

The film used for the detailed XRD study were representative of the YBCO/$SrTiO_3$ samples, and it's critical temperature and transition width was $T_c = 89.5$ K and $\delta T = 1.5$ K respectively as determined by resistivity measurement. This film was 220 nm thick as determined by RBS. The deposition parameters for the film is summarised in **Table 4.3***(98-JAN-A)*. $YBa_2Cu_3O_7$ and $SrTiO_3$ has an extremely close lattice match of -1.3%. This influences the quality of the superconducting film, resulting usually in films of high critical temperature, narrow transition width and high critical current density. **Fig. 4-10**, a $\theta - 2\theta$-scan of YBCO/$SrTiO_3$ structure clearly indicates the close lattice match of YBCO with $SrTiO_3$. The close lattice match, together with the fact that $SrTiO_3$ is cubic, causes the $SrTiO_3(00l)$ reflections to coincide with the $(00, 3l)$, $(h00)$ and $(0k0)$ reflections of YBCO, at least in the lower orders. This is

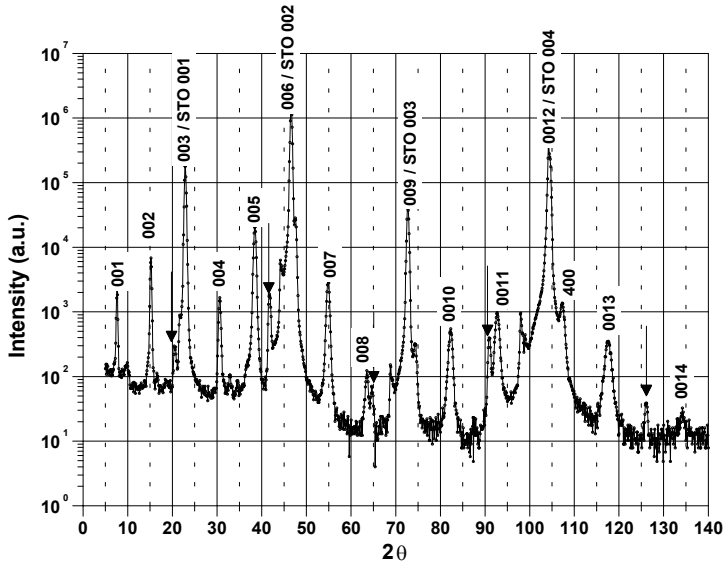

Figure 4-10: *Bragg-Brentano measurement of 220 nm YBCO on $SrTiO_3$. All the YBCO*(00k) *reflections are visible, as well as the* (00k) *reflections of $SrTiO_3$. This indicates that the majority of the material formed an epitaxial layer on the substrate. The $Cu_{K\beta}$ lines are indicated by arrows. Their indices are* (001) *to* (005).

shown in the figure and summarised in **Table 4.6**.

As in the case with YBCO/MgO, all the (00l)-lines are visible ($l = 1..14$), indicating that the YBCO grew predominantly c-axis orientated. The figure indicates some a-axis orientation through the presence of the YBCO(400) line in the spectrum at $\sim 107°$ (see **Fig. 4-10**). Using Bragg's law, a c-parameter of 1.170 ± 0.003 nm can be calculated from the figure; resulting in a stretching of 0.3% compared to the 0.5% in the case of MgO. This stretching is marginally less than the MgO case, indicating a less stressed film. In **Fig. 4-10** the (001)...(004) reflections of $SrTiO_3$ coincide with the YBCO (003), (006), (009) and $(00, 12)$ reflections respectively. Also visible is the Cu-Kβ lines on the smaller angle sides of $SrTiO_3$ (00l), indicated by arrows. The Cu-Kβ lines are tabulated in **Table 4.7**. In **Fig. 4-11** the YBCO (0012) and the $SrTiO_3$ (004) peaks are clearly separated.

A ϕ-scan and pole figure plot of the $YBa_2Cu_3O_7$ film

As discussed above, the film is dominated by c-axis orientated matter, with a trace of a/b-axis orientation, perceived via the presence of the (400)-line at $\sim 107°$ in **Fig. 4-10**. One would expect, due to the close lattice match of YBCO with the $SrTiO_3$ single crystal substrate, that the film grains would be closely

Table 4.6: *The* $(00l)$ *reflections of various substrates.*

Planes	**MgO (2θ)**	**$SrTiO_3$ (2θ)**
001	extinct	22.783°
002	42.953°	46.485°
003	extinct	72.545°
004	94.151°	104.154°
lattice parameter	0.42112 nm	0.39050 nm
powder diffraction file	45-0946	35-0734
lattice mismatch μ	-8.8%	-1.3%

Table 4.7: $Cu_{K\beta}$ $(00l)$ *reflections of* $SrTiO_3$.

$SrTiO_3$	**$Cu_{K\beta}$ lines (2θ)**
001	20.537°
002	41.773°
003	64.658°
004	90.966°
005	126.075°

aligned with the substrate surface. The substrate presents a square grid surface to the YBCO material during deposition, and it is to be expected that the a/b axis would align precisely on the square grid.

To check that this is indeed the case one needs to look beyond the basic $\theta - 2\theta$ analysis. The position of a $YBa_2Cu_3O_7$ crystal plane not parallel to the film surface would reveal the direction of the a/b-axis. The a- and b-axis are used here interchangeably, since their lattice constants are very close, make distinction unnecessary when talking about orientation of the a/b-axis on the substrate surface. A "diagonal" plane such as (102) has an a-axis component. The significance of this plane lies in the fact that it's orientation would reveal the direction of the a-axis. The procedure is as follows: Initially the XRD system assumed the $\theta - 2\theta$-configuration for the (102) peak ($2\theta = 27.898°$). The film is then tilted an angle $\psi_{(102)}$ (see **Fig. 2-3(b)**) from the horizontal to bring the (102) plane into the reflection plane. Finally, the film is rotated through $\phi = 90°$ around an axis $\mathbf{n}_{(hkl)}$ normal to the film surface to locate the (102)-reflection. This would reveal the distribution of the a-axis orientation. The angle between the normal of the film surface and a normal on the (102) plane had to be calculated. In general, a normal vector on the (hkl) plane for a orthorhombic crystal is given by

$$\mathbf{n}_{(hkl)} = \frac{bc}{kl}\hat{\mathbf{x}} + \frac{ca}{lh}\hat{\mathbf{y}} + \frac{ab}{hk}\hat{\mathbf{z}}. \tag{4.12}$$

The angle $\psi_{(hkl)}$ between the c/z-axis and the vector $\mathbf{n}_{(hkl)}$ is thus given by

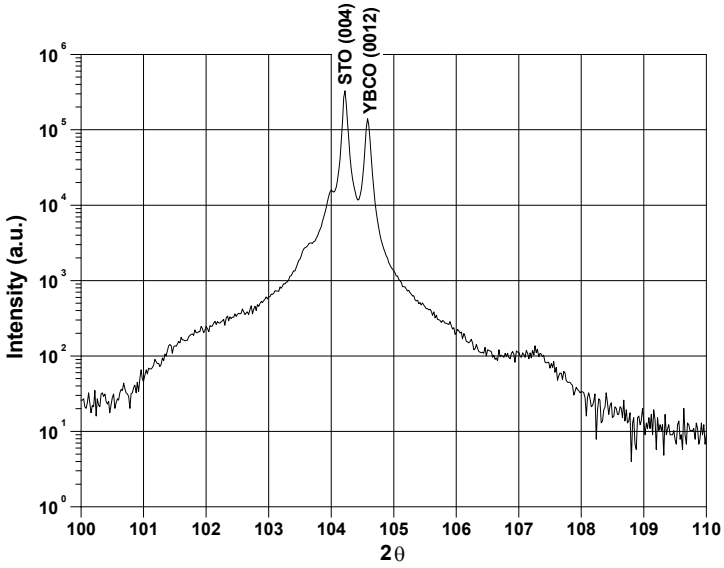

Figure 4-11: *Separation of the $YBa_2Cu_3O_7(0012)$ and $SrTiO_3(004)$ peaks.*

$$\cos\psi_{(hkl)} = \frac{\mathbf{n}_{(hkl)}\cdot\hat{\mathbf{z}}}{n} = \frac{\frac{ab}{hk}}{\sqrt{\left(\frac{bc}{kl}\right)^2 + \left(\frac{ca}{lh}\right)^2 + \left(\frac{ab}{hk}\right)^2}}. \tag{4.13}$$

This yields

$$\psi_{(102)} = 56.73^\circ. \tag{4.14}$$

Fig. 4-12(a) is a ϕ-scan on the YBCO (102) peak. The *FWHM* is 1.1°, indicating that the film is not only c-axis orientated, but that those matter with c perpendicular to the substrate surface have their a/b axis pointing in the same direction, and there are very little or no random component present (peak to noise ratio $\simeq$ 200). To determine whether some of superconducting material is a/b axis orientated, a second ϕ-scan on the YBCO (102) peak was conducted, with $\psi^*_{(102)} = 90^\circ - 56.73^\circ = 33.27^\circ$. This peak is 25% of the height of the peak for the c-axis orientated material, and the *FWHM* is 1.7°. Both peaks occur at the same angle ($\phi \sim 67^\circ$), indicating that c- and a-orientated material are closely related to each other in nucleation and growth orientations. Judging from the peak heights, there are at least 5 times more c-orientated matter in the film than a/b-orientated matter.

Fig. 4-12(b) is a pole figure plot of the YBCO film. The angle ϕ was scanned as in the ϕ-scan graph, but through the full 360°, while ψ was scanned from 0° to 90°. Clearly visible is the four $\psi_{(102)} = 56.73^\circ$ peaks, each paired with one of four smaller $\psi^*_{(102)} = 33.27^\circ$ peaks. The peaks represent the four possible

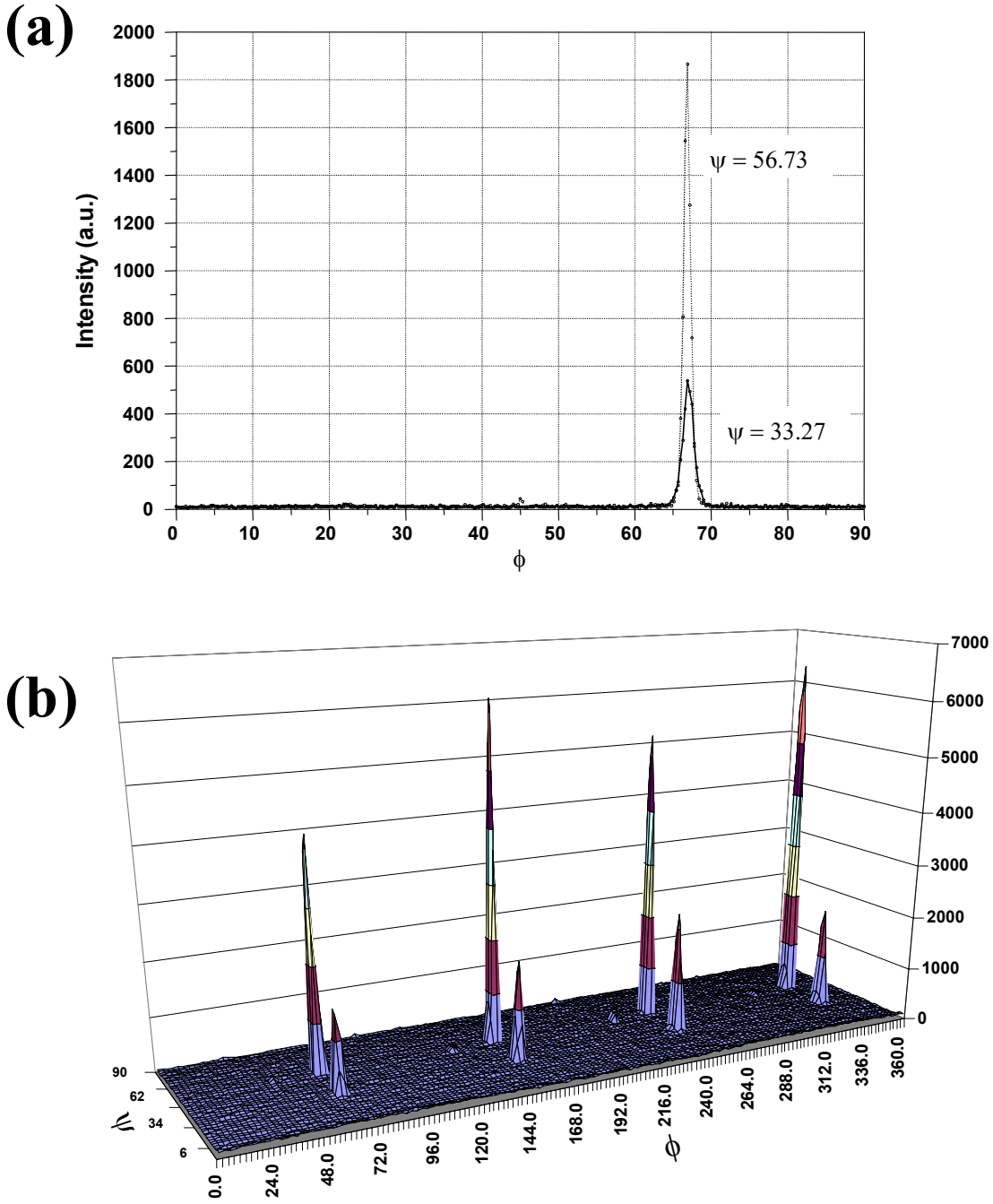

Figure 4-12: *(a) ϕ-scan of the YBCO* (102) *plane. Indicated are the peaks produced by the two orientations : the $\psi_{(102)} = 56.73°$ for c-axis orientated matter and the $\psi^*_{(102)} = 90° - 56.73° = 33.27°$ for a/b-axis orientated matter. (b) Pole figure plot of the $YBa_2Cu_3O_7/SrTiO_3$ sample. Indicated are the azimuthal angle ϕ and the pole distance angle ψ.*

Table 4.8: *The* FWHM *of the poles in the ψ- and ϕ-directions.*

	***c*-orientation**	***a*/*b*-orientation**
ϕ	1.1°	1.7°
ψ	5.9°	4.8°

manifestations of the {102}-family of planes, separated 90° from each other. The *FWHM* of the poles in the ψ- and ϕ-directions are shown in **Table 4.8**.

The film is thus highly textured, it's grains perfectly aligned according to the crystal directions of the $SrTiO_3$ substrate. Furthermore, one can conclude that the larger spread in ψ indicates that the grains show a larger vertical misorientation than a horizontal misorientation.

4.4.3 Discussion

Detailed x-ray analysis of two representative samples (YBCO/MgO and YBCO/$SrTiO_3$) were performed. Bragg-Brentano measurements on both samples revealed almost exclusively $(00l)-$lines, indicating $c-$axis oriented film, with little evidence for misorientation of grains. A glancing angle scan on the YBCO/MgO sample further revealed an almost complete absence of randomly aligned YBCO grains. Rocking curve scans on the YBCO/MgO sample using the (005) and (006) lines showed that the $c-$axis spread is quite narrow, of the order of 0.5°. The YBCO/$SrTiO_3$ sample revealed similar features.

A $\phi-$scan of the YBCO/$SrTiO_3$ sample showed that the orientation of grains are not random, but in fact very tightly determined by the substrate, with a *FWHM* of the peak 1.1°. This indicates very highly textured film, with almost perfect epitaxy. A pole figure scan confirmed this conclusion.

4.5 Surface morphology of films

It is well known that quality epitaxial $YBa_2Cu_3O_7$ thin films on suited substrates such as MgO, $SrTiO_3$, $LaAlO_3$ and the like are characterised by shiny, black surfaces, while non-superconducting films are dull, and usually brownish in colour. While the reason for this distinction is well known, as evidenced by x-ray spectroscopy of the films, it was thought to be worthwhile to determine the extend of smoothness of the superconducting films, and likewise the extend of roughness of the non-superconducting films.

Furthermore, PLD is known to introduce boulders to the surface of deposited films, as discussed in Chapter 1. The extend of this by-product of PLD can be characterised by high-resolution surface profilometry, which atomic force microscopy (AFM) provides. It is important to discover whether the density of these boulders can be reduced by varying the laser energy density, or other deposition parameters. Thus the influence of PLD conditions can by correlated with surface morphology.

AFM can also help is distinguish between surface roughness introduced by the deposition process and that which is introduced by the film growth process. This can aid to construct a link between surface morphology, critical temperature and composition. Finally, an AFM study can also shed light on the nucleation and growth mechanisms of thin film $YBa_2Cu_3O_7$.

4.5.1 Atomic force microscopy of the films

Films were prepared under identical conditions ($T_{dep} = 780°C$, $D = 35$ mm, $P_{O_2} = 0.2$ mbar) except for the laser energy density which was stepwise increased from 2 J/cm^2 to about 4 J/cm^2.

The film thickness was about 400 nm. The films were superconducting with $T_c = 84 - 90$ K. Their composition was very close to the ideal 1.0 : 2.0 : 3.0 of $YBa_2Cu_3O_{7-\delta}$. A film was also deposited at $T_{dep} = 680°C$ to manufacture a control sample which would be non-superconducting, called sample B. AFM scans were made at various random positions on the film to obtain representative information; scan sizes ranged from 100×100 μm down to 5×5 μm.

All the superconducting samples presented AFM images which were very similar in character. In fact, the only quality where these films differ is regarding the number of fragments originating from the deposition process — a topic discussed later in section 4.5.2. A superconducting sample is selected as representative, called sample A. **Figs. 4-13 & 4-14** show 100×100 μm and 20×20 μm AFM images of sample A.

Clearly visible is a very flat background surface with pronounced almost half spherical boulders present on the film. **Figs. 4-15 & 4-16** show similar sizes of images for sample B.

In striking contrast to sample A, the surface of the non-superconducting sample B have a course, granular appearance. Similar boulders to sample A is present in sample B. Evidently then, these boulders are an artifact of the deposition process and it is unlikely that it result from the film growth process, since they are present in more or less equal quantities on both superconducting and non-superconducting films. Visual inspection of **Figs. 4-13, 4-14, 4-15 and 4-16** reveal the presence of micron-sized boulders on a flat or grainy background.

Films were prepared at 780°C and 600°C, and their surfaces were investigated using AFM. **Figs. 4-13 & 4-14** show a superconducting film grown at 780°C, of magnified areas 100 μm $\times$ 100 μm and 20 μm $\times$ 20 μm respectively, while **Figs. 4-15 and 4-16** show a non-superconducting film grown at 600°C. These representative films will be referred to as sample A (superconducting) and sample B (non-superconducting) through out this section. Qualitatively, the AFM images of the superconducting and non-superconducting films appear very different. The first set of images appear relatively flat with some large boulders, while the non-superconducting films have a course, granular appearance. This reflects the different growth conditions and will be discussed in the next section. The area parameters

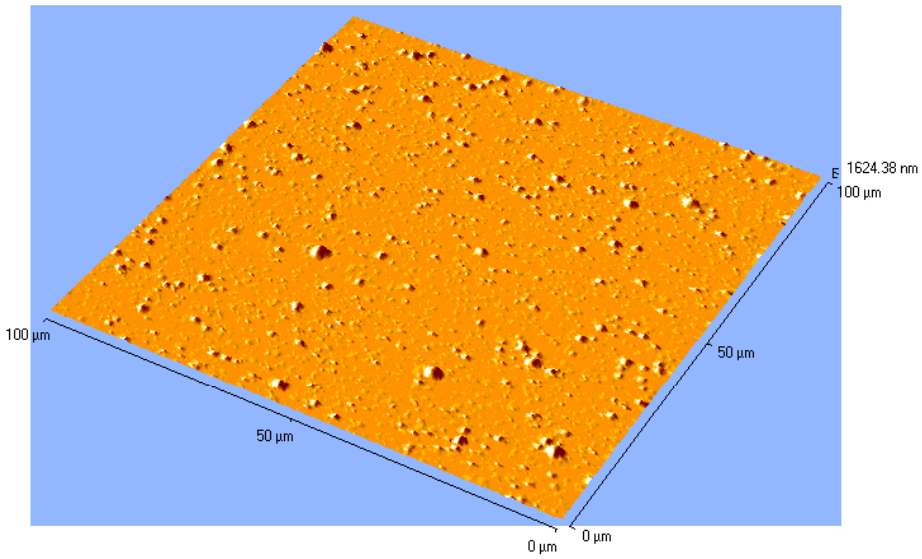

Figure 4-13: *Sample A :* 100 $\mu m \times 100\ \mu m$ *AFM image of a superconducting YBCO film deposited at* 780° *C.*

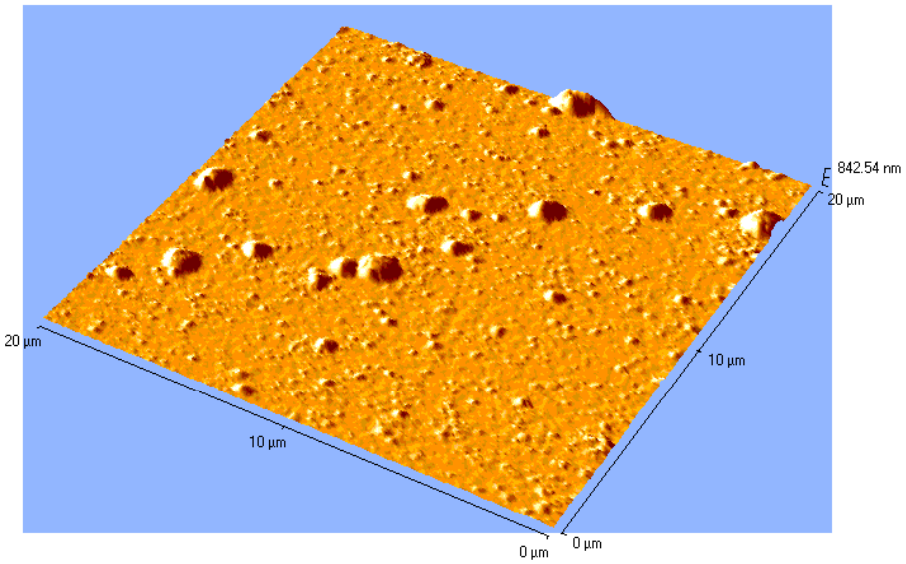

Figure 4-14: *Sample A :* 20 $\mu m \times 20\ \mu m$ *AFM image of a superconducting YBCO film deposited at* 780° *C.*

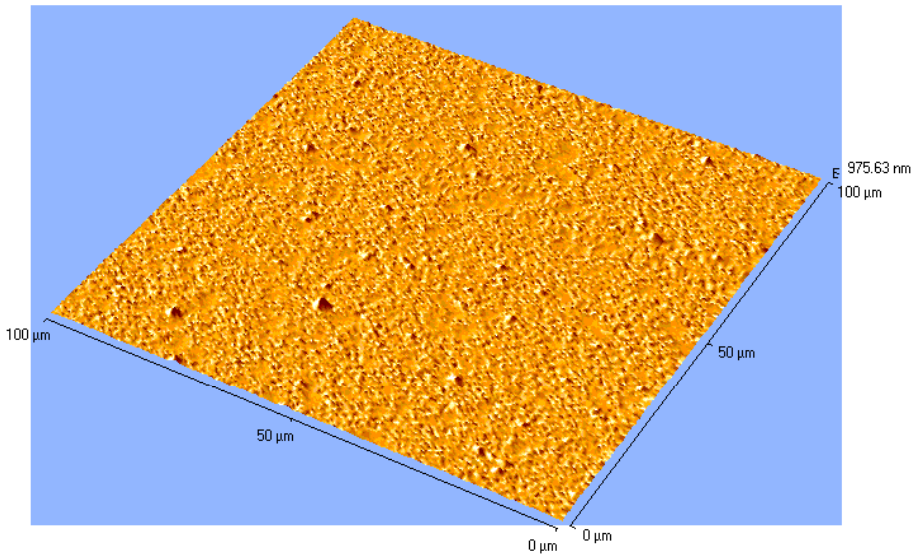

Figure 4-15: *Sample B :* 100 $\mu m \times 100$ μm *AFM image of a non-superconducting YBCO film deposited at* 600° *C.*

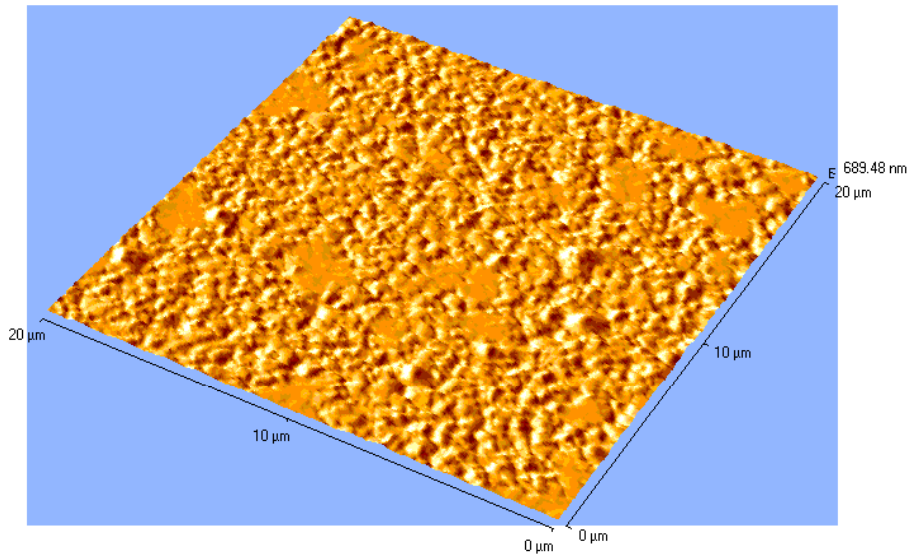

Figure 4-16: *Sample B :* 20 $\mu m \times 20$ μm *AFM image of a non-superconducting YBCO film deposited at* 600° *C.*

Table 4.9: *Deposition parameters and area parameters of the samples used in the comparative AFM study.*

Quantity	**A : Superconducting**	**B : Non-superconducting**
T_{dep}	780°C	600°C
P_{O_2}	0.2 mbar	0.2 mbar
D	35 mm	35 mm
Φ	2-4 J/cm^2	3 J/cm^2
Roughness R_a	14 nm	84 nm
Roughness R_{RMS}	29 nm	118 nm
Surface ratio	1.02	1.32

are summarised in **Table 4.9**. Surface ratio is the measured surface area divided by the projected area, this is another measure of the surface roughness. Contactless, interferometric measurement of the microtopography of the MgO substrate (by the manufacturer) used in this study revealed that the substrates were extremely smooth. The substrates surfaces' were flat to a specification of 1 μm across a 2 inch diameter. The roughness parameters are given in **Table 4.10**[131].

Table 4.10: *Substrate roughness parameters.*

Quantity	**MgO**
R_a	0.163 nm
R_t	1.330 nm
R_{RMS}	0.207 nm

The deposited films are thus about two orders of magnitude rougher than the original substrates. The roughness parameter of sample A is $R_a = 14$ nm. This means that roughly 66% of the surface positions are not higher or lower than the mean surface height by more than 14 nm. The equivalent parameter for the starting substrate is around 0.16 nm, indicating a hundredfold increase in roughness. Using the AFM images, it was determined that the globules vary from 500 nm to 1500 nm in diameter, and 100 nm to 400 nm in height. The density of particles vary between 10000 per mm^2 and 70000 per mm^2. Line analysis was also done for both samples A and B (**Figs. 4-17, 4-18, 4-19 & 4-20**).

Line analysis is a very good way to determine the size of various features on the surface, such as the boulders seen in **Figs. 4-13 & 4-14**. The line analysis of sample A deposited at 780°C, **Fig. 4-13** shows the cross-section of boulders/globules and one can determine their dimensions to high accuracy. The typical boulder is about $200 - 1000$ nm in height and about $500 - 2000$ nm wide. It is a rounded hump on the surface, and it is unlikely to be caused by normal film growth phenomenon of grain growth and coalescence. Apart from the large boulders, do the surface features of the superconducting sample appear

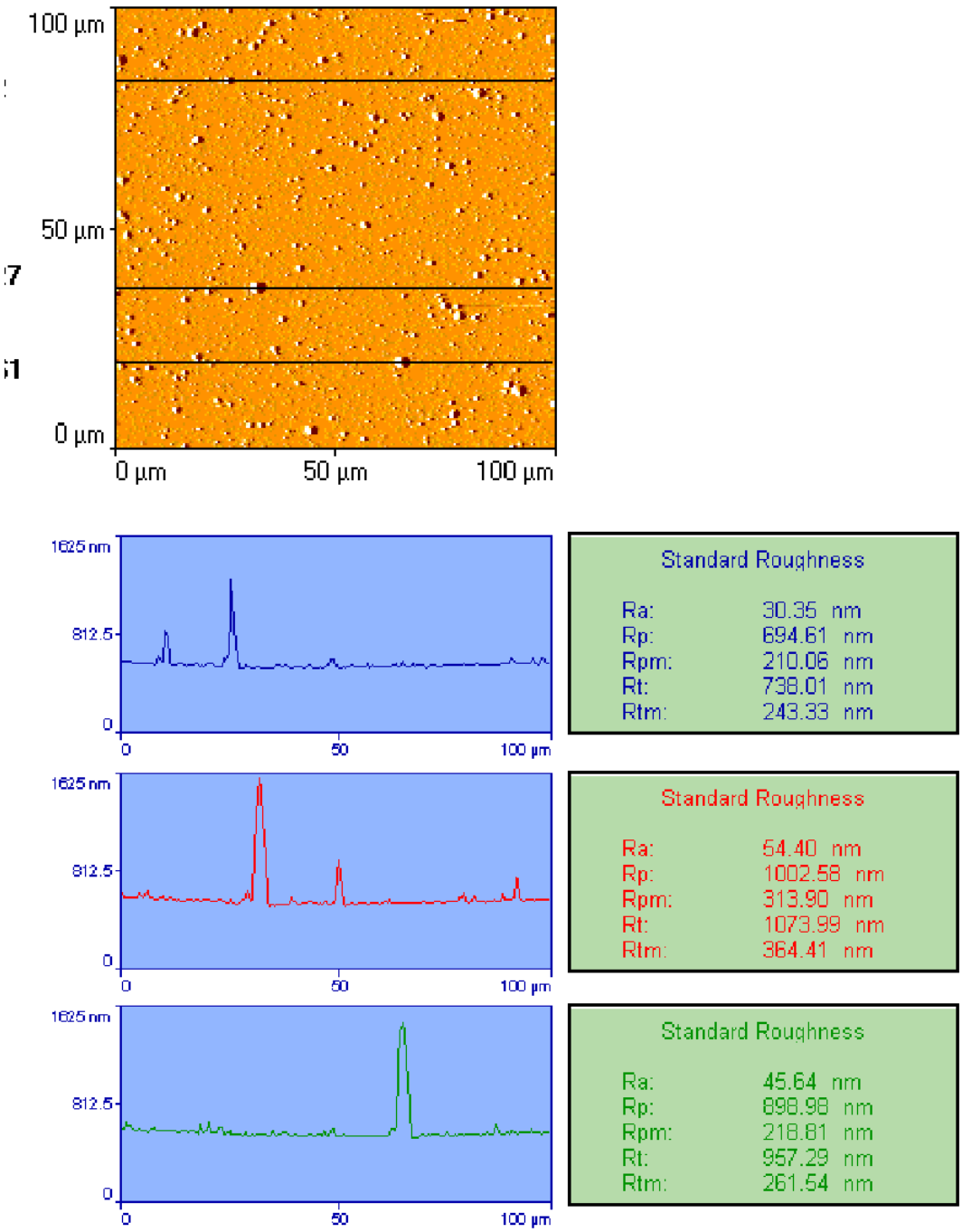

Figure 4-17: *Line profile analysis of an 100 µm × 100 µm image of sample A indicating the positions of the three lines which was subject to further analysis.*

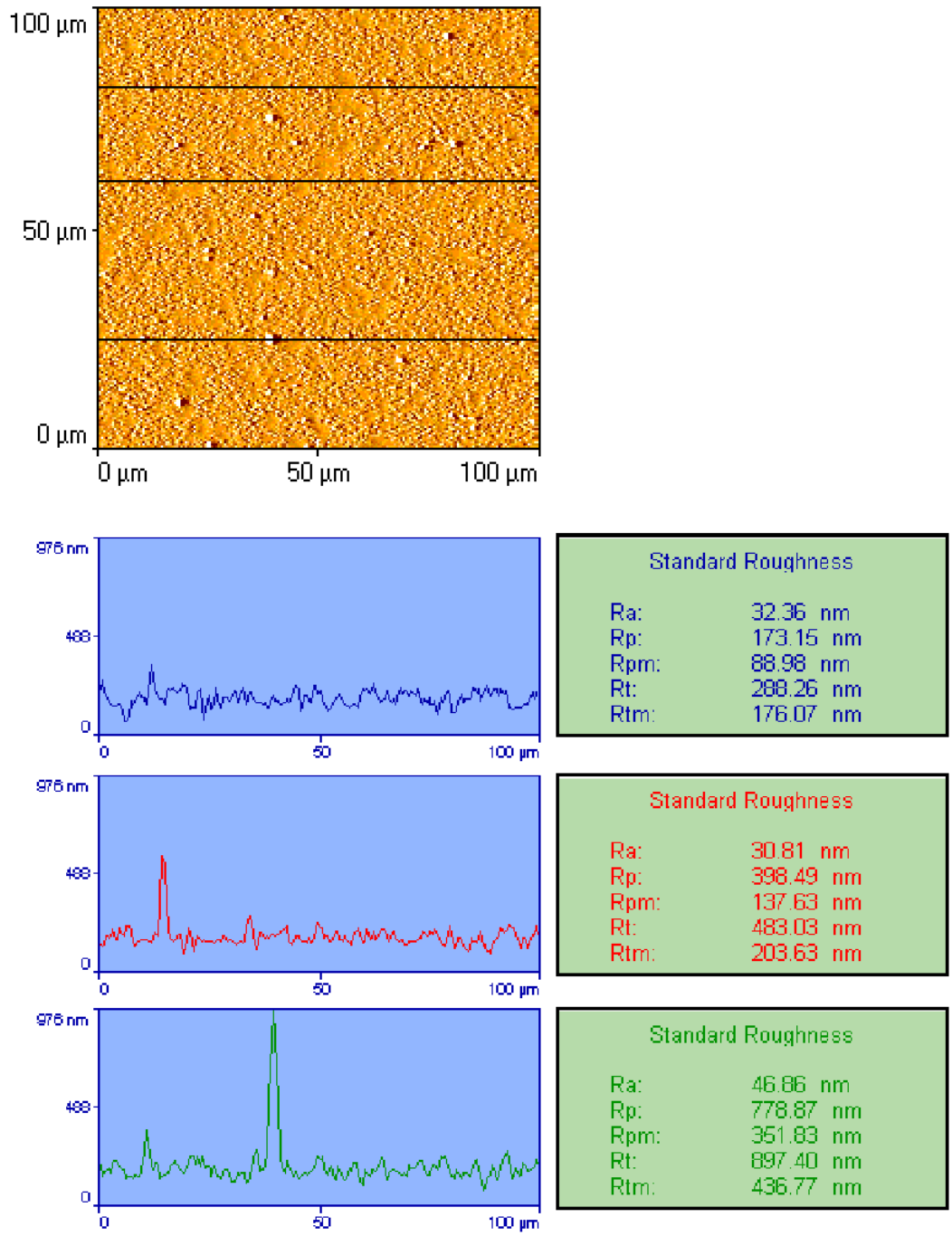

Figure 4-18: *Line profile analysis of an 100 µm × 100 µm image of sample B indicating the positions of the three lines which was subject to further analysis.*

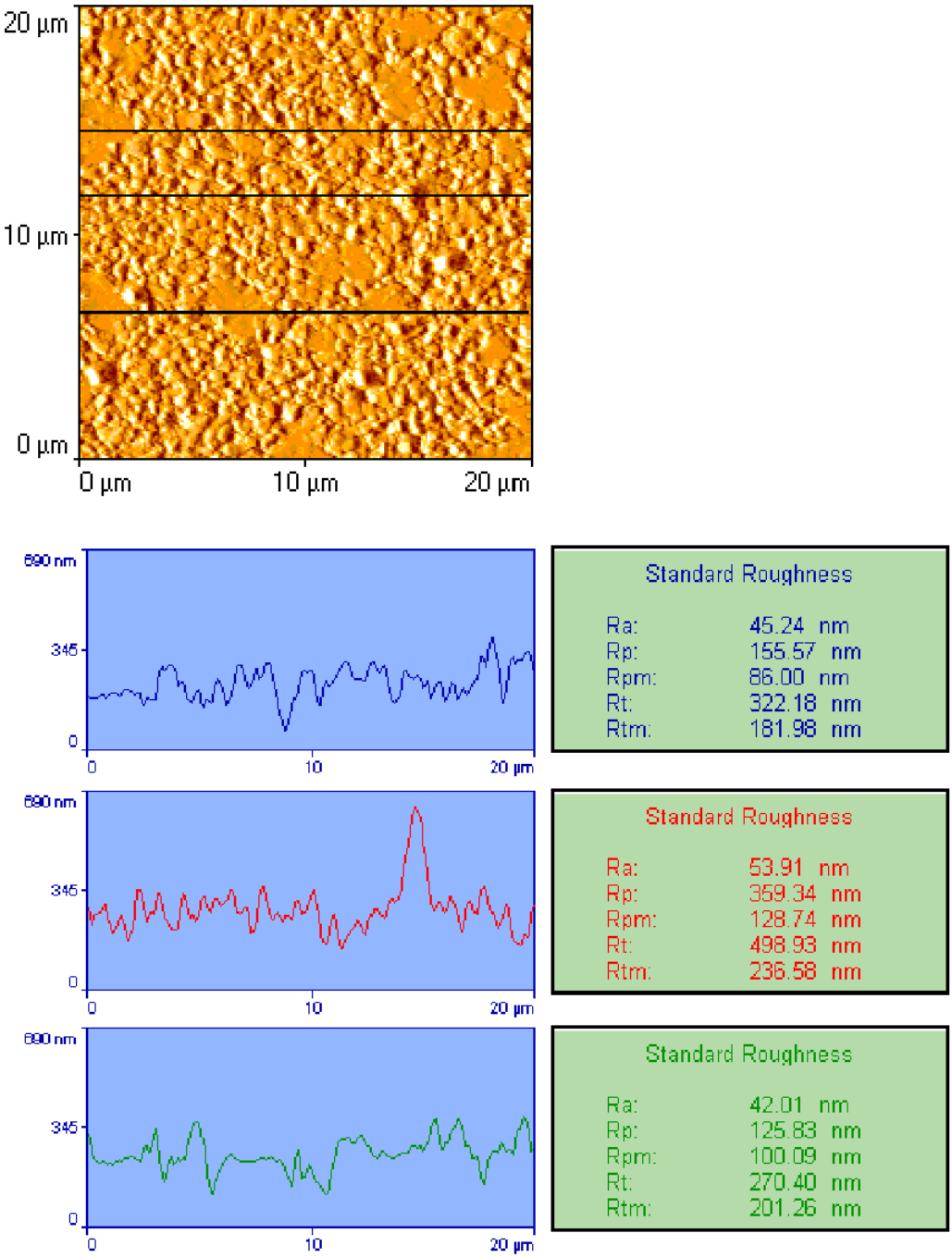

Figure 4-19: *Line profile analysis of an 20 µm × 20 µm image of sample B indicating the positions of the three lines which was subject to further analysis.*

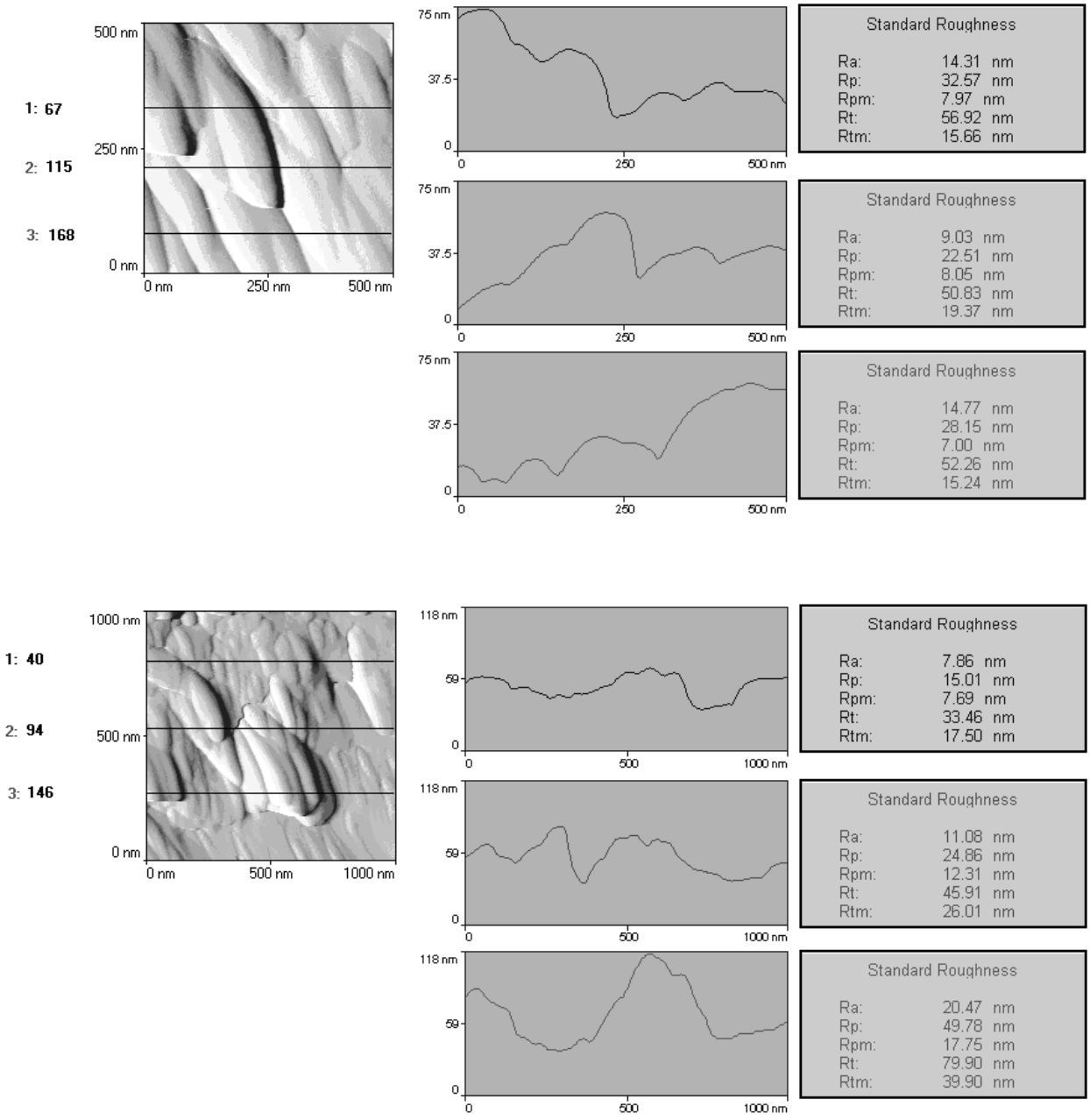

Figure 4-20: *Line profile analysis of higher magnification images of sample A. The top two images suffered drift due to sample movement, resulting in elongated features.*

to be very flat. Visual inspection of the line profiles show large peaks against a background of a much smaller scale of roughness. This qualitative observation is supported by the large difference in scale between R_a and R_{pm}: $R_{pm}/R_a \sim 5.7 - 7.0$. Thus the average of the 20 highest points on a typical line profile of sample A is $5.7 - 7.0$ times higher than the average surface roughness.

The line analysis done on sample B also reveal some boulders especially prominent for line 2 in **Fig. 4-19** and lines 2 and 3 in **Fig. 4-18**. These boulders are of the same size range as for sample A, establishing that they originate from the deposition process and not from film growth. Visual inspection of sample B's images show that it presents a very rough background for the boulders. The R_{pm}/R_a ratio of $1.9 - 4.5$ is distinctly different from sample A's. This large irregular roughness is caused by film growth processes and will be discussed and compared to that of sample A in the conclusion.

Higher magnification

Sample A was imaged with higher magnification to produce **Fig. 4-20**. These images show rounded features of low roughness : $R_a \sim 9 - 14$ nm for 100 nm and 500 nm images. A certain amount of convolution occur due to the finite size of the probe tip (30 nm). This has the effect that features of about 40 nm or smaller are lost. It can also account for the rounded features visible in **Fig. 4-20**. This features form the lowest level roughness in sample A, and are caused by film growth phenomenon. These features are most likely caused by island growth and coalescence of $YBa_2Cu_3O_{7-\delta}$ grains, and show very clear similarities to studies that appeared in the literature[132]. J.Z. Liu and L. Li[133] determined via AFM that for both PLD and *dc* magnetron sputtering prepared film the nucleation and growth of the YBCO films have the customary island and coalescence mode. For PLD films both screw dislocation islands and terrace islands occurred. They also observed droplet-particles consistent without PLD-produced boulders. A. Roshko *et al*[134] obtained similar results using scanning tunneling microscopy (STM).

X-ray diffraction spectra of the superconducting and non-superconducting films are depicted in **Fig. 4-21**. **Fig. 4-21(a)** shows the peaks $(00l)$ consistent with $c-$axis orientated growth on the $\langle 001 \rangle$ surface of MgO. **Fig. 4-21(b)** shows some of the peaks of YBCO, but clearly indicated decomposition of YBCO, since it is not stable under the deposition parameters.

4.5.2 Particle density

Using the *SPMLab* image processing software, the particle density was established for the various films. **Fig. 4-22** show the particle count on 100×100 μm squares for each sample as a function of laser energy density Φ. The graph shows a counter-intuitive decrease of particle density with increasing laser energy density. This is possibly due to increased uptake of energy by the ablated plasma during the laser pulse's

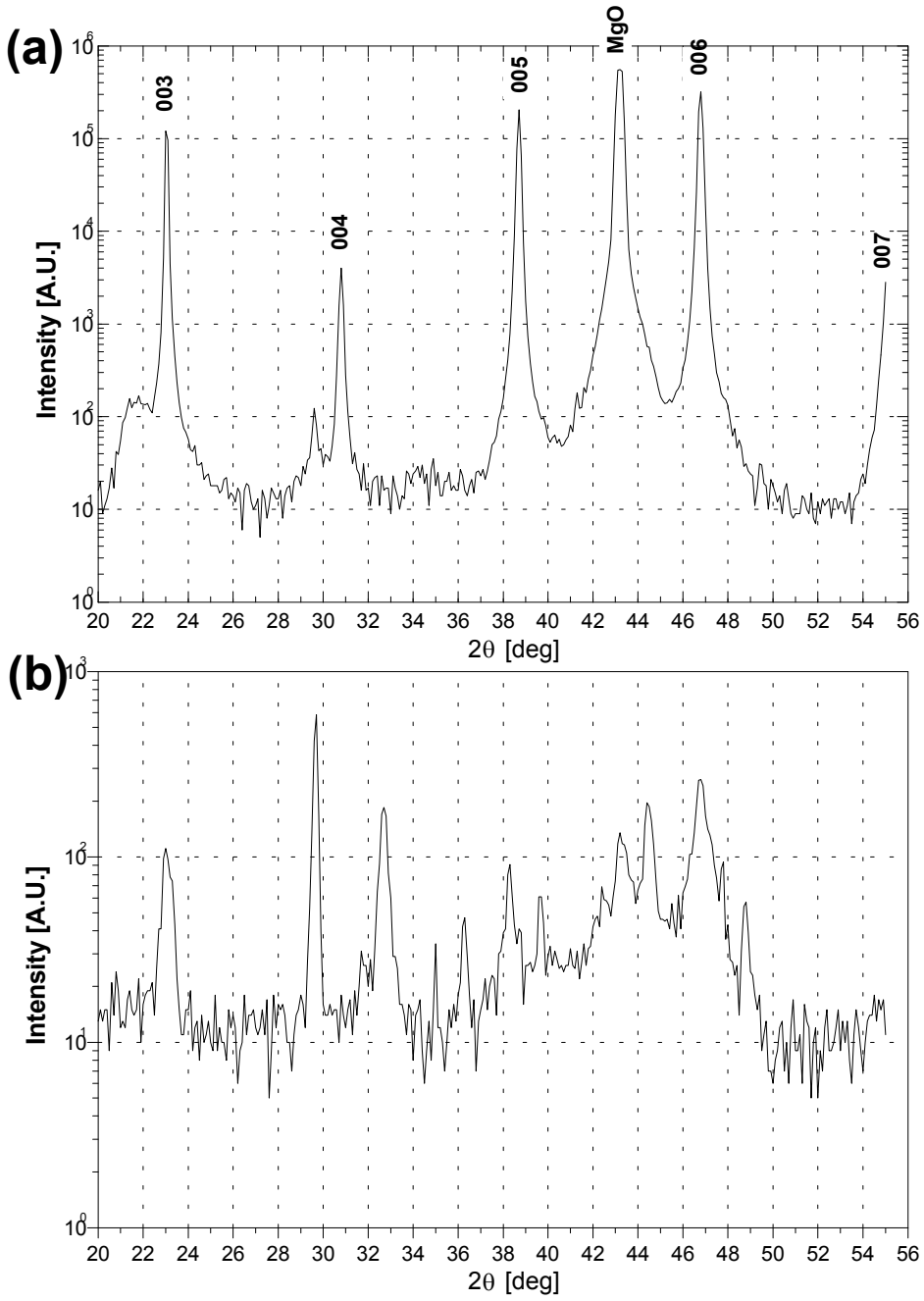

Figure 4-21: *(a) X-ray diffraction spectrum for sample A. The peaks* $(00k)$ *are consistent with c-axis orientated growth on the* $\langle 001 \rangle$ *surface of MgO. (b) X-ray diffraction spectrum for sample B. Some of the YBCO lines are discernible, but clearly indicates decomposition of YBCO, since it is not stable under the deposition conditions of low temperature.*

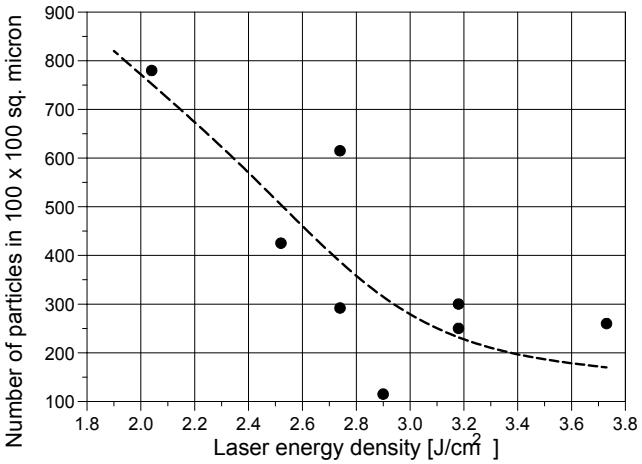

Figure 4-22: *Number of particles on a* 100×100 μm *square as a function of increasing laser energy density. The broken line indicates the possible trend suggested by the data.*

final stages. The fragments present in the plasma might melt and vapourise as the laser heats the plasma.

It is important to establish prior to particle count the threshold for particle identification to be used by the software. This was determined by making various cross-sections of the surfaces and determining some minimum particle. **Figs. 4-17, 4-18, 4-19, and 4-20** show such line profiles. The area threshold was selected to include all particles with an area of at least 0.2 μm^2, which corresponds to a diameter of about 500 nm.

4.5.3 Discussion

At 780°C the formation of the (semiconducting) tetragonal $YBa_2Cu_3O_x$ ($6 \leq x \leq 6.5$) is thermodynamically preferred in the presence of at least about 0.1 mbar of oxygen pressure P_{O_2}. The material undergoes a transition to the (superconducting) orthorhombic phase with $6.5 \leq x \leq 7$ when annealed at about $400 - 490$°C with $P_{O_2} \approx 1$ atm (1000 mbar) for 20-30 minutes. This solid state chemistry is of vital importance when trying to grow epitaxial thin films of $YBa_2Cu_3O_7$ on lattice matched substrates.

Surface particles and precipitate outgrowths appearing on films prepared by PLD are undesirable obstacles for their electronic application and for multilayer growth. Although in this study no attempt was made to minimise the amount of particles on a film, they where characterised to understand the behaviour of the PLD process.

Very smooth films can be formed with PLD. When depositing YBCO with laser deposition (or other methods) on lattice matched substrates at 780°C, tetragonal YBCO forms initially on the substrate, growing in a layer by layer fashion. Later, during the high pressure anneal, the material converts to the superconducting phase. This film is very smooth, and shiny, and black in colour. However at lower deposition temperatures (below 700°C), the formation of the approximate lattice matched tetragonal YBCO is no longer thermodynamically favoured, and the material decomposes into simpler oxides, such as Cu_2O, BaCuO and Y_2BaCuO_5. These oxides are not lattice matched to the substrate, and thus form randomly orientated microcrystals on the substrate, causing a very rough, non-shiny surface. The introduction of some roughness during film formation is thought to be due to the initial phase of film formation, where the atoms on the surface of the substrate nucleate into clusters and only later start to grow layer by layer. During the laser ablation atoms, ions and molten globules are ejected from the target, and are deposited on to the substrate. The molten globules are caused by subsurface heating of the target. The particles visible on the flat films (**Figs. 4-13 & 4-14**) are from two possible sources:

- Round micron sized boulders originate from the target due to sub-surface boiling. Diameter about 1 μm and height about $200 - 800$ nm.
- Smaller irregular shaped Cu-rich outgrowths, as suggested in the literature[127].

M.R. Cimberle *et al*[135] showed that by using a pulsed oxygen pressure of 2×10^{-3} mbar and exciting the gas molecules with a splitted part of the laser beam, high quality films (T_c = 89 K, $J_c = 50 \times 10^6$ A/cm^2 at 10 K) can be obtained. This was prompted by earlier studies which revealed that in high oxygen partial pressures the growth mode of YBCO is an island mode and that precipitates form in the earlier stages of the growth.

Outgrowths can also be minimised via treatment of the substrate prior to deposition. S. King *et al*[136] found that annealing MgO substrates at 1340°C in air for 40 minutes promoted the growth of very smooth samples. Unfortunately no roughness parameters were given in their study for comparison with our results. Essentially annealing reduces the number of surface steps on the substrate, thus providing longer diffusion paths and decreasing the number of nucleation sites for the Volmer-Weber[137] growth. The Volmer-Weber (VW) process forms part of a general film growth scheme proposed by E. Bauer[138]. The VW mode implies initial film nucleation by three-dimensional crystallite growth. **Fig. 4-23** shows the roughness parameters R_a and R_{RMS} as a function of energy density Φ, the roughness decrease more than 50% from $\Phi = 2.0$ to $\Phi = 3.0$, and then rises again. The dip in roughness can possible result from the interaction of the latter stage of laser beam with the early stages of the plume, causing breakup of the particulates. Increased energy then would result in greater efficiency of the breakup. This is one possible explaination, and the rise of the roughness is not explained by it. This corroborates with the

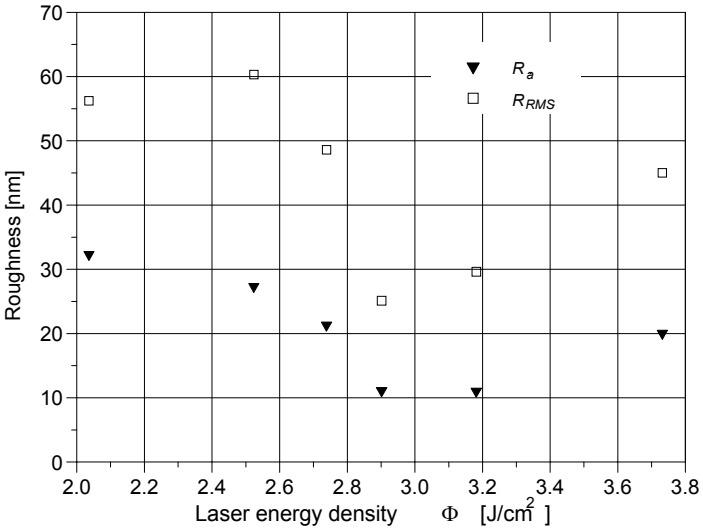

Figure 4-23: *Roughness vs. laser energy density for the series of films examined. The R_a and R_{RMS} roughness parameters are displayed, and show the same functional relationship.*

result that T_c is also independent of Φ over the same range, see **Fig. 4-7**.

4.6 Conclusion

The most important result of this work is the rather obvious fact that high quality $YBa_2Cu_3O_7$ can be successfully deposited using the PLD system described in Chapter 3. A critical temperature of ~ 90 K was achieved in *c*-orientated films deposited on MgO and $SrTiO_3$. The composition of such optimal films was found to be the ideal 1-2-3 of $YBa_2Cu_3O_7$ within the precision of the RBS measurement. Moreover, the material was found to be predominantly *c*-axis orientated; with ideal orientation on the underlying substrate. None or very little impurity phases were present. This was found by detailed XRD analysis of two selected samples. YBCO films on $SrTiO_3$ were found to align their a/b-axis with the a-axis of $SrTiO_3$.

The deposition profile of the laser ablation plume was studied by depositing a thin film on a large area Si substrate. The plume was verified to have a $f(\theta) \propto \cos^p \theta$ density profile, resulting in a $T(\theta) \propto \cos^{p+3} \theta$ thickness profile on the substrate. The spatial anisotropy of the profile also agreed with established observations of the plume behaviour.

Another result was the understanding gained of the role of the deposition parameters in PLD, and

in particular for our PLD system. Although the stated purpose of this study was not to undertake a complete investigation of the influence of all the deposition parameters, the following conclusions were made:

- Best film ($T_c \sim 90$ K) was obtained for the deposition parameters given in **Table 4.11**, using a XeCl excimer laser running at 10 pulses per second.

Table 4.11: *Best film ($T_c \sim 90$ K) was obtained for the following deposition parameters.*

Laser energy density Φ	2.0-3.0 J/cm^2
Substrate temperature T_{dep}	780°C
Oxygen partial pressure P_{O_2}	0.2 mbar
Target-substrate distance D	35 mm

- At 780°C the deposition process is much less sensitive for small changes in the deposition parameters : $P_{O_2} = 0.2 - 0.3$ mbar and $\Phi = 2 - 3$ J/cm^2 etc. than at 680°C. This is a direct result from easier surface activation for deposited species at the elevated temperature. At 680°C the deposited species must arrive with high enough kinetic energy to cause surface diffusion and the breaking of surface bonds necessary for epitaxial growth.

- In contrast, surface roughness of films deposited at 780°C with a range of $\Phi = 2 - 4$ J/cm^2 do vary significantly, first decreasing, and then increasing, with a minimum around $\Phi = 3.0$ J/cm^2.

The results of this work seem supported by the existing corpus of literature on the PLD of $YBa_2Cu_3O_7$. All the results on RBS, XRD, AFM, the role of the deposition parameters are in agreement with the current knowledge. Finally, in the light of this research, we suggest the following interesting line of research:

- The interplay of kinetic energy of the ablated species and the surface temperature seems to be a very important unresolved question. By using low angle *in situ* surface analysis tools such as LEED, this topic can be researched for various materials : metals, ceramics, semiconductors and the like. This is of technological importance since the lowering of the substrate temperature during deposition is sometimes crucial to prevent undesired reaction or diffusion.

Chapter 5

Studies of Superconductivity near the Critical Temperature

5.1 Introduction

The magnetisation of $YBa_2Cu_3O_7$ films and the time decay of the remanent magnetisation of these films due to thermally activated flux creep were studied at temperatures below T_c. In the vicinity of the critical temperature $T_c - T \lesssim 1$ K the thermal fluctuation of the order parameter should dominate the superconducting properties. In the past, studies of flux creep could not reach the critical region in the $B - T$ phase space, thus there was very little data on the critical current density and the flux creep activation energy in the fluctuation dominated region. The present study, in contrast, was conducted in the regime close to T_c. This fact makes the research basically important[139, 140].

The Bean model and it's two dimensional extension, introduced in Chapter 1, predicts a hysteretic magnetisation behaviour. This model has been verified to predict the qualitative magnetisation behaviour of thin disk-like superconducting films, and the experimental data is compared with the model calculations.

After the films were magnetised and the applied field was reduced to zero, the isothermal relaxation of the trapped flux, so-called *flux creep*, was observed. Flux creep was thermally activated. The activation energy $U(T)$ was derived from the flux versus time decay curves through a power law. The temperature dependence of $U(T)$ was determined experimentally.

It was observed that the flux decay was extremely sensitive to small temperature variations. In particular, a small decrease in temperature of the sample undergoing isothermal flux decay in the region $T_c - T < 10$ K led to a complete freeze of flux creep. This phenomenon of flux creep freezing was

investigated, and a quantitative model was suggested to explain the results.

5.2 Experimental set-up

5.2.1 Experimental cell

A contactless method was developed for studying magnetisation phenomenon in HTSC thin films using a commercial HTSC SQUID[1] *"Conductus iMAG"* magnetometer. An experimental cell was designed to house and support the various elements of the experimental set-up that had to be cooled, shown in **Fig. 5-1**. **Fig. 5-2** shows a schematic diagram of the various electronic control and data acquisition devices used in the experiments. The various subsystems of the experimental set-up will be discussed by reference to these two figures in the text.

Temperature measurement and control were critical components of the experiments. It was necessary to stabilise the sample temperature in the range $77 - 95$ K with high accuracy (5 mK or better). At the same time, the SQUID should be kept at the constant temperature of liquid nitrogen to ensure it's stable operation. In this geometry, one could introduce a system of cylindrical coordinates (r, ϕ, z) with it's origin in the centre of the film, and the z-axis perpendicular to the film's surface, pointing towards the SQUID. The SQUID would then be in a position to measure the field component B_z.

The experimental requirements were that a superconducting film (position **H**, refer to **Fig. 5-1**) be placed co-axially inside a field coil (**F**), and the SQUID (**D**) should be co-axially located to sense the z-component of the field (B_z) resulting from the magnetisation of the film. A compensation coil (**C**) designed to eliminate the magnetic field contribution of the primary field coil at the SQUID sensor while simultaneously contributing only negligibly to the field at the films surface, was positioned co-axially near the SQUID. The superconducting sample was placed in a non-magnetic copper sample holder (**G**). An outer tufnol support tube (**A**) was used to support the field coil, and an inner tube (**B**) supported the SQUID, the compensation coil and the sample holder. The SQUID's nose fits in the upper opening of the inner tube, and it is held firmly in position with nylon screws.

5.2.2 Temperature measurement

The sample holder could be heated and it's temperature could be controlled to high stability in the range $77 - 100$ K, while the SQUID remained at 77 K. The copper sample holder was a cylinder of thickness 3 mm and diameter 16 mm. It's high heat conductivity facilitated effective temperature measurement and control, and ensured temperature uniformity at the film. The sample was glued at the back to the

[1] **S**uperconducting **QU**antum **I**nterference **D**evice

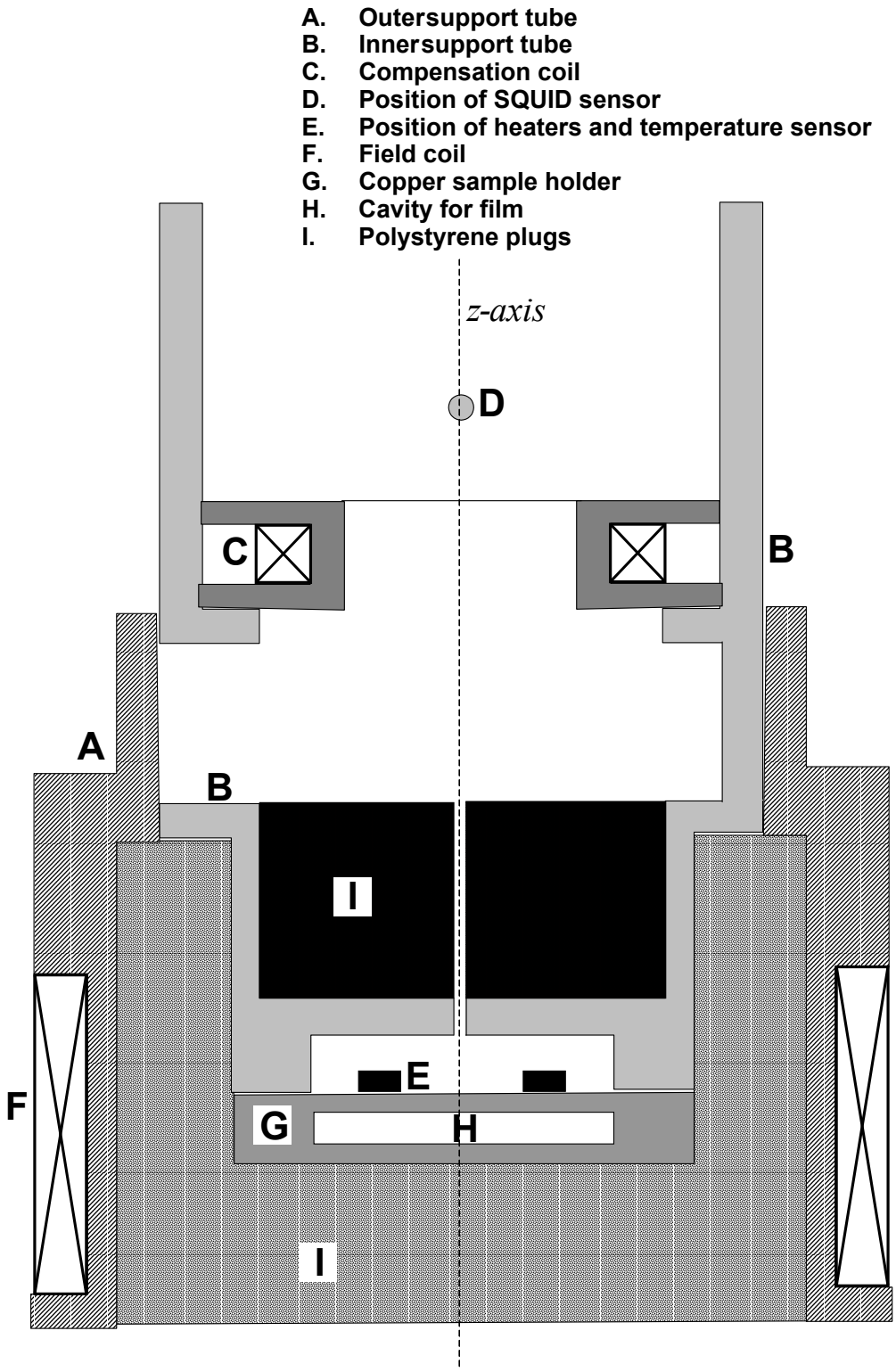

Figure 5-1: *Schematic diagram of the experimental cell used with the SQUID. The film is positioned in the centre of the primary coil, while the compensation coil was located near the SQUID sensor. All the materials used were non-magnetic, the majority of the cell is manufactured from tufnol or polystyrene, only the sample holder is from copper to facilitate heating and temperature uniformity of the sample. The SQUID probe is clamped in the recess in the inner tube just above the compensation coil.*

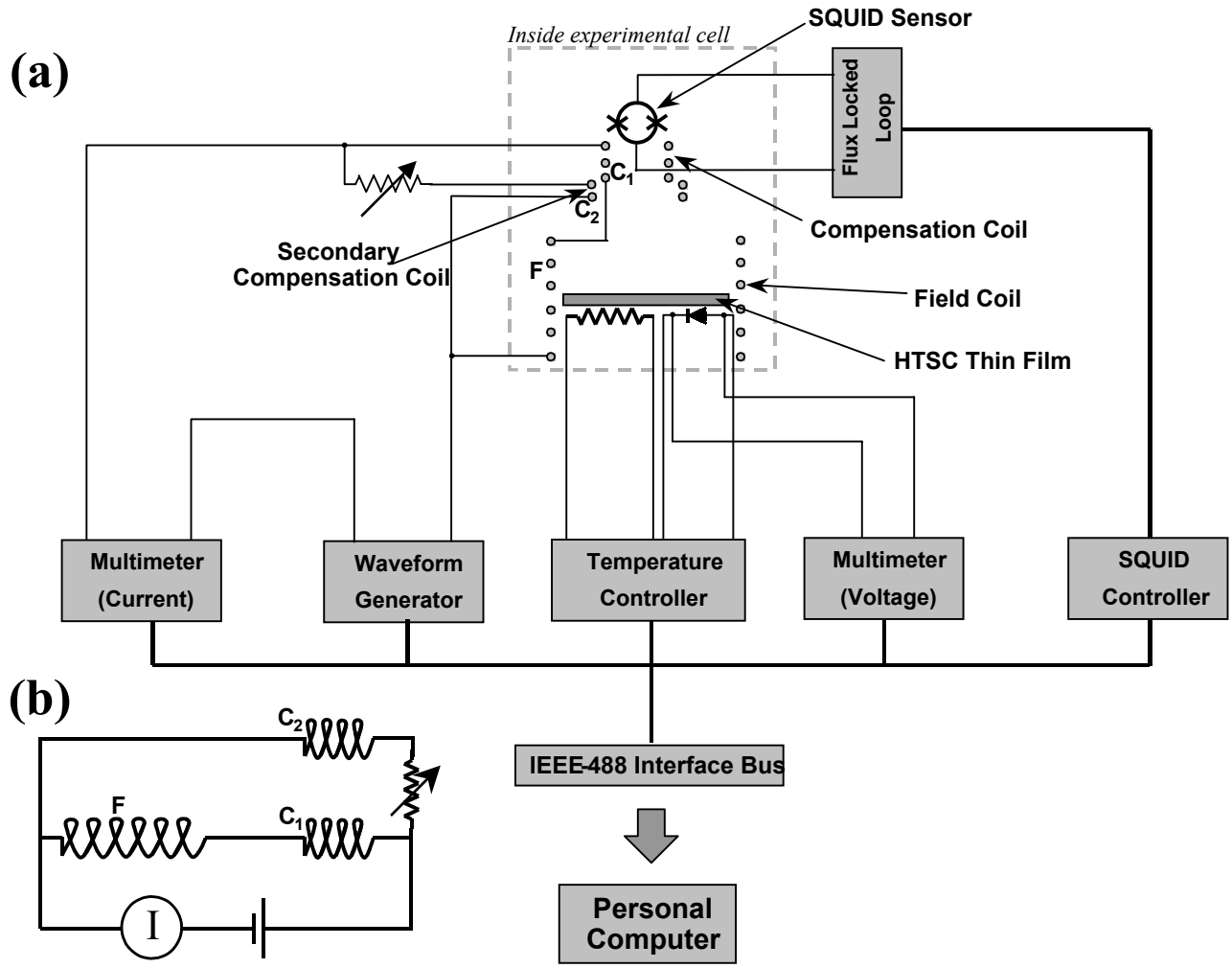

Figure 5-2: *(a) Schematic diagram of the experimental set-up for magnetisation experiments. The temperature controller was used to measure and control the film temperature. The SQUID sensor was kept at liquid nitrogen temperature. The SQUID sensor is connected to a flux locked loop via a cryogenic cable, which is then connected to the iMAG SQUID controller through a composite cable. The waveform generator's signal is passed through a multimeter acting as a current meter to record the current passed to the field coil. All instruments are connected to the personal computer through an IEEE-488 interface system. (b) Circuit diagram of the compensation system.*

cell using *Apiezon* grease to ensure good thermal contact, and the two heater resistors (chip resistors of dimensions 2 mm × 2 mm and resistance ∼ 100 Ω) and the Si-diode temperature sensor (*LakeShore model DT-470-SD-13*) (**E**) was glued on top of the sample holder using Araldite epoxy resin.

An insulating polystyrene plug (**I**) was glued to the bottom of the cell, and another one was placed inside the inner tube. Wires to the temperature sensor and resistors passed through the inner plug to the outside of the support tubes. The whole cell was immersed in liquid nitrogen to cool the SQUID to 77 K. When the heater was turned off, the experimental cell was immersed in liquid nitrogen, and when the heater was turned on, the liquid nitrogen inside the cell evaporated and the vapours filled the sample holder and the inside of the polystyrene plugs. In this way, the SQUID was kept at 77 K, while the sample could be heated to above T_c. With ∼ 20 mW of heater power, the nitrogen inside the sample holder evaporated. The film could be heated to about 100 K, while the usual heater power was ∼ 100 mW.

By connecting the *LakeShore DRC-91CA* temperature controller to the resistors and the temperature sensor, it could be used to stabilise the temperature at the required set-point temperature.

The temperature controller has an input *A/D* converter accuracy of 50 μV, relating to a temperature difference of 25 mK (dV/dT = 2 mV/K) in the range $77 - 200$ K. This temperature sensitivity is not always satisfactory for our purposes, since the magnetic field may change significantly when sample temperature changes only 25 mK. The temperature resolution was increased by an order of magnitude by using a sensitive multimeter (*Hewlett-Packard model 34401A*) to read the voltage across the diode. The voltage reading was then converted using a calibration function supplied by the manufacturer of the temperature sensor. The multimeter had a theoretical sensitivity of 0.1 μV, but in practice noise limited the sensitivity to about 5.0 μV, relating to a temperature sensitivity of 2.5 mK. In this configuration, the temperature controller was used to provide an accurate forward bias to the diode of 10 μA (±0.05%), as shown in **Fig. 5-2(a)**.

The Si-diode is factory calibrated against a standard resistive thermometer, of which the temperature is known to an accuracy better than 0.1 mK. In the calibration (as also during normal operation), the diode is excited with 10 μA (±0.05%) and the voltage (typically in the range $1.0 - 2.0$ V) recorded to an accuracy of 5 significant digits after the decimal (10 μV)[142]. A calibration curve for the Si-diode was provided by the manufacturer based on interpolating Chebychev polynomials.

Coefficients a_i for Chebychev polynomials were provided to generate the temperature T from an accurate measurement of the diode voltage when biased by 10 μA (±0.05%). If the range of voltages over which the interpolation is done is $V_L < V < V_U$, then

$$T(V) = \sum_{i=0}^{n} a_i t_i(x) \tag{5.1}$$

where

$$x = \frac{(V - V_L) - (V_U - V)}{V_U - V_L} \tag{5.2}$$

$t_i(\cdot)$ is the i^{th} order Chebychev polynomial, and could be calculated by $t_i(x) = \cos(i \arccos(x))$. The interpolation temperature function $T(V)$ differs from the temperature (measured with the high accuracy standard) by not more than 15 mK in the range $76 - 300$ K; temperature differences of 2.5 mK could be determined.

5.2.3 Magnetic field measurement

The SQUID of noise limited sensitivity $\sim 10^{-6}$ G was used to measure the magnetic field generated by circulating currents in the samples[141]. The output of the SQUID controller was given as voltage, with a calibration of 0.52 V/Φ_0. The SQUID sensor was situated 27.7 mm above the film, with the SQUID loop parallel to the film's surface.

The experimental cell, including the SQUID and the superconducting sample, was shielded from the stray fields emanating from the earth and surrounding power lines by a triple layer mu-metal magnetic shield of shielding efficiency above 100 dB. Thus the stray fields of order 10^{-6} G were negligible as compared with the field created by the current generated in the film.

To measure the magnetisation directly, without any contribution from the field coil, it was decided to incorporate in the design a compensation system to cancel the effect of the field coil ($\mathbf{F}$) at the position of the SQUID. Thus only the magnetic field arising from the film's magnetisation would be sensed by the SQUID. The superconducting film was placed at the centre of the field coil, while the compensation coil ($\mathbf{C}_1$) was located close to the SQUID sensor. The field at the centre of the field coil was measured directly using a Hall probe, and found to be 600 G/A. This figure is quite reliable since, a 1 mm shift from the centre of the Hall probe vertically produces only a 0.8% decrease in field strength, while a 1 mm horizontal shift from the centre produces only a 0.4% increase of field strength.

The magnetic field produced by a coil can easily be calculated by modelling the coil as a number of concentric current rings of equal radius, evenly spaced in the vertical dimension. The magnetic field ($\mathbf{B} = \boldsymbol{\nabla} \times \mathbf{A}$) produced by a current ring of radius a lying in the horizontal plane $z = 0$ can be calculated from relation for the vector potential $\mathbf{A}$ of such a current ring, which is, in spherical coordinates (r, θ, ϕ) :

$$A_\phi(r,\theta) = \frac{4Ia}{c\sqrt{a^2 + r^2 + 2ar\sin\theta}} \left[\frac{(2-k^2)K(k) - 2E(k)}{k^2}\right] \quad \text{(cgs)} \tag{5.3}$$

$$A_z = A_\theta = 0 \tag{5.4}$$

where K and E are the first and second complete elliptic integrals (refer to Chap. 1), respectively, and $k^2 = 4ar\sin\theta/(a^2 + r^2 + 2ar\sin\theta)$.

By deriving the magnetic field from the vector potential one arrives at (in cylindrical coordinates (ρ, ϕ, z))

$$B_z(\rho, z) = \frac{2}{c}\frac{I}{\sqrt{(a+\rho)^2 + z^2}}\left[K(k) + \frac{a^2 - \rho^2 - z^2}{(a-\rho)^2 + z^2}E(k)\right], \tag{5.5}$$

with $k^2 = 4a\rho/((a+\rho)^2 + z^2)$, for the z-component of the magnetic field, and we have the special case for B_z at any position along the vertical axis:

$$B_z(z) = \frac{2\pi I}{c}\frac{a^2}{(a^2 + z^2)^{3/2}}. \tag{5.6}$$

Using eq. 5.6 one can estimate the number of turns necessary at the compensation coil to cancel the field coil. The physical dimensions of the field coil and other related parameters are given in **Table 5.1**.

Table 5.1: *Physical dimensions related to the experimental cell.*

Field coil	
Field coil center to SQUID	27.7 mm
Field coil diameter	27 mm
Field coil height	11 mm
Field coil number of turns	139
Compensation coil	
Compensation coil center to SQUID	9.7 mm
Compensation coil diameter	10 mm
Compensation coil height	2 mm
Compensation coil number of turns	47
General	
SQUID-film distance	27.7 mm
SQUID sensitivity	0.52 V/Φ_0
Field-voltage conversion at gain 1	3.32×10^{-3} G/V
Typical coil current	$1 - 30$ mA
Field at centre of field coil	600 G/A
Typical field at SQUID	$1 - 6$ Φ_0
Typical field at film	$0.6 - 18$ G

Using the data from **Table 5.1**, taking into account the height of the coils, one can calculate that the relation should be

$$\frac{n_{C_1}}{n_F} = \frac{33.559}{100}. \tag{5.7}$$

Fig. 5-3(a) shows the calculated profile of the magnetic field z-component (using eq. 5.5 and the ratio above) along the film surface. The magnetic field increases slightly towards the edges of the film. At a distance 5 mm from the center, the uncompensated B_z is 8.2% larger than at the center. With

the compensation coil, the magnetic field at the film surface is between 1.4% (edges) and 1.9% (center) lower than without the compensation.

Fig. 5-2(b) shows the circuit diagram of the compensation coil set-up. The compensation coil C_1 is wound and positioned to almost compensate for the field of the primary field coil F. The same current passes through both F and C_1. The compensation is achieved in practice in the following manner:

- The compensation coil (C_1) is wound according to the calculated ratio.
- Constant current is driven through F and C_1 (in series). The location of the compensation coil is slightly adjusted along the vertical axis to minimize the magnetic flux reading on the SQUID.
- An additional compensation coil (C_2) was necessary for fine tuning, because it is impossible to position the coil C_1 very accurately. Thus a potentiometer was placed in series with C_2, and the combination in parallel with C_1.

The current through C_2 is proportional to the current through F, thus guaranteeing permanent compensation, once balanced correctly.

Fig. 5-3(b) shows the sensitivity of the magnetic field at the SQUID to a change in the position of the compensation coil, calculated using eq. 5.6. At 9.7 mm the sensitivity is 0.0102 G/mm at a current of 1 mA. When using the conversion factor of $\kappa = 3.32 \times 10^{-3}$ G/V (at a 1 times gain), we find 3.07 V/mm at 0.01 mA at gain 1.

Determination of the field-voltage conversion factor of the SQUID

The calibration of the SQUID output (in terms of magnetic field — the factor κ in $B_z = \kappa F$ — at the sensor) versus volts output F was determined as follows:

- The film was completely magnetised, such that all the circulating currents was at the critical current density. (See relevant section in Chapter 1.)
- The magnetic moment was determined by

$$m = \frac{\pi}{3c} j_c d a^3, \tag{5.8}$$

  where $j_c = 1.6 \times 10^6$ A/cm^2, film thickness : $d = 3 \times 10^{-5}$ cm and film radius : $a = 0.5$ cm. This results is $m = 0.63$ emu.

- Using the relation for the far field of a magnetic dipole moment

$$B_z = \frac{2m}{r^3} \tag{5.9}$$

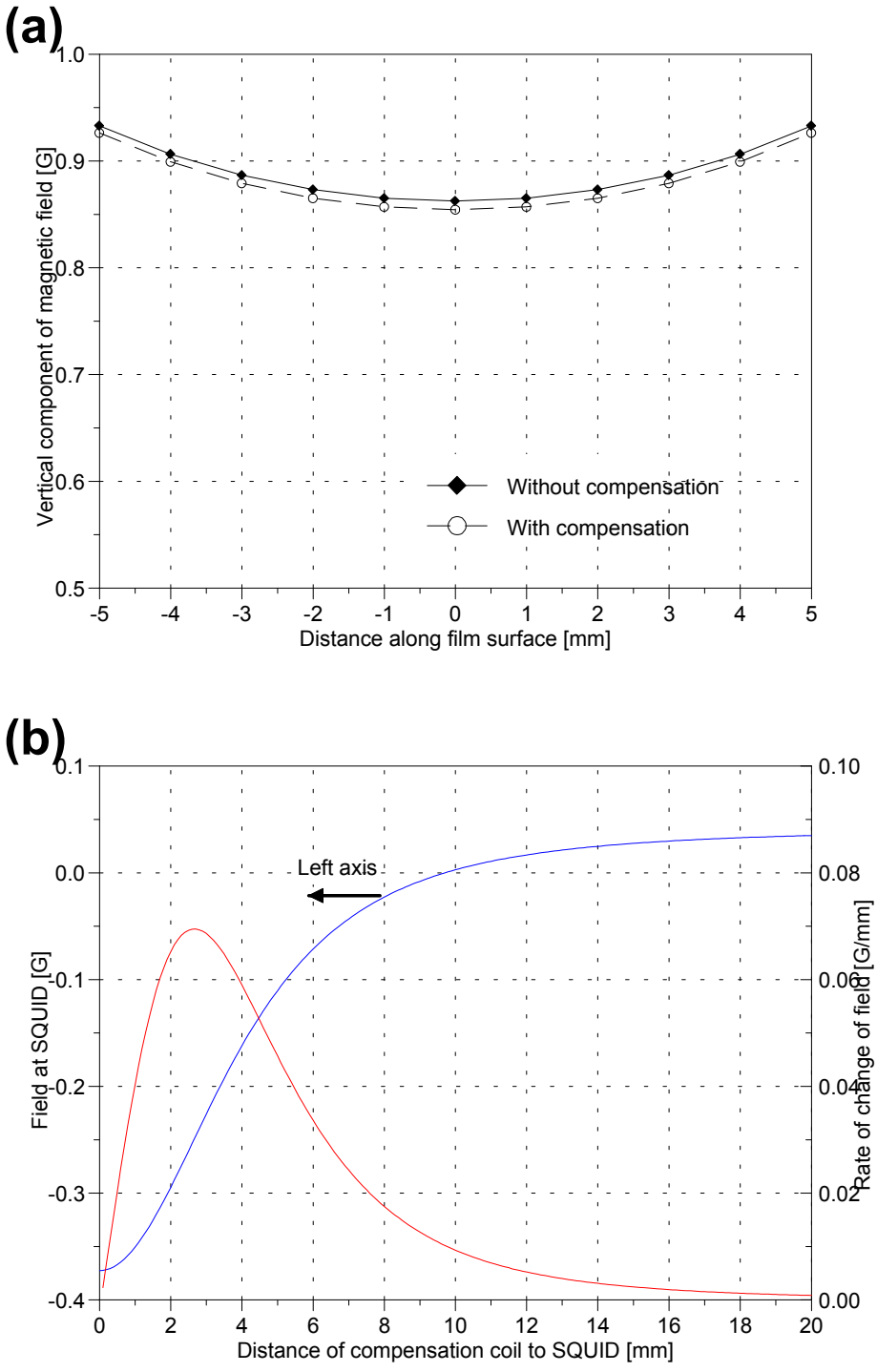

Figure 5-3: *(a) Calculated magnetic field z-component (B_z) along the film surface. The solid line is the field without any compensation, and the broken line is the field with the compensation according to the calculated ratio (n_F=200, n_{C_1}=67). The current was $I = 1\ mA$. The influence of compensation is minimal at the film surface, as desired. (b) The sensitivity of the magnetic field at the SQUID as a function of the vertical distance between the SQUID and the center of the compensation coil. The rate of change is also shown, associated with the right hand side axis.*

we determined the magnetic field at the sensor, and thus the conversion factor is $\kappa = 3.32 \times 10^{-3}$ G/V at a gain of 1:

$$B_z = \kappa F \tag{5.10}$$

$$\kappa = 3.32 \times 10^{-3} \text{ G/V}. \tag{5.11}$$

This means the effective probe area of the SQUID is 1.197×10^{-4} cm^2 at 1 times gain.

A *Hewlett-Packard HP33120A* function generator provided the current to the field and compensation coil system. The shape, amplitude and duration of the waveform could be precisely controlled. A *RC*-filter was added between the function generator and the SQUID to remove any electromagnetic interference on the signal. A *Hewlett-Packard HP34401A* multimeter measured the current delivered by the function generator. In contrast, the *Keithley 224* current source which was tried initially, produced high frequency noise superimposed on the *dc* signal which caused the SQUID to overload rapidly. The noise was confirmed to originate from the internal electronic circuitry of the current source. The problem could not be satisfactory solved using analogue filters. The SQUID became erratic, and we had to abandon using the current source in favour of the function generator.

The function generator could produce noiseless sawtooth waveforms of the required amplitude and period for the recording of hysteresis loops and magnetising thin films in general. The longest period was 100 s (10 mHz) with a amplitude of 5 V. This corresponds to a current amplitude of 26 mA (coil resistance was 192 Ω).

Interpretation of the SQUID signals

The SQUID signal can be interpreted in terms of the current distribution in the film. We proceed with Bean's assumption[60, 61] that the critical current density is independent of the local density of vortices, which is reasonable since the magnetic field in the film is very small (less than 100 G - determined through spreadsheet simulation) in these experiments. The two-dimensional critical state model introduced by J. Zhu *et al*[67] can be applied in this case. The film is approximated by a disk of radius $a = 5$ mm. Assuming cylindrical symmetry, the only non-zero component of the current density is the azimuthal component $j_\phi = j$. The SQUID loop is located at $z = z_S > a$ to measure the component B_z. In the film, thickness d, the current can be regarded as uniform in the z-direction (see, e.g. ref. [71]). The perpendicular field component can be calculated with the formula

$$B_z = \frac{2\pi d}{c} \int_0^a \frac{j(r) r^2 dr}{(r^2 + z^2)^{3/2}}. \tag{5.12}$$

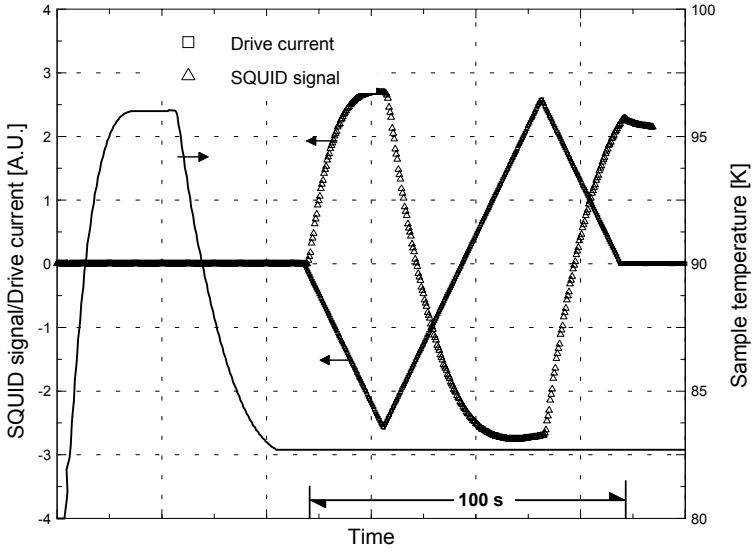

Figure 5-4: *Schematic diagram of the magnetisation procedure of a thin film. Initially, the film is heated to above T_c, to get rid of all trapped flux. The film is then zero field cooled to the desired temperature. After the temperature stabilises, a saw tooth waveform is passed through the field coil. The magnetic field is sensed by the SQUID, and the SQUID response is also indicated. The heating procedure took about 5 minutes, while the magnetisation took 100 seconds.*

The current distributions in the film follows the scheme derived in Chapter 1, shown in **Fig. 1-16**.

5.3 Experimental procedures

5.3.1 Film magnetisation procedure

A typical experimental run was as follows: Initially, the film was heated to above T_c to cause trapped flux to escape completely from the film. The film was then allowed to stabilise at some desired temperature $T^* < T_c$ - zero field cooled (ZFC). The software would then become operational, taking the film through a magnetisation cycle by ramping the current in the coil system through a single sawtooth waveform cycle, as shown in **Fig. 5-4**. The SQUID signal was compensated to cancel the field contribution from the field coil, thus the SQUID sensed the magnetic moment of the film directly, $F \propto m$. The current is zero at the end of the cycle. The magnetising cycle took 100 s. The SQUID signal, temperature, current through the coil system and time elapsed was recorded at regular time intervals. The virgin state could be restored by heating the sample at $T \geqslant T_c$ in zero applied field.

The field component B_z was increased to a value B_0, which is high enough to produce a critical

state with screening currents of current density j_c in most of the film, leaving only the innermost part in the Meissner state. (Refer to the section on the critical state in superconducting films in Chapter 1.) The external field is then steadily decreased to zero, and a remanent flux parallel to the magnetising field was trapped inside the film owing to the pinning of vortices. At the same time, superconducting currents continued to circulate in the film. The required characteristic magnetising field was $B_z \sim 3$ G at $(T_c - T) \sim 1$ K, and increased proportionally to j_c up to 100 G at $(T_c - T) \simeq 10$ K.

After the magnetisation stage, the temperature could be changed, or an isothermal flux decay run could be completed, depending on the nature of the experiment, and the physical parameters was recorded on computer disk.

5.3.2 Experimental hysteresis loops

The magnetic response of a thin superconducting film with an applied field perpendicular to it's surface is of particular importance for both fundamental and technological reasons. From an applications point of view, the critical current density is the most important parameter of a superconductor, and naturally we wanted to determine j_c for any film. The standard four point method[143, 144] is not desirable, since the film has to be etched and contact points have to be deposited. This processing can degrade the film quality and render it useless for further processing. An alternative method is to induce currents in the film though a magnetic field, and to infer j_c indirectly. Many authors have reported hysteresis behaviour in both low and high temperature superconductors, ie. m depends on the previous history of how the magnetic fields were applied[145, 146, 147], and we have observed similar behaviour.

We have recorded the hysteresis loop at various temperatures for a zero field cooled $YBa_2Cu_3O_7$ thin film in the experimental set-up described in Section 5.2. Although various films were used in this work, the best film was selected for presentation purposes, and for the rest of the chapter all results presented will be with respect to this particular sample, called *sample A*. The vital statistics for *sample A* is:

T_c	88.7 K
Size	10 mm × 10 mm
Thickness	300 nm

Fig. 5-5(a) show hysteresis curves for various temperatures close to T_c (in the order of larger to smaller height loops : 85.0 K, 86.0 K, 87.0 K and 87.5 K). **Fig. 5-5(b)** shows curve **d** on a different scale. **Table 5.2** shows the critical current density calculated using Eq. 5.14, using data from **Fig. 5-5** — the methodology will be explained below.

Each loop starts at the origin, as the films were initially flux free. From the virgin state, the films were magnetised, initially following a reversible line given by $m(B) = -\frac{2}{3\pi}BR^3$[67]. The slopes of curves

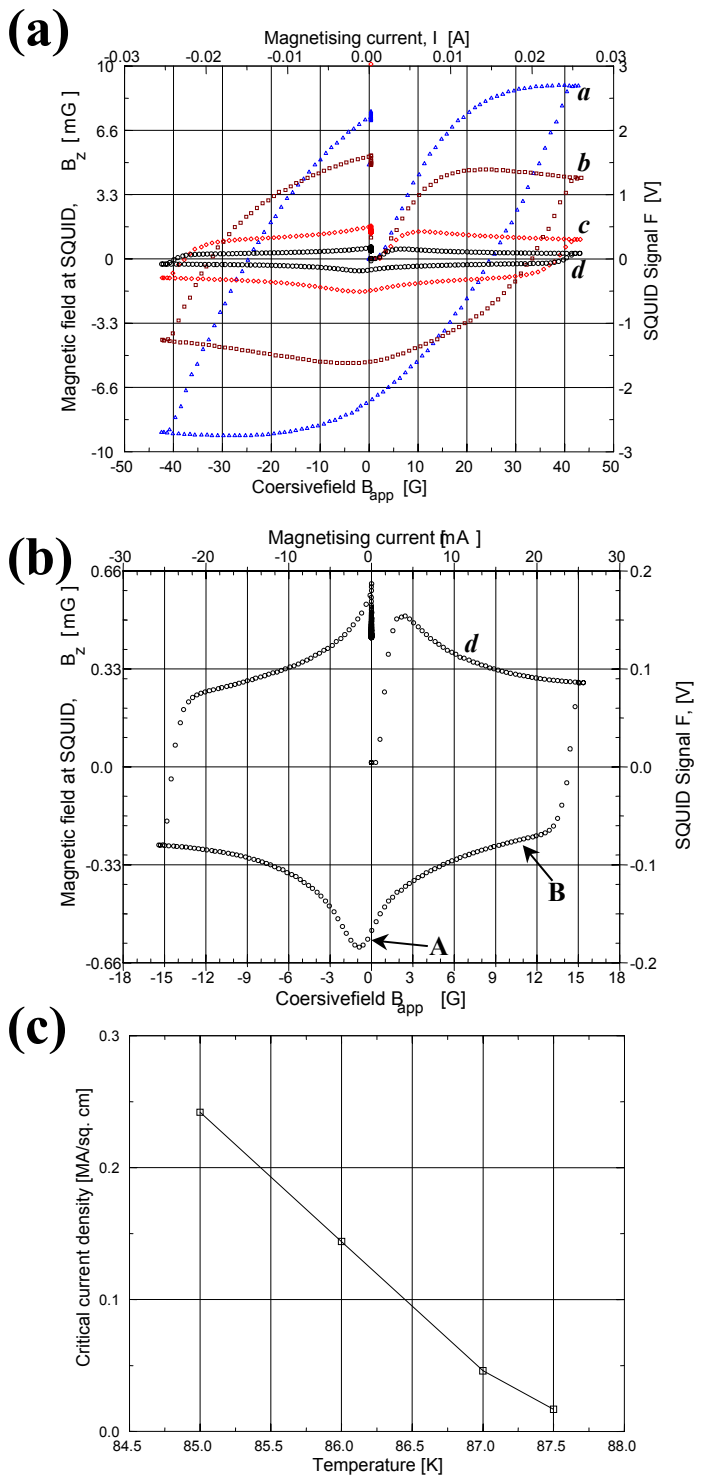

Figure 5-5: *(a) Hysteresis curves of the SQUID signal for various T and the same ramping procedure — in the order of larger to smaller height loops : 85.0 K, 86.0 K, 87.0 K and 87.5 K. One needs to multiply the magnetic field with $2r^{-3} = 0.0941$ to obtain m in units of emu. (b) Hysteresis curve at $T = 87.5$ K. This is the inner loop* **d** *of (a), with the vertical axis expanded. Notice the effect of the field dependent j_c. (c) Temperature dependence of SQUID signal maximum, proportional to critical current, as a function of T. The data is derived from* ***Table 5.2.***

Table 5.2: *The critical current density calculated using Eq. 5.13 and data from* ***Fig. 5-5a****.*

Loop	T [K]	$F_{\max}$ [V]	B_z [10^{-3} G]	m_{sat}	j_c [10^6 Acm^{-2}]
a	85.0	2.695	8.947	0.0951	0.242
b	86.0	1.606	5.330	0.0567	0.144
c	87.0	0.512	1.699	0.0181	0.0460
d	87.5	0.187	0.621	0.00660	0.0168

b, **c** and **d** then becomes negative, an observation which is not predicted by the two-dimensional critical state model (2DCSM) presented in Chapter 1. The critical current density is thus not field independent, but it is steadily reduced with increased external field. The applied field completes it's cycle, leaving the film in the remanent state, with zero applied field. The critical state model however provides some valuable insights into the current dynamics in the thin film. In 2DCSM, the magnetic moment saturates at

$$m_{sat} = \frac{\pi}{3c} R^3 d j_c \tag{5.13}$$

and $m_{sat} = \frac{\pi}{30} R^3 d j_c$ when j_c is expressed in A/cm^2. Using $R = 0.5$ cm and $d = 3 \times 10^{-5}$ cm, we have $j_c = 2.5465 \times 10^6 m_{sat}$.

If we assume the highest point of each curve represents a current distribution where the bulk of the film is in the critical state, but the field on the film has not yet significantly reduced the critical current, we can estimate j_c. The far field of a magnetic dipole moment is given by $B_z = 2mr^{-3}$, where the SQUID is located on the imaginary $z-$axis running through the film's center, and the film lies in the $xy-$plane, as discussed in Chapter 1. Using Eq. 5.10 and Eq. 5.13 we have

$$j_c = \frac{30}{2\pi d} \frac{r^3}{R^3} \kappa F \tag{5.14}$$

$$j_c = 8.984 \times 10^4 \times F \tag{5.15}$$

Fig. 5-5(c) shows the relation of $j_c - T$ close to T_c (from Table 5.2). Extrapolating the critical current down to 77 K, yields $j_c(77\text{ K}) = 1.026 \times 10^6$ A/cm^2. This value is in line with results in the literature. In the region close to T_c, j_c rapidly rises with a decrease in T. This explains why the height of the loops increases strongly with lower temperatures. The shape of the hysteresis loops changes dramatically, due to field dependance of the critical current. Loop **a** shows the hysteresis when j_c is fairly high and not as field dependent as with loops **c** and **d** for the small field operative in the experiment. The suppression of j_c with increasing B is more pronounced at temperatures very close to T_c (loops **c** and **d**), but the scale of the graph prevents the reader to fully appreciate the extent, see **Fig. 5-5(b)**. In fact, the dependence of j_c on the applied magnetic field can be approximated from the shape of the

hysteresis curve in **Fig. 5-5(b)**, where the section indicated by **A** and **B** shows the functional form of j_c versus B_{app}.

Discussion

The use of critical state models to qualitatively and quantitatively explain hysteresis phenomenon in superconductors is an established practice. For example, R.J. Charles *et al*[145] reported hysteresis in a bulk sample of lead in uniform fields, at 4.2 K, and found very good correspondence with the Bean model[60, 61] up to applied fields of 5500 G.

Due to the large aspect-ratio as compared to the long cylinder initially considered by Bean, the analysis is complicated because of the large demagnetisation effect. Inhomogeneous self-fields of currents become rather important in the film, especially near the periphery. A proper experimental analysis of the current and perpendicular field (B_z) distribution was not possible, since the means to probe the local field or current was not at our disposal. However, the magnetisation hysteresis loops can be studied to determine j_c and to estimate the magnetic field dependence of the critical current. In our experiment, the films were driven to saturation, and j_c was determined using the 2DCS model of P.N. Mikheenko *et al*[66] and J. Zhu *et al*[67]. The hysteresis curves were compared to the loops calculated in Chapter 1 from the 2DCS model, and a satisfactory fit was found for the curve taken at 85 K, but for loops recorded at higher temperature, the field dependence of j_c caused the loops to deviate significantly from the theoretical curves. In contrast, at liquid helium temperature, E. Moriatakis *et al*[147] found that the 2DCS model agrees with magnetisation measurements of thin film $YBa_2Cu_3O_7$ at 4 K. In their case, for fields much higher than $B_c \approx 590$ G the film can be considered a superconducting disk in the critical state with current density $j(r) = j_c$ flowing in most of the sample area.

Several authors have reported on magnetic field mapping experiments on their samples, usually superconducting thin films or discs. Various methods were employed: scanning Hall probe[148], Hall probe mounted on a three-dimensional robotic system[149], magneto-optical layers where the angle of Faraday rotation of polarised light indicated the magnetic field strength[150, 151] and high resolution scanning SQUID microscope[152] These papers report on field mapping at various temperatures for different geometries. However, none reports any result on the flux creep dynamics, and this area of research would be of particular interest, since there are no data on the change of field or current profiles during flux creep.

5.3.3 Isothermal flux decay

Flux creep in high temperature superconductors is an active area of research because many of the processes of this complex phenomenon are still only partially understood. The flux creep behaviour

near the critical temperature is particularly controversial, and theoretical work has not explained all the observed behaviour[139, 140].

We investigated flux decay in a high-temperature superconducting thin film at temperatures close to T_c. The $c-$axis oriented $YBa_2Cu_3O_7$ film (*sample A*) was magnetised to the remanent state in the experimental set-up described in Section 5.2, the magnetisation procedure was described in Section 5.3.1. During the magnetisation run and subsequent flux decay run, the sample temperature was kept constant for the duration of the experiment.

During the flux decay run, lasting from several minutes up to 3 hours, the isothermal relaxation of the SQUID signal $F(t)$ was observed. The decay of the magnetic moment $m(t) \propto F(t)$ occurred due to flux creep, causing a decay of the circulating superconducting currents. The relaxation was recorded for various levels of maximum magnetisation current ($1.2 - 25$ mA) and various ramp rates ($10 - 100$ mHz); the functional form of the curves was reproducible to high accuracy. The long time dependence (10 s and longer) follows a power law dependence with time. **Fig. 5-6** shows the isothermal flux decay for the sample at various temperatures close to the critical temperature.

In **Fig. 5-6**, the raw data is shown for increasing temperatures in the first column (a). The second column (b) shows the same data on a logarithmic scale. Clearly, the data points in column (b) depart significantly from a straight line in all cases, thus the data does not follow a logarithmic dependence

$$\frac{F(t)}{F_0} = 1 - \frac{kT}{U_0} \ln\left(\frac{t}{t_0}\right), \tag{5.16}$$

on time as predicted by Anderson and Kim[3, 4], see Chapter 1. Instead, the magnetic signal follows a power-law time decay

$$\frac{F(t)}{F_0} = (1 + t/t_0)^{-p} \tag{5.17}$$

with parameter $p < 1$ and a time scale t_0, which could be determined as non-zero only close to T_c. Experimental points represent the SQUID signal $F(t) \propto (t + t_0)^{-p}$. The fitting parameters for the different curves are given in **Table 5.3**.

Table 5.3: *Fitting parameters for* ***Fig. 5-6****.*

$T_c - T$ [K]	F_0 (normalization factor)	p	t_0 [s]
0.05	$F(t = 1.1$ s)	0.78	12
0.12	$F(t = 1.1$ s)	0.34	4
0.15	$F(t = 4$ s)	0.18	0.3
0.21	$F(t = 1.1$ s)	0.12	0
0.32	$1.3F(t = 2$ s)	0.087	0

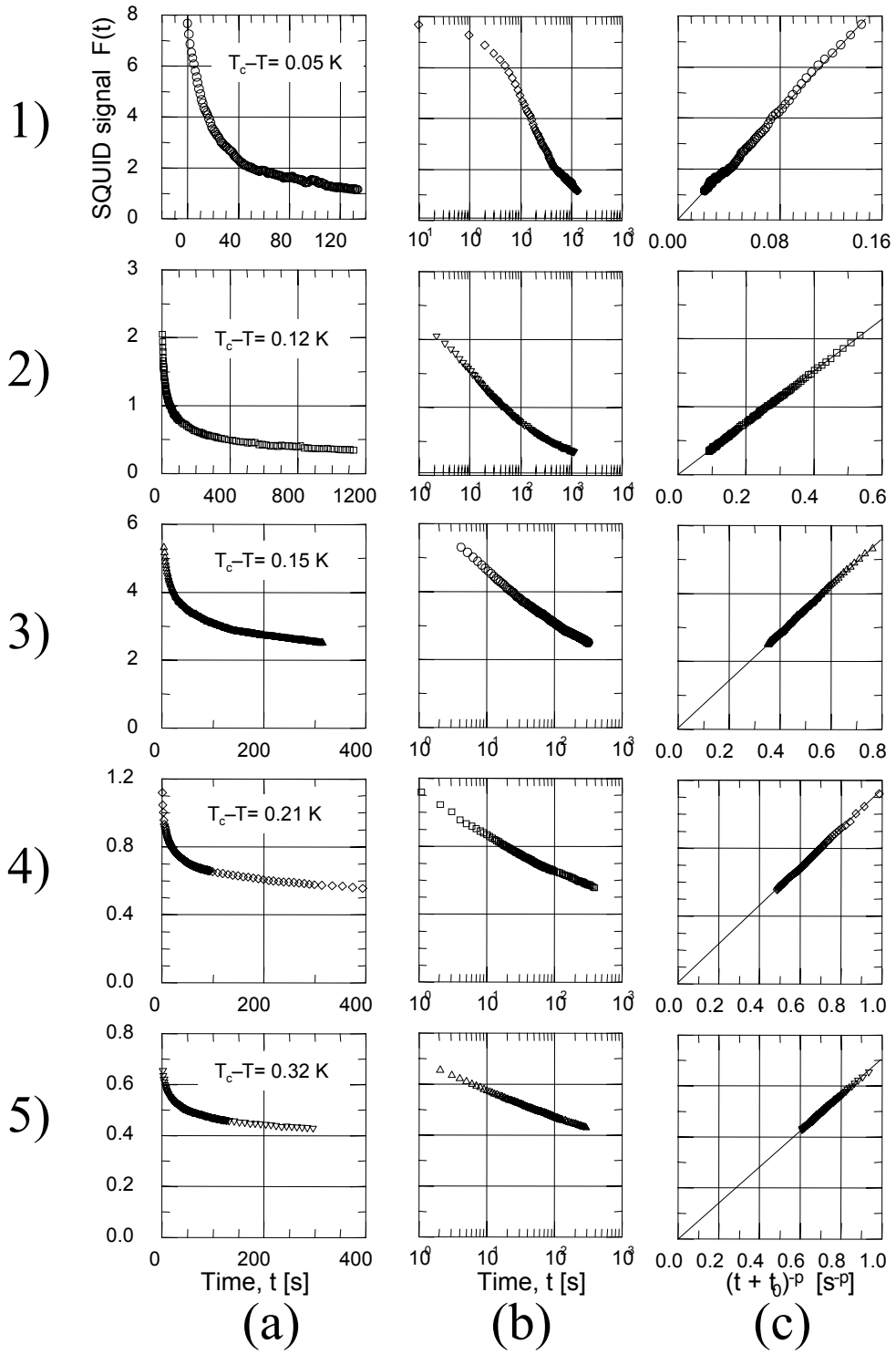

Figure 5-6: *Remanent flux relaxation data (SQUID signal F vs. time) at various temperatures in the vicinity of T_c = 88.7 K. The different rows 1-5 show the experimental data recorded at the indicated temperatures. The columns (a), (b) and (c) show the time parameter in linear, logarithmic and power law ($(t+t_0)^{-p}$) scales, respectively. The fitting parameters for the different curves are given in the text. The solid straight lines are the result of linear regression analysis of the experimental data.*

The power law decay has been reported by other authors[7, 1]. For not very long relaxation such that $\ln(t/t_0) \ll 1/p$, the power-law dependence could be reduced[2] to the well known Anderson-Kim logarithmic decay described in Chapter 1:

$$\frac{F}{F_0} \simeq 1 - p\ln(1 + t/t_0). \tag{5.18}$$

The question arises whether the power law dependence $F = F_0(1 + t/t_0)^{-p}$ has any theoretical reasons. In the case of a plate in a parallel field, the nonlinear diffusion equation describing current flow has been solved exactly by V.M. Vinokur *et al*[59], using a logarithmic barrier

$$U = U_0 \ln(j_c/j) \tag{5.19}$$

with $\sigma \equiv U_0/kT \gg 1$. Their solution yielded a power-law time dependence $j/j_c \simeq (1 + t/t_0)^{-1/\sigma}$ with macroscopic time scale t_0. This type of decay is in agreement with our observation, eq. 5.17.

We verified the validity of this decay for our case of a superconducting disk magnetised in a perpendicular field. The differential equation is determined by Maxwell's equations and the nonlinear relation between current density and electric field $E = E(j)$. Due to the axial symmetry, only circumferential components of $\mathbf{E}$ and $\mathbf{j}$ contribute. Thus,

$$\frac{\partial j}{\partial t} = \frac{c^2}{4\pi}\frac{\partial}{\partial r}\left(\frac{1}{r}\frac{\partial(rE)}{\partial r}\right). \tag{5.20}$$

The nonlinear relation $E = E(j)$ can be constructed if we realise that the electric field is generated by the vortex motion, thus $E \propto v$, (from $\mathbf{E} = \frac{1}{c}\mathbf{B} \times \mathbf{v}$) the vortex drift velocity, introduced in Chapter 1. The vortex drift velocity is due to thermally activated motion of vortices, and follows the relation

$$v = v_0 e^{-U(j)/kT}. \tag{5.21}$$

Using the logarithmic barrier eq. 5.19, we find

$$v = v_0 \left(\frac{j}{j_c}\right)^{\sigma}, \tag{5.22a}$$

$$\sigma = U_0/kT. \tag{5.22b}$$

[2] For the derivation, use the well known relation $x^p = e^{p \ln x}$, the above relation then follows from an expansion to first order.

If we also take into account that the magnetic field is caused by the current, we have

$$E = \frac{4\pi}{c^2} v_0 d \left(\frac{j}{j_c}\right)^{\sigma} j. \tag{5.23}$$

Using eq. 5.20 and eq. 5.23, we derive

$$\frac{\partial j}{\partial t} = v_0 d \frac{\partial}{\partial r}\left(\frac{1}{r}\frac{\partial (r j^{\sigma+1}/j_c^{\sigma})}{\partial r}\right) \tag{5.24}$$

Eq. 5.24 can be solved by separation of variables: $j(r,t) = f(r)g(t)$. Of particular importance is the time component solution. We found that

$$\frac{\partial}{\partial t} g(t) = \beta g(t)^{\sigma+1} \tag{5.25}$$

where β is a constant to be determined by boundary conditions. The temporal differential equation yields a solution of the form $g(t) = (\beta_1 \sigma t + \beta_2)^{1/\sigma}$. An approximate solution of Eq. 5.24 for uniform j_c is:

$$j = j_c \left(\frac{(r/R)(2 - r/R)}{1 + \sigma t/t_0'}\right)^{1/\sigma} \tag{5.26}$$

where the time scale constant is $t_0 = R^2/(3v_0 d) \sim 3$ s[139]. One should note that the shape of the spatial profile remains unchanged during the flux decay run, except that the magnitude decreases with time as $(1 + t/t')^{-1/\sigma}$ (with $t' = t_0'/\sigma$). This agrees with the experimental relation, as expressed in eq. 5.17. The solution 5.26 is in agreement with our experimental results 5.17, if we set $p = 1/\sigma = kT/U_0$.

The relative creep activation energy was extracted from several long decay runs, by fitting eq. 5.17 to the data to obtain the parameter p. **Fig. 5-7** shows the relative creep activation energy U_0/kT as a function of temperature. The large scatter of the experimental points is due to a temperature instability during the long decay runs. H. Darhmaoui *et al*[148] found values of U_0 in agreement with our results, but they did not measure U_0 in the range $0 < T_c - T < 2$. A sharp bend is visible at $T \approx 87$ K in **Fig. 5-7** which indicates that a regime dominated by different physical processes regarding vortices is entered. Krylov *et al*[139, 140] interprets this sharp bend that the critical region, where the fluctuations in the amplitude $|\psi|$ of the superconducting parameter becomes comparable with $|\psi|$ itself, is entered.

5.3.4 Warm-up run

The temperature dependence of the critical current density $j_c(T)$ of a $YBa_2Cu_3O_7$ thin film was obtained in the warming runs. The $YBa_2Cu_3O_7$ film (*sample A*) was magnetised to the remanent state in the experimental set-up described in Section 5.2, the magnetisation procedure was described in Section 5.3.1.

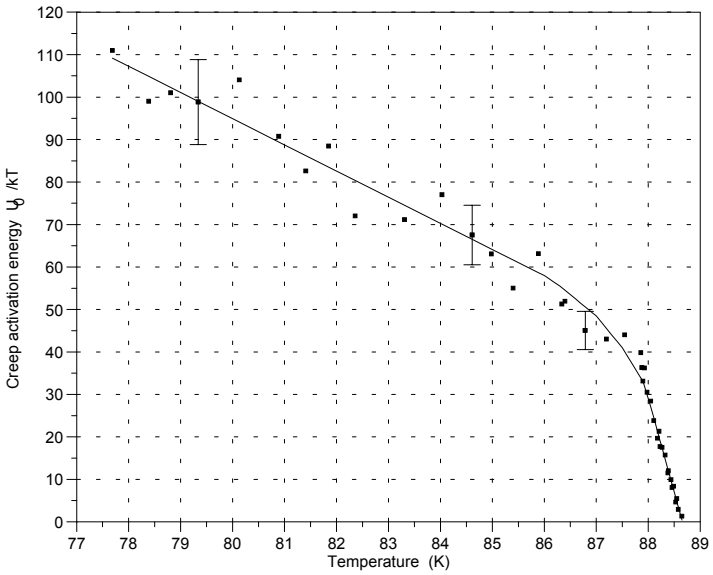

Figure 5-7: *Relative creep activation energy* $1/p = \sigma = U_0/kT$*, determined using eq. 5.17.*

After the magnetisation cycle and an initial short relaxation at some temperature 77 K $< T_1 < T_c$, the heater power was increased and during several minutes the sample was slowly heated to above the critical temperature. During the warming run, the signal $F(t)$ was recorded, thus monitoring directly the change in the circulating superconducting current density $j_c(T)$ with temperature. The warming rate $dT/dt \sim 10$ mK/s was fast enough to register nonrelaxed current density $j_1(T) \simeq j_c(T)$, as discussed in detail in ref. [139]. **Fig. 5-8(a)** shows a warm-up run of a magnetised YBCO thin film. The experimental error for j_c data is less than the symbol size. The temperature dependence of the calculated current density ($j_1 \simeq j_c \propto F$) is shown. **Fig. 5-8(b & c)** shows the temperature dependence of $\sqrt{F}$ in the critical region. Note near T_c, the temperature dependence of $\sqrt{F}$ is almost linear. The relation $F = a(T_c^* - T)^q$ was tested for the range -1.5 K$< T - T_c < -0.2$ K. T_c^* is determined in **Fig. 5-8(b & c)** as the temperature where the linear regression cuts the horizontal axis. It was found that $q = 2.00$ with standard error 0.05.

Very close to T_c, at $T_c - T \sim -0.2$, $\sqrt{F}$ departs from the linear relationship. This phenomenon is related to sample inhomogeneity which manifests in regions of slightly differing critical temperature. Krylov *et al*[139] estimated that a part of the film has the zero current critical temperature of 88.7 K, while the remainder of the film has a critical temperature centered around $T_c - 0.1$ K. **Fig. 5-9** shows the T dependence of j_c and the relative creep activation energy U_0/kT, determined as described in Section 5.3.3. The solid lines are guides to the eye. **Fig. 5-9** is a combination of **Fig. 5-7** and **Fig. 5-**

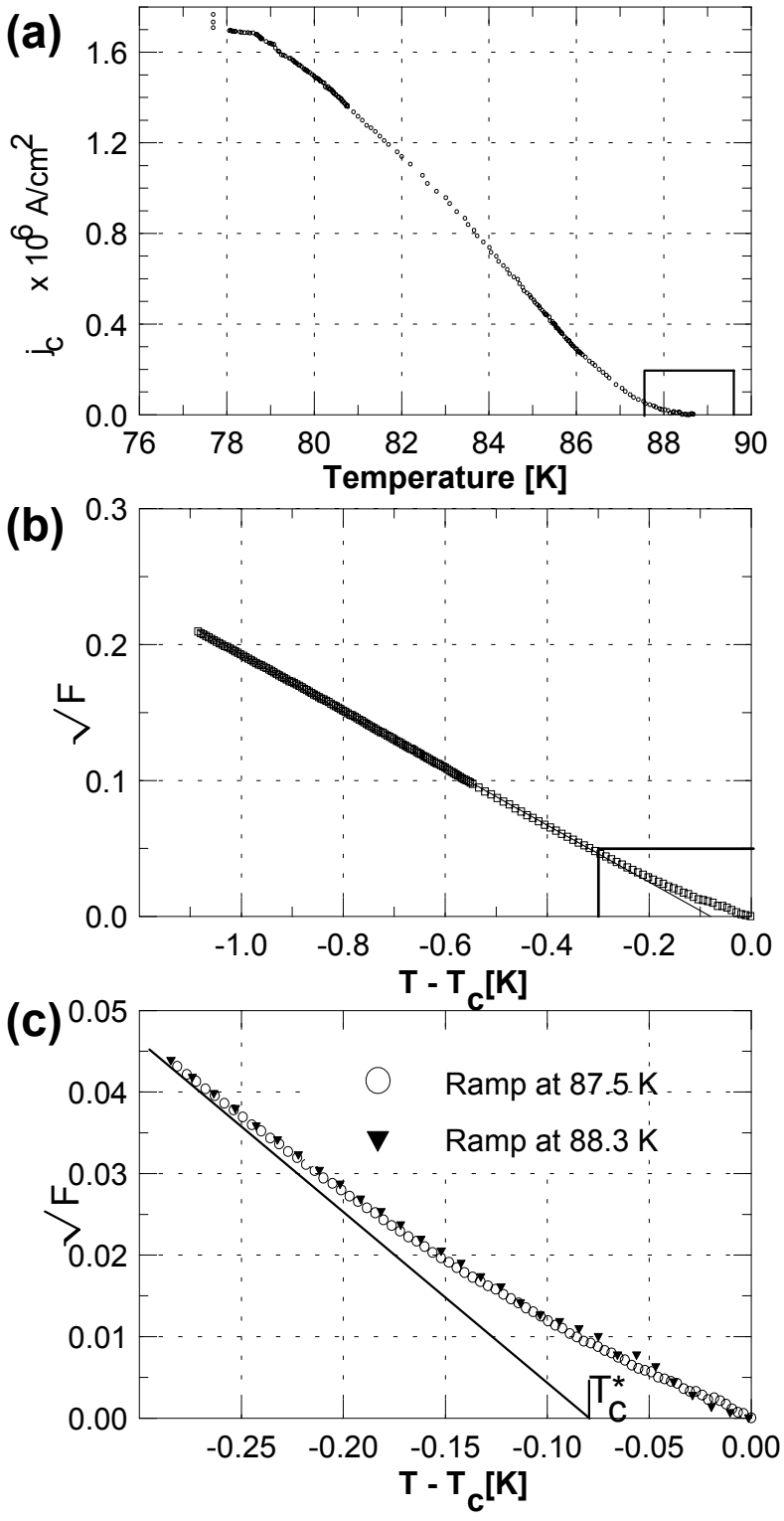

Figure 5-8: *(a) Temperature dependence of the critical current density j_c. The experimental error for j_c data is less than the symbol size. (b) Temperature dependence of $\sqrt{F}$ in the critical region. (c) Temperature dependence of $\sqrt{F}$ in the region $T_c - T < 0.3$ K presented on an enlarged scale. Different symbols correspond to different warming runs after magnetizing cycles at indicated temperatures. The straight solid lines are the result of linear regression analysis of experimental data taken in the range 0.3 K $< T_c - T <$ 1.1 K.*

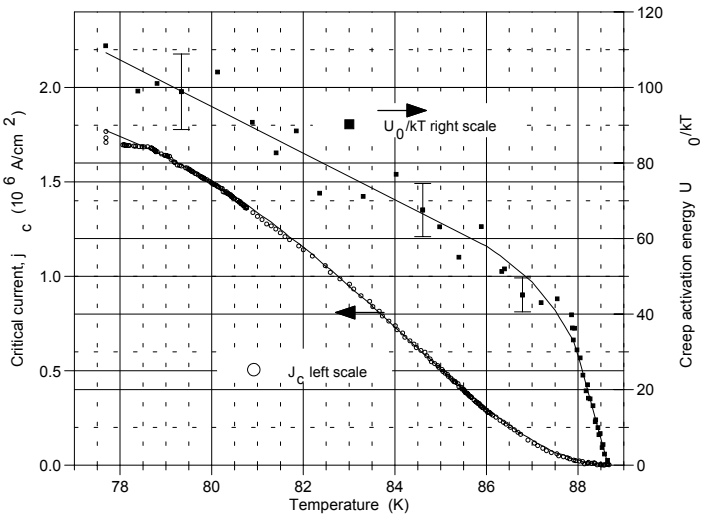

Figure 5-9: *Temperature dependence of the critical current density j_c and the relative creep activation energy U_0/kT, determined as described in the text. The experimental error for j_c data is less than the symbol size. The solid lines are guides to the eye.*

8(a). As indicated in Section 5.3.3, the activation energy undergoes a change in slope at $T = 87$ K, and this is reflected in a change of curvature of j_c in the same temperature region, indicating a different physical process driving flux decay.

5.3.5 Creep freezing effect

An interesting phenomenon regarding the temperature dependence of the relaxation rate of magnetised film has been observed during our relaxation experiments as described in Section 5.3.3. It is well known that the relaxation rate is temperature dependent as can be seen from **Fig. 5-6** and explicitly from eq. 5.17 via the parameter $p = kT/U_0$, j_c and U_0. A similar effect was reported earlier in experiments at low temperatures[1]. However, the pronounced slowing of relaxation with only a small drop in temperature from a starting temperature close to T_c warrants some further study to explain the effect.

Experimental runs were performed as follows: The magnetisation cycle was made at the sample temperature T_1, after the sample (*sample A*) was zero field cooled in the usual configuration, described in Sections 5.2 and 5.3.1. **Fig. 5-10(a)** shows a schematic diagram of the progress of the experiment. At some moment (indicated by **C** in **Fig. 5-10(a)**), during the isothermal relaxation the heating power was decreased, and the sample cooled. During this process the film temperature T could be determined

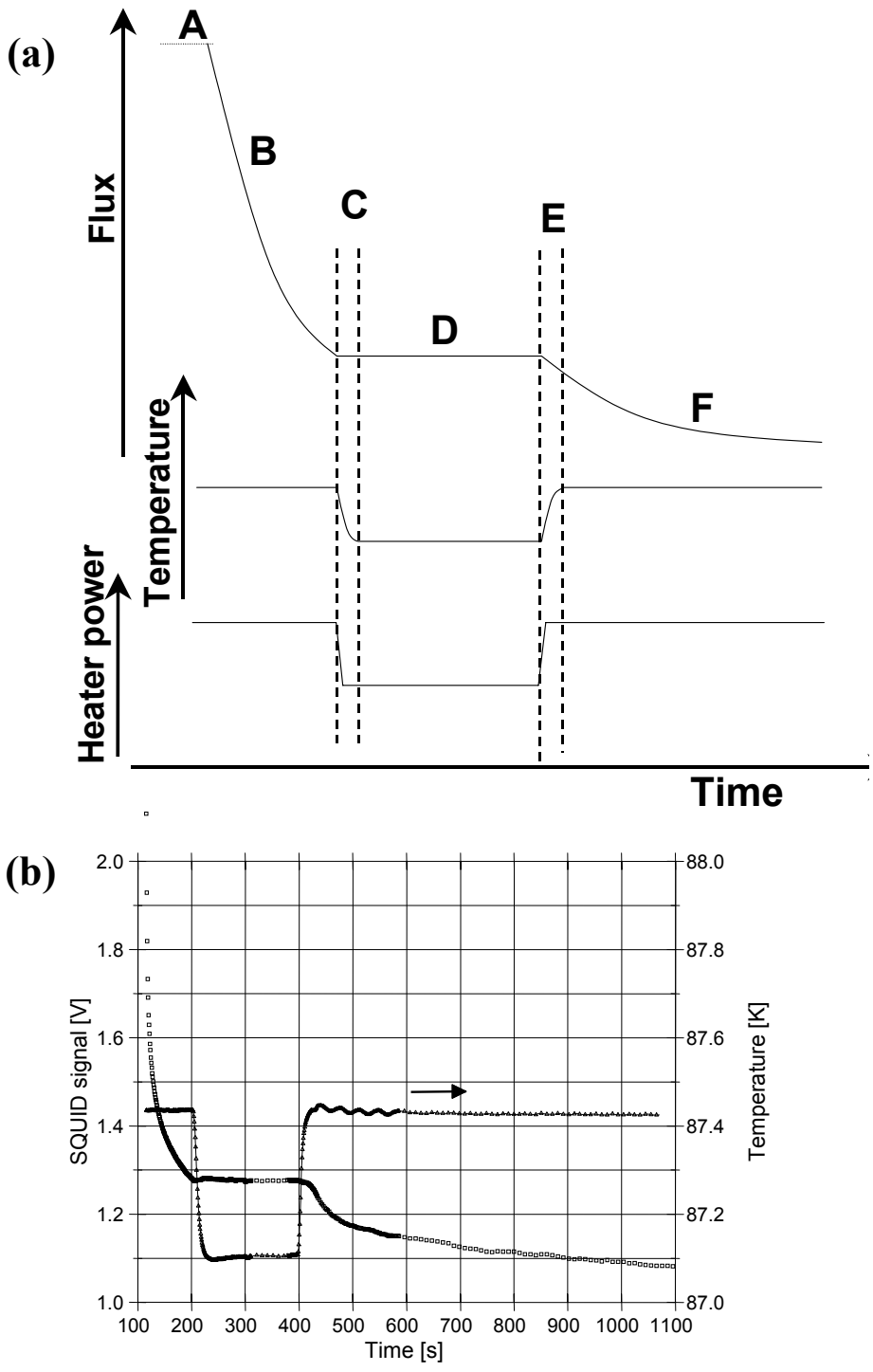

Figure 5-10: *(a) Schematic representation of the change in flux, sample temperature and heater power during the course of the experiment. A: magnetisation cycle, B: isothermal relaxation, C: cooling of sample, D: frozen flux region, E: heating of sample, F: relaxation rate regained. (b) Time history of a creep freezing experiment.*

with sufficient accuracy from the measured block temperature.

The flux creep rate responded sharply to the decrease in temperature, as shown in **Fig. 5-10(b)**. Within the interval $\delta T = T_1 - T = 10$ mK, the flux relaxation rate $|dF/dt|$ dropped several times, and at still lower temperatures became practically zero. In the range 0.3 K $\leq T_c - T_1 \leq$ 1.0 K, when the temperature drop $\delta T > 0.2$ K, the magnetic field was completely frozen inside the sample, and the SQUID showed constant field for hours. To release again the frozen flux, the sample was heated (indicated by **E**).

In the experimental run depicted in **Fig. 5-10(b),** the initial temperature was $T_1 = 87.43$ K. After about 200 s, the temperature was lowered by adjusting the set-point of the temperature controller, and the temperature stabilised at $T_2 = 87.11$ K. The sample was kept at T_2 until $t = 400$ s, when the set-point was increased and the sample temperature returned to T_1. The rate of heating and rate of cooling was the same order of magnitude, the cooling rate was 18 mK/s and the heating rate was 27 mK/s. After the heating ramp, the sample temperature fluctuated around the set-point temperature, with a period of 35 s and an initial amplitude of 27 mK, but the oscillations died out after about 150 s. This is an artifact of the *PID*-type *LakeShore* temperature controller.

The SQUID signal remained constant (within the sensitivity limit of 0.1%) until the rising temperature reached the value $T \simeq T_1 - 10$ mK. Within the interval $\delta T \simeq 10$ mK the flux creep recovered it's initial value $|dF/dt|_1$ which occurred before freezing, and as the temperature continued to grow linearly with time, the signal dropped exponentially for several seconds more, finally approaching much lower values corresponding to the lower $j_c(T)$ at elevated temperatures $T > T_1$. We can analyse the effect of lowering the temperature on the vortex motion in the following manner:

The vortex drift velocity is given by eq. 5.22:

$$v = v_0 \left(\frac{j}{j_c}\right)^{U_0/kT} . \tag{5.27}$$

We read the relevant physical parameters from **Fig. 5-9**:

T [K]	$\sigma = U_0/kT$	j_c [$\times 10^6$ A/cm^2]
$T_1 = 87.43$	$\sigma_1 = 42.5$	$j_{c1} = 1.04$
$T_2 = 87.11$	$\sigma_2 = 47.0$	$j_{c2} = 1.30$

We now can write

$$v_1 = v_0 \left(\frac{j}{j_{c1}}\right)^{\sigma_1} = v_0 \omega_1^{\sigma_1} \tag{5.28a}$$

$$v_2 = v_0 \left(\frac{j}{j_{c2}}\right)^{\sigma_2} = v_0 \omega_2^{\sigma_2} = v_0 (k\omega_1)^{\sigma_2} \tag{5.28b}$$

$$= v_0 \omega_1^{\sigma_1} \omega_1^{\sigma_2 - \sigma_1} k^{\sigma_2} = v_1 \omega_1^{\sigma_2 - \sigma_1} k^{\sigma_2} \tag{5.28c}$$

where $k = j_{c1}/j_{c2} = 0.8$ in our case. We can estimate ω_1 from **Fig. 5-9**, $\omega_1 \lesssim 0.6$. This yields the result

$$v_2 \lesssim 2.8 \times 10^{-6} \times v_1. \tag{5.29}$$

We thus estimate a 6 orders of magnitude reduction in number of vortices able to escape the pinning potentials and participate in flux creep, for a reduction of 32 mK in temperature from an initial value of $T_1 = 87.43$ K. This is quite dramatic and explains the almost immediate freezing of flux as soon as the temperature is lowered. In our data we have $\ln(t/t_0) \ll 1/p = \sigma$, (see the analysis in Section 5.3.3) therefore we can use the Kim-Anderson logarithmic decay described in Chapter 1. **Fig. 5-11(a)** shows the experimental data of **Fig. 5-10(b),** with the frozen part removed. The same data is repeated in **Fig. 5-11(b)** on a logarithmic scale.

As can be clearly seen from **Fig. 5-11(b)**, the data does not indicate that the sample returns to the same state as before the creep freezing. The creep is marked slower. The influence of the thermal oscillations after T_1 is reached (after the flux freezing) could be responsible for the slower creep. Thus its effect should be further investigated to determine whether the sample in fact returns to the same magnetisation situation. The temperature fluctuations should be stabilised however.

5.4 Conclusions

In this chapter we have explored the flux creep behaviour of a $c-$axis oriented $YBa_2Cu_3O_7$ thin film near the critical temperature $|T - T_c| \leqslant 10$ K. An experimental cell was designed and manufactured to support a field coil with the sample in it's center. A very sensitive SQUID magnetometer was positioned to measure magnetic field directed perpendicular to the film's surface. A compensation coil was used to cancel the field coil's contribution at the SQUID, such that only the magnetisation of the film was measured by the SQUID.

The measurement setup was computer controlled, to facilitate accurate data acquisition. Sample temperature was determined to an accuracy of 2.5 mK. Model calculations showed that the magnetic field did not vary over the width of the film by more than 8.2%. The compensation coil did not reduce field strength at the film surface by more than 2%. The $YBa_2Cu_3O_7$ film was magnetised after being cooled in zero field (ZFC). The magnetisation cycle was accomplished by ramping the current through the field coil with a wave form generator using a single sawtooth wave form cycle, lasting 100 s.

Hysteresis loops were recorded at various temperatures. The loop recorded at lower temperatures $T \leqslant 86.0$ K did not reveil any magnetic field dependence, since the field was not strong enough. For loops recorded above 86.0 K, the strong field dependence of the critical current rendered the loops too complex for the simple Zhu model[67], since a field dependance structure was introduced. An estimate

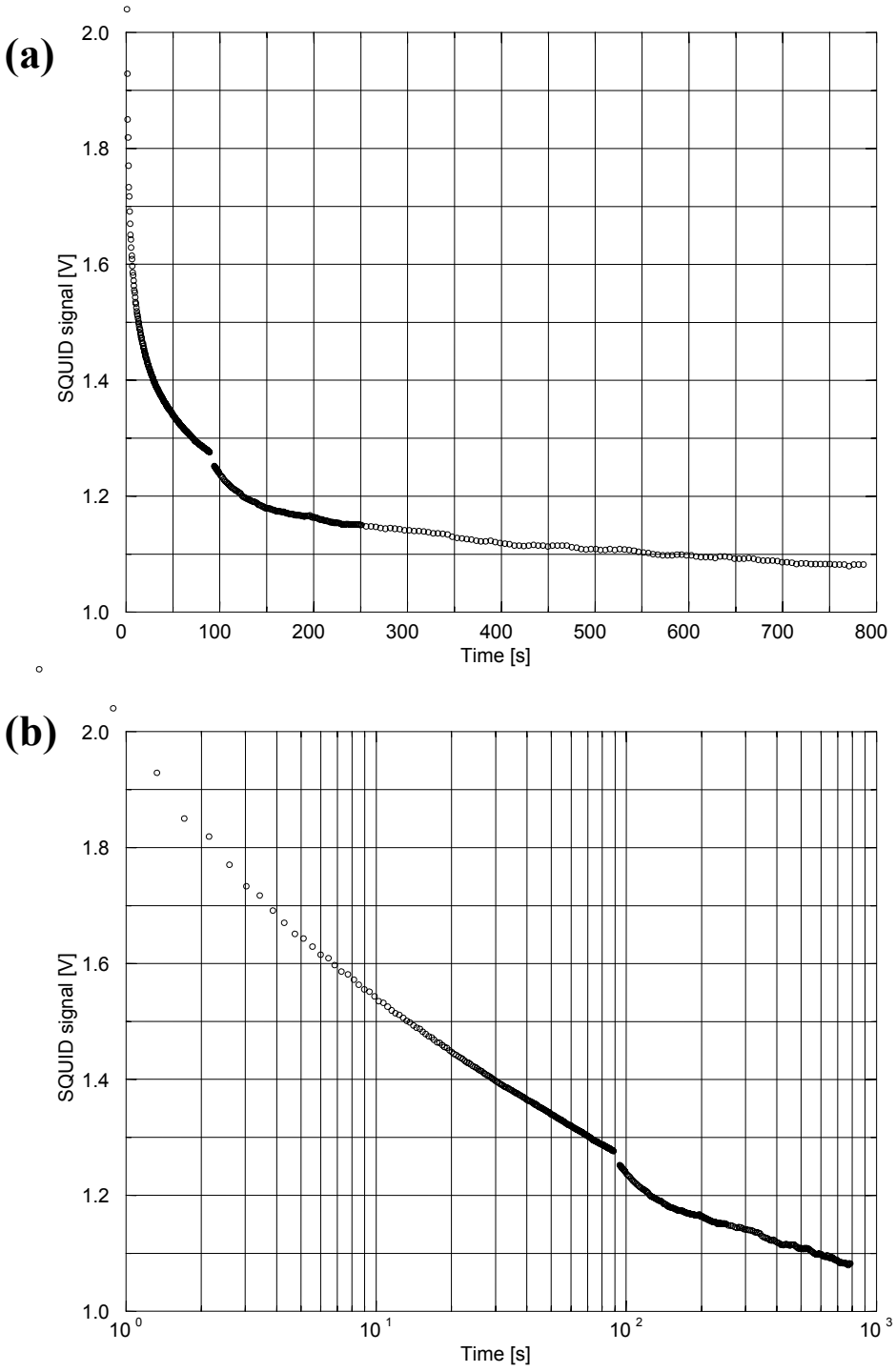

Figure 5-11: *(a) Time decay of the remanent flux, where the frozen part have been deleted. (b) Logarithmic view of the time decay of the remanent flux, where the frozen part has been deleted.*

for $j_c(T)$ in the range $85 - 87.5$ K was made using the hysteresis loops.

Isothermal flux decay experiments were conducted using the same sample as mentioned above. The sample was zero field cooled and then magnetised to the remanent state, in the manner described above. The long time decay (10 s and longer), followed a power law decay

$$\frac{F(t)}{F_0} = \left(1 + \frac{t}{t_0}\right)^{-p} \tag{5.30}$$

with $p < 1$. We identified the exponent p with the creep activation energy U_0 by

$$\frac{1}{p} = \frac{U_0}{kT}. \tag{5.31}$$

The creep activation energy is determined as a function of temperature close to T_c and is shown in **Fig 5-7**. A sharp bend is visible at $T \approx 87$ K in **Fig. 5-7** which indicates that a regime dominated by critical fluctuations is entered. In ref. [139, 140] it was suggested that the critical region is entered where the fluctuations of the order parameter ψ becomes comparable with the amplitude of ψ itself.

The temperature dependence of the critical current density $j_c(T)$ of the YBCO thin film close to T_c was obtained in warming runs. Again, after ZFC and magnetisation to the remanent state, the sample was heated at a rate $dT/dt \sim 10$ mK/s, fast enough to register non-relaxed current density. Experimental results are shown in **Fig. 5-8**. It was found that

$$\sqrt{F(T)} \sim (T_c - T) \tag{5.32}$$

to high accuracy, in the range $-1.5 \leqslant T - T_c \leqslant -0.2$ K.

During the isothermal flux creep experiments a *creep freezing effect* was observed related to the strong temperature dependence of the relaxation rate and j_c. A pronounced slowing of relaxation with only a small drop in temperature from a starting temperature close to T_c was observed. Experiments were conducted by initiating an isothermal flux decay run as described above. At a certain point the temperature was slightly lowered, and the flux decay came to an end within experimental accuracy. When the temperature was restored to the original, the flux decay resumed again at the original rate. An argument based on vortex drift velocity was employed to explain the phenomenon qualitatively.

In summary, flux creep was studied close to T_c in c-axis oriented $YBa_2Cu_3O_7$ thin film. Creep activation energy U_0 and critical current density j_c was determined as a function of temperature close to T_c, providing important data to an aspect of high T_c-superconductivity which is still a matter of debate. In particular it is still an open question whether restoring the temperature in a creep freezing experiment in fact restores the film to it's original state before the freezing.

Chapter 6

Conclusions

The main technological achievement of the present work is the design, manufacturing and installation of a pulsed laser deposition (PLD) system, which resulted in the production of good quality $YBa_2Cu_3O_7$ thin film with $T_c \gtrsim 88$ K. These films were $c-$axis orientated, epitaxial and thus aligned with the MgO or $SrTiO_3$ substrates. At the *National Accelerator Centre*, we designed and produced a versatile PLD system, the first such system in Africa, capable of accurately controlling the deposition environment i.e. ambient gas pressure, substrate temperature, laser energy density at the target and substrate-target distance. A multi-target system was later added to the PLD system.

Various techniques were employed to study the deposited films. Rutherford backscattering spectroscopy (RBS) was used to determine stoichiometry and film thickness. Naturally, the correct cation ratio's Ba/Y and Cu/Y are important to ensure a high critical temperature. X-ray diffraction analysis yielded information on the structural properties and orientation of crystalline grains. In particular, a representative sample was subjected to pole-figure analysis, which confirmed that the grains all pointed in the same direction, imposed by the cubic lattice of the single crystal substrate material.

The PLD system proved to be quite versatile. It was used to deposit different materials, most notable was good quality thermochromic VO_2 thin films, magnetoresistive $La_xCa_{1-x}MnO_3$ thin films, and superconducting $YBa_2Cu_3O_7$ thin films. Metallic Au and Ag layers were also successfully deposited on $YBa_2Cu_3O_7$ thin films, to serve as protective coatings. The critical temperature of the best superconducting films was 90 K as measured by resistivity measurement.

The heater system was particularly problematic, because of the ease with which the *Thermocoax* heating elements overheat if not properly thermally connected to the stainless steel block in which it is housed. Resistive heaters are quite commonly used in deposition chambers, see e.g. [100], but their tungsten heating elements degrade in oxygen rich ambients. The solution was to use inconel sheathed

heating elements, e.g. *Thermocoax* by *Philips*, which was brazed into the heating block.

The correct mounting of the substrates to the substrate heater is very important to achieve good thermal contact and thus the desired substrate temperature. One must ensure that the silver paint is evenly spread between the substrate and the substrate holder and properly dry before attempting to commence the deposition process. Non-shiny parts on a deposited film are indicative of non-epitaxial, amorphous film growth resulting from under heated parts of the substrate.

An infrared pyrometer was used to verify the temperature indicated by the thermocouple. Taking the emissivity of stainless steel into account ($\varepsilon \approx 0.4$), the temperature indicated by the pyrometer and the value measured by the thermocouple did not differ by more than 10°C in the range $650 - 800$°C.

Finally, two different studies which the author participated in, were reported. Thermochromic VO_2 thin films were deposited on silicon, quartz and sapphire substrates using the PLD system. The thin films exhibited the desired optical transmittance transition at ~ 65°C. The results were published in ref. [95]. The author also, together with E.B. Nyeanchi, deposited magnetoresistive $La_xCa_{1-x}MnO_3$ thin films on $LaAlO_3$ substrates. The samples demonstrated ferromagnetic metallic behaviour at low temperatures, in particular they exhibited a magnetoresistive transition at -73°C[99].

The physical properties of deposited $YBa_2Cu_3O_7$ thin films was investigated and described in **Chapter 4**. A critical temperature of ~ 90 K was achieved in *c*-orientated films deposited on MgO and $SrTiO_3$. The composition of such optimal films was found to be the ideal 1-2-3 of $YBa_2Cu_3O_7$ within the precision of the RBS measurement. Moreover, the material was found to be predominantly *c*-axis orientated; with ideal orientation on the underlying substrate. None or very little impurity phases was present. This was found by detailed XRD analysis of two selected samples. YBCO films on $SrTiO_3$ were found to align their *a*/*b*-axis with the *a*-axis of $SrTiO_3$.

The deposition profile of the laser ablation plume was studied by depositing a thin film on a large area Si substrate. The plume was verified to have a $f(\theta) \propto \cos^p \theta$ density profile, resulting in a $T(\theta) \propto \cos^{p+3} \theta$ thickness profile on the substrate. The spatial anisotropy of the profile also agreed with established observation of the plume behaviour.

Another result was general understanding of the role of deposition parameters in our PLD system. Although the stated purpose of this study was not to undertake a complete investigation of the influence of all the deposition parameters, certain conclusions could be made:

- Best film ($T_c \sim 90$ K) was obtained for the deposition parameters given in **Table 6.1**,

  using a XeCl excimer laser running at 10 pulses per second.

- At 780°C the deposition process is much less sensitive for small changes in the deposition parameters : $P_{O_2} = 0.2 - 0.3$ mbar and $\Phi = 2 - 3$ J/cm^2 etc. than at 680°C. This is a direct result

Table 6.1: *Best film ($T_c \sim 90$ K) was obtained for the deposition parameters.*

Laser energy density Φ	2.0-3.0 J/cm^2
Substrate temperature T_{dep}	780°C
Oxygen partial pressure P_{O_2}	0.2 mbar
Target-substrate distance D	35 mm

from easier surface activation for deposited species at the elevated temperature. At 680°C the deposited species must arrive with high enough kinetic energy to cause surface diffusion and the breaking of surface bonds necessary for epitaxial growth. Thus, T_{dep} plays the predominant role in determining the quality of films.

- Similarly, the surface roughness of films deposited at 780°C with a range of $\Phi = 2 - 4$ J/cm^2 does not change significantly.

The results of this work seems supported by the existing corpus of literature on the PLD of $YBa_2Cu_3O_7$. All the results on RBS, XRD, AFM, the role of the deposition parameters are in agreement with the current knowledge.

The production of films was predominantly for studies of superconductivity, which started with *ac* measurements. A cryo-insert containing a two-coil transformer-like set-up for measuring film *susceptibility* was designed, manufactured and used to study the superconducting transition. The method operates with oscillating current in the frequency range $1-100$ kHz. Initially, the secondary astatically wound coil is positioned co-axially inside the primary such that the total induced e.m.f. is zero due to cancellation in the two parts of the secondary. When the film has completed it's superconducting transition, currents induced in the film results in a disbalance in the secondary and an induced oscillating *e.m.f.* is detected using a lock-in amplifier.

A critical state model for thin superconducting films has been extended to yield first order Fourier components $\sim \cos\omega t$ and $\sim \sin\omega t$ in the case of uniform harmonic field applied perpendicular to the film's surface. Together with a simple model for critical current near T_c, $j_c \propto (1 - T/T_c)^p$; $p \sim 2$. Good fits have been obtained from experimental data, yielding T_c, and confirming the plausibility of the model. The model has the appealing property of being simple and in-phase and $90°-$components are easy to calculate.

As an advanced part of our research on superconductivity, we have investigated flux creep of a $c-$axis oriented $YBa_2Cu_3O_7$ thin film (10 mm $\times$ 10 mm $\times$ 300 nm, $T_c = 88.7$ K) near the critical temperature $|T - T_c| \leqslant 10$ K (**Chapter 5**). An experimental cell has been designed and manufactured to support a field coil with the sample in it's center. A very sensitive SQUID magnetometer was positioned to measure

magnetic field directed perpendicular to the film's surface. A compensation coil was used to cancel the field coil's contribution at the SQUID, such that only the magnetisation of the film was measured by the SQUID.

The measurement setup was computer controlled, to facilitate accurate data acquisition. Sample temperature variation was determined to an accuracy of 2.5 mK. Model calculations showed that the applied magnetic field did not vary over the width of the film by more than 8.2%. The compensation coil did not reduce field strength at the film surface by more than 2%. The $YBa_2Cu_3O_7$ film was magnetised after being cooled in zero field. The magnetisation cycle was accomplished by ramping the current through the field coil with a wave form generator using a single sawtooth wave form cycle, lasting 100 s.

Hysteresis loops were recorded at various temperatures. The loops recorded at lower temperatures $T \leqslant 86.0$ K can be qualitatively understood using the Zhu model[67]. For loops recorded above 86.0 K, the strong field dependence of the critical current rendered the loops too complex for the simple Zhu model, since a field dependance structure was present. An estimate for $j_c(T)$ in the range $85 - 87.5$ K was made using the hysteresis loops.

Isothermal relaxation of trapped flux was investigated. The sample was zero field cooled and then magnetised to the remanent state. The long time decay (10 min and longer), followed a power law

$$\frac{F(t)}{F_0} = \left(1 + \frac{t}{t_0}\right)^{-p} \tag{6.1}$$

with $p < 1$.

We identified the exponent p with the creep activation energy U_0 by

$$\frac{1}{p} = \frac{U_0}{kT}. \tag{6.2}$$

The creep activation energy is determined as a function of temperature close to T_c and is shown in **Fig 5-7**. A sharp bend is visible at $T \approx 87$ K in **Fig. 5-7** which indicates that a regime dominated by different physical processes regarding vortices is entered. In refs. [139, 140] it was suggested that the critical region is entered where the fluctuations in the amplitude of the superconducting order parameter ψ become comparable with the amplitude $|\psi|$ itself.

The temperature dependence of the critical current density $j_c(T)$ of the YBCO thin film close to T_c was obtained in warming runs. Again, after ZFC and magnetisation to the remanent state, the sample was heated at a rate $dT/dt \sim 10$ mK/s, fast enough to register non-relaxed current density. Experimental results are shown in **Fig. 5-8**.

It was found that

$$\sqrt{F(T)} \sim (T_c - T) \tag{6.3}$$

to high accuracy, in the range $-1.5 \leqslant |T - T_c| \leqslant -0.2$ K.

During flux creep experiments an interesting phenomenon *"creep freezing"* related to the strong temperature dependence of the relaxation rate was observed. A pronounced slowing of relaxation with only a small drop in temperature from a starting temperature close to T_c was observed. Experiments were conducted by initiating an isothermal flux decay run as described earlier. At a certain point the temperature was slightly lowered, and the flux decay stopped within experimental accuracy. When the temperature was restored to the initial value, the flux decay resumed at the previous rate before cooling. An argument based on vortex drift velocity was employed to explain the phenomenon qualitatively.

In summary, flux creep was studied close to T_c in $c-$axis oriented $YBa_2Cu_3O_7$ thin film. Creep activation energy U_0 and j_c was determined as a function of temperature close to T_c, providing important data to a problem of high$-T_c$ superconductivity which is still a matter of debate. In particular it is still an open question whether restoring the temperature in a creep freezing experiment in fact restores the film to it's original state before the freezing. The most important novel results concern the regime of critical fluctuations in the vicinity $T_c - T \lesssim 1$ K.

Bibliography

[1] Yeshurun Y., Malozemoff A.P., and Shaulov A. Magnetic relaxation in high-temperature superconductors. *Rev. Mod. Phys.*, **68**(3), 911, 1996.

[2] Cohen L.F. and Jensen H.J. Open questions in the magnetic behaviour of high-temperature superconductors. *Rep. Prog. Phys.*, **60**, 1581, 1997.

[3] Anderson P.W. Theory of flux creep in hard superconductors. *Phys. Rev. Lett.*, **9**(7), 309, 1962.

[4] Anderson P.W. and Kim Y.B. Hard superconductivity : Theory of the motion of Abrikosov flux lines. *Rev. Mod. Phys.*, **36**, 39, 1964.

[5] Worthington T.K., Gallagher W.J., Kaiser D.L., Holtzberg F.H., and Dinger T.R. The anisotropic nature of the superconducting properties of single crystal $YBa_2Cu_3O_{7-x}$. *Physica C*, **153-155**, 32, 1988.

[6] Yeshurun Y. and Malozemoff A.P. Giant flux creep and irreversibility in an Y-Ba-Cu-O crystal : An alternative to the superconducting-glass model. *Phys. Rev. Lett.*, **60**, 2202, 1988.

[7] Blatter G., Feigel'man M.V., Geshkenbein V.B., Larkin A.I., and Vinokur V.M. Vortices in high temperature superconductors. *Rev. Mod. Phys.*, **66**, 1125, 1994.

[8] Breech F. and Cross L. Optical micromission stimulated by a ruby laser. *Appl. Spectroscopy*, **16**, 59, 1962.

[9] Miller J.C. *History, Scope and Future of Laser Ablation in Laser Ablation : Principles and Applications by J.C. Miller (ed.)*, chapter 1. Springer-Verlag, 1994.

[10] Ready J.F. *Appl. Phys. Lett.*, **3**, 1362, 1963.

[11] Smith H.M. and Turner A.F. Vacuum deposited thin films using a ruby laser. *Appl. Optics*, **4**, 147, 1965.

[12] Dijkkamp D., Venkatesan T., Wu X.D., Shaheen S.A., Jisrawi N., Min-Lee Y.H., McLean W.L., and Croft M. Preparation of Y-Ba-Cu oxide superconductor thin films using pulsed laser evaporation from high T_c bulk material. *Appl. Phys. Lett.*, **51**, 619, 1987.

[13] Wu X.D., Dijkkamp D., Ogale S.B., Inam A., Chase E.W., and Miceli P.F. Epitaxial ordering of oxide superconducting thin films on (001) $SrTiO_3$ prepared by pulsed laser evaporation. *Appl. Phys. Lett.*, **51**, 861, 1987.

[14] Venkatesan T.V. *Pulsed-Laser Deposition of High-Temperature Superconducting Thin Films in Laser Ablation : Principles and Applications by J.C. Miller (ed.)*, chapter 4, page 85. Springer-Verlag, 1994.

[15] Venkatesan T., Wu X.D., Inam A., and Wachtman J.B. Observation of two distinct components during pulsed laser deposition of high-T_c superconducting films. *Appl. Phys. Lett.*, **52**, 1193, 1988.

[16] Saenger K.L. Bibliography of films deposited by pulsed laser deposition. In Chrisey D.B. and Hubler G.K., editors, *Pulsed Laser Deposition of Thin Films*, chapter Appendix A, page 581. John Wiley and Sons, 1994.

[17] Moon B.M., Platt C.E., Schweinfurth R.A., and Van Harlingen D.J. In situ pulser laser deposition of superconducting $Ba_{1-x}K_xBiO_3$. *Appl. Phys. Lett.*, **59**, 1905, 1991.

[18] Chern M.Y., Gupta A., and Hussey B.W. Layer-by-layer deposition of $La_{1.85}Sr_{0.15}CuO_x$ films by pulsed laser ablation. *Appl. Phys. Lett.*, **60**, 3045, 1992.

[19] Cheenne A., Perriere J., Kerherve F., and Hauchecorne G. Laser-assisted deposition of thin BiSrCaCuO films. *Mater. Rec. Soc. Symp. Proc.*, **191**, 229, 1990.

[20] Geohagan D.B., Mashburn D.N., Culbertson R.J., and Pennycook S.J. Pulsed laser deposition of thin superconducting films of $HoBa_2Cu_3O_{7-x}$ and $YBa_2Cu_3O_{7-x}$. *J. Mater. Res.*, **3**, 1169, 1988.

[21] Gupta A., Koren G., Tsuei C.C., Segmuller A., and McGuire T.R. Deposition of epitaxial thin films of $Nd_{1.85}Ce_{0.15}CuO_{4-y}$. *Appl. Phys. Lett.*, **55**, 1795, 1989.

[22] Narayan J., Biunno N., Singh R., Holland O.W., and Auciello O. Formation of thin superconducting films by the laser processing method. *Appl. Phys. Lett.*, **51**, 1845, 1987.

[23] Neifeld R.A., Gunapala S., Liang C., Shaheen S.A., and Croft M. Systematics of thin films formed by excimer laser ablation: results on $SmBa_2Cu_3O_7$. *Appl. Phys. Lett.*, **53**, 703, 1988.

[24] Johs B., Thompson D., Ianno N.J., Woollam J.A., and Liou S.H. Preparation of high-T_c Tl-Ba-Ca-Cu-O thin films by pulsed laser evaporation and Tl_2O_3 vapor processing. *Appl. Phys. Lett.*, **54**, 1810, 1989.

[25] Gallop J.C. Developments in HTS devices. *Supercond. Sci. Technol.*, **3**, 20, 1990.

[26] Lynn J.W. Magnetic properties. In J.W. Lynn, editor, *High Temperature Superconductivity*, chapter 8, page 268. Springer-Verlag, 1990.

[27] Jorgenson J.D., Beno M.A., Hinks J.D., Soderholm L., Volin K.J., Hitterman R.L., Grace J.D., and Schuller I.K. Oxygen ordering and the orthorhombic-to-tetragonal phase transistion in $YBa_2Cu_3O_{7-x}$. *Phys. Rev. B*, **36**, 3608, 1987.

[28] Wu M.K., Ashburn J.R., and Torng C.J. *et al.* Superconductivity at 93K in a new mixed-phase Y-Ba-Cu-O compound system at ambient pressure. *Appl. Phys. Lett.*, **58**, 908, 1987.

[29] Wang. C.S. Electronic structure, lattice dynamics and magnetic interactions. In Lynn J.W., editor, *High Temperature Superconductivity*, chapter 5. Springer-Verlag, 1990.

[30] Poole C.P., Farach H.A., and Creswick R.J. *Superconductivity.* Academic Press, San Diego, 1st edition, 1995.

[31] Beech F., Miraglia S., Santora A., and Roth R.S. Neutron study of the crystal structure and vacancy distribution in the superconductor $Ba_2YCu_3O_{9-\delta}$. *Phys. Rev. B*, **35**, 8778, 1987.

[32] Rothman S.L., Routbort J.L., Welp U., and Baker J.E. Anisotropy of oxygen tracer diffusion in single crystal $YBa_2Cu_3O_{7-\delta}$. *Phys. Rev. B*, **44**, 2326, 1991.

[33] Sequeira A., Rajagopal H., and Sastry P.V. Stability of 4-year old $YBa_2Cu_3O_{7-x}$. *Physica B*, **180-181**, 429, 1992.

[34] Phillips J.A. Substrate selection for high-temperature superconducting thin films. *J. Appl. Phys.*, **79**, 1829–1848, 1996.

[35] Pashley D.W. In Matthews J.W., editor, *Epitaxial Growth.* Academic Press, New York, U.S.A., 1975.

[36] Guo R., Bhalla A.S., Cross L.E., and Roy R. *J. Mater. Res.*, **9**, 1644, 1994.

[37] Superconductive Components Inc. 1995 Product Guide. Columbus, Ohio., U.S.A., 1995.

[38] Escete Single Crystal Technology. HTSC Substrates Catalogue. Enschede, The Nederlands, 1995.

[39] Chiang Y.M., Birnie D.P., and Kingery W.D. *Physical Ceramics : Principles for Ceramic Science and Engineering.* John Wiley and Sons, New York, 1997.

[40] Moeckly B.H., Russek S.E., Lathrop D.K., Buhrman R.A., Li J., and Mayer J.M. Growth of $YBa_2Cu_3O_7$ thin films on MgO : The effect of substrate preparation. *Appl. Phys. Lett.*, , 1687, 1990.

[41] Awaji T., Sakuta K., Sakagutchi Y., and Kobayashi T. *Jpn. J. Appl. Phys.*, **31**, L642, 1992.

[42] De Gennes P.G. *Superconductivity of Metals and Alloys.* Addison-Wesley, New York, 1966.

[43] Ullmaier H. Springer Tracts in Modern Physics. In G. Hohler, editor, *Irreversible Properties of Type-II Superconductors.* Springer-Verlag, Berlin, 1975.

[44] Li J. *Flux Pinning Phenomenon in High-T_c Superconductors.* PhD thesis, University of Amsterdam, 1992.

[45] Iye Y., Tamegai T., Sakakibara T., Goto T., and Miura N. The anisotropic superconductivity of $RBa_2Cu_3O_{7-\delta}$ (R=Y, Gd and Ho) single crystals. *Physica C*, **153-155**, 26, 1988.

[46] Chaki T.K. and Rubinstein M. Normal-state resistivity of the high-T_c compound $YBa_2Cu_3O_{7-\delta}$. *Phys. Rev. B*, **36**, 7259, 1987.

[47] Abrikosov A.A. On the magnetic properties of superconductors of the second group. *Soviet Phys.-JETP*, **5**, 1174, 1957.

[48] Huebener R.P. *Magnetic Flux Structures in Superconductors.* Springer-Verlag, Berlin, 1979.

[49] Sonier J.E., Brewer J.H., and Kiefl R.F. Muon spin resonance of the vortex state in type-II superconductors. *Rev. Mod. Phys.*, **72**, 769, 2000.

[50] Orlando T.P. and Delin K.A. *Foundations of Applied Superconductivity.* Addison-Wesley, Reading, Massachusetts, U.S.A., 1991.

[51] Pathria R.K. *Statistical Mechanics.* Pergamon Press, Oxford, 1972.

[52] Porter D.A. and Easterling K.E. *Phase Transformations in Metals and Alloys.* Chapman and Hall, 2nd edition, 1992.

[53] Geskenbein V.B. and Larkin A.I. Time dependence of the magnetic moment of high-temperature superconductors. *Sov. Phys. JETP*, **68**, 639, 1989.

[54] Thompson J.R., Sun Y.R., Malozemoff A.P., Christen D.K., Kerchner H.R., Ossandon J.G., Marwick A.D., and Holtzberg F. Reduced flux motion via flux creep annealing in high-j_c single-crystal YBa_2Cu_3O. *Appl. Phys. Lett.*, **59**, 2612, 1991.

[55] Maley M.P., Willis J.O., Lessure H., and McHenry M.E. Dependence of flux-creep activation energy upon current density in grain-aligned $YBa_2Cu_3O_{7-x}$. *Phys. Rev. B*, **42**, 2639, 1990.

[56] Hagen C.W. and Griessen R. Distribution of activation energies for thermally activated flux motion in high-T_c superconductors: An inversion scheme. *Phys. Rev. Lett.*, **62**, 2857, 1989.

[57] Feigel'man M.V., Geshkenbein V.B., Larkin A.I., and Vinokur V.M. Theory of collective flux creep. *Phys. Rev. Lett.*, **63**, 2303, 1989.

[58] E. Zeldov, N.M. Amer, G. Koren, A. Gupta, M.W. McElfresh, and R.J. Gambino. Flux creep characteristics in high-temperature superconductors. *Appl. Phys. Lett.*, **56**, 680, 1990.

[59] Vinokur N.M., Feigel'man M.V., and Geshkenbein V.B. Exact solution for flux creep with logarithmic $U(j)$ dependence: Self-organized critical state in high-T_c superconductors. *Phys. Rev. Lett.*, **67**, 915, 1991.

[60] Bean C.P. Magnetization of hard superconductors. *Phys. Rev. Lett.*, **8**, 250, 1962.

[61] Bean C.P. Magnetization of high-field superconductors. *Rev. Mod. Phys.*, **36**, 31, 1964.

[62] Kim Y.B., Hempstead C.F., and Strnad A.R. Critical persistent currents in hard superconductors. *Phys. Rev. Lett.*, **9**, 306, 1962.

[63] Kittel C. *Introduction to Solid State Physics*. John Wiley and Sons, new york, u.s.a. edition, 1996.

[64] Frankel D.J. Critical state model for the determination of critical currents in disk-shapes superconductors. *J. Appl. Phys.*, **50**, 5402, 1979.

[65] Daumling M. and Larbalestier D.C. Critical state in disk-shaped superconductors. *Phys. Rev. B.*, **40**, 9350, 1989.

[66] Mikheenko P.N. and Kuzovlov Y.E. Inductance measurements of HTSC films with high critical currents. *Physica C*, **204**, 229, 1993.

[67] Zhu J., Mester J., Lockhart J., and Turneaure J. Critical states in 2D disk-shaped Type-II superconductors in periodic external magnetic field. *Physica C*, **212**, 216, 1993.

[68] Jackson J.D. *Classical Electrodynamics*. John Wiley and Sons, second edition, 1975.

[69] Hildebrand F.B. *Advanced Calculus for Applications.* Prentice-Hall, 1962.

[70] Landau L.D. and Lifshitz E.M. *Theoretical Physics : Electrodynamics of continuous media*, volume 8. Nauka, Moscow, 1982.

[71] Gupta D., Donaldson W.R., and Kadin A.M. Rapid flux motion and critical state dynamics in a superconducting disk. *J. Appl. Phys.*, **78**, 372, 1995.

[72] Chu W.K., Mayer J.W., and Nicolet M.A. *Backscattering Spectrometry.* Academic Press, New York, U.S.A., 1978.

[73] Doolittle L.R. Algorithms for the rapid simulation of Rutherford backscattering spectra. *Nucl. Inst. Meth.*, **B9**, 344, 1985.

[74] Rutherford E. and Geiger H. *Phil. Mag.*, **6**, 698, 1910.

[75] Maritz E.L. Private communication. 2001.

[76] Cullity B.D. *Elements of X-ray diffraction.* Addison-Wesley, Reading, Massachusetts, U.S.A., 1978.

[77] Magonov S.N. and Whangbo M.H. *Surface Analysis with STM and AFM.* VCH Verlaggesellschaft, Weinheim, Germany, 1996.

[78] Binnig G., Quate C.F., and Gerber C. Atomic force microscope. *Phys. Rev. Lett.*, **56**, 930, 1986.

[79] Topometrix, http://www.topometrix.com. *Topometrix scanning probe microscope - user's guide*, 1998.

[80] D.G. Xenikos and T.R. Lemberger. *ac* Susceptibility apparatus for measuring the transition temperature of high-T_c crystals, sintered samples, and films. *Rev. Sci. Instrum.*, **60**, 831, 1989.

[81] Hatta S., Higashini H., and Wasa K. Meissner effect in high-T_c superconductive thin films. *Japan. Jour. Appl. Phys.*, **26**, 724, 1987.

[82] Fiory A.T. and Hebard A.F. Penetration depths of high-T_c films measured by two-coil mutual inductances. *Appl. Phys. Lett.*, **52**, 2165, 1988.

[83] Jaccard Y., Theron R., Jeanneret B., Meyer R., Leeman C., and Martinoli P. Ac inpedance measurements of two-dimensional superconductors. *IEEE Trans. Appl. Supercond.*, **3**, 1640, 1993.

[84] Lee J.Y., Kim Y.H., Hahn T.S., and Choi S.S. Determining the absolute value of penetration depth of large area films. *Appl. Phys. Lett.*, **69**, 1637, 1996.

[85] Lee J.Y., Kim Y.H., Hahn T.S., and Choi S.S. Optimization of drice coil for inductive measurement of absolute $\lambda(T)$ of superconductor films. *IEEE Trans. Appl. Supercond.*, **7**, 1620, 1997.

[86] Miller J.C. and Huglund R.F., editors. *Laser Ablation and Desorption.* Academic Press, San Diego, 1998.

[87] Chrisey D.B. and Hubler G.K., editors. *Pulsed Laser Deposition of Thin Films.* John Wiley and Sons, New York, 1994.

[88] Paine D.C. and Bravman J.C., editors. *Laser Ablation for Materials Synthesis.* Materials Research Society, Pittsburgh, 1990.

[89] Xu S.F., Tian Y.J., Lu H.B., Cui D.F., Chen Z.H., Li L., and Yang G.Z. The effect of laser energy density and target-substrate distance on the quality on $YBa_2Cu_3O_{7-x}$ thin films. *Supercond. Sci. Technol.*, **7**, 435, 1994.

[90] Kim H.S. and Kwok H.S. Correlation between target-substrate distance and oxygen pressure in pulsed laser deposition of $YBa_2Cu_3O_7$. *Appl. Phys. Lett.*, **61**(18), 2234, 1992.

[91] Kumar V. and Gupta A.K. Design and performance of a simple substrate heater for *in situ* deposition of high-T_c superconducting thin films. *Meas. Sci. Technol.*, **4**, 790, 1993.

[92] Balachandran U., Poeppel R.B., Emerson J.E., Johnson S.A., Lanagan M.T., Youngdahl C.A., Shi D., and Goretta K.C. Systhesis of phase pure orthorhombic $YBa_2Cu_3O_x$ under low oxygen pressure. *Materials Lett.*, **8**, 454, 1989.

[93] Bunker B.C., Voigt J.A., Doughty D.A., Lamppa D.L., and Kimball K.M. *High Temperature Superconducting Materials Preparation, Properties and Processing.* Marcel Dekker Inc., 1988.

[94] Superconductive Components Inc., Columbus, Ohio, U.S.A., 1995 Product Guide, 1995.

[95] Maaza M., Bouziane K., Maritz E.J., McLachlan D.S., Swanepoel R., Frigerio J.M., and Every M. Direct production of thermochromic VO_2 thin film coatings by pulsed laser ablation. *Optical Materials*, **15**, 41, 2000.

[96] Adler D. Mechanisms for metal-nonmetal transitions in transition-metal oxides and sulfides. *Rev. Mod. Phys.*, **40**(4), 714, 1968.

[97] Jorgensen C. Electrochromic and thermochromic materials for solar energy applications with emphasis on niobium and vanadium oxides. Technical report, Lawrence Berkeley Laboratory, Berkeley, CA, USA, 1984.

[98] Granqvist C.G. *Handbook of Inorganic Chromogenic Materials.* Elsevier, Amsterdam, 1995.

[99] E.B. Nyeanchi, X. Zhu, I.P. Krylov, and N. Jacobs. Ferromagnetic ground state in $La_{0.5}Cu_{0.5}MnO_3$ thin films. *EuroPhysics Letters*, **48**, 228, 1999.

[100] Vlasov V.P., Gel'man Y.A., and Yakimkin V.N. Substrate heater for molecular beam epitaxy. *Instrum. Experim. Tech.*, **37**, 519, 1994.

[101] Inameti E.E., Raven M.S., Wan Y.M., and Murray B.G. A substrate heater design for high temperature deposition in an oxidizing plasma. *Vacuum*, **43**, 121, 1992.

[102] Appleyard N.J., Jackson T.J., Welch R.G., Palenque E.R., and Palmer S.B. Design and performance of an inexpensive substrate heater for off-axis thin film deposition. *Meas. Sci. Technol.*, **6**, 337, 1995.

[103] Vase P., Shen Q.Y., Holst T., Hagensen M., and Freltoft T. Substrate heater for large area $YBa_2Cu_3O_x$ film growth without electrical feedthroughs. *Physica C*, **235-240**, 641, 1994.

[104] Campion R., Ormson R.G., Bashford C.A., and King P.J. Design and persformance of a reliable and low cost substrate heater for superconducting thin film deposition. *Vacuum*, **46**, 195, 1995.

[105] Reade R.P. *Ion-Assisted Laser Deposition of Intermediate Layers for $YBa_2Cu_3O_{7-\delta}$ Thin Film Growth on Polycrystalline and Amorphous Substrates.* PhD thesis, University of California, 1993.

[106] Vase P., Jensen M.B., Hansen K.L., Gadegaard N., and Gaarde P. Deposition of high j_c $YBa_2Cu_3O_x$ films on 2" sapphire substrates. *Inst. Phys. Conf. Ser.*, **148**, 871, 1995.

[107] Clark J.H. and Weston R.G. An inexpensive multi-target carousel for PLD systems. *Meas. Sci. Technol.*, **7**, 823, 1996.

[108] Clark J.H., Donaldson G.B., and Bowman R.M. A fully automated pulsed laser deposition system for HTS multilayer devices. *IEEE Trans. Appl. Supercond.*, **5**, 1661, 1995.

[109] Robertazzi R.P. and Oh B.D. Non-silver paste method for making thermal contact to substrates for high-T_c film growth. *IEEE Trans. Appl. Supercond.*, **3**, 1094, 1993.

[110] Kromann R., Bilde-Sørensen J.B., de Reus R., Andersen N.H., Vase P., and Freltoft T. Relation between critical current densities and epitaxy of $YBa_2Cu_3O_7$ thin films on MgO(100) and $SrTiO_3$(1000). *J. Appl. Phys.*, **71**, 3419, 1992.

[111] Lowndes D.H. Growth and doping of compound semiconductor films by pulsed laser ablation. In Miller J.C. and Haglund R.F., editors, *Laser Ablation and Desorption*, volume 30 of *Experimental Methods in the Physical Sciences*, chapter 11, pages 475–571. Academic Press, San Diego, 1998.

[112] Geohegan D.B. Diagnostics and characteristics of pulsed laser deposition laser plasma. In Chrisey D.B. and Hubler G.K, editors, *Pulsed Laser Deposition of Thin Films*, chapter 5, pages 115–165. John Wiley and Sons Inc., New York, U.S.A., 1994.

[113] Nemchinov I.V. and Popov S.V. Time of start of screening of a surface evaporating under the influence of laser radiation. *JETP Lett.*, **11**, 312, 1970.

[114] Singh R.K. and Narayan J. Pulsed laser evaporation technique for deposition of thin films : Physics and theoretical model. *Phys, Rev. B.*, **41**, 8843, 1990.

[115] Becker C.H. and Pallix J.B. Laser ablation in bulk $YBa_2Cu_3O_{7-\delta}$ and cluster emission. *J. Appl. Phys.*, **64**, 5152, 1988.

[116] Saenger K.L. Angular distribution of ablated material. In Chrisey D.B. and Hubler G.K., editors, *Pulsed Laser Deposition of Thin Films*, chapter 7, pages 199–227. John Wiley and Sons, New York, U.S.A., 1994.

[117] Muenchausen R.E., Hubbard K.E., Foltyn S., Estler R.C., Nogar N.S., and Jenkins C. Effects of beam parameters on excimer laser deposition of $YBa_2Cu_3O_{7-x}$. *Appl. Phys. Lett.*, **56**, 578, 1990.

[118] Akhsakhalyan A.D., Gaponov S.P., Luchin V.I., and Chirimanov A.P. Angular distribution of a laser ablation plasma expanding into vacuum. *Sov. Phys. Tech. Phys.*, **33**, 1146, 1988.

[119] Geohegan D.B. Fast ICCD photography of YBCO laser ablation plume propagation in vacuum and ambient oxygen. *Appl. Phys. Lett.*, **60**, 2732, 1992.

[120] Carlson D.J., Siegal M.P., Phillips J.M., Tiefel T.H., and Marchall J.H. Stoichiometric effects in epitaxial $Ba_{2-x}Y_{1-y}Cu_{3-z}O_{7-\delta}$ thin films on $LaAlO_3(100)$. *J. Mater. Res.*, **5**(12), 2797, 1990.

[121] Venkatesan T., Chase E.W., Wu X.D., Inam A., Chang C.C., and Shokoohi F. *Appl. Phys. Lett.*, **53**, 243, 1988.

[122] Foltyn S.R. Surface modification of materials by cumulative laser irradiation. In Chrisey D.B. and Hubler G.K., editors, *Pulsed Laser Deposition of Thin Films*, page 89. John Wiley and Sons, New York, U.S.A., 1994.

[123] Sakeek H.F., Smyth C.C., Rowan C.M., and Tuner R.J. YBaCuO/PrBaCuO multilayers by excimer laser ablation. *Supercond. Sci. Technol.*, **4**, 613, 1991.

[124] Sakeek H.F., Higgens M., Graham W.G., Morrow T., Turner R.J., and Walmsley D.G. Superconducting $YBa_2Cu_3O_7$ thin films on MgO by KrF laser ablation : Optimization of deposition parameters. *J. Appl. Phys.*, **70**, 2455, 1991.

[125] Inam A. and Wu X.D. Pulsed laser etching of high-T_c−superconducting films. *Appl. Phys. Lett.*, **51**, 1112, 1987.

[126] Dam B., Rector J., Chang M.F., Kars S., de Groot D.G., and Griessen R. The laser ablation threshold of $YBa_2Cu_3O_{6+x}$ as revealed by using projection optics. *Appl. Surf. Science*, **86**, 13, 1995.

[127] Bierleutgeb K. and Proyer S. Pulsed-laser deposition of Y-Ba-Cu-O films : The influence of fluence and oxygen pressure. *Appl. Surf. Sci.*, **109/110**, 332, 1997.

[128] Schneider M., Shuller I.K., and Rahman A. Expitaxial growth of silicon: A molecular-dynamics simulation. *Phys. Rev. B.*, **36**, 1340, 1987.

[129] Shen W.P. and Kwok H.S. Crystalline phases of II-IV compound semiconductors grwon by pulsed laser deposition. *Appl. Phys. Lett.*, **65**, 2162, 1994.

[130] Zheng J.P. and Kwok H.S. Low resistivity indium tin oxide films by pulsed laser deposition. *Appl. Phys. Lett.*, **63**, 1, 1993.

[131] Kristallhandel Kelpin. *Surface Characterisation of Substrates*, 1995.

[132] Mannhart J., Anselmetti D., Bednorz J.G., Gerber C., Muller K.A., and Scholm D.G. Pinning centers in $YBa_2Cu_3O_{7-\delta}$ films. *Z. Phys. B*, **86**, 177, 1992.

[133] Liu J.Z. and Li L. The growth mechanism of pulsed laser deposited and dc magnetron sputtered high-T_c $YBa_2Cu_3O_7$ thin films. *Physica C*, **282-287**, 549, 1997.

[134] Roshko A., Rudman D.A., Vale L.R., Goodrich L.F., Moreland J., and Beck H.L. Influence of deposition parameters on properties of laser ablated $YBa_2Cu_3O_{7-\delta}$ films. *IEEE Trans. Appl. Supercond.*, **3**, 1590, 1993.

[135] Cimberle M.R., Diaspro A., Giannini E., Grassano G., Marre D., Pallecchi I., Putti M., Rolandi R., and Siri A.S. RHEED/AFM analysis of YBCO epitaxial thin films grown by laser MBE. *Physica C*, **282-287**, 679, 1997.

[136] King S., Coccia L., and Boyd I.W. SEM observations of YBCO on as-received and heat-treated MgO substrates. *Appl. Surf. Sci.*, **86**, 134, 1995.

[137] Volmer M. and Weber A. *Z. Phys. Chem.*, **119**, 277, 1926.

[138] Bauer E. *Z. Krist.*, **110**, 372, 1958.

[139] Krylov I.P., Maritz E.J., and Nyeanchi E.B. Remanent flux creep in $YBa_2Cu_3O_{7-\delta}$ films in the critical region. *Phys. Rev. B*, **58**, 14609, 1998.

[140] Krylov I.P., Maritz E.J., and Nyeanchi E.B. Remanent flux creep in $YBa_2Cu_3O_{7-\delta}$ films in the regime of critical fluctuations. In P. Vincenzini, editor, *Science and Engineering of HTC Superconductivity*, page 491, Faenza, Italy, 1999. Techna.

[141] Conductus. *User's Manual for iMAG HTS Multi-Channel SQUID System.* Conductus, San Diego, California, 1st edition, 1995.

[142] LakeShore. *The Model DRC-91CA Temperature Controller Users Guide.* LakeShore, Westerville, Virginia, U.S.A., 1990.

[143] Van der Pauw L.J. A method of measuring specific resistivity and Hall effect of discs of arbitrary shape. *Philips Research Reports*, **13**, 1, 1958.

[144] Smits F.M. Measurement of sheet resistivities with the four-point probe. *The Bell System Technical Journal*, **37**, 711, 1958.

[145] Charles R.J. and Harrison W.A. Size effect in nuclear magnetic resonance. *Phys. Rev. Lett.*, **11**, 75, 1963.

[146] Sosnowski J., Clad R., Kuentzler R., and Villminot S. Magnetic hysteresis effects in high-T_c oxide superconductors. *Supercond. Sci. Technol.*, **5**, 85, 1992.

[147] Moraitakis E., Pissas M., and Niarchos D. High-field behaviour of the magnetic response of a hard superconducting thin disc and application to hysteresis loops of $YBa_2Cu_3O_{7-\delta}$. *Supercond. Sci. Technol.*, **8**, 647, 1995.

[148] Darhmaoui H., Jung J., Talvacchio J., Mohamed M.A.K., and Friedrich L. Temperature dependence of the magnetic-flux penetration into disk-shaped $YBa_2Cu_3O_{7-\delta}$ thin films. *Phys. Rev. B*, **53**, 12330, 1996.

[149] Klupsch T., Strasser T., Habisreuther T, Gawalek W., Gruss S., May H., Palka R., and Mora Serrano F.J. Field mapping characterization for axially magnetized, superconducting cylinders in the remanent critical state: Theory and experiment. *J. Appl. Phys.*, **82**, 3035, 1997.

[150] Dorosinshii L.A. and Polyanskii A.A. Determination of the critical current distribution in $1-2-3$ single crystals by magnetic flux patterns observed on the sample surface. *Physica C*, **212**, 211, 1993.

[151] Joos C., Warthmann, Forkl A., and Kronmuller. High-resolution magneto-optical imaging of critical currents in $YBa_2Cu_3O_{7-\delta}$ thin films. *Physica C*, **299**, 215, 1998.

[152] Jeffery M., Van Duzer T., Kirtley J.R., and Ketchen M.B. Magnetic imaging of moat-guarded superconducting electronic circuits. *Appl. Phys. Lett.*, **67**, 1769, 1995.